Title

An Oligomer Approach for Advancing the Field of Organic Electronics

Permalink

https://escholarship.org/uc/item/24v191k4

Author

Wang, Yue

Publication Date

2014

Peer reviewed|Thesis/dissertation

UNIVERSITY OF CALIFORNIA

Los Angeles

An Oligomer Approach for Advancing the Field of Organic

Electronics

A dissertation submitted in partial satisfaction of the

requirements for the degree Doctor of Philosophy

in Chemistry

By

Yue Wang

2014

ABSTRACT OF THE DISSERTATION

An Oligomer Approach for Advancing the Field of Organic Electronics

By

Yue Wang

Doctor of Philosophy in Chemistry

University of California, Los Angeles, 2014

Professor Richard B. Kaner, Chair

The rapid development of synthetic conjugated materials has enabled organic electronic devices such as solar cells, field-effect transistors and sensors to rival their inorganic counterparts in performance at significantly lower cost. Conducting polymers such as polyaniline constitute an important class of such materials, but their properties are difficult to study due to polydispersity, complex chain conformations and lack of solubility. In particular, assembling conducting polymers into highly crystalline domains similar to that of small molecule (semi)conductors has proven to be challenging, which has limited their integration into electronic devices that require high carrier mobility and stability such as organic field-effect transistors and solar cells. On the other hand, oligomers represent a unique middle ground between conducting

polymers and molecular (semi)conductors because oligomers (e.g. oligoanilines) retain the chemical properties of the parent polymer, while also possessing properties typically associated with molecular (semi)conductors especially in regard to monodispersity and self-assembly. In this thesis, an oligomer approach for advancing the field of conducting polymers is presented. A myriad of conjugated oligomers are examined as the more structurally rigid, pure, and soluble model systems to tackle important challenges in this field. This approach has opened new opportunities for (1) understanding the fundamental packing, transport, and self-assembly properties for polymers; (2) the rational design of high performance conducting polymers by analyzing the oligomer building blocks; (3) realizing the long-sought solution-based bottom-up growth for vertically oriented arrays of organic single crystals; and (4) deciphering the role of oligomers in improving the crystallinity of the parent polymers. The advancement of knowledge in these fields has also allowed us to create high performance hybrid solar cells, complex core/shell nanostructures, and microcontact printing methods with nanoscale resolution.

The dissertation of Yue Wang is approved.

_____

Xiangfeng Duan

_____

Yang Yang

_____

Richard B. Kaner, Committee Chair

University of California, Los Angeles

2014

Dedicated to Les

Table of Contents

Acknowledgments

Choose a job you love, and you will never have to work a day in your life.

–Confucius

Graduate school was a journey that I embarked upon out of pure passion for science. Looking back, I have to say that the past five years have been the time of my life. Many people rush through life without ever finding their true passion, let alone given the opportunity to pursue it without any reservations. I feel truly blessed to be among the fortunate ones who has a job that requires extremely hard work, yet does not feel like working while doing it. Now, at the end of this amazing journey, I would like to express my most sincere gratitude to all the people who helped me find my destiny, supported me through the hard times, and shared my excitement and accomplishments wholeheartedly.

Hidden gold does not always appear shiny, and I have not always been good at chemistry. I was the worst student in my chemistry class when I first took it. Fortunately, my chemistry teacher, Ms. Hongmei Wang, offered nothing but patience and support. She stepped out of her way and tirelessly spent many hours after class to help me understand the subject in a way that finally made sense to me. Thank you, Ms. Wang, for perceiving my unique abilities and not judging me on a universally set standard when everyone else was busy criticizing me. It was through your kindness and mentorship that I first felt that spark of passion in chemistry, that propelled me to always offer my help, expertise and compassion to those in need.

An interest in science does not always lead to a career in research, and I probably would not be here writing this dissertation if not for my first organic chemistry professor, Dr. Jenny Chen, for perceiving my potential hidden behind the extreme shyness at the time, and consistently encouraging me to explore research, helping me build self-confidence, and the tremendous amount of support that she so selflessly offered. Thank you Jenny, for being that influential mentor who led me to that defining moment in my academic journey.

Nobel laureate Albert Szent-Györgyi described doing science as to see what everyone else has seen but think what no one else has thought. It would have been virtually impossible to develop such an ability without the guidance of all the research advisors I am fortunate enough to have. I cannot express enough gratitude to my first research mentor, Prof. Phoebe Dea from Occidental College, for her sensitivity and patience when I first joined her group as a scared summer REU student who could not get anything right. I would also like to thank my graduate student mentor at the Kaner lab, Dr. Henry Tran, for his very hands-off mentoring style when I worked with him as an undergrad, and for getting me interested in materials research. My first advisor in grad school as well as a current long-term collaborator, Prof. Xiangfeng Duan, has helped me greatly expand my vision and ways of thinking, and embodied me with the working ethics necessary for succeeding in grad school, for which I am truly grateful. My most sincere gratitude goes to my Ph.D. advisor, Prof. Ric Kaner, who was also my undergrad research advisor for one and a half years, for being the source of wisdom and foundation of support. The research freedom that he offered allowed me to find my own style, explore my research interests without any reservations, and most importantly, maintain that pure scientific curiosity that often gets lost when working under the pressure of funding or publishing.

on electrochemistry, Rui Cheng for turning device physics a language possible for me to understand, Yu Chen for his expertise on the Titan TEM, and Jonathan Shaw for providing various transition metal chalcogenide samples. I was fortunate enough to work with two very talented undergrads, Sharon Guan and Xiao Zhang, and would like to thank them for helping with various experiments that saved me so much time. Furthermore, my sincere gratitude goes to all the other Kaner group members that I worked with during grad school, Dr. Robert Kojima, Dr. Sabah Bux, Dr. Jon Wassei, Dr. Tom Farrell, Dr. Miao Xie, Dr. James Ma, Kan Wang, Lisa Wang, Brian McVerry, Chris Turner, Jee Youn Hwang, William Huang, Kris Marsh, Wanmei Sun, Jialin Liu, Cheng-Wei Lin, Mengping Li, Haosen Wang, Yuanlong Shao, Avalon Dismukes, Matt Kowal, Prof. Mir Fazlollah Mousavi, Prof. Jang Myoun Ko, Dr. Hiro Sakurai, for making the Kaner lab such a great place to work and explore!

At last, I'd like to dedicate a very personal thank you to my close friend, C. LesPerance, who untimely passed away during my Ph.D. study. There is an old Chinese saying: I do not want a friend who smiles when I smile, who weeps when I weep, for my own shadow in the pool can do better than that. Thank you for being that entrusted friend who I can always count on for brutal honesty, and for constantly challenging my thoughts and perspectives, being the source of my courage and strength, and helping me believe that "everything is possible" can indeed be possible if I set my mind to it. Thank you for making me the person I am today. This dissertation wouldn't have been possible if not for you.

As Albert Einstein so eloquently put, "Everybody is a genius, but if you judge a fish by its ability to climb a tree, it will live its whole life believing that it is stupid." I have always been that underdog, been that miserable fish attempting to climb. If not for all the good mentors, close

friends, and inspiring role models in my life who supported and believed in me through all the ups and downs, I would have never found who I am and my true passion. Because of all of you, graduate school has been such an amazing journey. Because of all of you, it will be my life-long pursue to be a good mentor to my potential students, uncover their unique qualities, help them feel the excitement of science, and support them through any obstacles in life. Thank you!

Vita

2003	High School Diploma Southwest Weiyu High School Shanghai, China
2008	Bachelor of Science University of California, Los Angeles Los Angeles, CA
2008-2009	Research staff member Fibron Technologies, Inc. Inglewood, CA
2009-2010	NSF-IGERT: Clean Energy for Green Industry (CGI) Fellowship
2010-2013	NSF-Graduate Research Fellowship Program (GRFP)
2011	Excellence in Second Year Academics and Research Award University of California, Los Angeles Los Angeles, CA
2011	Best Poster Award Materials Research Society (MRS) Meeting Boston, MA

2011-current	Norma Stoddard Award Committee University of California, Los Angeles Los Angeles, CA
2012	Ralph and Charlene Bauer Research Award University of California, Los Angeles Los Angeles, CA
2013	First Place, Science as Art Competition Materials Research Society (MRS) Meeting San Francisco, CA
2013	Excellence in Graduate Polymer Research American Chemical Society (ACS) New Orleans, LA
2013	Finalist, Science as Art Competition Materials Research Society (MRS) Meeting San Francisco, CA
2013-current	Reviewer *Organic Electronics* (Elsevier)
2014-current	Reviewer *Journal of Solid State Chemistry* (Elsevier)

Chapter 1. Applications of oligomers for nanostructures conducting polymers

This chapter provides an overview of the distinctive nanostructures that aniline oligomers form and the applications of these oligomers for shaping the nanoscale morphologies and chirality of conducting polymers. We focus on the synthetic methods for achieving such goals and highlight the underlying mechanisms. The clear advantages of each method and their possible drawbacks are discussed. Assembly and applications of these novel organic (semi)conducting nanomaterials are also outlined. We conclude this article with our perspective on the main challenges, new opportunities, and future directions for this nascent yet vibrant field of research.

1.1 Introduction

Since their discovery, conducting polymers have been extensively studied and show great promise in a variety of applications such as light emitting diodes, chemical sensors, photovoltaics, batteries, and supercapacitors.[1] Among the family of conducting polymers, polyaniline has attracted considerable interest because of its stability and unique acid-base doping-dedoping chemistry.[1-2] Polyaniline nanostructures, especially 1-D morphologies such as nanofibers, nanorods, nanowires, and nanotubes have been a particularly attractive class of materials.[2b-e]

There are many different routes to synthesize nanostructured polyaniline. Aside from physical routes to nanofibers such as electrospinning[3] and mechanical stretching,[4] 1-D

nanostructures can be synthesized with the assistance of hard-templates that contain nanoscale pores such as zeolites, anodized aluminum oxide (AAO), and diblock copolymer templates.[5] Soluble soft templates such as surfactants or bulky dopant acids that self-assemble into micelles can also orchestrate the growth of 1-D polymeric nanostructures.[6] Additional methods to produce these structures include nanowire seeding[(7)] and the use of biotemplates.[8] Beside all these approaches that involve additives that are not inherent to the polymer, nanofibers of polyaniline have been produced without any templates or external structural-directing agents.[9] This process involves the spontaneous formation of polyaniline nanofibers by exploiting the intrinsic nature of polyaniline to form anisotropic structures by carefully tuning the polymerization conditions. These methods include interfacial polymerization,[9a, 9b] dilute polymerization of aniline,[9c-e] rapid mixing of monomer and oxidant,[(9f)] and sonochemical and radiolytic-assisted syntheses.[9g, 9h] Nanostructures produced by these routes are easy to purify and scalable, which eliminates the need for external reagents that are not inherent to the polymer. 1-D nanostructures of polyaniline produced via template-free methods have been used in several applications such as sensors and generally exhibit superior performance compared to those that use their conventional bulk counterparts.[10]

Compared to the parent polymer, oligomers of aniline have received far less attention. Reports on aniline oligomers focus mainly on organic synthetic routes to an oligomeric material possessing a bulk, granular morphology.[11] Furthermore, their properties are generally studied experimentally and theoretically to serve as model compounds for polyaniline.[12] Despite the rapid developments in nanostructured polyaniline, little effort has been invested in investigating oligoaniline nanostructures. This is especially surprising considering the success that thiophene oligomers have had both as a useful functional material and as a promising nanomaterial.[13] Both

2

bulk and nanostructured oligothiophenes such as sexithiophene and its derivatives have been studied as independent organic semiconductors and have led to many novel, high performance devices.[13d-i]

Recently, aniline oligomers have finally been brought into the context of nanoscience and quickly made an impact on two areas of nanostructured organic conductive materials.[14] To date, several reports exist on the role of oligoanilines in guiding the shape of polyaniline nanostructures[14a-h] and only a few reports exist on the independent investigation of oligoaniline nanostructures.[14i-k] For example, aniline oligomers can serve as intrinsic additives that can effectively orchestrate the nanostructures of the parent polymers in simple template-free polymerizations.[14a-f] As an independent class of organic nanostructured (semi)conductors like the oligothiophenes, several recent studies have demonstrated their syntheses.[14i-k] Reexamination of structure-property relationships at the nano-level reveals that they exhibit many intriguing properties and have advantages over the parent polymer in a number of ways. In this section, we discuss the developments in this nascent branch of nanostructured organic (semi)conductors and provide an outlook on the enormous amount of untapped opportunities.

1.2 Oligomers as Additives to Polymerizations

Oligomers of aniline have been investigated as an additive in the electrochemical polymerization of aniline almost 20 years before the recent interest in nanoscience research.[13i, 15] Past kinetic studies have shown that the rate-determining step in the initial oxidation of aniline is the generation of dimeric species such as *p*-aminodiphenylamine (aniline dimer), *N,N'*-diphenylhydrazine, and benzidine.[16] Wei *et al*. appear to be the first group to intentionally

3

introduce a small amount of aniline oligomers into the electrochemical polymerization of aniline.[13i] The result, as they anticipated, is a greatly enhanced reaction rate. This suggests that the lower oxidation potential of selected additives could allow them to serve as reaction initiation centers, thus bypassing the usual rate-determining step of monomer coupling to dimer. However, when additives such as *N,N'*-diphenylamine or hydroquinone, which also have a lower oxidation potential than aniline, are used in the system, the rate of polymerization is reduced. Thus, in addition to the lower oxidation potential, the additives also need to have at least one sterically accessible aromatic amino group that can enable them to be incorporated into the polymer chain as part of the backbone. This catalytic effect also applies to the polymerization of aniline derivatives such as *o*-toluidine, *m*-toluidine, and *o*-ethylaniline when approximately 1% of aniline dimer or *p*-phenylenediamine is introduced into the reaction mixture.[15a] Furthermore, the molecular structure and conductivity of the resulting polymer exhibits no apparent difference from that synthesized without any oligomeric additives. This self-catalytic phenomenon is also observed for other conducting polymers including the poly(3-alkylthiophenes) when a thiophene oligomer such as 2,2'-bithiophene (thiophene dimer) or 2,2':5',2"-terthiophene (thiophene trimer) is included in the reaction medium.[15b]

1.2.1 Rapidly mixed reactions

Before exploring the role of oligomer additives in producing nanostructured polyaniline, we briefly review templateless routes to polyaniline nanofibers such as the rapid mixing of monomer and oxidant.[9f] In this process, monomer and oxidant solutions are simply mixed rapidly to suppress secondary growth of nanofibers that eventually leads to micron sized, agglomerated particles. It has been suggested that polyaniline predominately forms nanofibers

when aniline is polymerized under conditions that promote homogeneous nucleation.[17] However, when aniline is polymerized under heterogeneous nucleation conditions, agglomerated morphologies are observed. Despite the advantages of this and other template-free methods, the resulting nanofibers often possess a low aspect ratio, are entangled, and form an interconnected porous film on drying. This material, although suitable for applications that require high surface area, is problematic when post-synthetic assembly or fabrication of single fiber devices is desired. In addition, template-free routes to nanofibers appear to be exclusive to polyaniline. Derivatives of polyaniline and most of other conducting polymers fail to form 1-D nanostructures under similar or identical conditions. Much effort has been devoted to studying the formation mechanism of this process for elucidating the underlying mechanism which would allow ways to extend this simple process to other conducting polymers.[2d, 9, 14i, 18]

1.2.2 Polyaniline nanofibers synthesized with an oligomeric additive

Previous studies indicate that minute amounts of a selected aniline oligomer as an additive can enhance the rate of polymer chain formation.[13i, 15a] Therefore, it was reasoned that introducing an oligoaniline additive into a rapidly mixed reaction could promote homogeneous nucleation by accelerating the rate of polymerization which would thereby produce high aspect ratio 1-D nanostructures.[14a] Indeed, experiments confirm that 1-D nanostructures that are longer and less entangled than what is typically observed form when a catalytic amount of aniline dimer or other structurally similar additives like *p*-phenylenediamine are intentionally introduced into a standard rapidly mixed reaction (**Figure 1.1**).[14a] In a typical reaction, 1-2 mol % of the selected aniline oligomer is dissolved in a minimal amount of methanol. This solution is then added to

the aniline monomer in a 1.0 M HCl aqueous solution. The mixture is rapidly mixed with an oxidant solution and left undisturbed for 1 day for the reaction to proceed. The final product is purified by dialysis, centrifugation, or filtration to remove the excess acid and byproducts of the oxidant. No special purification steps are required to obtain pure polyaniline nanofibers because the oligomeric additives are incorporated into the polymer backbone.
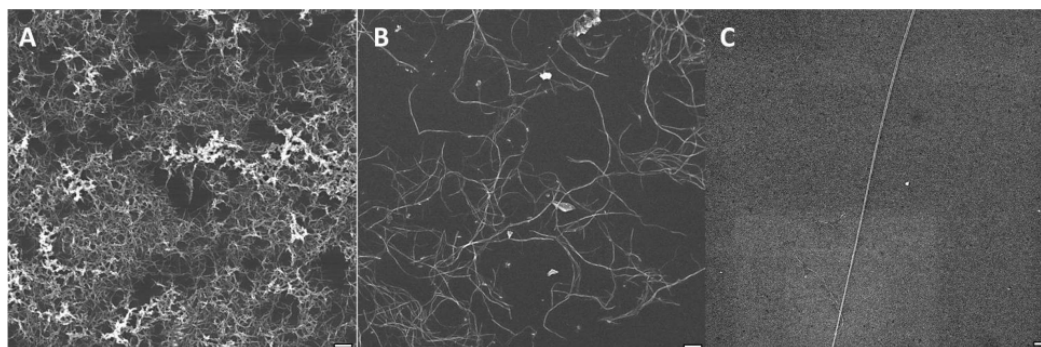
Figure 1.1. SEM images of polyaniline nanofibers synthesized (a) without any additives, (b) with *p*-phenylenediamine, and (c) with aniline dimer. Scale bars = 1 μm. Adapted with permission from (14a). Copyright **2008**, American Chemical Society.

Open-circuit potential (OCP) has been widely used to study the kinetics of oxidative chemical polymerizations.[19] The OCP of polyaniline and its derivatives typically contains three regions: a short induction period (t_1), the formation of the pernigraniline oxidation state (t_2), and finally a rapid decay in potential characteristic of reduction of pernigraniline to the emeraldine oxidation state (t_3). Therefore a shorter $t_1 + t_2$ time represents a faster polymerization rate. When a small amount of aniline dimer or *p*-phenylenediamine is added to the polymerization of aniline, the $t_1 + t_2$ time in OCP is significantly reduced, indicating a substantial increase in polymerization rate. This enhancement in reaction rate appears to be the most important factor

6

that leads to the change in morphology from an entangled mat of nanofibers without oligomers to the longer, less entangled nanowires with an oligomeric additive. According to classical nucleation theory, homogeneous nucleation is achieved in aqueous solutions by creating sufficiently high levels of supersaturation. When the degree of supersaturation increases to a critical value, the activation energy becomes sufficiently low that spontaneous and rapid nucleation can occur. In other words, when the nucleus of the stable phase reaches a critical size, growth can occur if the surroundings of the nuclei are sufficiently supersaturated. With the addition of an oligomeric initiator such as the aniline dimer to the aniline polymerization medium, supersaturation is quickly achieved, thereby greatly enhancing the polymerization rate. Therefore, homogeneous nucleation dominates, while diffusion to heterogeneous nucleation centers is limited, leading to nanofiber formation. The homogeneous nucleation mode is also evident from simply examining the container side walls. For polymerization with an oligomeric promoter, the container side walls are clear, indicating the growing polymer chain did not diffuse to heterogeneous nucleation sites such as the container wall. On the other hand, a thin film of polyaniline covers the sidewalls and any other exposed surfaces in control reactions where an additive was not used. The fibrillar morphology can be further explained by the intermolecular oligomeric nucleation pathway: the aniline oligomeric additives rapidly create a high oligomer concentration in the formative stages of the reaction and form semi-ordered regions that serve as embryonic nuclei for further polymerization, leading to the observed anisotropic growth. In addition, the ratio of monomer to additive is critical for obtaining the observed longer and less entangled nanofibrillar morphology. Too high a ratio results in nanofibers that are indistinguishable from those formed without any additives, while too low a ratio results in a smooth, film-like morphology.

No apparent differences in redox properties and oxidation states are observed for the oligomer-initiated polyaniline nanofibers compared to conventional polyaniline nanofibers as supported by cyclic voltammetry (CV) and UV-vis data. However, including an oligomeric additive in the aniline polymerization reaction has a profound effect on the molecular weight of the resulting polyaniline nanofibers. Gel permeation chromatography (GPC) studies reveal that the molecular weight distribution and polydispersity index (PDI) of the oligomer-initiated polyaniline is lower than what is typically observed without the addition of an oligomeric initiator (**Table 1.1**).

Table 1.1. Summary of Weight-Average Molecular Weight (M_w), Number-Average Molecular Weight (M_n), and Polydispersity Index (PDI = M_w/M_n) of Conventional Polyaniline Nanofibers, Polyaniline Nanofibers Synthesized with the Addition of Aniline Dimer, and Selected Substituted Polyaniline Nanofibers Synthesized with the Aniline Dimer

Polymer	M_w	M_n	PDI
Polyaniline	22,000	8,300	2.6
Polyaniline with aniline dimer	8,200	5,300	1.5
Polyethylaniline	7,800	4,200	1.7
Poly-*N*-ethylaniline	5,300	2,900	1.8
Polyanisidine	14,400	6,300	2.3
Polychloroaniline	7,100	2,800	2.5

Aniline oligomers can also assist in the formation of chiral polyaniline nanofibers.[14b] Chiral polyaniline and its derivatives are of considerable interest because of their potential applications in chiral separations, surface-modified electrodes, and chemical and biological sensors.[20] Conventional approaches for producing chiral polyaniline include co-dissolving polyaniline and a chiral acid in a solvent or polymerizing aniline in the presence of a chiral acid.[20b, 21] Unfortunately, polyaniline from these routes suffer from low chirality and are generally not satisfactory for applications. In addition, most such reported routes yield conventional bulk polyaniline; therefore, the surface area is not sufficiently high for tasks such as efficient chemical separations of enantiomers.

Wang *et al*. found that there are three key factors in synthesizing nanofibers of polyaniline with high chirality.[14b] First, the polymerization needs to be carried out in a solution containing a high concentration of an enantiomer of camphorsulfonic acid (CSA). The high concentration of (+)-CSA or (−)-CSA ensures the close proximity of polyaniline chains and the chiral doping acid anions and lessens the interaction of aniline and the achiral sulfate ions that are generated from the decomposition of the oxidant, ammonium persulfate. Second, the oxidant needs to be added incrementally to the aniline monomer solution as adding the ammonium persulfate all at once causes overheating of the solution and promotes competing interactions of sulfate anions with aniline monomers and the growing polymer chains, which in turn decreases the chirality of the final polymer. Third, an aniline oligomer needs to be added to accelerate the polymerization rate. The authors found that polyaniline nanofibers synthesized with an oligomeric additive and incremental addition of oxidant exhibit chirality five orders of magnitude higher than those produced without any oligomers and adding the oxidant all at once. Oligomers that can promote chiral polyaniline nanofiber formation include *p*-phenylenediamine,

aniline dimer, aniline trimer, amine-capped aniline trimer, and amine-capped aniline heptamer. All of those oligomeric additives satisfy the aforementioned required properties and structure for being a polymerization accelerant. Specifically, (1) they have a lower oxidation potential than the aniline monomer; (2) they have at least one sterically accessible amino group for the oligomer to act as the initiation center for polymerization, and (3) they are ultimately incorporated into the polymer as part of the backbone.

Polyaniline nanofibers produced following these three criteria have twists and are generally entangled with diameters ranging from 20 to 40 nm with lengths up to several microns (**Figure 1.2**). Similar to achiral polyaniline nanofibers synthesized without a template, the chiral nanofibers form a highly porous thin film upon drop-casting. UV-vis and circular dichroism (CD) spectra of the as-synthesized chiral polyaniline nanofibers reveal that they have an anisotropy factor of 2.3×10^{-2}, the highest reported so far for polyaniline. The strong mirror image of the CD spectrum also indicates that these chiral nanofibers could be enantioselective (**Figure 1.2**). Furthermore, UV-vis and conductivity measurements reveal that the chiral polyaniline nanofibers are structurally identical to conventional polyaniline.
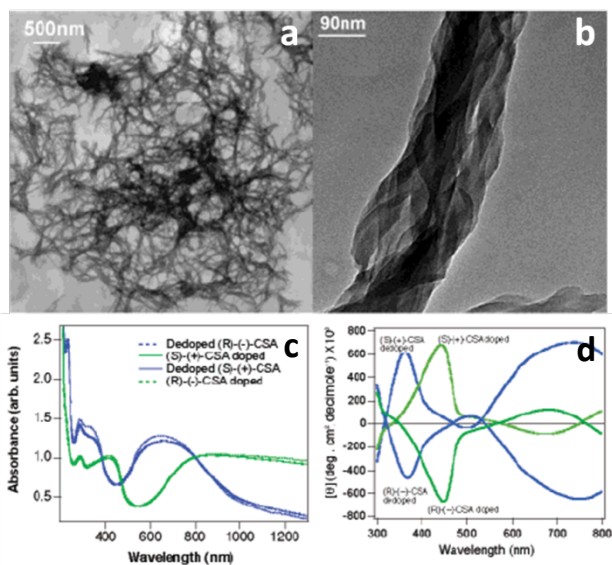
Figure 1.2. TEM images of (a) a network of chiral polyaniline nanofibers, and (b) a magnified view of a fiber bundle. (c) UV-vis and (d) CD spectra of the as-synthesized chiral polyaniline nanofibers. Adapted with permission from (14b). Copyright **2004**, American Chemical Society.

1.2.3 1-D nanostructures of polyaniline derivatives

Polyaniline derivatives have several potential advantages over the parent polymer despite their often reduced conductivity. First, several polyaniline derivatives exhibit improved dispersability in organic solvents.[22] Second, certain derivatives have higher resistance against microbial and chemical degradation.[23] Third, the wide selection of functional groups among the polyaniline derivatives renders them attractive candidates for the active layer in chemical sensing devices. However, unlike the parent polymer, there are few reports of synthetic routes to 1-D nanostructures for polyaniline derivatives. This may be attributed to the fact that many methods for producing polyaniline nanofibers are not applicable to polyaniline derivatives. Rather, they

only lead to agglomerates or nanofibers of poor quality. This is likely due to the slower polymerization rate of substituted aniline caused by both steric and electronic effects. Examination of conventional polymerization of a polyaniline derivative such as poly(*o*-toluidine), revealed that only spherical agglomerates formed during the early stages of polymerization and no fibrillar morphologies were observed at any point.[14d] These experiments suggest that, unlike the parent polymer, fibrillar structures may not be intrinsic to substituted polyanilines. Thus, nucleation sites that can promote anisotropic growth must be intentionally introduced.

Our work indicated that when 1-2 mol % of a selected aniline oligomer such as the aniline dimer or *p*-phenylenediamine was added to a typical rapidly mixed polymerization of an aniline derivative, the resulting polymer was comprised of high quality nanofibers reminiscence of the parent polymer (**Figure 1.3**).[14d, 14e] Monomers that can be polymerized into polymer nanofibers with this method include alkyl-substituted anilines such as 2-ethylaniline, 3-ethylaniline, *o*-toluidine, *m*-toluidine, and 2-propylaniline, halogenated anilines like 2-fluoroaniline, 3-fluoroaniline, 2-chloroaniline, 3-chloroaniline, amine-alkylated *N*-methylaniline and *N*-ethylaniline, and *o*-anisidine, 2-methylthioaniline, and 2,3-dimethylaniline. Nanofibers are the dominant morphology observed under such polymerization conditions.
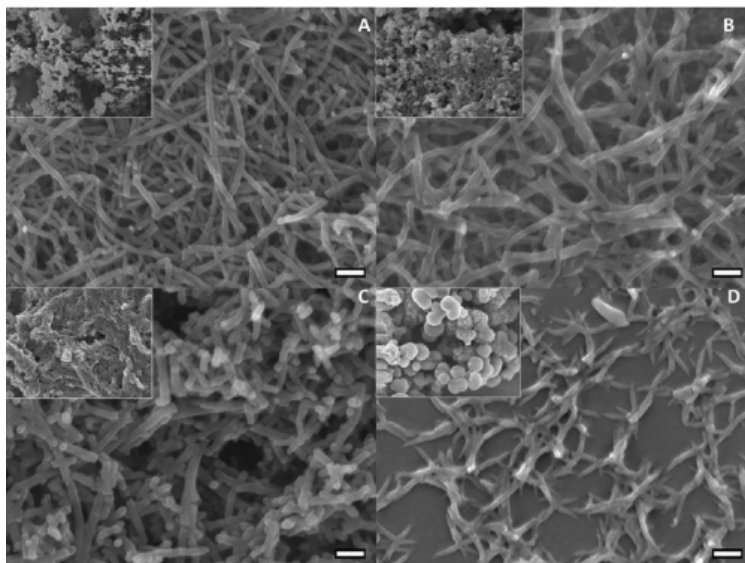
Figure 1.3. SEM images of nanofibers of (a) polychloroaniline, (b) polyethylaniline, (c) poly-*N*-ethylaniline, and (d) polyanisidine synthesized with the addition of an oligomeric additive. Insets are SEM images of the corresponding control reactions performed in the absence of additives. Scale bars = 100 nm. Adapted with permission from (14d). Copyright **2008**, American Chemical Society.

As with the polymerization of the parent polymer, an accelerated reaction rate plays a key role in orchestrating 1-D nanostructure formation for polyaniline derivatives. When the oligomeric initiator is added to the polymerization of the aniline derivative, the polyaniline derivative precipitates out of solution within seconds as opposed to hours or days for reactions carried out without any additives. OCP of the polymerization of an aniline derivative such as anisidine with an appropriate oligomeric additive such as the *p*-aniline dimer confirms the increased polymerization rate. A significantly lower $t_1 + t_2$ value is observed as compared to the

reaction performed without the initiator present. The accelerated reaction rate leads to homogeneous nucleation that results in nanofiber formation for aniline derivatives.

CV and UV-vis of the substituted polyaniline nanofibers indicate that they do not differ significantly in molecular structure and oxidation state from their conventional counterparts. Hence, the oligomeric additives do not simply homopolymerize, but indeed serve as an initiator for the polymerization of the derivative monomer. As with the parent polymer, the molecular weight distribution and PDI are significantly lower than their conventionally synthesized counterparts. The weight-average molecular weight (M_w), number-average molecular weight (M_n), and PDI of selected substituted polyaniline nanofibers are summarized in **Table 1.1**. It is likely that the oligomeric initiators serve as homogeneous growth centers for polymer chains, thus allowing polymer growth simultaneously throughout the solution in similar environments, which in turn lowers the PDI. It is also possible that a lower PDI may assist in nanofiber formation as it is known that a more uniform polymer distribution is advantageous for supramolecular, interchain packing of polymer chains.

An interesting phenomenon for the polymerization of aniline derivatives into nanofibers is that certain additives appear to be more selective towards certain monomers. For instance, using aniline dimer as the initiator in the *o*-anisidine polymerization leads to uniform nanofibers, while only agglomerates are obtained in the presence of *p*-phenylenediamine. On the other hand, the effect is reversed for poly(2-ethylaniline), while nanofibers form for most polyaniline derivatives regardless of the additive used. Thus, the selection of the oligomeric promoter can play a crucial role in the synthesis of nanofibers for some derivatives. This phenomenon has not yet been clearly explained and remains under study.

14

Among all the substituted aniline monomers that have been polymerized into polymer nanofibers, poly(*o*-anisidine) is unique because with a slight modification of the reaction procedure, aligned bundles of polyanisidine nanowires can be obtained.[14f]

For the polymerization of *o*-anisidine with the addition of 1-2 mol % of aniline dimer, uniform nanofibers are obtained just like with other substituted polyanilines. However, when the reaction time is extended to 3 days instead of the typical 1 day, aligned bundles of non-entangled, non-woven, and high aspect-ratio nanowires are produced. This so far has only been observed for poly(*o*-anisidine), but not for other substituted polyanilines. The nanowires in these aligned bundles are up to several microns long with diameters between 30-100 nm (**Figure 1.4**). UV-vis, CV, and FT-IR confirm that the resulting polymer is polyanisidine and the molecular structure and oxidation state does not vary significantly from its conventional counterpart. 4,4'-diaminodiphenylamine (amine-capped aniline dimer) can also be used as the oligomeric additive. Note that this promoter shares the same characteristics with aniline dimer as it has a lower oxidation potential than the monomer and a sterically accessible amino group that enables it to be incorporated into the polymer backbone.
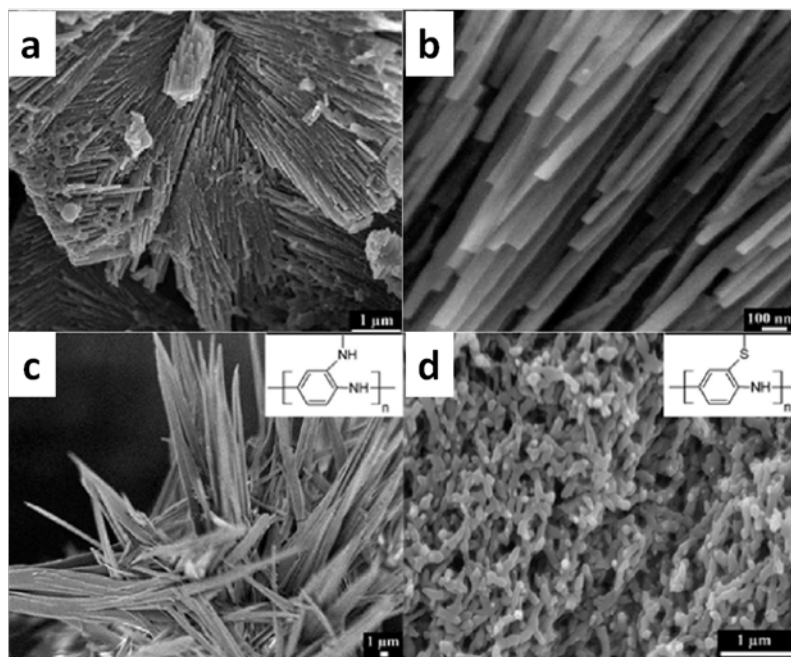
Figure 1.4. SEM images of (a) oriented bundles of polyanisidine nanowires, (b) a closer view of (a), (c) nanowires of poly(*N*-methyl-1,2-diamine), and (d) nanostructured poly(2-methylthioaniline) nanofibers. Adapted with permission from (14f). Copyright **2009**, American Chemical Society.

The extra reaction time for the polymerization of *o*-anisidine appears to be the key factor facilitating more ordered molecular stacking and growth along the fibers' long axis. However, it is interesting to ask why this alters the nanostructure of poly(*o*-anisidine), but not of any of the other aniline derivatives tested. The answer may partially be explained by examining the position and type of the substituent on the monomer. It is likely that the methoxy moiety in poly(*o*-anisidine) can provide additional non-covalent intermolecular interactions such as hydrogen bonding, which has been demonstrated to be important in modulating supramolecular assembly.[24] Furthermore, when two structurally similar aniline derivatives, *N*-methyl-1,2-

diamine and 2-methylthioaniline, in which the oxygen in *o*-anisidine is replaced by nitrogen and sulfur, respectively, are polymerized under identical conditions, long and non-entangled nanowires form for poly(*N*-methyl-1,2-diamine) and exhibit some degree of alignment. On the other hand, only short, entangled, and randomly oriented nanofibers are observed for the poly(2-methylthioaniline) sample (**Figure 1.4**). The results further emphasize the importance of extensive hydrogen bonding in shaping the nanostructure of the polymers: the nitrogen atom in poly(*N*-methyl-1,2-diamine) can also form strong hydrogen bonds with the protonated backbone nitrogens similar to poly(*o*-anisidine), while the lower propensity of the sulfur atom in poly(2-methylthioaniline) to form hydrogen bonds results in the typical nanofibrillar morphology of the final polymer.

Oriented 1-D nanostructures are highly desirable as they can promote directional carrier transport in devices and may be crucial for commercial applications. However, compared to the nanofibrillar portion of the sample, the aligned nanowire bundles of poly(*o*-anisidine) consist of only a small part of the final polymer. Effectively separating the two morphologies and incorporating pure oriented nanowires into devices is still a challenge. Therefore, the interesting observations reported in this study should be considered as a starting point for the rational design of molecular structures to achieve more functionality and unique properties.

1.2.4 Other conducting polymers

The general approach of incorporating minute amounts of an oligomeric additive into the polymerization of aniline and substituted anilines can be extended in order to produce 1-D nanostructures of other conducting polymers such as polypyrrole and polythiophene. Most

17

reports on template-free routes to nanofibers of conducting polymers have been limited to polyaniline. Unlike polyaniline, the 1-D nanofibrillar morphology does not appear to be "intrinsic" to other conducting polymers and, as a result, when template-free techniques used for polyaniline nanofibers are applied to polythiophene or polypyrrole, only micron-sized, agglomerated particles are produced. Like polyaniline derivatives, the lack of anisotropic growth of conventional polypyrrole and polythiophene particles suggests that anisotropic growth leading to 1-D nanostructures must be induced. With the aid of small amounts of their oligomers, such as bipyrrole and terthiophene for the polymerizations of pyrrole and thiophene, respectively, high quality nanofibers of the resulting conducting polymer can now be produced.[14a, 14c] The mechanism of nanofiber formation for polypyrrole and polythiophene nanofibers may be similar to that of polyaniline nanofibers. Like the aniline system, the addition of thiophene or pyrrole oligomers into the polymerization of thiophene or pyrrole enhances the polymerization rate and promotes homogeneous nucleation which, in turn, orchestrates polypyrrole and polythiophene nanofiber formation. Polypyrrole nanofibers possess a morphology with an average diameter of 20 nm and extend up to several microns in length (**Figure 1.5**), while nanofibers of polythiophene exhibit a 50 nm average diameter with similar length (**Figure 1.6**).
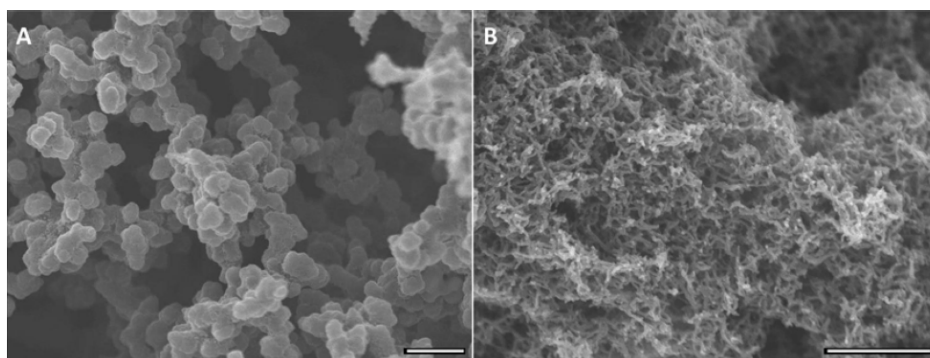
Figure 1.5. SEM images of polypyrrole synthesized (a) without any additives and (b) with bipyrrole. Scale bars = 1 μm. Adapted with permission from (14a). Copyright **2008**, American Chemical Society.
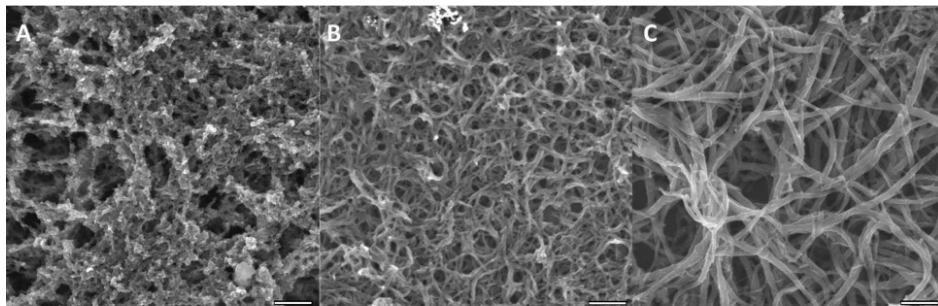
Figure 1.6. SEM images of polythiophene synthesized (a) without any oligomer additives, (b) with the addition of terthiophene, and (c) with the addition of sexithiophene. Scale bars = 1 μm. Adapted with permission from (14a). Copyright **2008**, American Chemical Society.

The addition of different oligomers into the polymerization of thiophene also has a profound effect on its morphology. For instance, when a catalytic amount of sexithiophene is incorporated into the polymerization of thiophene, the resulting nanofibers possess a larger diameter of 90 nm and are less entangled and longer than nanofibers produced with terthiophene as the additive (**Figure 1.6**). This is consistent with the proposed model for nanofiber formation for polyaniline because as the length of the oligomeric promoter increases, a larger and more ordered nuclei may form, which leads to polymer nanofibers with larger diameters.

The success of producing polypyrrole and polythiophene 1-D nanofibers, in addition to nanofibers for polyaniline derivatives, demonstrates that oligomeric additives can be a general and versatile promoter for anisotropic growth of the corresponding parent polymer. Furthermore, the oligomeric initiators become incorporated as part of the polymer backbone, which eliminates any post-synthetic purification steps. This approach may be applicable to a wide variety of semi-rigid rod precipitation polymerizations, including derivatives of polypyrrole and polythiophene and other conducting polymers.

1.2.5 Polyaniline nanotubes

In addition to the aforementioned 1-D conducting polymer nanostructures, nanotubes of polyaniline can be produced without any external templates by controlling the molecular structure of the oligomers formed during the early stages of aniline polymerization. Typical polymerizations of aniline are carried out at low pH in a medium comprised of an aqueous solution of a strong acid. These conditions are known to promote head-to-tail coupling of aniline monomers in order to produce polyaniline with high structural regularity. However, a "falling pH" method was reported in which the polymerization of aniline was carried out in a high pH medium in which oligomers with mixed ortho and para coupling form during the initial stages of polymerization.[14g, 24a, 25] These intermediates are then oxidized into phenazine-like moieties through intramolecular or intermolecular coupling and subsequently serve as the nucleation centers for further polymerization. The pH of the solution slowly drops as the reaction proceeds because of the sulfuric acid generated from the reduction of APS. Polymerization of aniline can thus be initiated from the phenazine-like centers through the typical para-coupling route once the

pH becomes sufficiently low. These phenazine-like oligomers are shown to self-assemble into well-organized clusters in the insoluble aqueous medium through hydrophobic interactions and π-π stacking. The nanosized crystalline clusters serve as inherent nucleation templates for further para-coupling polymerizations, and therefore dictate the morphology of the final polymer, which comes in as a mixture of nanorods and nanotubes. Studies indicate that the inner-walls of the nanotubes are likely to be the self-assembled phenazine template, with the polymer chains extending outward generating the thickness of the nanotube wall. Hydrogen bonding and π-π interactions between neighboring polyaniline chains has been suggested as the driving force for stabilizing the initial phenazine scaffold.[14g, 24a, 25a, 25c-e] The resulting nanotubes typically have an outer diameter of 100-200 nm with a wall thickness of 50-100 nm, and extend several microns in length (**Figure 1.7**). Conductivities of these nanotubes are not really comparable to polyanilines produced in the low pH medium due to the presence of the insulating phenazine-like cores.
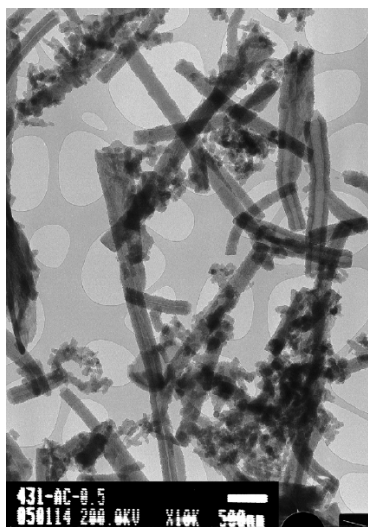
Figure 1.7. Polyaniline nanotubes and nanorods produced via the "falling-pH" polymerization method. Adapted with permission from (24a). Copyright **2006**, Elsevier.

Recent work by Zujovic *et al*. further confirms the two pH-dependent growth stages for the nanotubes in a "falling pH" experiment.[14h, 26] Furthermore, they reported that well-defined nanosheets of mixed ortho and para cross-linked aniline oligomers form at the early stage of the polymerization when the pH value is high.[14h] Those nanosheets tend to decrease surface energy through either stacking to form relatively thick nanoflakes or rolling or curling to form oligomeric nanotubes. The polymerization then proceeds through the regular para-coupled mechanism as the pH of the solution decreases. Polyaniline polymerizes from these preformed oligomeric nanotubes and thickens the tube walls. Nanorods are also observed in the final product when the cavity in the tube becomes filled with polyaniline.

The key factor for forming polyaniline nanotubes in such template-free syntheses appears to be the formation of well-organized phenazine-like oligomeric cores that serve as templates to dictate the morphology of the final polymer. Combining this mechanism with the aforementioned concept of intentionally adding an oligomeric initiator into the polymerization, it is likely that a dazzling array of nanostructures could be created using oligomers with different molecular structures in the polymerization.

1.3 Oligomers as a new class of organic (semi)conductors

Nanofibers of polyaniline have exhibited enhanced performances in applications such as chemical sensors, catalysis, and actuators.[1c, 1d, 2a, 2c-e] However, the output and stability of devices utilizing these structures are largely governed by how the molecules or polymer chains are assembled in the solid-state.[27] The lack of order at the chain level has limited polyaniline nanofibers from being integrated into electronic devices that require high carrier mobility and

stability, such as organic field-effect transistors and solar cells, which are dominated by molecular semiconductors that can self-assemble into single-crystal nanowires or nanoribbons.[28] Moreover, polyaniline nanofibers typically possess low aspect ratios and are entangled and inter-connected, which makes single-wire devices or post-synthetic alignment difficult. In contrast to polyaniline, aniline oligomers are capable of more ordered solid-state packing.[29] However, reports on oligoanilines are sparse and are mainly limited to synthetic routes to bulk materials.[11] The scant attention that oligoanilines have received can be partly attributed to their lower conductivity. For instance, conductivities measured on pressed pellets of bulk tetraaniline range from 3×10^{-6} to 3×10^{-2} S/cm, depending on which synthetic routes and doping acids were used.[11a, 14i] The modest conductivities in turn leads to another underlying assumption—higher molecular weight polyaniline is necessary for achieving reasonable conductivities as longer chains could increase the intrachain movement of charge carriers. Careful examination of the components of bulk conductivity (σ_{bulk}) demands further evaluation:

$$\sigma_{bulk} = f(\sigma_{intrachain}) \cdot f(\sigma_{interchain}) \cdot f(\sigma_{domain});^{[1a, 11b, 11e]}$$

The bulk conductivity of a conducting polymer is governed by both the transport properties within a molecular chain ($\sigma_{intrachain}$) and between the chains ($\sigma_{interchain}$). Although oligoanilines contribute more modestly to intrachain transport, they have strong potential for improvement of the material's interchain transport component. Therefore, reported pressed pellet conductivity values for oligoanilines represent their lower limit due to the fact that interchain transport has not been optimized. Therefore, organizing oligoanilines into well-ordered and defined domains, such as 1-D nanostructures, is highly desirable and long overdue.

23

1.3.1 *In-situ* methods

The nanofibrillar morphology of aniline tetramer was recently reported during a mechanistic study of polyaniline nanofibers.[14i] When aniline dimer was treated with APS in aqueous 1.0 M HCl, a blue-green powder formed almost instantaneously. This powder is analytically and spectroscopically consistent with HCl-doped aniline tetramer and SEM analysis revealed that it is composed of long nanofibers that are 40-80 nm in diameter (**Figure 1.8**). A one-step coupling reaction was also demonstrated for tetraaniline nanofibers by carrying out the reaction in a high ionic strength system.[14j] The insoluble aniline dimer could be added to an aqueous solution of 1.0 M HCl saturated with NaCl followed by adding an aqueous solution of H_2O_2. The resulting product is again nanofibers of aniline tetramer that are microns in length. The four-probe conductivities of a pressed pellet of aniline tetramer nanofibers from both synthetic routes are on the order of 10^{-2} S/cm.
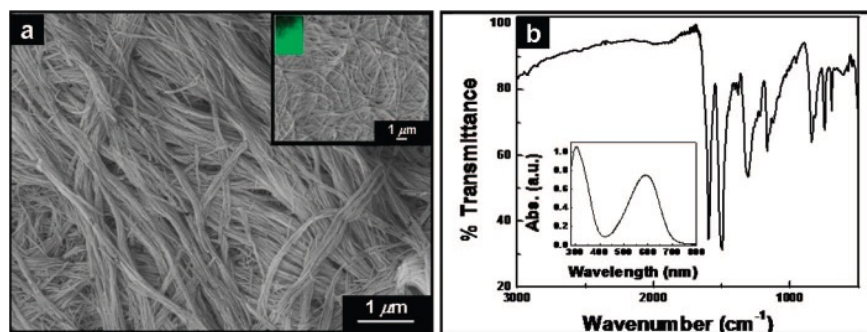
Figure 1.8. (a) SEM image of aniline tetramer synthesized *in-situ*. The inset shows a tetraaniline nanofiber film deposited on PET. (b) Attenuated Total Reflectance FT-IR of dedoped aniline tetramer. The inset shows its UV-vis spectrum in NMP. Adapted with permission from (14i). Copyright **2009**, American Chemical Society.

It is interesting that such short oligomeric chains, i.e. four units of aniline, can lead to the formation of high aspect ratio 1-D nanofibers. However, when considered in the context of the entire field of organic conductors, this phenomenon is, in fact, not that surprising. Aniline oligomers can be viewed as a middle ground between polymers and molecular conductors such as pentacene, perylene, and their derivatives because oligoanilines retain the chemical properties of the parent polymer, while providing advantages with regard to chemical purity and self-assembly that are mostly associated with small conjugated molecules. These small molecular conductors, such as acenes and perylenes can form highly ordered 1-D nanostructures in an environment that promotes self-assembly.[28] Therefore, it is not surprising that short-chain oligomers such as aniline tetramers can form extended 1-D nanostructures since they can pack in an anisotropic manner like the aforementioned small molecules. From this perspective, methods for producing oligoaniline nanostructures should not be limited to *in-situ* reactions reminiscence of the parent polymer. Instead they could be studied systematically as a unique class of small molecular (semi)conductors whose nanostructures could be produced via post-synthetic methods similar to poly(3-hexylthiophene) (P3HT) or pentacene nanofibers.[28, 30]

1.3.2 Post-synthetic methods

Following this logic, our group recently demonstrated nanoscale shape and size control of various aniline oligomers through a simple post-synthetic solvent-exchange process.[14k] A variety of aniline oligomers were either purchased or synthesized via reported routes: *N*-phenyl-1,4-phenylenediamine (aniline dimer) and *N, N'*-diphenyl-1,4-phenylenediamine (phenyl-capped aniline dimer) were commercially available and were used as received, while bulk aniline

25

tetramer was synthesized following a reported coupling reaction route,[31] and phenyl-capped aniline tetramer and phenyl-capped aniline octamer were synthesized by a Honzl-Wudl condensation reaction.[11c, 32] We started our investigation with tetraaniline because it is the smallest unit that can represent the structure of polyaniline since the most conducting oxidation state of polyaniline, the emeraldine oxidation state, is comprised of 3 benzene rings for every quinoid ring. In a typical process for producing tetraaniline nanostructures, a small amount of finely powdered dedoped tetramer was added to a solvent mixture containing a small amount of a good solvent for tetraaniline such as ethanol and a large quantity of an acidic non-solvent such as aqueous HCl. The mixture was left undisturbed for several days. During this time, the large particles that initially precipitated to the bottom of the vial gradually turned into the green, doped form of tetraaniline and slowly dispersed into the surrounding medium. Only doped tetramer was observed floating in the solvent at the end of the process. SEM and TEM images revealed that the resulting dispersion was composed of long, rigid, non-woven nanowires with high aspect ratios typically ranging from 70 to 200 nm in diameter and up to hundreds of microns in length (**Figure 1.9**). We proposed that tetraaniline nanowires formed because of the controlled aggregation of molecules through non-covalent interactions such as π-π stacking and hydrogen bonding in a balanced solvent environment.[28a, 28c, 33] Tetraaniline or other aniline oligomers are insoluble in acidic aqueous solvents, but can be doped in such an environment. On the other hand, these oligomeric molecules are soluble in common organic solvents such as ethanol or acetone. Therefore, the solubility and the degree of aggregation of tetraaniline molecules can be tuned by adjusting the ratio of the two solvents/non-solvents. As the aqueous component increases, the enhanced solvent polarity can create solvophobic association between the aromatic rings analogous to how surfactants and amphiphilic molecules assemble and thus allow for

controlled aggregation and stacking of tetraaniline molecules, which in turn leads to extended structures consisting of 1-D nanowires. This mechanism is supported by the established mechanism of nanoribbon formation for molecular conductors such as perylene tetracarboxylic diimide derivatives.[28c, 33-34] In addition, the prolonged nanowire growth time (4-5 days) has been demonstrated as an important factor in directional molecular self-assembly as also suggested in other systems of nanostructure formation.[28c, 33]
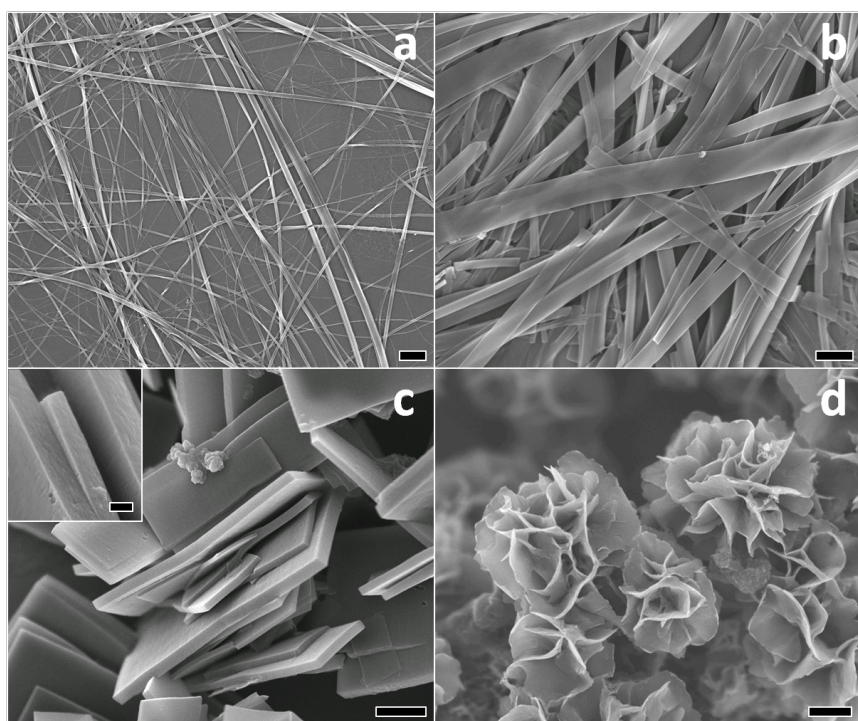
Figure 1.9. SEM images of (a) nanowires, (b) nanoribbons, (c) nanoplates, and (d) nanoflowers of aniline tetramer. The inset in (c) offers a closer view of the cross-section of the nanoplates. Scale bar = 100 nm for the inset and 1 μm for all others.

In addition to HCl-doped 1-D nanowires, other nanostructures with different dimensions can be created by simply varying the doping acid. When nitric acid (HNO_3) is used as the dopant, 2-D nanoribbons are obtained as opposed to 1-D nanowires with HCl (**Figure 1.9**). Changing the doping acid to perchloric acid ($HClO_4$) induces the formation of 3-D rectangular-shaped nanoplates, while sulfuric acid (H_2SO_4) leads to nanoflowers consisting of well-organized clusters of 2-D nanosheets (**Figure 1.9**). This exquisite nanoscale size and shape control of aniline tetramer can be attributed to the different sizes of the dopant acid anions. The size of the dopant anions can influence the interchain packing distance during the self-assembly process and thus lead to different supramolecular morphologies. In addition, we found that the size of the dopant anions have an impact on the crystallinity of the resulting nanostructures. For instance, when a small doping acid such as HCl is used, X-ray diffraction (XRD) indicates that the nanowires formed are the least crystalline among the four aforementioned nanostructures, while larger dopant anions such as ClO_4^- leads to the much more crystalline nanoplates. On the other hand, using a doping acid that is too bulky in size such as camphorsulfonic acid (CSA) prevents the oligomeric molecules from packing into ordered and discrete nanostructures.

This process appears to be a general and versatile approach for producing nanostructures for other aniline oligomers. Upon varying the proportion of the organic and aqueous solvent to accommodate the differences in solubility of each oligomer in the organic solvent, nanowires of aniline dimer, phenyl-capped aniline dimer, and phenyl-capped aniline tetramer have been obtained via the same process that is used for tetraaniline nanostructure formation. A 1-D nanowire morphology is produced when HCl is used as the doping acid for all three oligomers. Further tuning of reaction conditions to tailor each of these oligomers could lead to more well-defined supramolecular structures with different morphologies and dimensions. However, when

the same approach is applied to longer oligomers such as the phenyl-capped aniline octamer, only agglomerates are obtained, likely due to the fact that the increase in chain length results in a molecule with more polymer-like characteristics and its structure cannot be readily controlled by such self-assembly processes.

The electrical transport properties of single nanowires, nanoribbons, and nanoplates reveal interesting results. Conventional pressed-pellet measurements only measure the lower boundary of conductivity for nanostructures because the high contact resistance at the numerous junctions causes the overall conductivity to appear lower than the intrinsic conductivity of a single nanostructure. The conductivities were obtained with two-probe measurements using bottom-contact devices with a single nanowire, nanoribbon, or nanoplate bridging the two gold electrodes (**Figure 1.10**). We found that the conductivity for a single tetraaniline nanoribbon can be as high as 1.1 S/cm, which is two orders of magnitude larger than the highest previously reported value for tetraaniline and rivals that of conventional unprocessed polyaniline. Such results demonstrate that oligoanilines with proper processing can be as highly conducting as the parent polymer and could pave the way for many interesting syntheses, structure-property relationship studies, and applications.
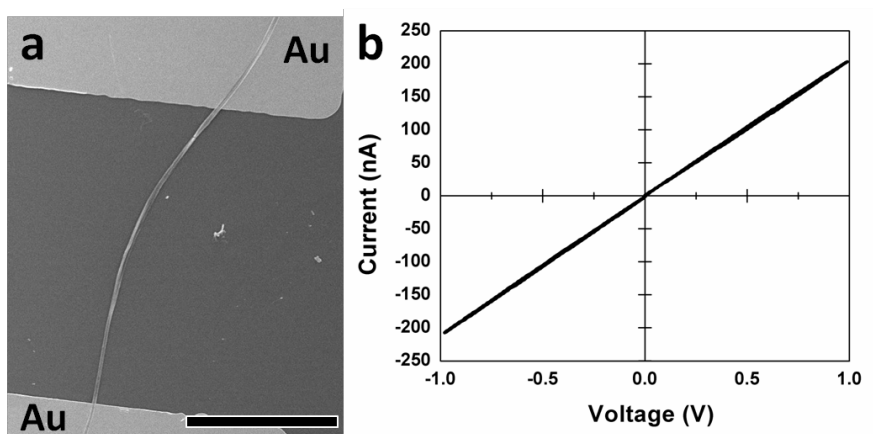
Figure 1.10. (a) SEM image of a bottom-contact tetraaniline single nanowire device. Scale bar = 10 μm. (b) *I-V* curve of the device.

1.4 Assembly and Applications

1.4.1 Alignment of aniline oligomeric nanowires

Having well-defined and high-aspect ratio nanowires of aniline oligomers provides opportunities for post-synthetic alignment of nanowires into oriented arrays over a macroscopic area. Since the properties of a material not only depend on individual nanostructures, but also on how they are assembled at the macroscopic level, alignment of these nanostructures are thus highly desirable in order to maximize transport properties. For example, oriented nanowire arrays could facilitate directional carrier transport and greatly lower or eliminate contact resistance compared to their non-oriented counterparts. Such properties are highly desirable for achieving high efficiency in organic thin-film microelectronic devices and high conductivity in transparent, flexible electrodes. However, solution-based directional assembly has been difficult to achieve for polymeric conductors such as polyaniline nanofibers due to their lack of rigidity and low aspect ratios. On the other hand, the high-aspect ratio tetraaniline nanowires can be readily aligned via common methods developed for inorganic nanostructures such as dewetting and microfluidic flow.

Dewetting alignment is induced by solvent evaporation.[35] For example, when tetraaniline nanowires are drawn towards the direction of evaporation in a drying droplet, the nanowires align in a radial fashion.[14k] The dispersion in the center continuously replenishes the evaporating

solvent at the edge. Nanowires are therefore continuously carried to the solvent-front which leads to a ring with aligned nanowires possessing high deposition density once dried (**Figure 1.11a**). Sections of this ring can be further transferred to a desired substrate for device fabrication. Nanowires can be potentially aligned horizontally rather than radially by dipping a substrate vertically into a drying nanowire dispersion.
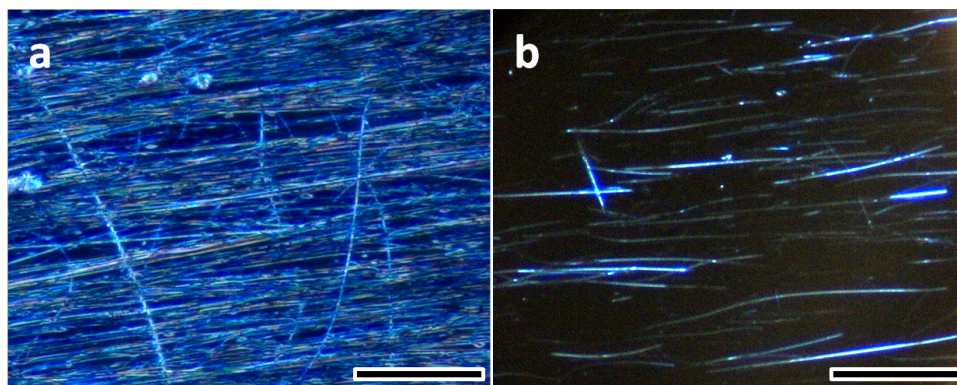
Figure 1.11. Optical microscope images of nanowires aligned by (a) a dewetting method and (b) a microfluidic flow method. Scale bar = 20 µm.

Another simple approach for the assembly of tetraaniline nanowires is microfluidic flow.[36] In this method, a dispersion of tetraaniline nanowires is continuously pushed through a microfluidic flow channel.[14k] The sheer force created by the directional flow leads the nanowires to align in the flow direction and deposit on a substrate (**Figure 1.11b**). The deposition density of the oriented nanowires can be further improved by proper surface treatment. This method could potentially allow large area alignment as has been demonstrated for inorganic materials.[36-37]

1.4.2 Sensors

Polymerization with the aid of an oligomeric additive to yield high quality nanofibers of conducting polymers is still in its infancy. Nevertheless, polypyrrole nanofibers produced via this route have already been explored for various types of chemical gas sensors.[14c, 38]

Polypyrrole has been extensively studied as a chemical sensor for a variety of analytes, in particular toxic gases such as ammonia, carbon monoxide, hydrogen sulfide, and nitric oxides.[1c, 39] Sensors based on polypyrrole are conventionally fabricated by lifting and redepositing an electrochemically grown film. With the water-dispersible polypyrrole nanofibers, chemical sensors can be fabricated by simply drop-casting a dispersion of such material directly onto an interdigitated electrode.[14c] The stable dispersion results in a high quality thin film that can be used as the active layer in a chemical sensor without the need for special additives to improve substrate adhesion or film quality. Furthermore, the porous features of the nanofibrillar film provide a high surface area that can enhance the sensitivity to target gas molecules. Such polypyrrole nanofiber chemical sensors exhibit reversible behavior with an approximately 19% increase in resistance upon exposure to 50 ppm ammonia.[14c] In contrast, drop-casting a dispersion of conventional agglomerated polypyrrole leads to a rough, uneven film that makes sensing behavior difficult to reproduce. Conductometric hydrogen gas sensors have also been fabricated with polypyrrole nanofibers.[38a] The high surface area of the nanofibrillar film allows the sensor to achieve a short response time of 43 s upon exposure to a 1% H_2 pulse with a resistance change of 312 Ω. In addition, the behavior of polypyrrole nanofibers in a surface acoustic wave (SAW) gas sensor has been studied in the presence of a reducing gas (H_2) and an oxidizing gas (NO_2).[38b] Exposure to 0.06%, 0.125%, 0.25%, 0.5%, and 1% H_2 in dilute synthetic

air resulted in frequency shifts of 8.5 kHz, 12.1 kHz, 16 kHz, 18.7 kHz, and 20.2 kHz, respectively. The 90% response time for 1 % H_2 is 39 s and the 90% recovery time is 219 s. Such polypyrrole nanofiber SAW sensors can also detect very low concentrations of NO_2. For example, 2.1 ppm of NO_2 mixed with synthetic air can be detected within 133 s with a 90% response time, demonstrating its potential for applications in environmental studies that monitor air quality.

1.5 Conclusions and Outlook

In this chapter, we have reviewed nanostructured aniline oligomers as well as their role in guiding the formation of polyaniline nanofibers. Aniline oligomers act not only as effective promoters for shaping the nanoscale structures and chirality of polyanilines, but also represent a new class of organic (semi)conductors. Interestingly, the process of using oligomers to guide the nanoscale shape of the resulting polymer is also applicable to polythiophenes and polypyrroles.

Using oligomers as an additive for the polymerization of a parent polymer can potentially have an impact on the entire family of precipitation polymerizations. For conducting polymers, because of the lower oxidation potential that the oligomers possess compared to the monomer, they can lower the oxidation potential of the rate-determining step in a polymerization and thus potentially initiate reactions that normally would be sluggish. In addition, their semi-rigid properties can enable them to act as "molecular templates" to shape the nanoscale morphology for a variety of conducting polymers as demonstrated by the study of oligoanilines to produce well-ordered nanostructures. Furthermore, properties such as the chirality of the parent polymer,

promoted by oligomer additives, offer an interesting opportunity to create nanostructures with new properties.

The study of aniline oligomers as a new class of nanostructured organic (semi)conductors is still in its infancy, yet has already demonstrated tremendous potential. Their ability to form well defined nanostructures and their interesting structure-property relationships will likely allow them to develop into a vibrant field of research.

1.6 References

(1)   (1a) A. G. MacDiarmid, *Angew. Chem. Int. Ed.* **2001**, *40*, 2581; (1b) P. Chandrasekhar, *Conducting polymers, fundamentals and applications: a practical approach* **1999**; (1c) J. Jang, *Adv. Polym. Sci.* **2006**, *199*, 189; (1d) H. D. Tran, D. Li, R. B. Kaner, *Adv. Mater.* **2009**, *21*, 1487.

(2)   (2a) Y. S. Negi, P. V. Adhyapak, *J. Macromol. Sci. Part C: Polym. Rev.* **2002**, *42*, 35; (2b) M. Wang, *Macromol. Rapid Commun.* **2009**, *30*, 963; (2c) J. Huang, R. B. Kaner, *Handbook of Conducting Polymers, 3rd ed., J. Reynolds and T. Skotheim, Eds. (Marcel Dekker, Inc., New York, 2006), Chapter 7* **2006**, 194; (2d) D. Zhang, Y. Wang, *Mater. Sci. Eng. B* **2006**, *134*, 9; (2e) D. Li, J. Huang, R. B. Kaner, *Acc. Chem. Res.* **2009**, *42*, 135.

(3)   (3a) N. J. Pinto, A. T. Johnson, A. G. MacDiarmid, C. H. Mueller, N. Theofylaktos, D. C. Robinson, F. A. Miranda, *Appl. Phys. Lett.* **2003**, *83*, 4244; (3b) A. G. MacDiarmid, W. E. Jones, I. D. Norris, J. Gao, A. T. Johnson, N. J. Pinto, J. Hone, B. Han, F. K. Ko, H. Okuzaki, M. Llaguno, *Synth. Met.* **2001**, 27.

(4)   H. X. He, C. Z. Li, N. J. Tao, *Appl. Phys. Lett.* **2001**, *78*, 811.

(5)   (5a) C. R. Martin, *Acc. Chem. Res.* **1995**, *28*, 61; (5b) C. G. Wu, T. Bein, *Science* **1994**, *264*, 1757; (5c) Y. C. Zhao, M. Chen, T. Xu, W. M. Liu, *Colloids Surf. A* **2005**, *257-258*, 363; (5d) S. I. Cho, S. B. Lee, *Acc. Chem. Res.* **2008**, *41*, 699; (5e) J. I. Lee, S. H. Cho, S. M. Park, J. K. Kim, J. K. Kim, J. W. Yu, Y. C. Kim, T. P. Russell, *Nano Lett.* **2008**, *8*, 2315.

(6)   (6a) H. J. Qiu, M. X. Wan, B. Matthews, L. M. Dai, *Macromolecules* **2001**, *34*, 675; (6b) Z. X. Wei, Z. M. Zhang, M. X. Wan, *Langmuir* **2002**, *18*, 917; (6c) G. Li, Z. Zhang, *Macromolecules* **2004**, *37*, 2683; (6d) Z. M. Zhang, M. X. Wan, Y. Wei, *Adv. Funct. Mater.* **2006**, *16*, 1100; (6e) P. Anilkumar, M. Jayakannan, *Macromolecules* **2007**, *40*, 7311.

(7)   (7a) X. Zhang, S. K. Manohar, *J. Am. Chem. Soc.* **2004**, *126*, 12714; (7b) X. Zhang, S. K. Manohar, *J. Am. Chem. Soc.* **2005**, *127*, 14156.

(8)   (8a) Z. W. Niu, M. A. Bruckman, S. Q. Li, L. A. Lee, B. Lee, S. V. Pingali, P. Thiyagarajan, Q. Wang, *Langmuir* **2007**, *23*, 6719; (8b) Z. Niu, J. Liu, L. A. Lee, M. A. Bruckman, D. Zhao, G. Koley, Q. Wang, *Nano Lett.* **2007**, *7*, 3729.

(9)   (9a) J. Huang, S. Virji, B. H. Weiller, R. B. Kaner, *J. Am. Chem. Soc.* **2003**, *125*, 314; (9b) J. Huang, R. B. Kaner, *J. Am. Chem. Soc.* **2004**, *126*, 851; (9c) N. R. Chiou, A. J. Epstein, *Adv. Mater.* **2005**, *17*, 1679; (9d) N. R. Chiou, A. J. Epstein, *Synth. Met.* **2005**, *153*, 69; (9e) N. R. Chiou, C. Lu, J. Guan, J. Lee, A. J. Epstein, *Nat. Nanotechnol.* **2007**, *2*, 354; (9f) J. X. Huang, R. B. Kaner, *Angew. Chem., Int. Ed.* **2004**, *43*, 5817; (9g) X. L. Jing, Y. Y. Wang, D. Wu, J. P. Qiang, *Ultrason. Sonochem.* **2007**, *14*, 75; (9h) S. K. Pilalamarri, F. D. Blum, A. T. Tokuhiro, J. G. Story, M. F. Bertino, *Chem. Mater.* **2005**, *17*, 227.

(10)   (10a) J. Huang, S. Virji, B. H. Weiller, R. B. Kaner, *Chem: A Euro. J.* **2004**, *10*, 1314; (10b) S. Virji, J. Huang, R. B. Kaner, B. H. Weiller, *Nano Lett.* **2004**, *4*, 491; (10c) R. J. Tseng, J. Huang, J. Ouyang, R. B. Kaner, Y. Yang, *Nano Lett.* **2005**, *5*, 1077; (10d) R. J. Tseng, C. O. Baker, B. Shedd, J. Huang, R. B. Kaner, J. Ouyang, Y. Yang, *Appl. Phys.*

Lett. **2007**, *90*, 053101; (10e) B. J. Gallon, R. W. Kojima, R. B. Kaner, P. L. Diaconescu, *Angew. Chem. Int. Ed.* **2007**, *46*, 7251; (10f) V. Gupta, N. Miura, *Mater. Lett.* **2006**, *60*, 1466.

(11)   (11a) Z. Wei, C. F. J. Faul, *Macromol. Rapid Commun.* **2008**, *29*, 280; (11b) A. G. MacDiarmid, Y. Zhou, J. Feng, *Synth. Met.* **1999**, *100*, 131; (11c) F. L. Lu, F. Wudl, M. Novak, A. J. Heeger, *J. Am. Chem. Soc.* **1986**, *108*, 8311; (11d) Y. Wei, C. Yang, G. Wei, G. Feng, *Synth. Met.* **1997**, *84*, 289; (11e) A. G. MacDiarmid, *Synth. Met.* **1997**, *84*, 27.

(12)   (12a) H. Zhekova, A. Tadjer, A. Ivanova, J. Petrova, N. Gospodinova, *Int. J. Quant. Chem.* **2007**, *107*, 1688; (12b) F. Lux, E. J. Samuelsen, E. T. Kang, *Synth. Met.* **1995**, *69*, 167; (12c) O. Kwon, M. L. McKee, *J. Phys. Chem. B* **2000**, *104*, 1686; (12d) G. D'Aprano, M. Leclerc, G. Zotti, *Synth. Met.* **1996**, *82*, 59.

(13)   (13a) G. Horowitz, B. Bachet, A. Yassar, P. Lang, F. Demanze, J.-L. Fave, F. Garnier, *Chem. Mater.* **1995**, *7*, 1337; (13b) A. Facchetti, Y. Deng, A. Wang, Y. Koide, H. Sirringhaus, T. J. Marks, R. H. Friend, *Angew. Chem., Int. Ed.* **2000**, *39*, 4547; (13c) A. Afzali, T. L. Breen, C. R. Kagan, *Chem. Mater.* **2002**, *14*, 1742; (13d) B. Servet, G. Horowitz, S. Ries, O. Lagorsse, P. Alnot, A. Yassar, F. Deloffre, P. Srivastava, R. Hajlaoui, P. Lang, F. Garnier, *Chem. Mater.* **1994**, *6*, 1809; (13e) G. Horowitz, F. Garnier, A. Yassar, R. Hajlaoui, F. Kouki, *Adv. Mater.* **1996**, *8*, 52; (13f) M. A. Loi, E. D. Como, F. Dinelli, M. Murgia, R. Zamboni, F. Biscarini, M. Muccini, *Nat. Mater.* **2005**, *4*, 81; (13g) S. Kawano, N. Fujita, S. Shinkai, *Chem: A Eur. J.* **2005**, *11*, 4735; (13h) I. O. Shklyarevskiy, P. Jonkheijm, P. C. M. Christianen, A. P. H. J. Schenning, E.

W. Meijer, O. Henze, A. F. M. Kilbinger, W. J. Feast, A. D. Guerzo, J.-P. Desvergne, J. C. Maan, *J. Am. Chem. Soc.* **2005**, *127*, 1112; (13i) Y. Wei, Y. Sun, G.-W. Jang, X. Tang, *J. Polym. Sci. Part C: Polym. Lett.* **1990**, *28*, 81.

(14)   (14a) H. D. Tran, Y. Wang, J. M. D'Arcy, R. B. Kaner, *ACS Nano* **2008**, *2*, 1841; (14b) W. Li, H.-L. Wang, *J. Am. Chem. Soc.* **2004**, *126*, 2278; (14c) H. D. Tran, K. Shin, W. G. Hong, J. M. D'Arcy, R. W. Kojima, B. H. Weiller, R. B. Kaner, *Macromol. Rapid Commun.* **2007**, *28*, 2289; (14d) H. D. Tran, I. Norris, J. M. D'Arcy, H. Tsang, Y. Wang, B. R. Mattes, R. B. Kaner, *Macromolecules* **2008**, *41*, 7405; (14e) H. D. Tran, R. B. Kaner, *Chem. Commun.* **2006**, 3915; (14f) Y. Wang, H. D. Tran, R. B. Kaner, *J. Phys. Chem. C* **2009**, *113*, 10346; (14g) I. Sapurina, J. Stejskal, *Polym. Int.* **2008**, *57*, 1295; (14h) Z. D. Zujovic, C. Laslau, G. A. Bowmaker, P. A. Kilmartin, A. L. Webber, S. P. Brown, J. Travas-Sejdic, *Macromolecules* **2010**, *43*, 662; (14i) S. P. Surwade, N. Manohar, S. K. Manohar, *Macromolecules* **2009**, *42*, 1792; (14j) S. P. Surwade, S. R. Agnihotra, V. Dua, N. Manohar, S. Jain, S. Ammu, S. K. Manohar, *J. Am. Chem. Soc.* **2009**, *131*, 12528; (14k) Y. Wang, H. D. Tran, L. Liao, X. Duan, R. B. Kaner, *J. Am. Chem. Soc.* **In Press**.

(15)   (15a) Y. Wei, G.-W. Jang, C.-C. Chan, K. F. Hsueh, R. Hariharan, S. A. Patel, C. K. Whitecar, *J. Phys. Chem.* **1990**, *94*, 7716; (15b) Y. Wei, J. Tian, *Macromolecules* **1993**, *26*, 457.

(16)   (16a) D. M. Mohilner, R. N. Adams, W. J. Argersinger, *J. Am. Chem. Soc.* **1962**, *84*, 3618; (16b) D. E. Stilwell, S.-M. Park, *J. Electrochem. Soc.* **1988**, *133*, 2254; (16c) Y.

Wei, Y. Sun, X. Tang, *J. Phys. Chem.* **1989**, *93*, 4878; (16d) Y. Wei, X. Tang, Y. Sun, W. W. Focke, *J. Polym. Sci., Polym. Chem. Ed.* **1989**, *27*, 2385.

(17)   D. Li, R. B. Kaner, *J. Am. Chem. Soc.* **2006**, *128*, 968.

(18)   J. X. Huang, R. B. Kaner, *Chem. Commun.* **2006**, 367.

(19)   (19a) S. K. Manohar, A. G. MacDiarmid, A. J. Epstein, *Synth. Met.* **1991**, *41-43*, 711; (19b) Y. Wei, K. F. Hsueh, G.-W. Jang, *Polymer* **1994**, *35*, 3572.

(20)   (20a) H. L. Guo, C. M. Knobler, R. B. Kaner, *Synth. Met.* **1999**, *101*, 1; (20b) J. Huang, V. M. Egan, H. Guo, J.-Y. Yoon, A. L. Briseno, I. E. Rauda, R. L. Garrell, C. M. Knobler, F. Zhou, R. B. Kaner, *Adv. Mater.* **2003**, *15*, 1158; (20c) J. C. Moutet, E. Saintaman, F. Tranvan, P. Angibeaud, J. P. Utille, *Adv. Mater.* **1992**, *4*, 7; (20d) P. A. Bross, U. Schoberl, J. Daub, *Adv. Mater.* **1991**, *3*, 198.

(21)   (21a) S. A. Ashraf, L. A. P. KaneMaguire, M. R. Majidi, S. G. Pyne, G. G. Wallace, *Polymer* **1997**, *38*, 2627; (21b) L. A. P. KaneMaguire, A. G. MacDiarmid, I. D. Norris, G. G. Wallace, W. G. Zheng, *Synth. Met.* **1999**, *29*, 171.

(22)   (22a) A. Gruger, A. Novak, A. Regis, J. Colomban, *J. Mol. Struct.* **1994**, *328*, 153; (22b) S. M. Yang, J. H. Chiang, *Synth. Met.* **1991**, *41*, 761.

(23)   (23a) A. H. Kwon, J. A. Conklin, M. Makhinson, R. B. Kaner, *Synth. Met.* **1997**, *84*, 95; (23b) A. Cihaner, A. M. Onal, *Eur. Polym. J.* **2001**, *37*, 1767.

(24)   (24a) J. Stejskal, I. Sapurina, M. Trchová, E. N. Konyushenko, P. Holler, *Polymer* **2006**, *47*, 8253; (24b) F. Würthner, *Chem. Commun.* **2004**, 1564.

(25)   (25a) E. N. Konyushenko, J. Stejskal, I. Šeděnková, M. Trchová, I. Sapurina, M. Cieslar, J. Prokeš, *Polym. Int.* **2006**, *55*, 31; (25b) G. Ćirić-Marjanović, M. Trchová, J. Stejskal, *Int. J. Quant. Chem.* **2007**, *108*, 318; (25c) J. Stejskal, I. Sapurina, M. Trchová, E. N. Konyushenko, *Macromolecules* **2008**, *41*, 3530; (25d) A. Janošević, G. Ćirić-Marjanović, B. Marjanović, P. Holler, M. Trchová, J. Stejskal, *Nanotechnology* **2008**, *19*, 135606; (25e) S. Mentus, G. Ćirić-Marjanović, M. Trchová, J. Stejskal, *Nanotechnology* **2009**, *20*, 245601.

(26)   (26a) Z. D. Zujovic, L. Zhang, G. A. Bowmaker, P. A. Kilmartin, J. Travas-Sejdic, *Macromolecules* **2008**, *41*, 3125; (26b) C. Laslau, Z. D. Zujovic, J. Travas-Sejdic, *Macromol. Rapid Commun.* **2009**, *30*, 1663; (26c) C. Laslau, Z. D. Zujovic, L. Zhang, G. A. Bowmaker, J. Travas-Sejdic, *Chem. Mater.* **2009**, *21*, 954.

(27)   (27a) D. M. DeLongchamp, S. Sambasivan, D. A. Fischer, E. K. Lin, P. Chang, A. R. Murphy, J. M. J. Fréchet, V. Subramanian, *Adv. Mater.* **2005**, *17*, 2340; (27b) D. M. DeLongchamp, R. J. Kline, E. K. Lin, D. A. Fischer, L. J. Richter, L. A. Lucas, M. Heeney, I. McCulloch, J. E. Northrup, *Adv. Mater.* **2007**, *19*, 833.

(28)   (28a) A. L. Briseno, S. C. B. Mannsfeld, S. A. Jenekhe, Z. Bao, Y. Xia, *Mater. Today* **2008**, *11*, 38; (28b) M. Mas-Torrent, C. Rovira, *Chem. Soc. Rev.* **2008**, *37*, 827; (28c) L. Zang, Y. Che, J. S. Moore, *Acc. Chem. Res.* **2008**, *41*, 1596.

(29)   (29a) M. Poncet, B. Corraze, S. Quillard, W. Wang, A. G. MacDiarmid, *Thin Solid Films* **2004**, *458*, 32; (29b) Y. Zhou, J. Geng, G. Li, E. Zhou, L. Chen, W. Zhang, *J. Poly. Sci. Part B: Poly. Phys.* **2006**, *44*, 764.

(30)   (30a) D. H. Kim, Y. Jang, Y. D. Park, K. Cho, *J. Phys. Chem. B* **2006**, *110*, 15763; (30b) A. L. Briseno, S. C. B. Mannsfeld, X. Lu, Y. Xiong, S. A. Jenekhe, Z. Bao, Y. Xia, *Nano Lett.* **2007**, *7*, 668.

(31)   W. J. Zhang, J. Feng, A. G. MacDiarmid, A. J. Epstein, *Synth. Met.* **1997**, *84*, 119.

(32)   J. Honzl, M. Tlustakova, *J. Poly. Sci. Part C.* **1968**, *22*, 451.

(33)   K. Balakrishnan, A. Datar, T. Naddo, J. Huang, R. Oitker, M. Yen, J. Zhao, L. Zang, *J. Am. Chem. Soc.* **2006**, *128*, 7390.

(34)   M. Kastler, W. Pisula, D. Wasserfallen, T. Pakula, K. Müllen, *J. Am. Chem. Soc.* **2005**, *127*, 4268.

(35)   (35a) R. D. Deegan, O. Bakajin, T. F. Dupont, G. Huber, S. R. Nagel, T. A. Witten, *Nature* **1997**, *389*, 827; (35b) R. v. Hameren, P. Schön, A. M. v. Buul, J. Hoogboom, S. V. Lazarenko, J. W. Gerritsen, H. Engelkamp, P. C. M. Christianen, H. A. Heus, J. C. Maan, T. Rasing, S. Speller, A. E. Rowan, J. A. A. W. Elemans, R. J. M. Nolte, *Science* **2006**, *314*, 1433; (35c) J. Huang, R. Fan, S. Connor, P. Yang, *Angew. Chem., Int. Ed.* **2007**, *46*, 2414.

(36)   Y. Huang, X. Duan, Q. Wei, C. M. Lieber, *Science* **2001**, *291*, 630.

(37)   X. Duan, C. Niu, V. Sahi, J. Chen, J. W. Parce, S. Empedocles, J. L. Goldman, *Nature* **2003**, *425*, 274.

(38)   (38a) L. Al-Mashat, H. D. Tran, W. Wlodarski, R. B. Kaner, K. Kalantar-zadeh, *IEEE Sens. J.* **2008**, *8*, 365; (38b) L. Al-Mashat, H. D. Tran, W. Wlodarski, R. B. Kaner, K. Kalantar-zadeh, *Sens. Actuators B* **2008**, *134*, 826.

(39)   Q. Ameer, S. B. Adeloju, *Sens. Act. B* **2005**, *106*, 541.

Chapter 2. Nanoscale morphology, dimensional control and electrical properties of oligoanilines

While nanostructures of organic conductors have generated great interest in recent years, their nanoscale size and shape control remains a significant challenge. Here we report a general method for producing a variety of oligoaniline nanostructures with well-defined morphologies and dimensionalities. 1-D nanowires, 2-D nanoribbons, and 3-D rectangular nanoplates and nanoflowers of tetraaniline are produced by a solvent exchange process in which the dopant acid can be used to tune the oligomer morphology. The process appears to be a general route for producing nanostructures for a variety of other aniline oligomers such as the phenyl-capped tetramer. X-ray diffraction of the tetraniline nanostructures reveals that they possess different packing arrangements, which results in different nanoscale morphologies with different electrical properties for the structures. The conductivity of a single tetraaniline nanostructure is up to two orders of magnitude higher than the highest previously reported value and rivals that of pressed pellets of conventional polyaniline doped with acid. Furthermore, these oligomer nanostructures can be easily processed by a number of methods in order to create thin films composed of aligned nanostructures over a macroscopic area.

2.1 Introduction

One-dimensional (1-D) nanostructures of molecular organic conductors and conducting polymers have attracted growing attention in recent years due to their solution processability,

easily tunable electronic properties, and potential use in many novel applications.[1,2,3] In addition, these materials can shed light on the structure-property relationships for this unique class of nanomaterials.[1] Among the family of conducting polymers, polyaniline has been extensively studied due to its unique oxidation-reduction chemistry, environmental stability, biocompatibility, and for its simple acid-base doping-dedoping process as illustrated in Figure 1.[4-8] Nanofibers of polyaniline have demonstrated enhanced performance in applications such as chemical sensors, catalysis, and supercapacitors due to their high surface area and porous nature.[9-11] However, the performance and stability of many devices are governed by how molecules or polymer chains assemble in the solid state.[12,13] The lack of order at the chain level has limited polyaniline nanofibers from being integrated into electronic devices that require high carrier mobility and stability such as organic field-effect transistors and solar cells. These applications are currently dominated by molecular semiconductors that can often self-assemble into highly ordered nanowires or nanoribbons.[1,2,14] Moreover, polyaniline nanofibers typically possess low aspect ratios and are highly flexible, which makes the fabrication of single-wire devices and post-synthetic alignment difficult.

In contrast to polyaniline, oligomers of aniline are capable of forming ordered extended structures; crystals of low molecular weight oligomers have already been characterized.[15-18] However, compared to polyaniline, reports on oligoanilines are sparse, especially in regards to generating nanoscale structures and/or improving their electrical conductivity.[19-21] Oligoanilines have generally been reported to possess low conductivities ranging from 10^{-6} to 10^{-2} S/cm for tetraaniline in pressed pellet form.[20,21] However, the bulk conductivity of a conducting polymer is governed by both the transport properties within a molecular chain and between chains.[16,19,22,23] In this regard, oligoanilines have great potential for improvements in the

44

material's interchain transport properties. Reports on the conductivity of oligoanilines from a pressed pellet are therefore typically low due to the fact that interchain transport is not optimized. Oligoanilines also represent an interesting middle ground between polyaniline and molecular semiconductors because oligoanilines retain the chemical properties of the polymer, e.g., the acid-base doping-dedoping chemistry (see **Figure 2.1**), while also possessing properties typically associated with molecular semiconductors especially in regard to monodispersity and self-assembly.

The most important oxidation state of polyaniline is the emeraldine base form, since it can be doped by strong acids to create the conducting form, which can be readily and reversibly reduced to the insulating emeraldine base form as shown in **Figure 2.1**. The emeraldine oxidation state of polyaniline possesses three benzene rings for every quinoid ring. Amine/phenyl-capped tetraaniline, hereafter referred to as tetraaniline (see **Table 2.1** for nomenclature and structures of aniline oligomers), therefore represents an important model compound for polyaniline because structure-wise, it is the shortest oligomer that can represent the emeraldine oxidation state. Here we report a general and versatile method for producing structurally ordered and well-defined oligoaniline nanostructures via the self-assembly of tetraaniline and other aniline oligomers in their most conductive emeraldine salt oxidation state. Exquisite nanoscale morphology and dimensionality control is demonstrated via a simple dopant-induced process. The conductivities of these nanostructures are measured via single wire, ribbon, or plate measurements. The values observed are two orders of magnitude higher than previously reported pressed-pellet values for oligoanilines and are comparable to that of conventional polyaniline.[20,21]

Benzenoid : Quinoid ratio

1 : 1

3 : 1

4 : 0
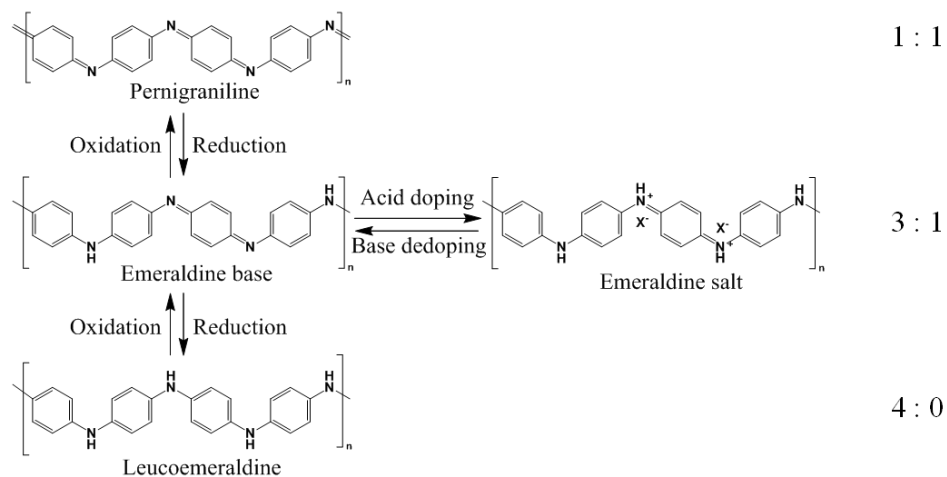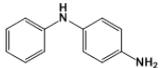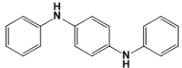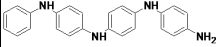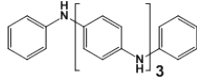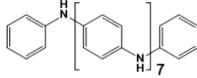
Figure 2.1. The oxidation-reduction chemistry of polyaniline: The fully reduced form of polyaniline, known as leucoemeraldine, can be half-oxidized to form emeraldine or fully oxidized to form pernigraniline. The electrically insulating emeraldine base form of polyaniline (conductivity $\leq 1 \times 10^{-10}$ S/cm) can be doped with a strong acid to produce the electrically conducting emeraldine salt form of polyaniline (conductivity ≥ 1 S/cm). This process can be reversed by adding a strong base. Note that only the emeraldine oxidation state of polyaniline can be doped to form an electrically conducting polymer. Tetraaniline is obtained when n = 1 and therefore is the smallest oligomer unit that can fully represent the structure of polyaniline.

Table 2.1. Common Abbreviations and Molecular Structures for Aniline Oligomers and Detailed

Conditions for Their Nanostructure Formation.

Oligomer	Common abbreviation	Molecular structure	Conditions for nanostructure formation				
			Oligo-mer	Aqueous solvent	Organic solvent	Process dura-tion	Final morph ology
Aniline dimer (*N*-phenyl-1,4-phenylenedia mine)			2 mg	4 mL 0.1 M HCl $_{(aq.)}$	1 mL ethanol	10 days	Nanofi bers/ nanow ires
Phenyl-capped aniline dimer (*N,N'*-diphenyl-1,4-phenylenedia mine)			2 mg	4 mL 1 M HCl $_{(aq.)}$	1 mL methan ol	15 days	Nano wires/ nanopl ates
Aniline tetramer	Ph/NH$_2$ TANI		2 mg	4 mL 0.1 M HCl $_{(aq.)}$	1 mL ethanol	4 days	Nano wires
			2 mg	4 mL 1 M HNO$_3$ $_{(aq.)}$	1 mL ethanol	4 days	Nanori bbons
			2 mg	4 mL 0.5 M HClO$_4$ $_{(aq.)}$	1 mL ethanol	4 days	Nanop lates
			2 mg	4 mL 1 M H$_2$SO$_4$ $_{(aq.)}$	1 mL ethanol	4 days	Nanofl owers
			2 mg	4 mL 1 M CSA $_{(aq.)}$	1 mL ethanol	4 days	Inter-connec ted nanofi

47

							bers
Phenyl-capped aniline tetramer	Ph/Ph TANI		2 mg	4 mL 0.1 M HCl (aq.)	1 mL ethanol	5 days	Nano wires/ nanori bbons
Phenyl-capped aniline octamer	Ph/Ph OANI		2 mg	4 mL 0.1 M HCl (aq.)	1 mL ethanol	4 days	Agglo merate s

2.2 Experimental

2.2.1 Synthesis

N-phenyl-1,4-phenylenediamine and *N*, *N'*-diphenyl-1,4-phenylenediamine were purchased from Sigma-Aldrich and TCI Chemicals, respectively, and were used without further purification. Tetraaniline was synthesized via a previously reported route.[24] In brief, iron (III) chloride dissolved in 0.1 M HCl was mixed with stoichiometric amounts of *N*-phenyl-1,4-phenylenediamine (aniline dimer) suspended in the same solvent. After 2 hours of vigorous stirring, the suspension was filtered and repeatedly washed with 0.1 M HCl until the filtrate became clear. The solid was collected and dedoped with 0.1 M ammonium hydroxide. The dedoped crude product was reduced to the leucoemeraldine oxidation state with hydrazine and recrystallized from ethanol three times in order to purify the product. Tetraaniline was then re-oxidized to the emeraldine base form with one equivalent of ammonium peroxydisulfate (APS). The final product was characterized by UV-Vis, Fourier transform infrared (FT-IR) spectroscopy, and matrix-assisted laser desorption/ionization-time of flight (MALDI-TOF) mass spectroscopy (**Figure 2.2**). Phenyl-capped octaaniline was synthesized by a condensation

reaction in an inert atmosphere via a previously reported route.[25] Phenyl-capped tetraaniline was synthesized using the same method with tetraaniline replaced by *N*-phenyl-1,4-phenylenediamine as the starting material. Characterizations for these two oligomers are shown in **Figure 2.3** and **2.4**, respectively.
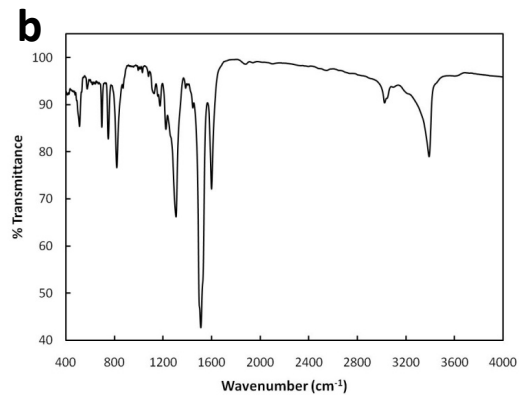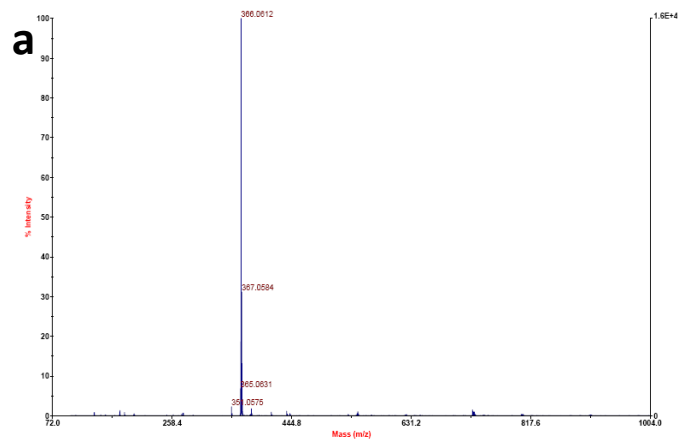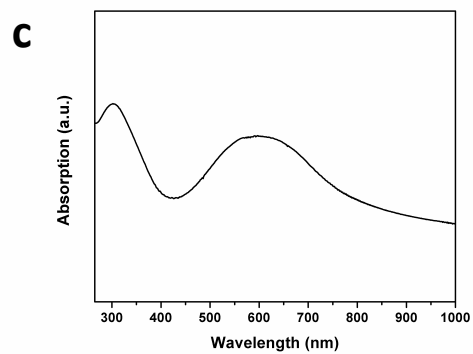
Figure 2.2. (a) MALDI, (b) FT-IR, and (c) UV-vis spectra of tetraaniline in its emeraldine base oxidation state. The UV-vis spectrum for tetraaniline is presented in **Fig. 2.5c**.
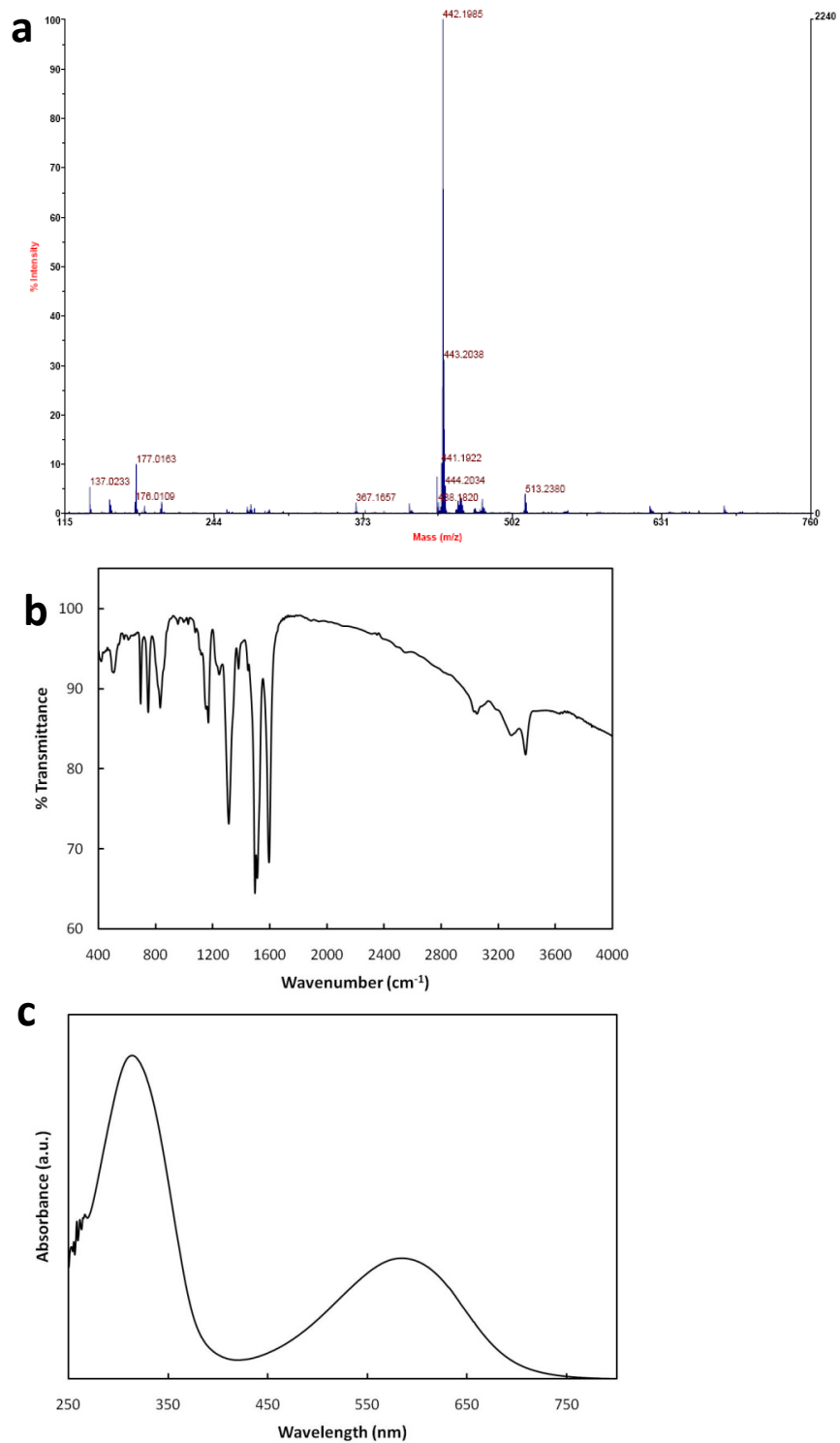
Figure 2.3. (a) MALDI, (b) FT-IR, and (c) UV-vis spectra of phenyl-capped tetraaniline in its emeraldine base oxidation state. The UV-vis spectrum was taken in ethanol.
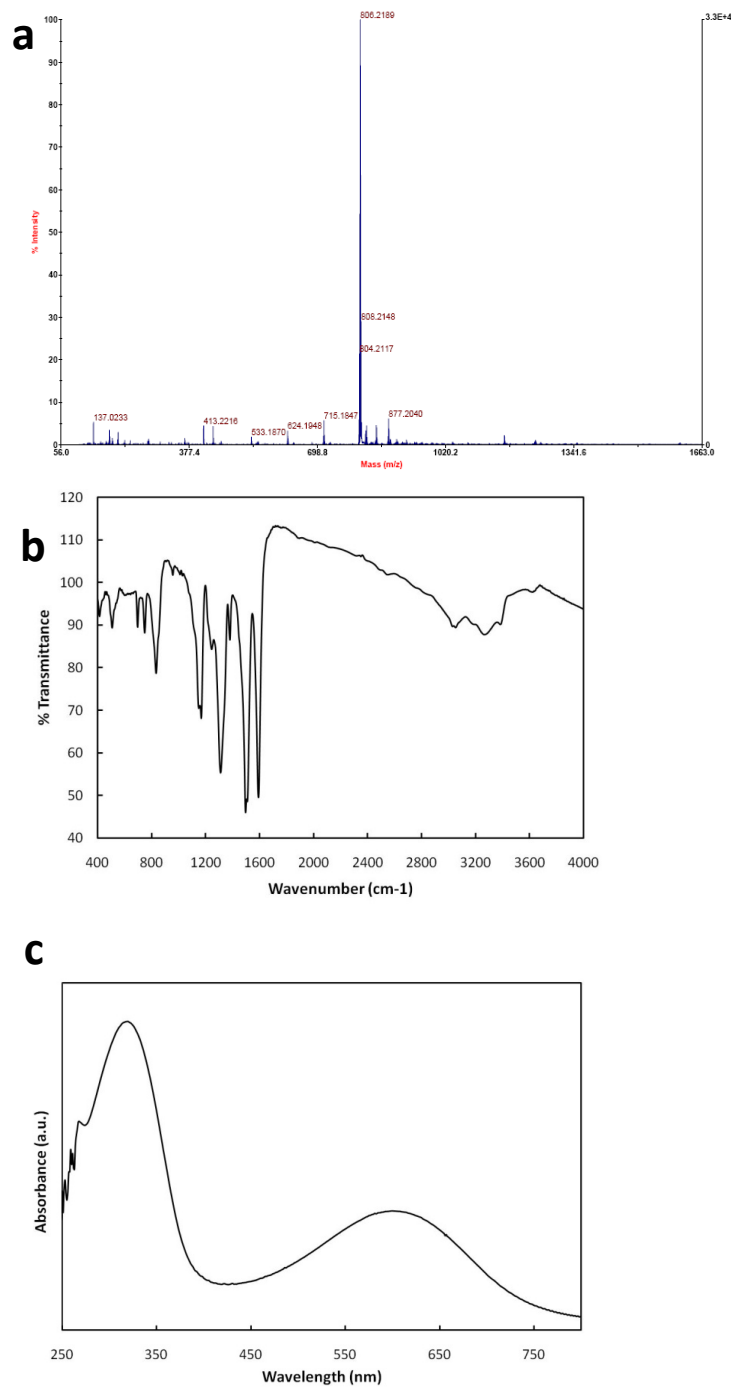
Figure 2.4. (a) MALDI, (b) FT-IR, and (c) UV-vis spectra of phenyl-capped octaaniline in its emeraldine base oxidation state. The UV-vis spectrum was taken in dimethylformamide (DMF).

2.2.2 Process for producing nanostructures

In a typical process, 2.0 mg of finely powdered tetraaniline is added to a solvent mixture comprised of 1.0 mL of ethanol and 4.0 mL of an aqueous acidic solution. The mixture is shaken for a few seconds and then left undisturbed for 4 to 5 days. Less ethanol is used for *N*-phenyl-1,4-phenylenediamine and *N,N'*-diphenyl-1,4-phenylenediamine than tetraaniline since they have a higher solubility in ethanol. Duration of the processes varied slightly depending on the oligomer. Molecular structures and common abbreviations for the aniline oligomers are summarized in **Table 2.1** along with the detailed conditions for their nanostructure formation. Each reaction mixture was purified by dialysis against deionized water for approximately one day. A small amount of granular debris often precipitated out and was visible at the bottom of the vial. The debris can be readily removed by agitating the vial since the granular debris settles out from the dispersion quickly, while the nanostructures remain well-dispersed for a lengthy period of time. As a result, the top nanostructured dispersion can be collected into a different container and the debris that accumulates at the vial bottom discarded.

2.2.3 Microscopy

Scanning electron microscopy (SEM) and transmission electron microscopy (TEM) samples were prepared by drop-casting one to two drops of a diluted oligoaniline dispersion onto a piece of silicon wafer or a TEM grid, respectively. SEM images were taken with a JEOL JSM-6700 Field Emission scanning electron microscope, and TEM images were taken with a FEI/PHILIPS CM 120 transmission electron microscope.

2.2.4 Other characterization techniques

Powder X-ray diffraction patterns of the tetraaniline nanostructures were taken on a Panalytical X'Pert Pro X-ray powder diffractometer with a scan rate of 2 degrees/min. Sodium chloride was used as an internal standard for the crystallite size calculations using the Scherrer equation. MALDI samples were prepared with 2,5-dihydroxybenzoic acid (DHB) as the matrix and the spectra were taken on an Applied Biosystems Voyager-DE-STR MALDI-TOF spectrometer. FT-IR samples were prepared with FT-IR grade KBr and the spectra were taken with a JASCO FT/IR-420 spectrometer. UV-vis-NIR (near infrared) spectra of the nanowire dispersion were taken with a quartz cuvette that has a 1 mm light path-length on a Shimadzu UV-3101 PC UV-vis-NIR Scanning Spectrophotometer.

2.2.5 Single wire measurements

Bottom-contact devices were fabricated for all single wire, ribbon, and plate measurements. Gold electrodes were thermally deposited on a Si/SiO_2 substrate with a 300 nm SiO_2 layer to create channels that are 2-10 μm in length. One drop of oligoaniline dispersion was drop-cast onto the electrodes, and the nanowires, nanoribbons, or rectangular nanoplates were allowed to settle for a few seconds. The rest of the droplet was then quickly removed with flowing nitrogen and the devices blown thoroughly dry. Measurements were carried out directly after deposition using a standard probe station under ambient conditions.

2.3 Results and Discussion

2.3.1 Nanostructure synthesis

Tetraaniline synthesized by previously reported methods possesses a granular, agglomerated morphology (**Fig. 2.5b**). However, *nanostructures* of tetraaniline can be grown by adding this granular powder to a mixture of 0.1 M HCl and ethanol, which is then left undisturbed for 4 to 5 days. During this time, large particles are observed that initially precipitate to the bottom of the vial and gradually turn into the green, doped form of tetraaniline. This material slowly disperses into the surrounding medium. At the end of this process, only doped tetraaniline is observed floating in the solvent. The mixture forms a stable dispersion upon simple agitation (**Fig. 2.5a**). SEM and TEM images of the resulting dispersion show that long, non-woven nanowires with high aspect ratios are created during this process (**Fig. 2.5d, e**). The nanowires typically range in diameter from 70 to 200 nm and are up to hundreds of microns long. A UV-vis-NIR spectrum of the resulting tetraaniline nanowires in the emeraldine salt form dispersed in water is shown as the "65 h" curve in **Figure 2.5c**, and a full spectrum that extends into the near infrared (NIR) up to 3000 nm is shown in **Figure 2.6**. The as-synthesized dedoped tetraaniline in its emeraldine base form dissolved in ethanol is presented in **Figure 2.2c** and is consistent with previous work on tetraaniline.[7,24]
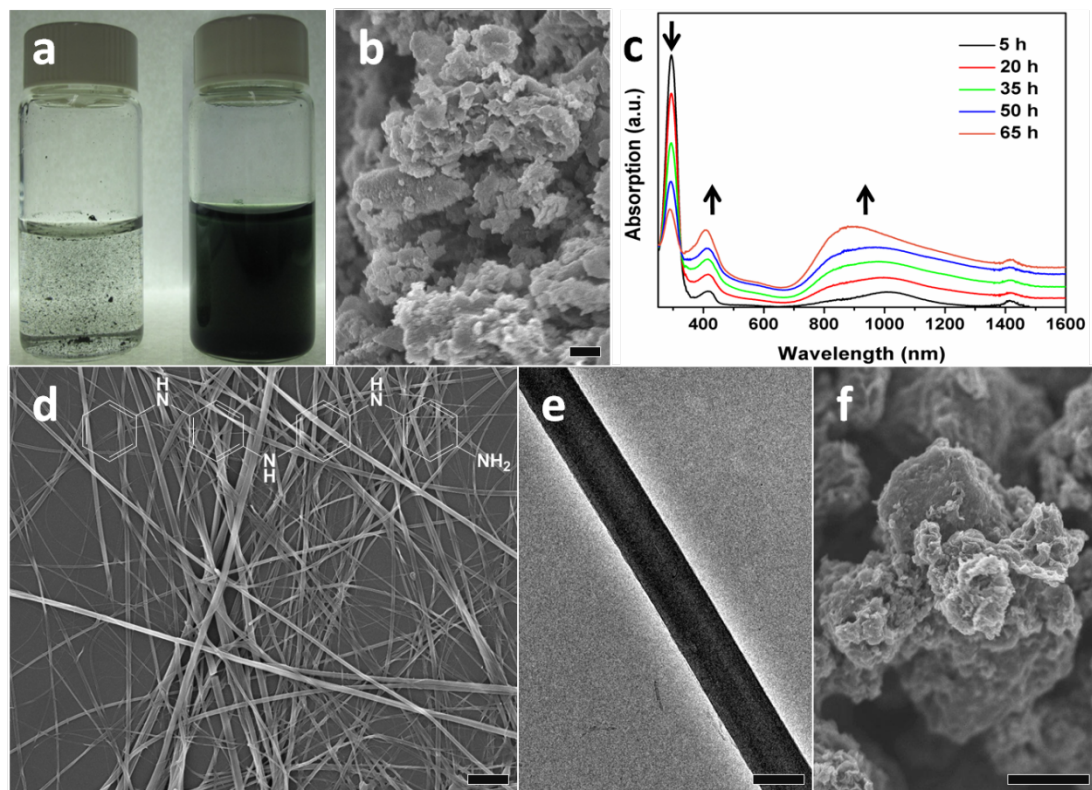
Figure 2.5. (a) Photographs show a mixture of tetraaniline, ethanol, and 0.1 M HCl at the beginning of the process (left vial) and the green tetraaniline nanowire dispersion produced at the end of 4 days (right vial). Both vials were agitated prior to taking the photos; (b) A scanning electron microscope (SEM) image of the as-synthesized tetraaniline powder; (c) UV-Vis spectra obtained at the given time intervals during the course of nanowire assembly; (d) An SEM image of a network of tetraaniline nanowires. The molecular structure of tetraaniline is shown across the top of the image; (e) A transmission electron microscope (TEM) image of a single tetraaniline nanowire; and (f) the results of the same process carried out in a mixture of ethanol and water in the absence of doping acids. Scale bars: 1 μm.
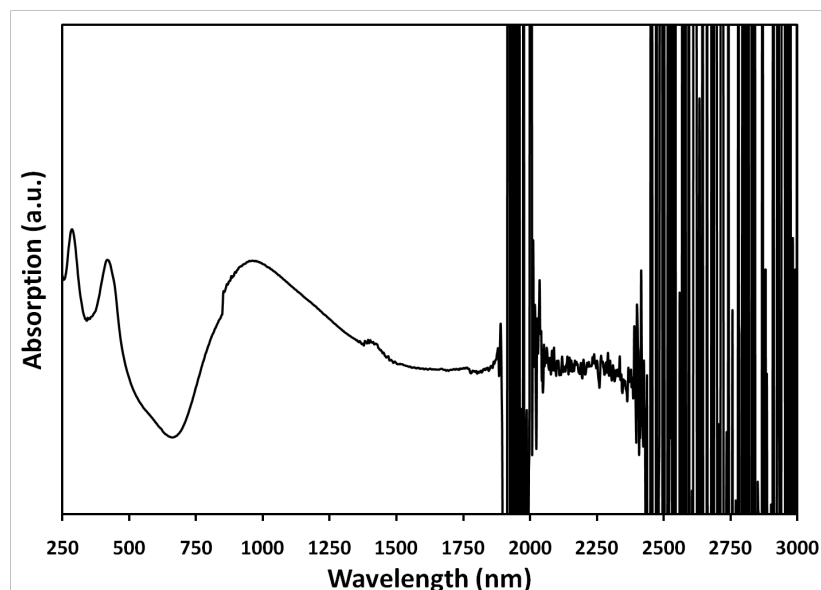
Figure 2.6. UV-vis-NIR spectrum of tetraaniline nanowires dispersed in water. The spectrum saturates beyond 1800 nm due to water absorption.

2.3.2 Formation mechanism

Literature reports indicate that π-conjugated molecules can form well-defined morphologies and molecular arrangements through non-covalent interactions such as π-π stacking and hydrogen bonding. Controlled aggregation of molecules through these non-covalent interactions in a non-solvent or in a mixture of a non-solvent and a good solvent can lead to the formation of nanowires or nanoribbons.[1,14] Tetraaniline nanowires may form in an analogous process to that known for other molecular semiconductor nanowires such as perylene tetracarboxylic diimide derivatives.[14,26,27] Although tetraaniline is not soluble in an acidic aqueous solvent, it can be doped in this environment. Tetraaniline is, however, soluble in common organic solvents such as ethanol. The solubility and the degree of aggregation of tetraaniline in different liquids can be easily tuned by adjusting the ratio of the two solvents/non-

57

solvents. Upon increasing the aqueous component, the enhanced solvent polarity can create solvophobic association between the aromatic rings, which promotes extended π-π stacking, in a similar manner to how surfactants and amphiphilic molecules assemble.[26,28] Tuning the solvent ratio thus allows for controlled aggregation and stacking of tetraaniline molecules. With a solvent mixture of 4:1 (v/v) of an aqueous solution of HCl (a non-solvent) and ethanol (a good solvent), tetraaniline molecules assemble into an extended superstructure consisting of nanowires. During this process, bulk tetraaniline powder slowly disperses into the solvent to form a suspension of tetraaniline nanowires. Control experiments carried out in a solely acidic aqueous environment leads to poorly-defined structures (see **Fig. 2.7**), which illustrates the importance of achieving the correct solvent polarity from a mixture of solvents.
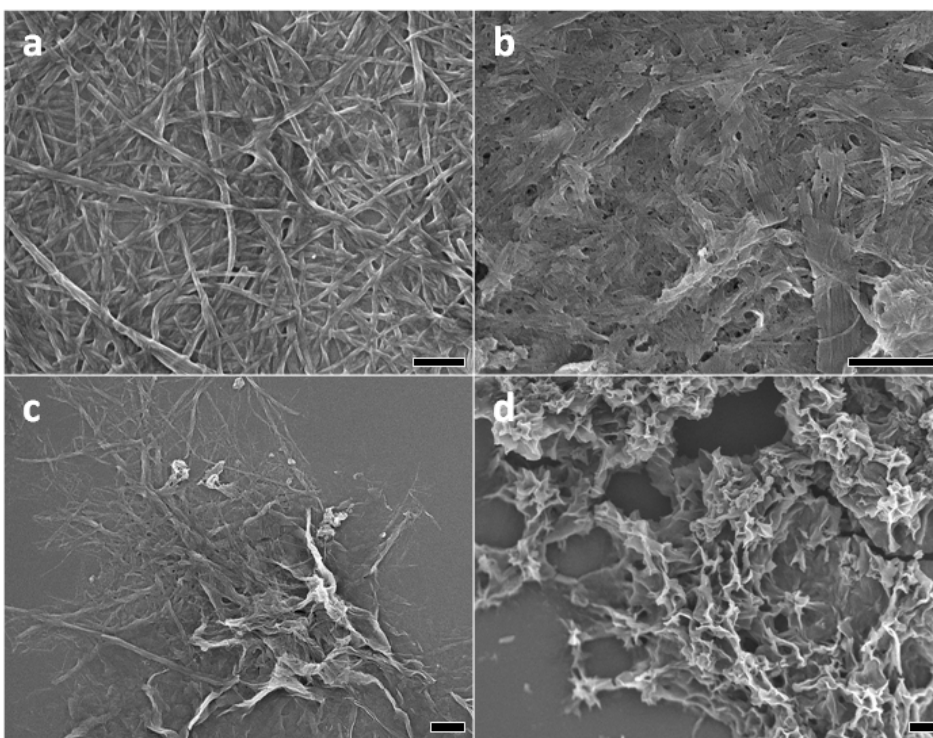
Figure 2.7. SEM images of tetraaniline that has undergone the same self-assembly process in (a) 0.1 M HCl, (b) 1.0 M HNO$_3$, (c) 0.5 M HClO$_4$, and (d) 1.0 M H$_2$SO$_4$ in the absence of any

organic solvent. Only poorly defined and interconnected structures are obtained, illustrating the importance of the solvation factor attributed to ethanol in our process.

The nanowire growth process requires approximately four days in order for directional molecular self-assembly to occur which has been suggested as a factor in forming ordered nanostructures for other molecules such as perylene diimide and pentacene.[14,26,27,29] Non-covalent forces such as hydrogen bonding can modulate the directional nature of nanowire formation.[27,30] Although high aspect ratio nanowires are obtained in a solvent mixture of ethanol and 0.1 M HCl, an identical process carried out in a mixture of ethanol and water without any dopant acid only yields agglomerates (**Fig. 2.5f**). Tetraaniline remains in its initial emeraldine base oxidation state in water, but becomes the protonated emeraldine salt form when the process is performed in an acid solution. This may be a result of extra hydrogen bonding associated with the protonation which has been proposed as a driving force to regulate supramolecular organization.[31,32] The transition in oxidation state from the initial emeraldine base form of tetraaniline to the final emeraldine salt form was monitored *in situ* via UV-vis-NIR spectroscopy during the course of nanowire assembly. UV-vis-NIR spectra were collected 5 hours into the process and then every 15 hours until the relative peak ratios stopped changing (**Fig. 2.5c**). At 5 hours, agglomerates that resemble the morphology of the as-synthesized tetraaniline are observed, and nanowires become the dominant product after 65 hours. Three peaks are present. The peak at 290 nm corresponds to the $\pi \rightarrow \pi^*$ transition. This transition typically appears between 350–360 nm for doped polyaniline;[33,34] however, it undergoes a blue shift to 290 nm due to the much shorter conjugation length of tetraaniline compared to polyaniline. Absorptions at 420 nm and around 950 nm are ascribed to the polaron $\rightarrow \pi^*$ and $\pi \rightarrow$ polaron band

transitions, respectively, indicating that the nanowires are in their conductive emeraldine salt form.[33] The weak peak around 1420 nm is due to water absorption.[35] As the assembly process progresses, the spectra changes significantly with a defined isosbestic point at 325 nm. The drastic decrease in the ratio of the 290 nm peak to the 420 nm peak indicates that the $\pi \rightarrow \pi^*$ transition energy is greatly reduced as the tetraaniline molecules equilibrate into a more preferred aggregate phase with extended π-π stacking as nanowires form. A similar effect has been observed in nanostructures of molecular conductors.[30] On the other hand, the ratio of the 420 nm peak to the 290 nm peak increases throughout the process, indicating an increase in doping level as more polarons are injected into the π^* band as assembly progresses. Simultaneously, the broad peak at ~900 nm which extends over several hundreds of nm from the visible to the NIR region also increases in intensity compared to the 290 nm peak. The broadening of this asymmetric peak is associated with the increasing linearity of polyaniline which leads to increased polaron delocalization.[33,34,36] The increase in absorption of this broad peak during tetraaniline nanowire assembly suggests that the intermolecular stacking between aniline tetramers leads to delocalization of carriers because of the enhanced π-π orbital overlapping. Therefore, the overall change in the ratios of peak absorptions indicates that tetraaniline molecules rearrange themselves from the initially agglomerated morphology into an extended, more thermodynamically favorable array with better carrier transport during the process of nanowire assembly.

2.3.3 Size and shape control

Size and shape control of 1-D organic nanostructures remains a significant challenge within the field of organic conductors and continues to draw increasing interest. For example,

studies have shown that using different doping acids during the synthesis of polyaniline nanofibers can change their diameter. When synthesized in 1.0 M HCl, polyaniline nanofibers typically have diameters around 30 nm, while in 1.0 M camphorsulfonic acid (CSA) the diameters average 50 nm.[37] For oligomers, their organization into extended supramolecular structures can be controlled by using different dopants that have different sizes. As shown in **Figure 2.5**, 1-D nanowires are formed when HCl is used as the doping acid; however, as the dopant is changed to HNO_3, 2-D nanoribbons are obtained (**Fig. 2.8a and b**). Using $HClO_4$ induces the formation of well-defined 3-D rectangular-shaped nanoplates (**Fig. 2.8c and d**), while H_2SO_4 produces tetraaniline molecules that pack into nanoflowers consisting of well-organized clusters of 2-D nanosheets (**Fig. 2.8e**).
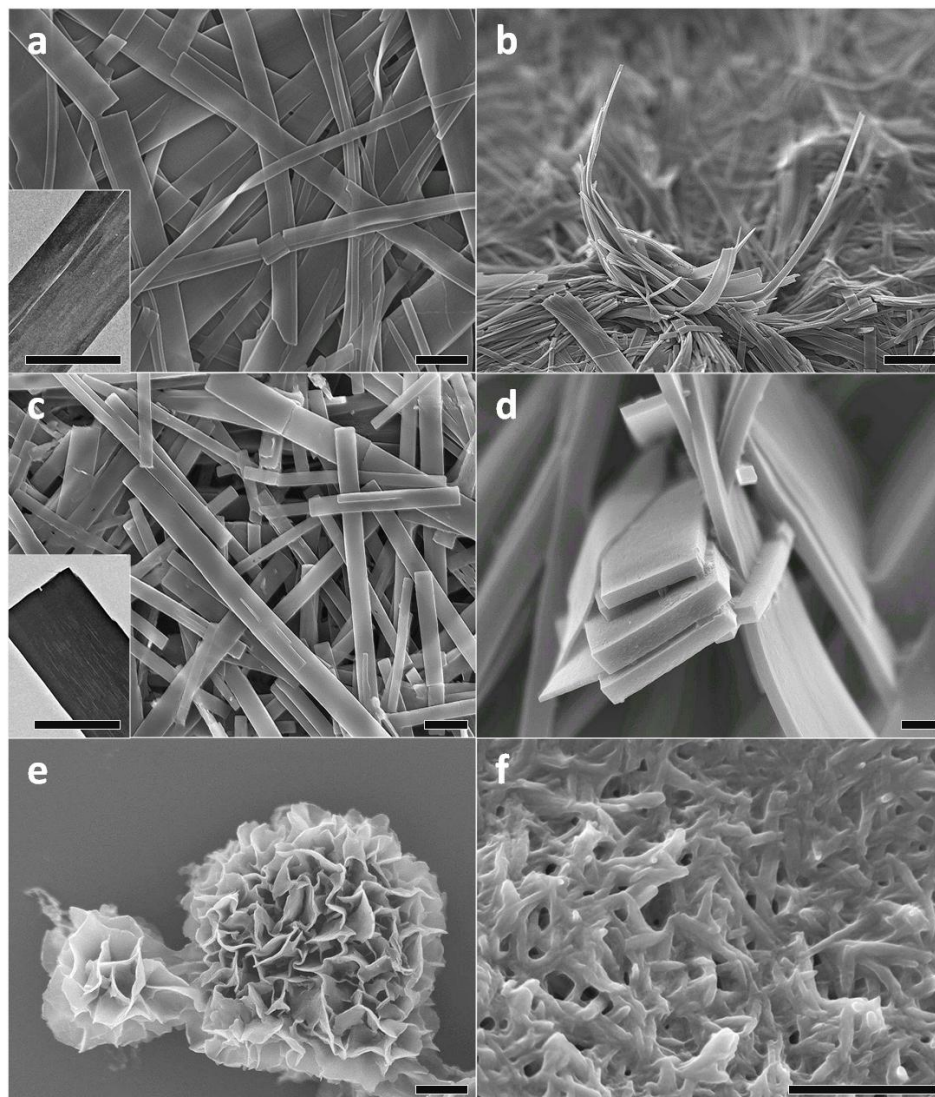
Figure 2.8. (a) An SEM image of tetraaniline nanoribbons obtained when 1.0 M HNO$_3$ is used as the doping acid. The inset shows a TEM image of a single ribbon; (b) An edge-on view of the nanoribbons; (c) An SEM image of rectangular-shaped tetraaniline nanoplates produced using 0.5 M HClO$_4$ as the doping acid. The inset shows a TEM image of a nanoplatelet; (d) An SEM cross-sectional view of the nanoplates; (e) An SEM image of nanoflowers produced using 1.0 M H$_2$SO$_4$ as the doping acid; and (f) an SEM image of inter-connected nanofibers obtained when 1.0 M CSA is used as the doping acid. Scale bar: 100 nm for (d), 1 μm for all the others.

The exquisite dopant-induced nanoscale control of the size and shape of aniline-based oligomers and polymers can be explained by examining and comparing the structural differences between the polymer and the oligomer. When polyaniline or oligoaniline is doped with an acid, the imine nitrogens become protonated and the negatively charged dopant anions reside near the positively charged nitrogens due to ionic attractions (**Fig. 2.1**). The size of the dopant anions thus influences the interchain packing distance and ultimately the supramolecular morphology. Polyaniline molecular chains are long and semi-rigid in sections; thus, dopant anion size does not have a large effect on the supramolecular structure observed for polyaniline since individual dopants only have a local effect on the polymer chains (**Fig. 2.9a**).[38] Thus, changing the dopant acid during the synthesis of polyaniline nanofibers primarily changes diameter, but has little affect on superstructure. However, oligoanilines such as tetraaniline are discreet, compact molecules. Consequently, the size of the dopant anion has a much more profound effect on the packing distances between tetraaniline molecules (**Fig. 2.9b**). This effect can be observed in the X-ray diffraction (XRD) patterns for the different tetraaniline nanostructures (**Fig. 2.9d**). For each of the four structures, the most intense peak in the X-ray diffraction pattern is centered around $2\theta = 20^o$, which has been ascribed to the periodicity parallel to the polymer chain.[39-42] When HCl is used as the doping acid to induce nanowire formation, Cl$^-$ ions remain between the chains, which results in a peak at $2\theta = 20.00^o$ corresponding to a d-spacing of 4.22 Å. This peak shifts to $2\theta = 19.87^o$ for HNO_3 doped nanoribbons, which indicates an increase in d-spacing to 4.46 Å. This is consistent with the fact that NO_3^- is a larger dopant anion than Cl$^-$. Nanoflowers doped by H_2SO_4 and rectangular nanoplates doped by $HClO_4$ have even larger d-spacings of 4.62 Å and 4.63 Å, respectively, as HSO_4^- and ClO_4^- ions are larger than NO_3^- and Cl$^-$.[43] To further illustrate the impact of dopant anion size, when a very large doping acid such as camphorsulfonic

acid (CSA) is employed, only poorly-defined, agglomerated tetraaniline nanofibers are obtained (**Fig. 2.8f**). This is due to the fact that CSA anions are bulky in size and they prevent oligomers from packing into ordered and discrete supramolecular structures (**Fig. 2.9c**). Their lack of packing order is evident in the corresponding XRD pattern, which does not have well-defined peaks and thus suggests an amorphous structure (**Fig. 2.9d**). Note that aside from the amorphous CSA-doped agglomerated nanofibers, the intensity of the X-ray diffraction patterns indicate that the nanowires are the least crystalline form of nanostructure, while the rectangular nanoplates and nanoribbons are far more crystalline. Such observations are consistent with the physical appearances of the nanostructures. Nanoflowers also produce intense diffraction peaks despite the fact that they do not appear as ordered as the nanoplates or nanoribbons. This can be attributed to the crystallinity of the stacked 2-D sheets/"petals" that comprise the nanoflowers. The Scherrer equation has been applied to assess the crystallite sizes of the four different morphologies. Using sodium chloride as an internal standard, the crystallite sizes were calculated to be 17 Å for the nanowires, 44 Å for the nanoribbons, 91 Å for the rectangular nanoplates, and 25 Å for the nanoflowers. Since the calculated crystallite sizes for the nanowires and the nanoflowers are well below the 50 Å accuracy limit of the Scherrer equation, the data for these materials should be considered qualitative. The rectangular nanoplates have the longest crystallite coherence length, approximately one-tenth of their average physical thickness, further confirming their high crystallinity. The calculated crystallite size of the nanoribbons falls between the nanocrystalline nanowires/nanoflowers and the more crystalline nanoplates, in agreement with the XRD data. In addition, well-defined 2θ peaks around 26° that correspond to classical π-π stacking between aromatic rings are observed for the more crystalline nanoribbons, nanoplates, and nanoflowers, further demonstrating that π-π stacking is likely an important

driving-force for nanostructure assembly. This is also supported by the previously discussed *in situ* UV-vis-NIR analysis (**Figure 2.5c**), where a greatly reduced $\pi \rightarrow \pi^*$ transition energy is observed due to the formation of extended π-π stacking as nanostructures assemble.
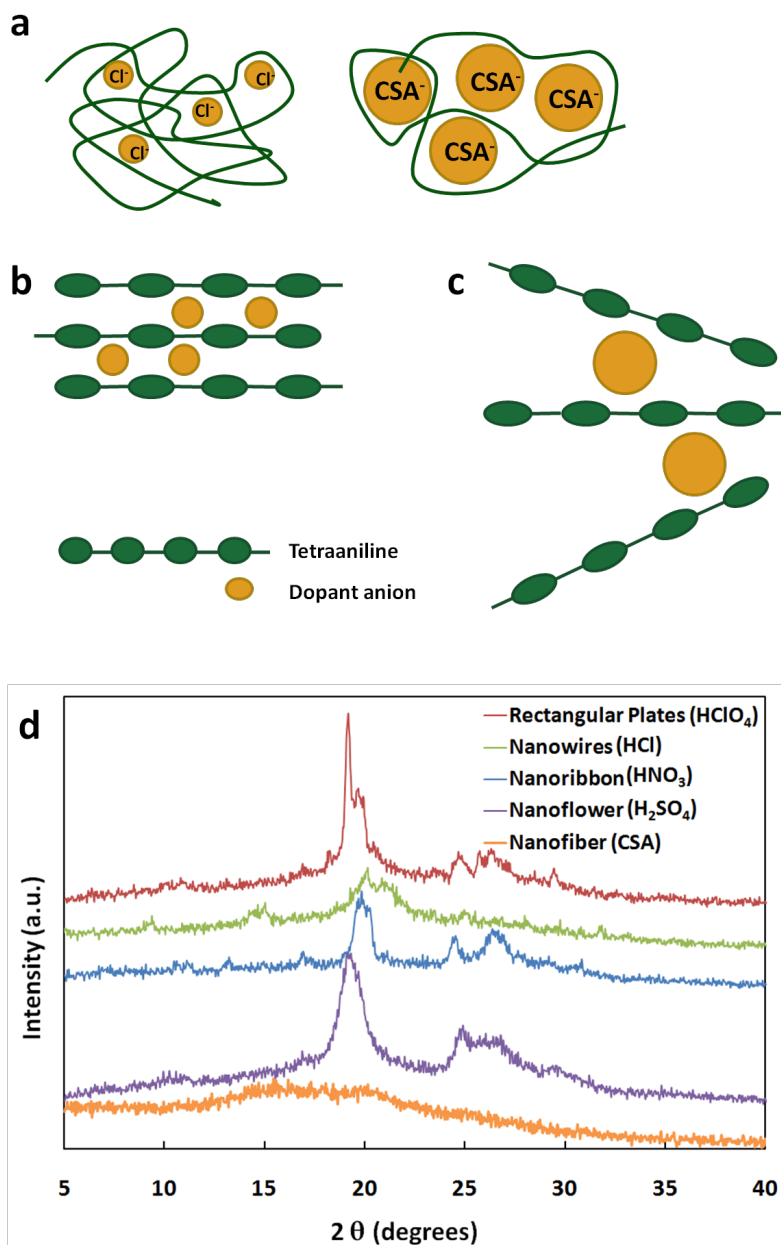
Figure 2.9. (a) An illustration of the polymer chain conformation typically found which is compactly coiled when a small doping acid such as HCl is used (left); the chain becomes more

expanded when doped with a bulky doping acid such as CSA and processed in certain solvents (right).[38] (b) The dopant anions likely reside between the tetraaniline molecular chains; therefore, the packing distance will be affected by the size of the anions. (c) Tetraaniline molecular chains do not pack well when a bulky doping acid such as CSA is used as the tetramers are prevented from arranging themselves into extended structures; and (d) X-ray diffraction patterns of nanowires (top), nanoribbons (second), rectangular nanoplates (third), nanoflowers (fourth), and agglomerated nanofibers (bottom).

2.3.4 Application to other oligoanilines

The synthetic methodology presented here appears to be a general and versatile route for producing nanostructures of other aniline oligomers. For example, nanowires of aniline dimer (*N*-phenyl-1,4-phenylenediamine) and phenyl-capped aniline dimer (*N,N'*-diphenyl-1,4-phenylenediamine) are obtained by the same method when HCl is used as the doping acid, and phenyl-capped tetraaniline forms a mixture of nanowires and narrow nanoribbons under the same conditions (**Fig. 2.10a to c**). Unfortunately, when the same approach is applied to phenyl-capped octaaniline, only agglomerates are obtained (**Fig. 2.10d**), likely due to the fact that the increase in chain length results in a molecule with more polymer-like characteristics so that its size and shape cannot be as readily controlled by this process.
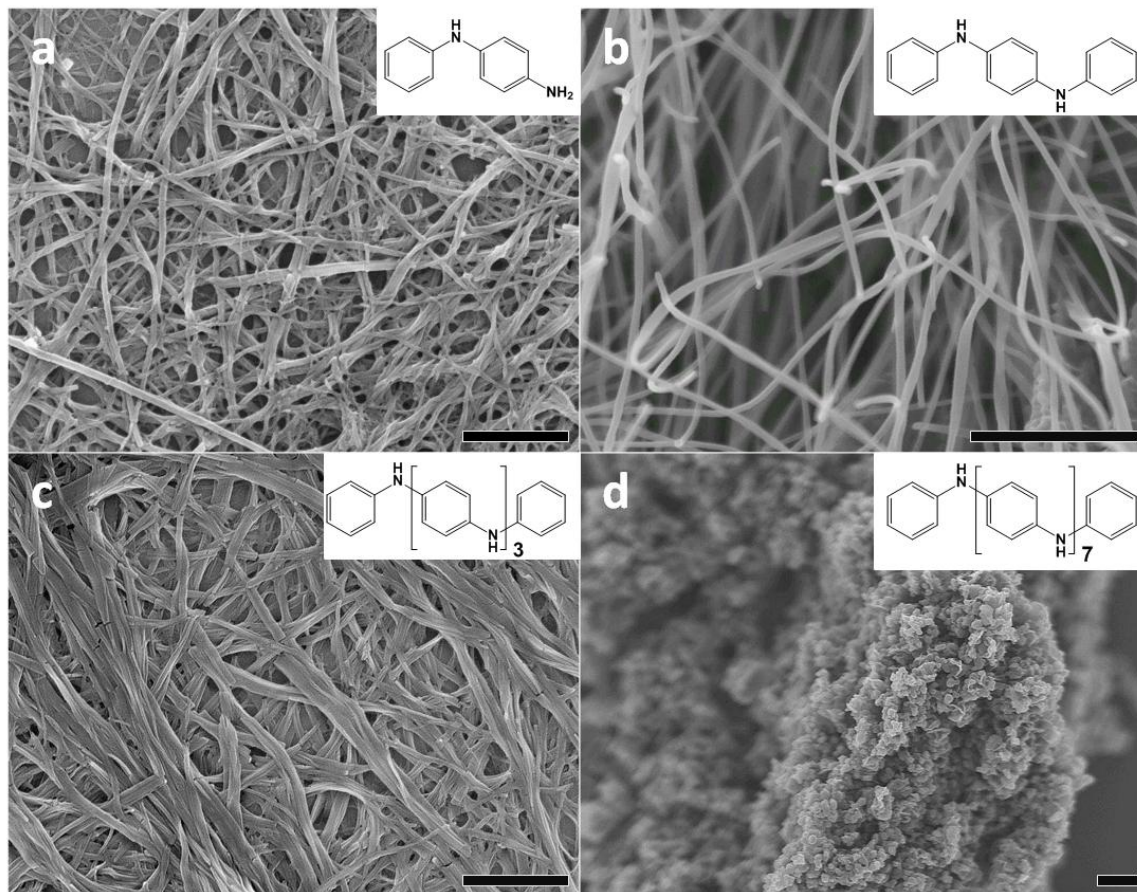
Figure 2.10. SEM images of (a) aniline dimer nanowires; (b) phenyl-capped aniline dimer nanowires; (c) phenyl-capped aniline tetramer nanowires and nanoribbons; and (d) phenyl-capped octaaniline agglomerates produced under the same experimental conditions that form tetraaniline nanostructures. Scale bar: 1 μm. Insets show the molecular structures of the corresponding aniline oligomer.

2.3.5 Electrical transport properties

Electrical transport studies on HCl-doped nanowires, HNO$_3$-doped nanoribbons, and HClO$_4$-doped rectangular nanoplates were performed in order to determine the conductivities of each of these nanostructures. Previous studies on the conductivity of doped tetraaniline measured

on pressed pellets have proven to be disappointing: the conductivity ranges from 10^{-6} to 10^{-2} S/cm depending on the synthetic method and doping acid used.[20,21] Our studies confirm that bulk tetraaniline has a conductivity of only 3×10^{-3} S/cm. However, pressed-pellet measurements represent the lower boundary for conductivity for oligoanilines due to high contact resistance between the numerous junctions between the nanostructures that can cause the conductivity to appear lower than the intrinsic conductivity of a single wire or ribbon. Measuring the conductivity of a single nanowire, nanoribbon or nanoplate therefore represents a method to determine the intrinsic conductivity of oligoaniline nanostructures.

Figure 2.11a shows a representative SEM image of an Au bottom-contact device constructed from a single tetraaniline nanowire. The nanowire was drop-cast across the source and drain electrodes from a freshly prepared dispersion of tetraaniline nanowires in water. The nanowires were allowed to deposit for a few seconds, and the rest of the droplet was quickly blown away by nitrogen flow, followed by taking an immediate measurement. This method of deposition reduces the amount of solvent impurities that would be left behind from solvent drying, which would decrease the quality of the measurements. Tetraaniline nanoribbon and nanoplate devices were fabricated in the same fashion. **Figure 2.11b** shows a typical *I-V* curve for a single nanowire device through a two-probe measurement. All measurements were carried out under ambient conditions with a standard semiconductor probe station. The linearity of the curve indicates that the tetraaniline nanostructures exhibit ohmic behavior. The conductivity of each nanostructure was calculated using the slope of the *I-V* plot along with the length of the nanostructure that bridges the source and drain electrodes. The actual length and width (or diameter in the case of a nanowire) of each channel were measured by SEM, and the thickness of the ribbon or plate was acquired through tilted SEM measurements assisted by AFM analysis

when needed. The conductivity of a single nanowire was found to be as high as 0.3 S/cm, and that for a nanoplate and nanoribbon were as high as 0.5 S/cm and 1.1 S/cm, respectively. This trend is consistent with the X-ray diffraction patterns and the crystallite coherence length obtained using the Scherrer equation as the nanowires were the least crystalline morphology with the smallest crystallite size, while the nanoribbons and rectangular nanoplates were much more crystalline and have larger crystallite sizes. The fact that the nanoplates have lower conductivity than the nanoribbons, despite their higher crystallinity and longer crystallite coherence length, can be ascribed to their poor contact with the Au electrodes since the plates are not as long or flexible as the ribbons. For measurements on different devices, conductivities in the range of 0.1 − 1.1 S/cm were obtained for nanoribbons. Such distribution of values was also observed for the nanowires and nanoplates. This range of variation can be partly attributed to (1) the differences in contact quality at the Au electrode-nanoribbon interfaces that are often associated with bottom contact devices, and (2) solvent impurities and/or microscopic debris trapped at the aforementioned interfaces. On this basis, it is evident that the conductivities we report here could likely be further improved if the contact quality and other issues are addressed; for instance, fabricating four-probe top-contact devices to reduce contact resistance. Despite these issues, the conductivity of the nanoribbon exhibits a two order of magnitude increase from the highest value reported previously for tetraaniline,[21] and a three order of magnitude increase from the method we followed for synthesizing bulk aniline tetramer.[24] It is worth emphasizing that the conductivity of the nanoribbons rivals that of conventional polyaniline, which has a conductivity on the order of 10^0-10^1 S/cm.[6,21,44] Such results clearly demonstrate that oligoanilines can be as highly conducting as the polymer once the interchain transport and the inter-domain transport components of bulk conductivity are optimized. The improved interchain transport as a result of

the increased intermolecular order is evident from the *in situ* UV-vis-NIR analysis and the XRD patterns. The conductivity may be further enhanced if a balance between the oligomer chain length and interchain packing is achieved.
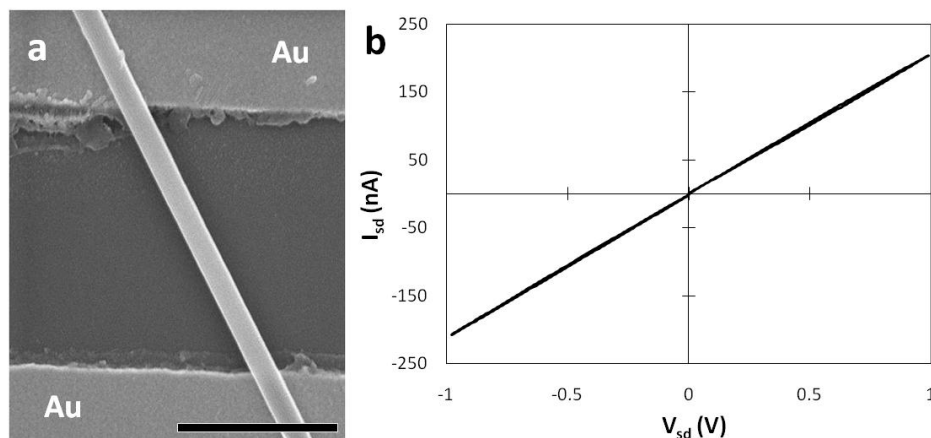
Figure 2.11. (a) An SEM image of a representative bottom-contact device fabricated from a single tetraaniline nanowire on a Si substrate covered by a 300 nm thick SiO_2 dielectric layer. The channel lengths between the Au electrode pairs were varied from 2 μm to 10 μm; a 2 μm channel length is shown. Scale bar = 1 μm.

2.3.6 Directional assembly

The inter-domain transport in a nanowire film could be further improved by assembling the randomly oriented oligoaniline nanostructures into oriented functional arrays onto a variety of substrates. This has been difficult to achieve for polyaniline nanofibers which typically form an interpenetrating network of nanofibers which makes individual fibers or wires difficult to separate. Fortunately, the oligoaniline nanowires tend to be much more rigid with high aspect ratios leading to discreet fibers. Initial experiments indicate that they can be readily aligned using dewetting alignment, in which nanowires that possess high aspect-ratios can be deposited

and aligned between the solvent front and the substrate as shown in **Figure 2.12a**.[45-47] Through this evaporation-induced assembly process, the tetraaniline nanowires are drawn towards the direction of the droplet evaporation, causing the nanowires to align in a radial fashion. The solution in the center continuously replenishes the solvent as it evaporates at the edges, thus increasing the nanowire deposition density at the edge of the droplet. A ring with high deposition density is formed as the droplet dries. Optical microscope images of a section of the ring are shown in **Figure 2.12b** and **c**, illustrating the high degree of alignment and high deposition density. These aligned sections could be transferred to a desired substrate for further device fabrication. In addition to dewetting alignment, the microfluidic flow method[48] is also applicable for the assembly of tetraaniline nanowires (**Figure 2.13**). Solution-based large-area alignment should facilitate directional carrier transport and greatly lower contact resistance versus their non-oriented counterparts,[49-51] which could prove to be beneficial for high efficiency organic thin-film microelectronic devices or for transparent, flexible organic electrodes.
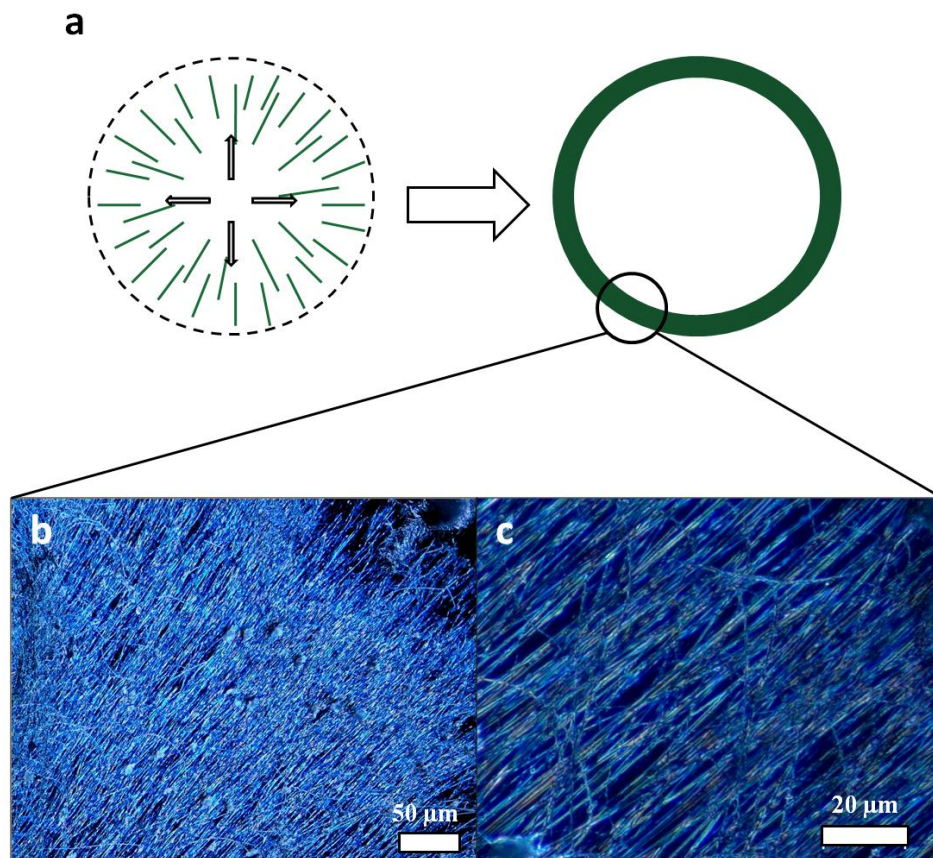
Figure 2.12. (a) A schematic representation of evaporation-induced (dewetting) deposition and alignment between the solvent front and the substrate. (b) An optical micrograph taken in dark field shows a small section of the ring. The nanowires align in the drying direction. (c) A dark field optical micrograph showing a closer view of (b).
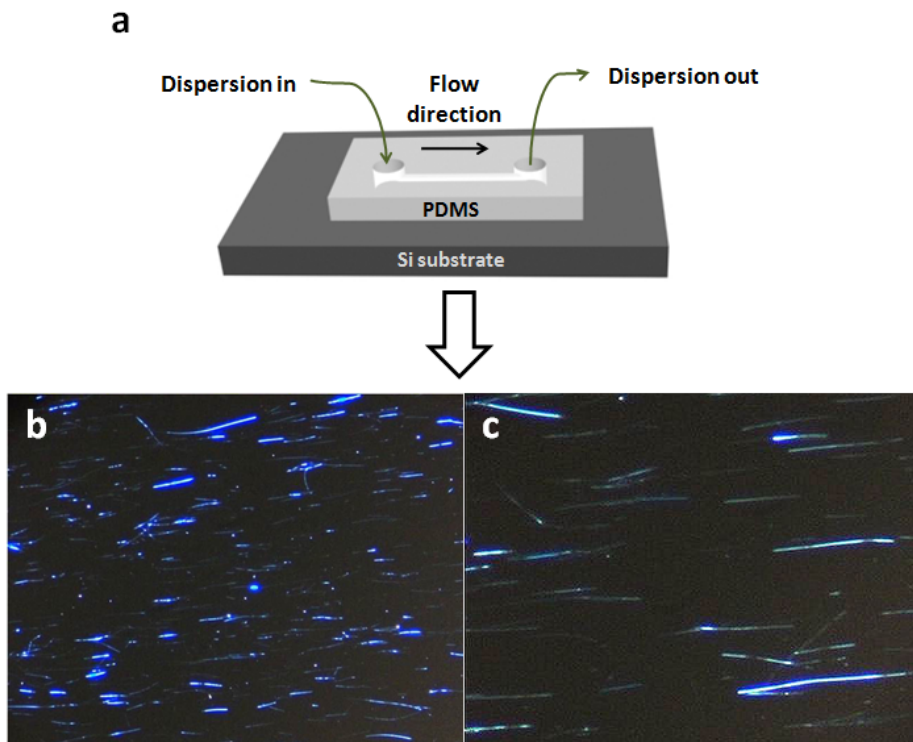
Figure 2.13. Schematic illustration of the microfluidic flow channel structure used to produce aligned nanofibers. (a) A thin rectangular cavity was cut into one side of a PDMS stamp. This created a channel when the stamp was brought into contact with a flat piece of a Si wafer. A dispersion of tetraaniline nanowires in an ethanol/water solvent mixture was then passed through the channel. (b) A dark field optical micrograph shows that the tetraaniline nanowires are aligned on the substrate under the flow channel. (c) A dark field optical micrograph shows a closer view of a selected area from (b).

2.4 Conclusions

Nanostructured aniline oligomers have been produced through a novel, simple one-step method in which bulk oligoanilines self-assemble in a suitable binary solvent system.

73

Supramolecular structures including nanowires, nanoribbons, rectangular nanoplates, and nanoflowers are obtained through a process in which the dopant induces a specific morphology in the oligoanilines. The variation in structures could prove useful for next-generation organic electronics; for example, the high surface area nanoflowers could be used for organic super-capacitors, while nanowires or nanoribbons could be well-suited for single-wire/ribbon nanoelectronic devices. Two-probe electrical measurements on single wires, ribbons, and plates reveal that the conductivity of the tetraaniline nanostructures increase by two orders of magnitude from the highest previously reported values for tetraaniline and now rival that of conventional polyaniline. This increase in conductivity from bulk tetraaniline is due to the increased intermolecular order as evidenced by XRD and *in situ* UV-vis-NIR analyses. The nanostructures can be readily assembled into thin films with orientation over a macroscopic area via a number of methods such as dewetting or microfluidic flow.

2.5 References

(1)   Briseno, A. L.; Mannsfeld, S. C. B.; Jenekhe, S. A.; Bao, Z.; Xia, Y. *Mater. Today* **2008**, *11*, 4, 38-47.

(2)   Mas-Torrent, M.; Rovira, C. *Chem. Soc. Rev.* **2008**, *37*, 827-838.

(3)   Roncali, J.; Leriche, P.; Cravino, A. *Adv. Mater*. **2007**, *19*, 2045-2060.

(4)   Tran, H. D.; Li, D.; Kaner, R. B. *Adv. Mater.* **2009**, *21*, 1487-1499.

(5)   Jang, J. *Emissive Mater.: Nanomater.: Adv. in Poly. Sci.* **2006**, *199*, 189-259.

(6)   Huang J.; Kaner, R.B. *Handbook of Conducting Polymers*, 3rd ed., Reynolds J.; Skotheim, T. Eds. (Marcel Dekker, Inc., New York, 2006), Chapter 7, pp. 194-241.

(7)   Li, D.; Huang, J.; Kaner, R. B. *Acc. Chem. Res.* **2009**, *42*, 1, 135-145.

(8)   Zhang, D.; Wang, Y. *Mater. Sci. Eng. B* **2006**, *134*, 9-19.

(9)   Huang, J.; Virji, S.; Weiller, B.; Kaner, R. B. *Chem: A Euro. J.* **2004**, *10*, 1314-1319.

(10)   Gallon, B. J.; Kojima, R. W.; Kaner, R. B.; Diaconescu, P. L. *Angew. Chem. Int. Ed.* **2007**, *46*, 7251-7254.

(11)   Gupta, V.; Miura, N. *Mater. Lett*. **2006**, *60*, 1466-1469.

(12)   DeLongchamp, D. M.; Sambasivan, S.; Fischer, D. A.; Lin, E. K.; Chang, P.; Murphy, A. R.; Fréchet, J. M. J.; Subramanian, V. *Adv. Mater*. **2005**, *17*, 2340-2344.

(13)   DeLongchamp, D. M.; Kline, R. J.; Lin, E. K.; Fischer, D. A.; Richter, L. J.; Lucas, L. A.; Heeney, M.; McCulloch, I.; Northrup, J. E. *Adv. Mater*. **2007**, *19*, 833-837.

(14)   Zang, L.; Che, Y.; Moore, J. S. *Acc. Chem. Res*. **2008**, *41*, 12, 1596-1608.

(15)   Poncet, M.; Corraze, B.; Quillard, S.; Wang, W.; MacDiarmid, A. G. *Thin Solid Films* **2004**, *458*, 32-36.

(16)   Zhou, Y.; Geng, J.; Li, G.; Zhou, E.; Chen, L.; Zhang, W. *J. Poly. Sci. Part B: Poly. Phys*. **2006**, *44*, 764-769.

(17)   Baughman, R. H.; Wolf, J. F.; Eckhardt, H.; Shacklette, L. W. *Synth. Met*. **1988**, *25*, 121-137.

(18)   Shacklette, L. W.; Wolf, J. F.; Gould, S.; Baughman, R. H. *J. Chem. Phys*. **1988**, *88*, 6, 3955-3961.

(19)   MacDiarmid, A. G.; Zhou, Y.; Feng, J. *Synth. Met*. **1999**, *100*, 131-140.

(20)   Wei, Z.; Faul, C. F. J. *Macromol. Rapid Commun*. **2008**, *29*, 280-292.

(21)   Surwade, S. P.; Agnihotra, S. R.; Dua, V.; Manohar, N.; Jain, S.; Ammu, S.; Manohar, S. K. *J. Am. Chem. Soc*. **2009**, *131*, 12528-12529.

(22)   MacDiarmid, A. G. *Synth. Met*. **1997**, *84*, 27-34.

(23)   Avlyanov, J. K.; Min, Y.; MacDiarmid, A. G.; Epstein, A. J. *Synth. Met*. **1995**, *72*, 65-71.

(24)   Zhang, W. J.; Feng, J.; MacDiarmid, A. G.; Epstein, A. J. *Synth. Met*. **1997**, *84*, 119-120.

(25)   Lu, F. L.; Wudl, F.; Nowak, M.; Heeger, A. J. *J. Am. Chem. Soc.* **1986**, *108*, 26, 8311-8313.

(26)   Che, Y.; Datar, A.; Balakrishnan, K.; Zang, L. *J. Am. Chem. Soc.* **2007**, *129*, 7234-7235.

(27)   Balakrishnan, K.; Datar, A.; Naddo, T.; Huang, J.; Oitker, R.; Yen, M.; Zhao, J.; Zang, L. *J. Am. Chem. Soc.* **2006**, *128*, 7390-7398.

(28)   Paramonov, S. E.; Jun, H-W.; Hartgerink, J. D. *J. Am. Chem. Soc*. **2006**, *128*, 7291-7298.

(29)   Briseno, A. L.; Mannsfeld, S. C. B.; Lu, X.; Xiong, Y.; Jenekhe, S. A.; Bao, Z.; Xia, Y. *Nano Lett*. **2007**, *7*, 668-675.

(30)   Würthner, F. *Chem. Commun*. **2004**, 1564-1579.

(31)   Stejskal, J.; Sapurina, I.; Trchova, M.; Konyushenko, E. N.; Holler, P. *Polymer* **2006**, *47*, 8253-8262.

(32)   Wang, Y.; Tran, H. D.; Kaner, R. B. *J. Phys. Chem. C* **2009**, *113*, 10347-10349.

(33)   Xia, Y.; Wiesinger, J. M.; MacDiarmid, A. G.; Epstein, A. J. *Chem. Mater*. **1995**, *7*, 3, 443-445.

(34)   Rannou, P.; Gawlicka, A.; Berner, D.; Pron, A.; Nechtschein, M. *Macromolecules* **1998**, *31*, 9, 3007-3015.

(35)   Irvine, W. M.; Pollack, J. B. *ICARUS* **1968**, *8*, 324-360.

(36)   MacDiarmid, A. G.; Epstein, A. J. *Synth. Met*. **1994**, *65*, 103-116.

(37)   Huang, J.; Kaner, R. B. *J. Am. Chem. Soc*. **2004**, *126*, 851-855.

(38)   MacDiarmid, A. G.; Epstein, A. J. *Synth. Met.* **1995**, *69*, 85-92.

(39)   Tang, Q.; Wu, J.; Sun, X.; Li, Q.; Lin, J. *Langmuir* **2009**, *25*, 5253-5257.

(40)   Anilkumar, P.; Jayakannan, M. *J. Phys. Chem. B* **2009**, *113*, 11614-11624.

(41)   Wang, J.; Wang, J.; Dai, Z.; Wang, Z.; Zhang, F. *Synth. Met.* **2009**, *159*, 1583-1588.

(42)   Winokur, M. J.; Mattes, B. R. *Macromolecules* **1998**, *31*, 8183-8191.

(43)   Conway, B. E. *Ionic Hydration in Chemistry and Biophysics* (Elsevier, Amsterdam, 1981), pp. 59-74.

(44)   Peng, C.-Y.; Kalkan, A. K.; Fonash, S. J.; Gu, B.; Sen, A. *Nano Lett.* **2005**, *5*, 3, 439-444.

(45)   Huang, J.; Fan, R.; Connor, S.; Yang, P. *Angew. Chem. Int. Ed.* **2007**, *46*, 2414-2417.

(46)   Deegan, R. D.; Bakajin, O.; Dupont, T. F.; Huber, G.; Nagel, S. R.; Witten, T. A. *Nature* **1997**, *389*, 827-829.

(47)   Hameren, R. v.; Schön, P.; Buul, A. M. v.; Hoogboom, J.; Lazarenko, S. V.; Gerritsen, J. W.; Engelkamp, H.; Christianen, P. C. M.; Heus, H. A.; Maan, J. C.; Rasing, T.; Speller, S.; Rowan, A. E.; Elemans, J. A. A. W.; Nolte, R. J. M. *Science* **2006**, *314*, 1433-1436.

(48)   Huang, Y.; Duan, X.; Wei, Q.; Lieber, C. M. *Science* **2001**, *291*, 630-633.

(49)   Long, Y.; Chen, Z.; Wang, N.; Ma, Y.; Zhang, Z.; Zhang, L.; Wan, M. *Appl. Phys. Lett.* **2003**, *83*, 9, 1863-1865.

(50)   Long, Y.; Zhang, L.; Ma, Y.; Chen, Z.; Wang, N.; Zhang, Z.; Wan, M. *Macromol. Rapid Commun.* **2003**, *24*, 938-942.

(51)   Li, G.; Martinez, C.; Janata, J.; Smith, J. A.; Josowicz, M.; Semancik, S. *Electrochem. Solid-State Lett*. **2004**, *7*, 10, H44-H47.

Chapter 3. Morphological and dimensional control via hierarchical assembly of doped oligoaniline single crystals

Single crystals of doped aniline oligomers are produced via a simple solution-based self-assembly method. Detailed mechanistic studies reveal that crystals of different morphologies and dimensions can be produced by a "bottom-up" hierarchical assembly where structures such as one-dimensional (1-D) nanofibers can be aggregated into higher order architectures. A large variety of crystalline nanostructures such as 1-D nanofibers and nanowires, 2-D nanoribbons and nanosheets, and 3-D nanoplates, stacked sheets, nanoflowers, porous networks, hollow spheres, and twisted coils, can be obtained by controlling the nucleation of the crystals and the non-covalent interactions between the doped oligomers. These nanoscale crystals exhibit enhanced conductivity compared to their bulk counterparts and interesting structure-property relationships such as shape-dependent crystallinity. Furthermore, the morphology and dimension of these structures can be rationalized and predicted by monitoring the molecule-solvent interactions via absorption studies. Using doped tetraaniline as a model system, the results and strategies presented here provide insight into the general scheme of shape and size control for organic materials.

3.1 Introduction

Conducting organic molecular and polymer materials are promising candidates for a variety of applications including organic photovoltaics, light-emitting diodes, field-effect

transistors, gas sensors, memory devices, and stretchable electrodes.[1-7] Compared to many of their inorganic counterparts, organic conductors are advantageous in terms of their improved solution processability, facile and scalable synthesis, and the ability to tune their chemical and physical properties via molecular design.[8-12] However, the performance and stability of devices are largely governed by the ordering of the molecules in the solid state.[13,14] Hence, the device performance for organic conductors are often inferior in comparison to their inorganic counterparts due to the lack of molecular order at the macroscopic level.[15,16] This is especially true for polymeric conductors such as polyaniline and, as a result, the growth of single crystals of organic conductors has become a highly desirable and rapidly evolving field of research.[13,17,18] Crystals possessing nanoscale morphologies are of particular interest as they facilitate anisotropic carrier transport, serve as model systems for elucidating intrinsic transport properties and structure-property relationships, and help address the role of nanoscale domains in micro- and macrostructures.[13,16] However, crystallizing conducting polymers such as polyaniline has not been possible due to the free energy and kinetic barriers associated with inducing the polymer chains to rearrange from their preferred coiled conformations to an ordered crystalline state.[19-22] Therefore, in order to achieve higher crystallinity, low molecular weight polyaniline or oligomers of aniline are the preferred choice because they resemble small molecules in regard to crystallization kinetics.[23,24] In particular, doped oligoanilines serve as a unique middle ground between polyaniline and molecular conductors since they retain most properties of the parent polymer, while their monodispersed molecular chains can be processed into more ordered states and have the potential to achieve precise ordering in crystalline domains or layers that can lead to high carrier mobility and conductivity—properties typically associated with small molecule conductors.[15,25,26]

Despite their advantages, reports on doped oligoanilines are sparse, and most previous studies in this field have focused on the synthesis of these molecules or their use as model systems for probing the properties of polyaniline.[27-30] Recently, we reported a solution-based self-assembly method for growing nanostructures for a variety of doped aniline oligomers.[24] By exploiting the interplay between various non-covalent interactions including hydrogen bonding, π-π stacking, hydrophobic and electrostatic interactions, four different shapes were obtained: nanowires, nanoribbons, nanoplates, and nanoflowers. The resulting nanostructures show enhanced crystallinity and conductivity compared to their bulk counterparts based on previous reports.[24]

Here, we demonstrate that *single crystals* of *electroactive*, *doped* phenyl/amine-capped tetraaniline (hereafter referred to as tetraaniline), the smallest repeat unit that can represent polyaniline in its conductive emeraldine salt oxidation state, can be grown from such a self-assembly process. Reports on single crystals of oligoanilines are exceedingly rare and have only focused on structural analysis.[29,31,32] We show that the ordered solid-state packing of our doped oligomers leads to a two-order-of-magnitude increase in their conductivity compared to the highest value from previous reports.[28] Furthermore, we thoroughly investigate the morphological evolution of these crystals at various assembly intervals in order to elucidate the effect of each driving force on the self-assembly process. The nanofiber structure, which appears to be a readily attainable morphology for organic conductors such as polyaniline and their derivatives,[8] can be transformed into a large array of higher dimensional nanocrystals with a variety of sizes and shapes by creating a suitable self-assembly environment. With a clearer understanding of this "bottom-up" hierarchical assembly mechanism, we demonstrate the ability to exquisitely tune the crystal's supramolecular architecture from 1-D nanofibers and nanowires to 2-D ribbons, sheets,

and plates, and eventually 3-D flower-like structures, hollow spheres, porous sheets, and twisted ropes. Moreover, due to the unique acid-base doping-dedoping properties of oligomers and polymers of aniline, the dopants can serve conveniently as one of the driving forces for self-assembly. During this process, the dopants are simultaneously incorporated producing tetraaniline crystals in their conductive emeraldine salt oxidation state. The sizes of many of these structures can be fine tuned simply by controlling the degree of aggregation dictated by pH.

3.2 Experimental

3.2.1 Synthesis

N-phenyl-1,4-phenylenediamine was purchased from Sigma-Aldrich and used without further purification. Amine/phenyl-capped tetraaniline was synthesized via a previously reported route.[33] In short, iron (III) chloride was mixed with stoichiometric amounts of *N*-phenyl-1,4-phenylenediamine in 0.1 M HCl with vigorous stirring for 2 h. The suspension was then filtered and washed repeatedly with water and acetone. The product was subsequently dedoped using 0.1 M ammonium hydroxide and recrystallized from ethanol three times. Phenyl/phenyl-capped tetraaniline was synthesized by a modified condensation reaction in an inert atmosphere via a published method.[34] In brief, the phenyl/amine-capped tetraaniline starting material in the reported reaction was replaced by a stoichiometric amount of *N*-phenyl-1,4-phenylenediamine. Characterization of these products can be found in references 24 and 33.

3.2.2 Self-assembly of nanostructures

In a typical process, 2.0 mg of finely powdered oligoaniline was added to a solvent mixture of 1.0 mL of an organic solvent and 4.0 mL of an aqueous acidic solvent at room

temperature. The resulting mixture was briefly swirled and left undisturbed for 4 to 5 days. At the end of the self-assembly process, the mixture was purified by dialysis against deionized water. The product was collected after approximately 1 day. For the time-lapsed experiments, the water bath was stirred and replaced with fresh water continually to accelerate the dialysis process; the final product was collected after approximately 5 hours.

3.2.3 Microscopy

Scanning electron microscopy (SEM) and transmission electron microscopy (TEM) samples were prepared by drop-casting an oligoaniline dispersion onto a piece of silicon wafer and a TEM grid, respectively. All SEM images were acquired on a JEOL JSM-6700 Field Emission scanning electron microscope.

The low dose electron diffraction patterns and the corresponding bright field images in **Figure 3.1** were taken with a JEOL JEM-2010F FasTEM at 200 kV accelerating voltage. D-spacings on electron diffraction patterns were calibrated using polycrystalline gold films and analyzed using ImageJ (National Institute of Health) software. The samples were observed to be beam sensitive. During *in-situ* observations of the electron beam-induced changes of the diffraction patterns, we found that the Bragg reflections transformed from sharp localized spots to streaks in the [001] direction at characteristic doses ranging from 0.02 to 0.07 C/cm^2. With extended exposure to the beam, the scattering faded completely.

Atomic force microscopy (AFM) images were acquired in the dynamic mode (AM-AFM) on a Nanoscope V Dimension Icon (Bruker AXS) under ambient conditions using phosphorus n^+-doped silicon cantilevers (PPP-NCST, Nanosensors) with a nominal spring constant of 7.4 N/m, first longitudinal resonance frequencies between 130-165 kHz, and a nominal tip radius

of <10 nm. Simultaneous height and phase images were acquired and reproduced from multiple samples. Simple plane fitting of the acquired images enabled subsequent cross-sectional analyses. The reported values exhibited no significant variation between different samples or cantilever probes.

3.2.4 Other characterization techniques

Powder X-ray diffraction patterns were obtained on a Panalytical X'Pert Pro X-ray powder diffractometer using a CuK$_\alpha$ radiation beam with a wavelength of 0.154 nm. The diffractometer was operated at 45 kV and 40 mA at a scan rate of 4.0° /min, with an angular 2θ range from 3° to 40°. UV-vis spectra were acquired on a HP 8452 spectrometer.

3.3 Results and Discussion

3.3.1 Nanostructure self-assembly

As-synthesized tetraaniline in its emeraldine base oxidation state lacks a well-defined structure and exhibits only granular features.[24,33] However, nanostructures of tetraaniline can be obtained by a post-synthetic self-assembly process in which a small amount of tetraaniline is placed in a solvent mixture that involves a good solvent such as ethanol, and a poor solvent such as aqueous 0.1 M HCl, to promote the molecule-molecule interactions that are essential for forming crystalline structures.[24,35] A number of nanostructures can be induced just by varying the dopant acid: HCl, HNO_3, $HClO_4$ and H_2SO_4. These acids can lead to nanowires, nanoribbons, nanoplates and flower-like structures, respectively. The products can readily be dispersed in water (**Figure 3.1a**), which allows convenient solution-based processing methods such as drop-

casting or spray-coating. UV-vis spectra confirm that the final nanostructures are in the emeraldine salt oxidation state with characteristic absorption maxima at 290, 405 and 735 nm (**Fig. 3.1b**). These values can be contrasted with the starting bulk material in the emeraldine base oxidation state with absorption peaks at 295 and 585 nm (**Fig. 3.1b**).[36] Powder X-ray diffraction indicates that these doped structures are significantly more crystalline than typical nanostructures of polyaniline (**Figure 3.1c**), which is in agreement with the fact that low molecular weight oligomers can more readily pack into ordered architectures.
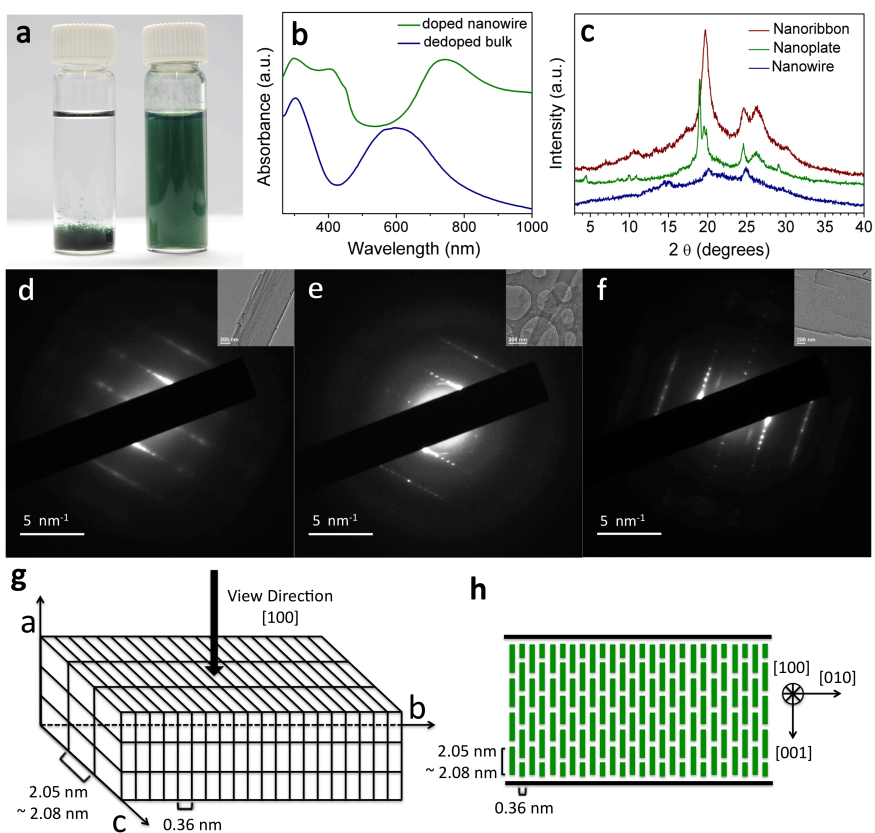
Figure 3.1. (a) Photographs showing the cotton-like state of tetraaniline nanowires in water (left) and the homogeneous dispersion formed upon agitation (right); (b) UV-vis spectra of the dedoped bulk powder prior to self-assembly and the final doped nanowires dispersed in water; (c) XRD patterns for tetraaniline nanowires, nanoribbons and nanoplates; (d-f) SAED patterns

for the nanowires (d), nanoribbons (e) and nanoplates (f). The insets show the corresponding bright-field TEM images for each structure; (g) a 3-D packing model of tetraaniline with the corresponding d-spacings in the b and c directions; (h) A 2-D packing model illustrated as a projection in the [100] direction for the nanoribbon and nanoplate samples. The green rectangles represent the tetraaniline molecules.

3.3.2 Crystal Structures

Selected area electron diffraction (SAED) is a powerful tool for characterizing the structure of nanosized domains and understanding the associated structure-property relationships for materials.[37] Low dose TEM techniques are employed here to collect SAED patterns for tetraaniline nanowires, nanoribbons and nanoplates (**Fig. 3.1d, e, f**, respectively) to minimize the possible beam damage to the samples.

The electron diffraction patterns show that all three tetraaniline morphologies are single crystals. The sharp spots in the diffraction patterns confirm a high degree of crystallinity and large crystallites, while the streaking in certain characteristic directions indicates the existence of planar defects. The diffraction patterns share a predominant d-spacing of ~0.36 nm in the direction along the long axes of the crystals, defined as b (**Fig. 3.1g**). This d-spacing is confirmed by the presence of a ~24.6° 2θ peak in the XRD patterns shared by all three samples (**Fig. 3.1c**). The nanoribbons and nanoplates show large d-spacings of ~2.08 nm and ~2.05 nm, respectively, in the direction defined as c (**Fig. 3.1g**). Similar large d-spacings are also expected for the nanowire sample, but the strong streaking in the c direction due to packing disorder between these planes prevents us from acquiring accurate values. The results also indicate a tendency for

the crystals to orient with the (100) planes parallel to the substrate, allowing the normal viewing direction to be [100], as illustrated in **Fig. 3.1g**. The angles between [001] and [010] are measured to be 90°, and the patterns seem to be nearly (but not always exactly) mirror symmetric.

Comparing the SAED patterns with the corresponding bright field TEM images, shown as insets of **Fig. 3.1d, e and f**, clearly suggests that the long axes of the crystals are always oriented along the [010] direction. Strong scattering along [010] indicates that the molecules are nominally perpendicular to this direction, i.e., perpendicular to the long axis of the crystal. For the nanoribbons and nanoplates, there are systematic odd absences on the (00l) planes, consistent with glide symmetry and therefore indicative of a possible alternating packing arrangement as shown in **Fig. 3.1h**. Interestingly, highly streaked diffuse diffraction intensity can also be observed for the nanoplates at intermediate scattering positions between (000) and (010) at one-third (weaker) and two-thirds (stronger) spacings.

The high degree of order in the diffraction patterns suggests that the conformation of the tetraaniline molecules is consistent and regular. SAED patterns collected at various tilt angles have shown that their solid-state structure in 3-D is single crystalline as well and experiments are currently underway to decipher the complete packing arrangements of these crystals.

The few previous reports on single crystals of oligoanilines have only provided structural information.[29,31,32] Here we demonstrate that the high molecular packing order of our crystals manifests itself in a significant increase in conductivity when comparing the crystals to conventional doped bulk tetramer.[24] Two-probe *I-V* measurements via bottom-contact devices for a single nanowire, nanoribbon, or nanoplate reveal their conductivities are as high as 0.3, 1.1, and 0.5 S/cm along the b-axis, respectively (**Fig. 3.2 and Table 3.1**). The conductivity values

can be readily correlated to the crystallinity of the nanostructures, as the least crystalline nanowires with highly streaked SAED patterns have the lowest conductivity, while the more crystalline nanoribbons and nanoplates with sharp SAED spots are more conductive. Nanoribbons exhibit higher conductivity than the nanoplates likely due to the nature of the bottom-contact electrode configuration. We have observed under SEM that the thin, flexible and high aspect ratio nanoribbons tend to adhere to the gold electrodes and the SiO_2 substrate surface nicely to provide larger interfacial contact areas, while the more rigid plates with lower aspect ratios often form poor contacts, or even tear, at the electrode-substrate junction. Note that the single-crystalline nature of these nanostructures enables their conductivity, particularly the nanoribbons (1.1 S/cm), to be two orders of magnitude higher than the highest previously reported values for bulk doped tetraaniline, and is on the same order of magnitude as conventional, doped, unprocessed polyaniline, whose molecular chain is hundreds of units longer.[28,38]
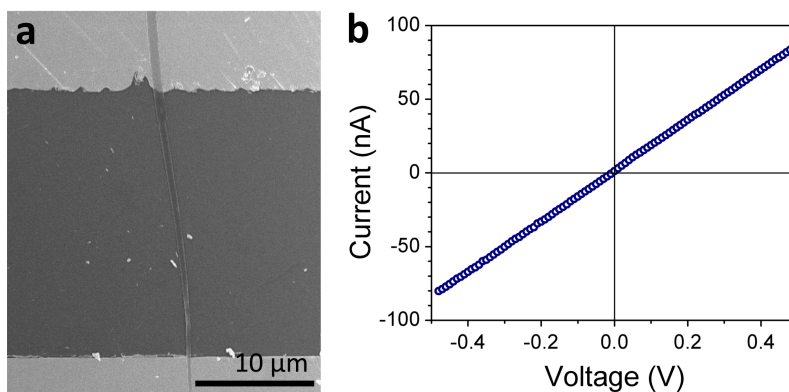
Figure 3.2. The current-voltage (*I-V*) characteristics for an individual tetraaniline nanowire, nanoribbon, and nanoplate were measured using bottom-contact, two-probe devices. (a). A SEM image of an actual device showing a single nanoribbon deposited across a pair of Ti/Au electrodes with a 20 μm gap; (b). A typical *I-V* curve for the nanocrystals.

Table 3.1. Conductivity Data for a Single Nanowire, Nanoribbon, and Nanoplate of Tetraaniline along its Long Axis (b-Direction) in Comparison to Bulk Tetraaniline and Conventional Polyaniline

	Conventional polyaniline	Tetraaniline			
Conductivity (S/cm)	1-10	Bulk	Nanowire	Nanoribbon	Nanoplate
		10^{-6}-10^{-2}	0.3	1.1	0.5

3.3.3 Crystal evolution

Time-lapsed mechanistic studies were carried out to monitor the evolution of the nanoscale morphologies produced for tetraniline. When the process is quenched via rapid dialysis after 1 day of growth, nucleation centers and small nanofeatures are found. For tetraaniline doped with HCl, directionally elongated nucleation centers comprised of aggregated, rigid wires are observed (**Fig. 3.3a**). In fact, clusters of such nucleation centers can still be seen in diluted areas of the final product after 5 days of assembly (**Fig. 3.4a**). Increased magnification of the same sample reveals that large amounts of nascent nanofibers with diameters of ~10-20 nm also exist at this stage of the crystallization process (**Fig. 3.3a**, inset). However, after 2 days of growth, most of the thin nanofibers have transformed into thicker and more rigid fibers with diameters ranging from 100-300 nm (**Fig. 3.3b**). The surfaces of these nanofibers show fringes of smaller nanofibers, which suggests that they form by the aggregation and merging of the pristine 10-20 nm nanofibers upon maturing. After three days, high aspect ratio crystalline

nanowires with diameters of ~100-400 nm and lengths of hundreds of micrometers have formed throughout the sample (**Fig. 3.3c**). The surfaces of the nanowires appear to be smooth in the SEM images, but TEM analysis of an individual wire reveals its genesis in multiple thinner nanofibers (**Fig. 3.3c**, inset), which is further confirmed by AFM measurements (**Fig. 3.5 and 3.6**)
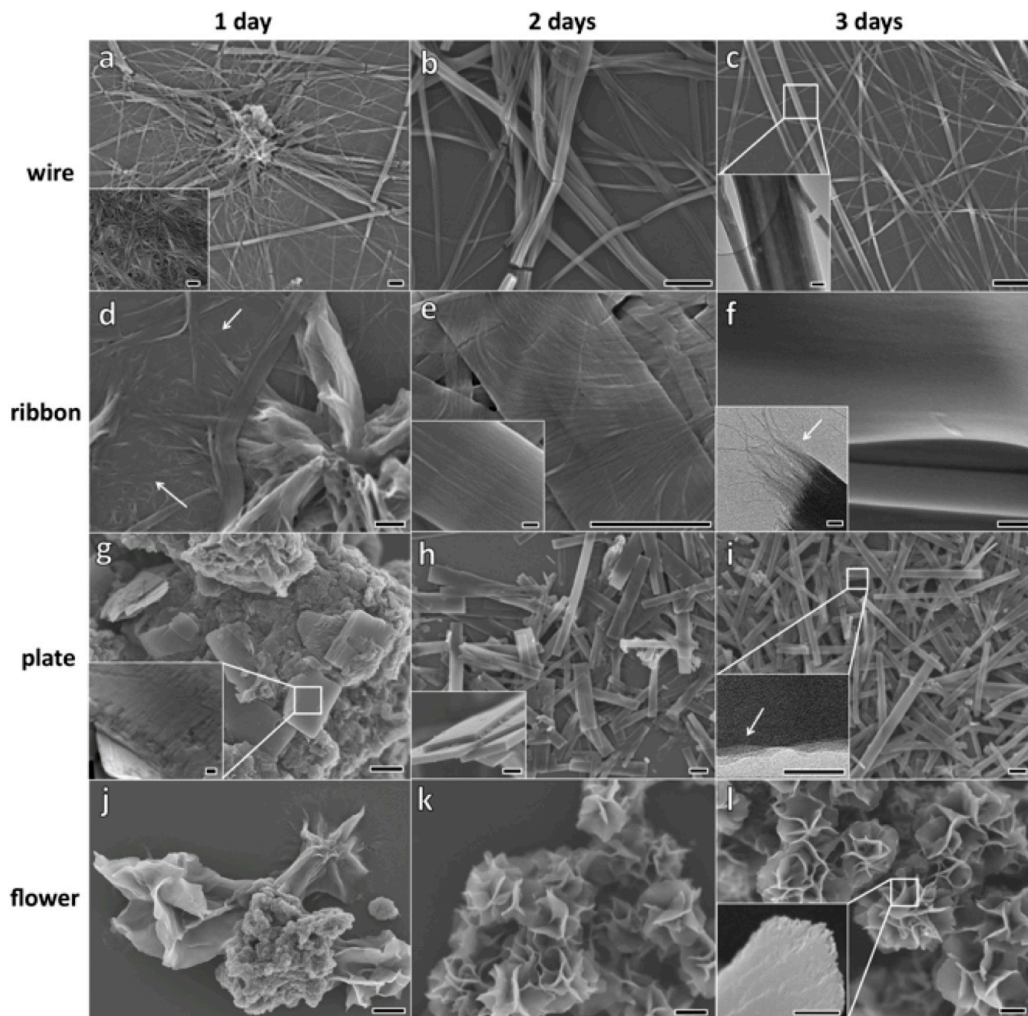
Figure 3.3. Evolution of tetraaniline crystals. SEM images showing nanowires (a-c), nanoribbons (d-f), nanoplates (g-i) and nanoflowers (j-l) collected after 1 day, 2 days and 3 days of assembly. Insets: (a) the thin nanofibers during the early stages of nanowire formation, (c) a

TEM image of a single wire, (e) a magnified view of a ribbon exhibiting clear nanofiber fringes on the surface, (f) a TEM image revealing the oriented fiber-like structures at one end of a ribbon. Insets in (g), (h), and (i) show a zoom-in on the surface of an initial plate, a tilted cross-sectional view and the edge of a plate observed via TEM, respectively. The inset in (l) illustrates the layered-structure of a single "petal." Scale bars: (a)-(e), (g)-(l), and inset of (l) = 1 μm; (f) and all other insets = 100 nm.
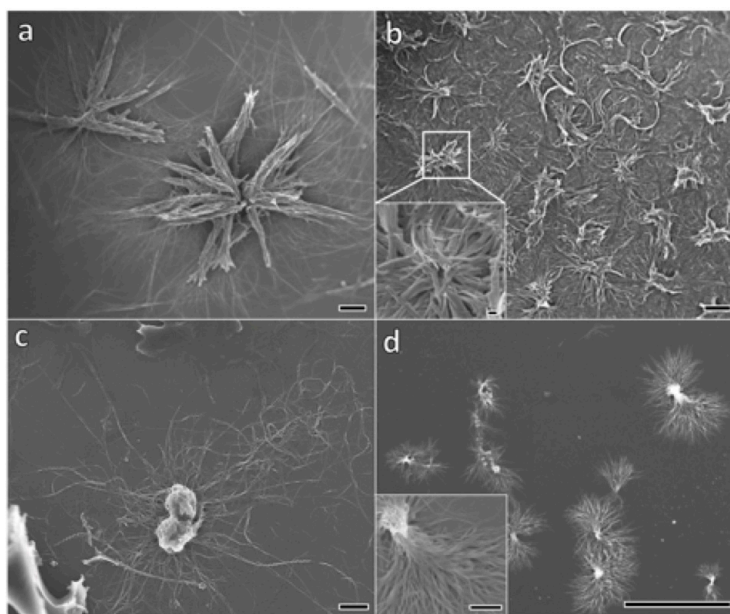
Figure 3.4. Distinctive nucleation centers are visible in diluted areas for various oligomers: (a) tetraaniline nanowires; (b) tetraaniline nanoribbons; (c) dianiline nanofibers; and (d) phenyl-capped tetraaniline nanofibers. Scale bars: (a), (b), and (d) = 10 μm; (c) and the insets in (b) and (d) = 1 μm.
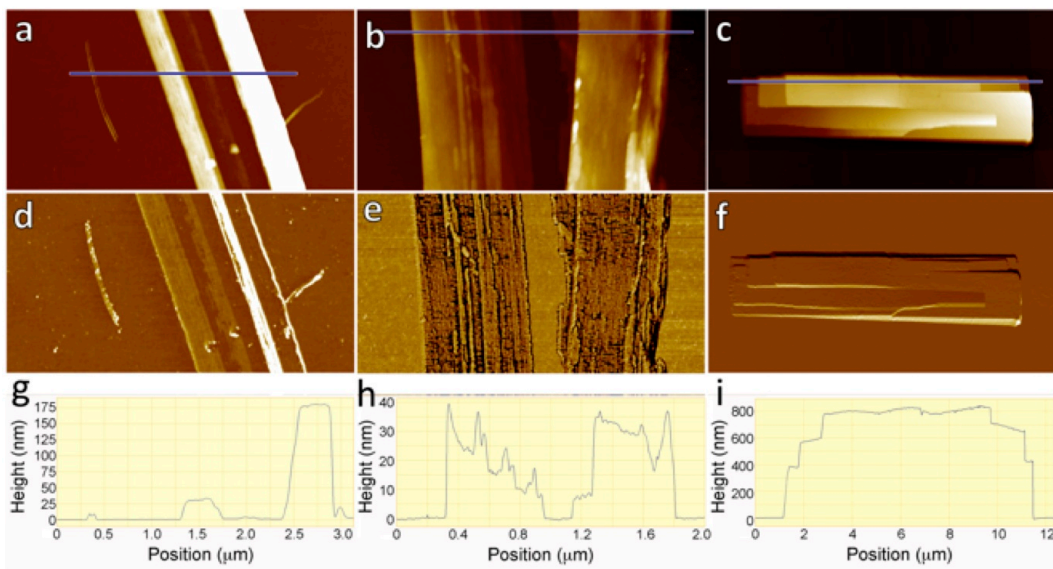
Figure 3.5. Representative atomic force microscope (AFM) height (a-c) and phase images (d-f) with extracted cross-sectional profiles (g-i) of nanowires (first column), nanoribbons (second column), and nanoplates (third column) illustrating that the higher order morphologies are hierarchically assembled from smaller features such as 7.5 nm diameter nanofibers. Image scale: (a, d) = 5 × 2.5 μm, (b, e) = 2.5 × 1.25 μm and (c, f) = 15 × 7.5 μm.
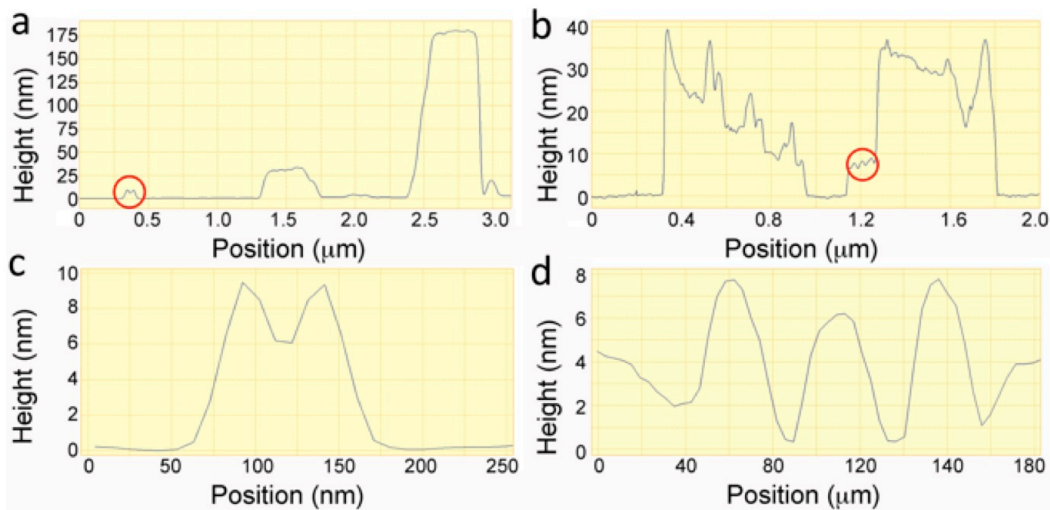
Figure 3.6. Representative cross-sections extracted from AFM height data presented in Figure S1 for nanowires (a, c) and ribbons (b, d). Zooming into the regions highlighted by the red circles (c and d) reveals the dimensions of individual nanowires and their contribution to the hierarchical formation of individual ribbons. The medium height and width of individual nanowires from 25 samples are 7.5 nm and 38.5 nm, respectively. These values correspond directly to those observed for individual, single layer ribbons (d). The applied loading force required to maintain stable, controlled feedback and nominal radius of the cantilever probe tip produced some image convolution and material deformation, generating slight variations in the reported dimensions.

A similar "nucleation and merging" mechanism is observed for HNO_3 doped tetraaniline. After one day, nucleation centers comprised of flexible sheet/ribbon-like clusters are found with significant amounts of smaller nanofibers scattered throughout (**Fig. 3.3d**). Similar to the nanowire sample, these nucleation centers are visible in the final product (**Fig. 3.4b**). After an additional day of aging, the randomly oriented thin nanofibers align parallel to each other and merge into nanoribbons that have a much larger width than thickness. **Figure 3.3e** shows a bundle of parallel oriented small nanofibers prior to forming a defined ribbon structure. The inset to **Fig. 3.3e** illustrates a mature ribbon with clear fringes on the surface which points to its nanofibrillar origin. The surface of most nanoribbons becomes smooth after three days (**Fig. 3.3f**). However, a TEM image (**Fig. 3.3f**, inset) of the terminus of a nanoribbon clearly shows that it is formed by the merging of oriented arrays of thin nanofibers, an observation that is

consistent with the time-lapsed morphological observations. Their genesis of nanofibers is further confirmed by the AFM analysis in **Figure 3.5** and **3.6**.

Unlike the nanowire and nanoribbon samples, the $HClO_4$-doped nanoplates nucleate off of the surface of the bulk agglomerates (**Fig. 3.3g**). A magnified view of a pristine plate (**Fig. 3.3g**, inset) illustrates its layered structure. Within each layer, aligned arrays of small nanofibers that are similar to those in the ribbon sample are also observed. Plates with well-defined features are formed after two days (**Fig. 3.3h**). Further aging appears to increase the aspect ratio of the plates and the yield (**Fig. 3.3i**). Although the surfaces of these plates appear to be smooth under SEM, a magnified view of the edge of a plate under TEM reveals their pristine layered structure which suggests that the plates originate from merged stacks of sheets (**Fig. 3.3i**, inset).

Tetraaniline doped with H_2SO_4 follows a similar pattern to that of the nanoplates in which the flower-like structures nucleate off of the agglomerates. Small clusters of randomly oriented sheets can be observed after one day of self-assembly (**Fig. 3.3j**). The clusters accumulate more sheets (or "petals") and evolve into flower-like structures after an additional day (**Fig. 3.3k**). Further growth appears to increase the yield, but does not appear to change the size of the nanoflowers (**Fig. 3.3l**). A magnified view of a single "petal" (**Fig. 3.3l**, inset) demonstrates that the layered structure within these petal-like sheets is responsible for the flowers.

The time-lapsed experiments provide a visualization of how the crystallization process evolves for tetraaniline nanostructure and suggest a 2-step formation mechanism: (1) nucleation and (2) hierarchical assembly. Dedoped tetraaniline, in its emeraldine base oxidation state, is soluble in common organic solvents such as ethanol. While insoluble in acidic aqueous solvents, tetraaniline can be doped into the conducting emeraldine salt state in such an environment. A

1:4 (v/v) ethanol : acidic aqueous solvent ratio is typically used in this self-assembly process. The 20% concentration of ethanol is sufficient to solvate the dedoped tetraaniline molecules. However, once doped into the emeraldine salt by the acids from the aqueous phase, tetraaniline becomes insoluble in both ethanol and water. Local super-saturation is then reached quickly, and clusters of doped tetraaniline molecules precipitate out forming nucleation centers in the solution.

The morphology of the nucleation centers appears to dictate the final tetraaniline crystal superstructure. For example, rigid rod-like nucleation centers that elongate directionally (**Figure 3.3a** or **3.4a**) lead to high-aspect ratio nanowires, while ribbon-like clusters result in the formation of nanoribbons (**Figure 3.3d** or **3.4b**). In fact, similar phenomena are also observed in other oligoaniline systems. For instance, using the same process, dianiline nanofibers often grow from clusters of very thin and short nanofibers (**Fig. 3.4c**), while phenyl/phenyl-capped tetraaniline nanofibers/nanowires form from dendrite-like nucleation centers (**Fig. 3.4d**). Such observations and conclusions are not surprising as the nanoscale size and shape tuning for many inorganic (semi)conductors are achieved partially by controlling the morphology of nucleation centers.[39] Comparable nucleation centers have also been observed for some small molecule conductors[35] and biomolecules[40].

Once well-defined nucleation centers are present, the nanostructures appear to form through a merging mechanism, where structures with smaller feature sizes, such as nanofibers, merge into larger architectures such as nanowires when doped with HCl or nanoribbons when doped with HNO_3. Based on the evolution of the crystal morphologies, a hierarchical assembly mechanism is proposed (**Fig. 3.7**). First, small 1-D nanoscale features such as thin nanofibers form during the initial stages of self-assembly along with the nucleation centers. Next, with

96

increasing growth time, the randomly oriented nanofibers either aggregate into larger and more rigid 1-D nanowires, or orient parallel with respect to each other and merge into ribbon- or sheet-like 2-D structures. Then the 2-D ribbons or sheets can further stack in an orderly fashion, leading to plate-like architectures with well-defined 3-D dimensions. Alternatively, random stacking can result in an as-grown flower-like morphology. Further evidence for hierarchical assembly comes from AFM measurements on the crystals found with fringes on their surfaces (**Fig. 3.5-3.6**). AFM phase images, (**Fig. 3.5d-f**) as well as high-resolution cross-sectional analyses (**Fig. 3.6**), clearly show the contribution of merged nanofibers in the formation of nanoribbons (**Fig. 3.5e**), and stacked nanoribbons in the formation of nanoplates (**Fig. 3.5f**). Nanowires are observed individually as well as in merged forms of various dimensions ranging from the nanowire pairs seen at the far left to larger ribbon-like bundles seen at the right (**Fig. 3.5a, d, g**). The median height and width of individual nanowires from 25 different random samples are 7.5 nm and 38.5 nm, respectively. Nanoribbons of variable width are composed of stacked single layer ribbons whose height profile (~7.5 nm) corresponds directly to the measured dimensions of merged nanowires (**Fig. 3.5b, e, h** and **3.6d**). Nanoplates are comprised of multiple layered structures of similar dimensions to those observed across multiple nanoribbon samples. The measured thicknesses of the layers that comprise the nanoplates are seen to be integer multiples of 7.5 nm, again corresponding to the measured height of the nanowires, the merged nanowires and the individual nanoribbon layers. The driving force for merging of the smaller morphologies into higher order structures is likely the minimization of surface energies, which has been proposed for various systems including biomolecules and carbon-based materials with similar evolutionary schemes.[41-43] Distinct self-assembly environments are created when different dopant anions are used to dope the positively charged

tetraaniline backbone, which leads to different types of electrostatic interactions. Hence, the aggregation of smaller features into higher order architectures terminates at different stages of the hierarchical assembly timeline for each system.
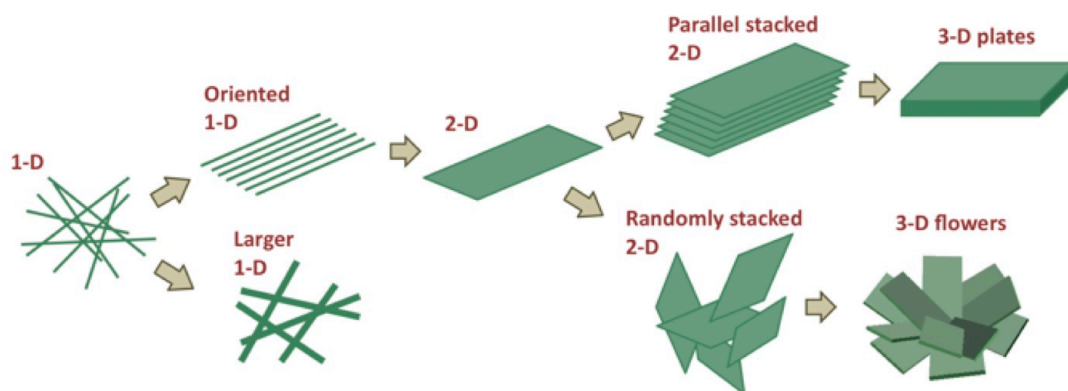
Figure 3.7. An illustration of the "bottom-up" hierarchical assembly mechanism believed responsible for the formation of oligoaniline crystals with different shapes and dimensions. The small features such as 1-D nanofibers (diameter <10 nm) either aggregate into more rigid 1-D nanowires or orient parallel to each other to form 2-D ribbons. The 2-D sheets can further stack in an orderly fashion leading to rigid 3-D plates, or stack randomly yielding a 3-D flower-like morphology.

The direct observation of crystal evolution not only sheds light on their formation mechanism, but also provides a convenient "bottom-up" approach to potentially "build" crystal structures for doped oligoanilines and polyanilines. Additional different structures can be obtained by quenching the process at an earlier stage in the process; for instance, pristine ultra-thin nanofibers with a diameter of ~7.5 nm can be acquired if the product is collected after one day of self-assembly when doped with HCl (**Fig. 3.3a**, inset).

Furthermore, higher-ordered structures tend to have more ordered crystal packing arrangements. For example, the SAED pattern for the 1-D nanowires (**Fig. 3.1d**) has the most streaking, while the ribbons or plates show sharp diffraction spots. It is likely that the merging process from the smaller features (i.e. nanofibers) into larger architectures allows the molecules to rearrange into a more preferred and ordered packing motif which results in higher crystallinity.

3.3.4 Controlling crystal morphology and dimension

Non-covalent interactions including π-π stacking, hydrophobic interactions, and hydrogen-bonding are key elements for the self-assembly of many organic (semi)conductors and biomolecules. Controlling the solvent conditions such as polarity and the ability to form hydrogen-bonds serves as a convenient method for tuning the molecule-molecule and solvent-molecule interactions, which in turn determine the inter-molecular aggregation that ultimately dictates the supramolecular structures.[13,18,44,45]

In order to study the non-covalent interactions controlled by the organic solvent leading to doped tetraniline nanostructures, we kept the electrostatic interaction factor constant, i.e. by using the same protonic doping acid. For example, all the tetraaniline morphologies shown in **Figure 3.8a1-a9** are assembled from the same aqueous component (0.1 M HCl), but using different organic solvents. On the other hand, the solvent is kept constant going across a row in **Figure 3.8**; for example, **Figure 3.8a2, b2, c2,** and **d2** are produced under an identical solvent environment (ethanol and water), but are subject to different electrostatic interactions (i.e. different doping acids).

	HCl	HNO₃	HClO₄	H₂SO₄
no organic solvent	a1	b1	c1	d1
EtOH	a2	b2	c2	d2
2-PrOH	a3	b3	c3	d3
MeOH	a4	b4	c4	d4
1-PrOH	a5	b5	c5	d5
DMSO	a6	b6	c6	d6
DMF	a7	b7	c7	d7
acetone	a8	b8	c8	d8
THF	a9	b9	c9	d9
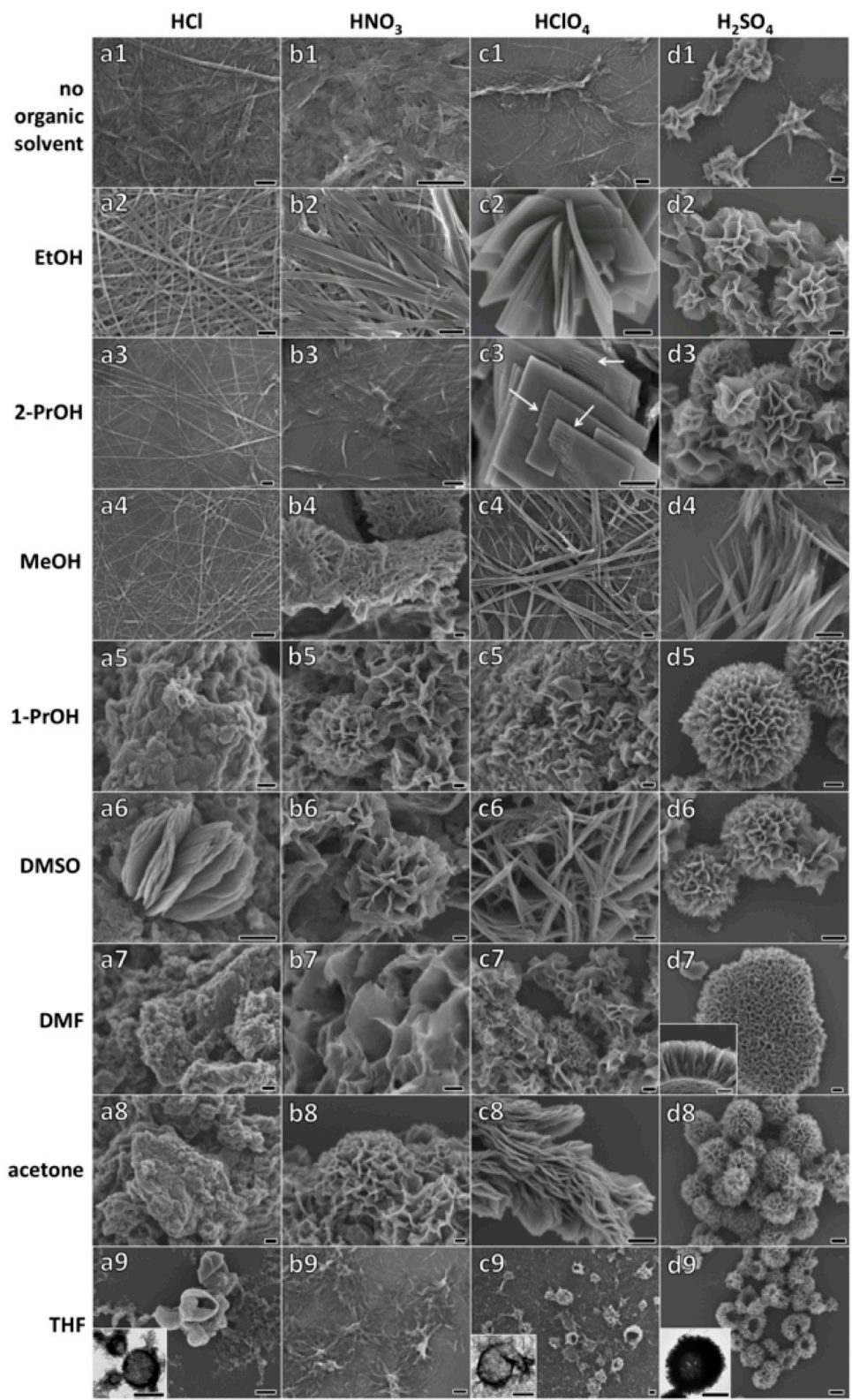
Figure 3.8. Extensive control over the morphology of the tetraaniline crystals can be achieved by creating distinct self-assembly environments using different combinations of the doping acids, HCl, HNO$_3$, HClO$_4$ and H$_2$SO$_4$ (as indicated at the top) with eight different organic solvents (as indicated along the left side). The SEM images of the structures formed using these different dopants and organic solvents are shown here along with an aqueous control (a1-d1) shown at the top. Inset in (d7) shows the cross section of the porous sheet. Insets in (a9), (c9) and (d9) are the corresponding TEM images illustrating the nanostructures' hollow nature. Scale bars = 1 μm.

Organic solvents clearly play an important role in tuning the self-assembly conditions. Note that without any organic solvents in the system, only poorly defined, amorphous structures can be obtained (**Fig. 3.8a1, b1, c1 and d1**). Electrostatic interactions by themselves do not appear to be sufficient to shape doped tetraaniline into crystalline structures. Only the lower order morphology on the hierarchical assembly scheme (**Fig. 3.7**), i.e. nanofibers, can be formed in most cases. However, when different organic solvents are used, distinct morphologies across all stages of the hierarchical assembly scheme can be produced for tetraaniline doped with the same acid. For example, when HCl is used, high aspect ratio 1-D nanowires are obtained using ethanol, 2-propanol, or methanol as the organic phase (**Fig. 3.8a2-a4**); 2-D sheet-like structures form with DMSO (**Fig. 3.8a6**), while THF leads to 3-D micrometer-sized hollow spheres (**Fig. 3.8a9**). As the dopant is changed to HNO$_3$, nanoribbons become the preferred morphology with a small amount of ethanol or 2-propanol (**Fig. 3.8b2-b3**). Incorporation of methanol, 1-propanol, DMSO, DMF, or acetone leads to randomly stacked sheets, mostly in the 3-D flower-like form

(see **Fig. 3.8b4-b8**). Only low aspect ratio nanofibers are observed when THF is used (**Fig. 3.8b9**).

A multitude of structures can be produced with $HClO_4$. Rigid and well-defined 3-D plates form using ethanol or 2-propanol as the organic solvent (**Fig. 3.8c2-c3**). The plates in **Fig. 3.8c3** clearly reveal their origin, as a layered 2-D sheet architecture comprised of oriented arrays of 1-D nanofibers (highlighted by arrows in **Fig. 3.8c3**) can be observed, further supporting the proposed hierarchical assembly mechanism (**Fig. 3.7**). With the same doping acid, crystalline 1-D nanowires/fibers are obtained when either methanol or DMSO is chosen as the organic solvent (**Fig. 3.8c4, c6**), while 3-D morphologies such as porous, layered, or flower-like structures comprised of randomly stacked 2-D sheets form using 1-propanol, DMF, or acetone (**Fig. 3.8c5, c7, c8**). Alternatively, THF leads to 3-D hollow spheres (**Fig. 3.8c9**). Finally, with H_2SO_4 as the doping acid, 3-D flowers appear to be the preferred structures with most organic solvents tested (see **Fig. 3.8d**). When THF is used, 3-D hollow flowers can be produced (**Fig. 3.8d9**), while DMF leads to rather flat, extended porous 3-D networks (**Fig. 3.8d7**). The cross-section shown in the inset to **Fig. 3.8d7** illustrates that such structures are, in fact, folded thin sheets oriented vertically. 1-D nanofibers are also possible if methanol is chosen as the organic solvent (**Fig. 3.8d4**).

To understand why such a small amount of organic solvent can have such a profound effect on the morphology of the tetraaniline, we dissolved the dedoped tetraaniline in its emeraldine base oxidation state in each of the eight different organic solvents used in Figure 4 to monitor the molecule-solvent interactions via absorption spectra. A solvatochromism effect can be observed from the combined, normalized UV-vis plot as shown in **Figure 3.9**. The peaks around 300 nm can be assigned to the π-π* transition.[36] Tetraaniline dissolved in short-chain

alcohols including ethanol, 2-propanol, methanol, and 1-propanol has a π-π* transition at around

310 nm. DMSO and DMF cause this peak to red shift to 325 nm, while acetone and THF further

moves the transition to higher wavelengths of *ca.* 328 and 340 nm, respectively. The red shift of

this absorption peak is often attributed to weaker intermolecular interactions as a more distorted

π-π stacking makes lower-energy excitonic transitions allowable.[46-48] To directly observe the

effect of organic solvents on the aggregation of molecules, dedoped tetraaniline is dried out from

each of these solvents. The resulting solid morphologies are shown in **Figure 3.10**. Well-defined

architectures such as nanospheres are obtained for tetraaniline dried from the alcohols in most

cases (**Fig. 3.10a-d**), indicating stronger intermolecular aggregation in agreement with the

conclusion from UV-vis. On the other hand, the solvents leading to higher wavelength π-π*

absorptions yield agglomerates without any defined structures in most cases (**Fig. 3.10e-h**), again

indicating weaker intermolecular interactions, consistent with the evidence provided by the UV-

vis spectra. The peaks at ~580 nm are responsible for the π-to-polaron band transition,[36] and

their positions also vary depending on the solvent. In short-chain alcohols such as ethanol, 2-

proponal, and methanol, this transition appears around 590 nm, while for acetone or THF the

transition occurs around 560 nm. The onset of the peaks at longer wavelength suggests a lower

π-to-polaron band transition energy, which corresponds to a more extended chain conformation

that often leads to higher crystallinity and enhanced conductivity.[21,36,49] Furthermore, it should

be noted that the effect of the organic solvent obtained from the absorption spectra coincides

with the SEM observations, as solvents that result in better π-π stacking and more extended chain

conformation, such as ethanol, 2-propanol, and methanol, tend to result in more ordered and

better-defined nanostructures (**Fig. 3.8**). In addition, a preferred morphology is often associated

with certain organic solvents. For example, methanol leads to 1-D wire/fiber structures

regardless of the doping acid (**Fig. 3.8a4, b4, c4, d4**). Various forms of stacked sheets, mostly

nanoflowers, can be obtained when using 1-propanol, DMF, or acetone, while different hollow

structures including hollow spheres or hollow flowers tend to form when THF is chosen as the

organic phase. Such observations suggest that the organic solvent molecules could have a

structural guiding effect by interacting, and possibly forming complexes, with the tetraaniline

molecules during self-assembly to shape their aggregates into a particular morphology. Similar

solvent templating behavior has been observed in other molecular systems.[50-52]
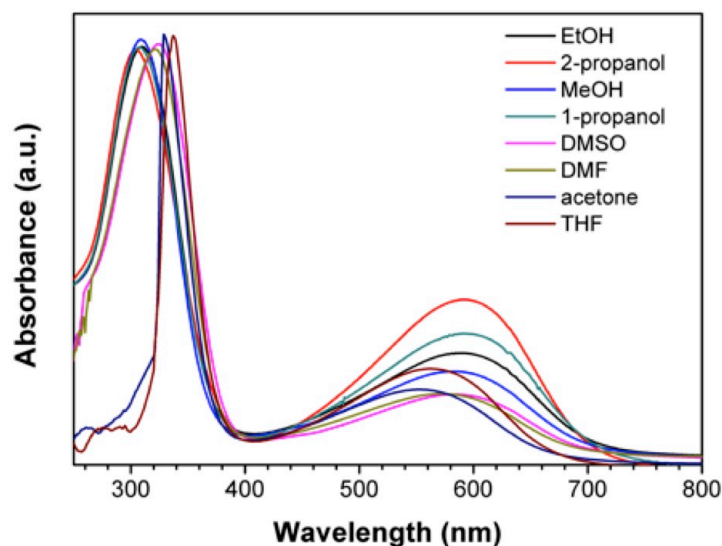
Figure 3.9. Normalized UV-vis spectra of tetraaniline in its emeraldine base oxidation state

dissolved in the eight organic solvents (0.167 mg/mL) used to produce morphologies in Fig. 4.

The solvatochromism observed here indicates that tetraaniline molecules aggregate differently in

these organic solvents: (a) ethanol, (b) 2-propanol, (c) methanol, (d) 1-propanol, (e) dimethyl

sulfoxide (DMSO), (f) dimethylformamide (DMF), (g) acetone and (h) tetrahydrofuran (THF).
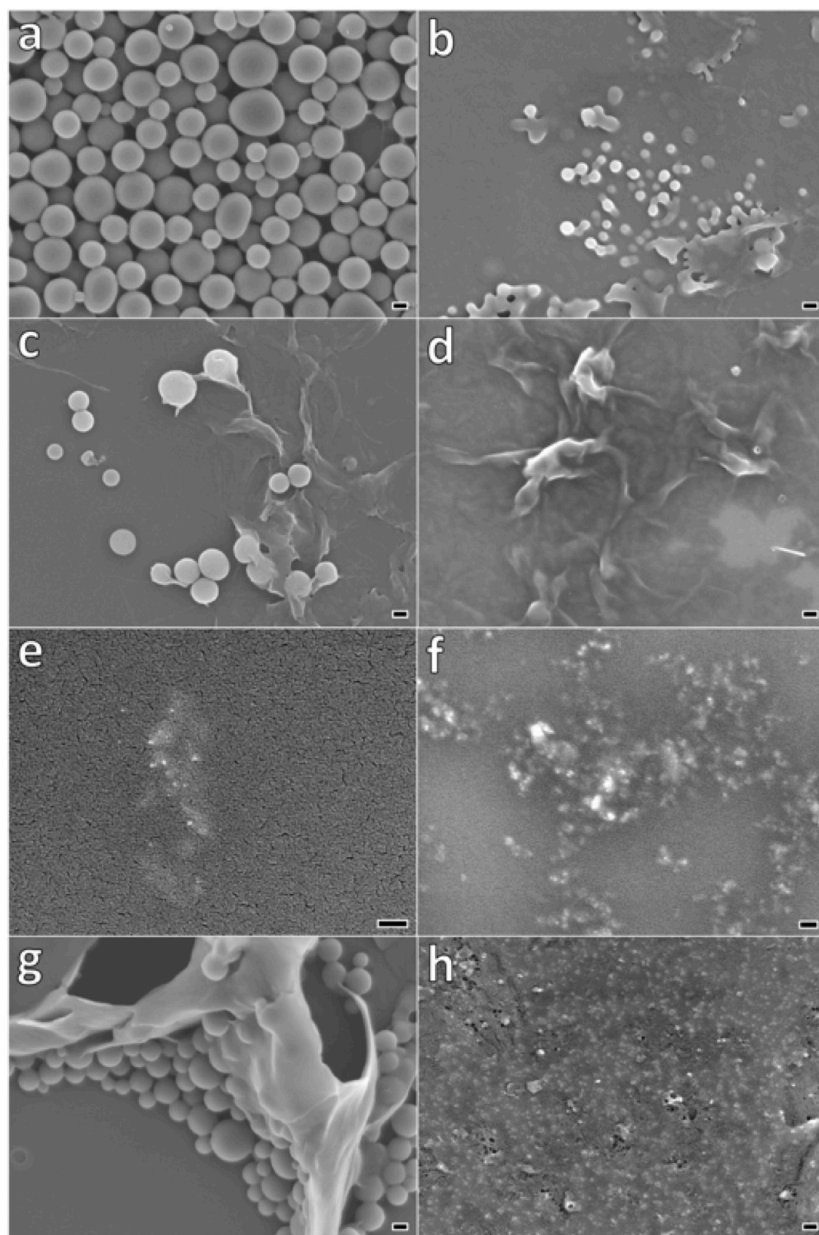
Figure 3.10. Different morphologies are obtained from bulk tetraaniline (EB) powder dissolved and then dried out from (a) ethanol, (b) 2-propanol, (c) methanol, (d) 1-propanol, (e) dimethyl sulfoxide (DMSO), (f) dimethylformamide (DMF); (g) acetone and (h) tetrahydrofuran (THF). Scale bar = 100 nm.

Different electrostatic interactions created by using selected protonic dopant acids when the organic solvent conditions are kept constant results in additional variation in nanostructures. This is evident by examining a row in **Figure 3.8**, e.g. compare **Fig. 3.8a2, b2, c2, and d2**. Therefore, by combining the electrostatic interactions provided by the dopants with hydrophobic and π-π interactions created using different organic solvents, a large library of nanostructures of all shapes and dimensions can be achieved from the hierarchical assembly (**Fig. 3.8**). Additionally, complex structures such as twisted coils (**Fig. 3.11**) are possible by varying other parameters, e.g. the self-assembly temperature. Such extensive morphological control has been hitherto difficult to achieve for organic materials.
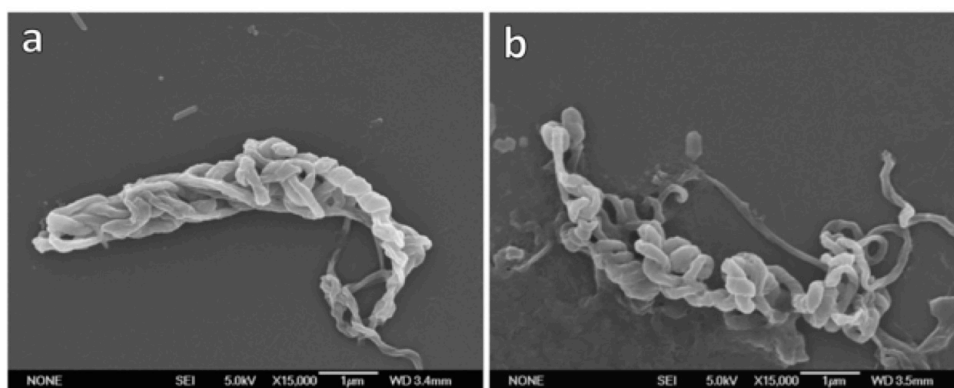
Figure 3.11. Complex coiled structures form from tetraaniline when the self-assembly process is carried out at low temperature (0 °C) using (a) $HCl_{(aq.)}$ and ethanol, or (b) $HClO_{4(aq.)}$ and ethanol.

Furthermore, the sizes of these nanocrystals can be readily tuned by taking advantage of the unique intermolecular electrostatic repulsion properties of oligo/polyaniline. Nanowires are the preferred morphology to form in the HCl/ethanol solvent system. When 0.1 M HCl is used, individual nanowires are well dispersed in solution (**Fig. 3.12a**). However, when the acid concentration is increased to 0.5 M or 1.0 M, bundles of nanowires are typically obtained (**Fig.**

3.12b, c and insets). Similar effects are observed for the HNO$_3$/ethanol (**Fig. 3.12d-f**) and the H$_2$SO$_4$/ethanol (**Fig. 3.12j-l**) systems, as lower acid concentration leads to smaller or less aggregated structures, while increased acidity results in larger or more aggregated architectures. Interestingly, an inverse trend is observed for the HClO$_4$/ethanol system, as stacks of thicker nanoplates (thickness ~100-500 nm) form when a low concentration, 0.1 M HClO$_4$ solution is used (**Fig. 3.12g**). As the acid concentration increases to 0.5 M and 1.0 M, well-dispersed individual plates and thin, somewhat flexible plates become the preferred morphology, respectively (**Fig. 3.12h, i**).
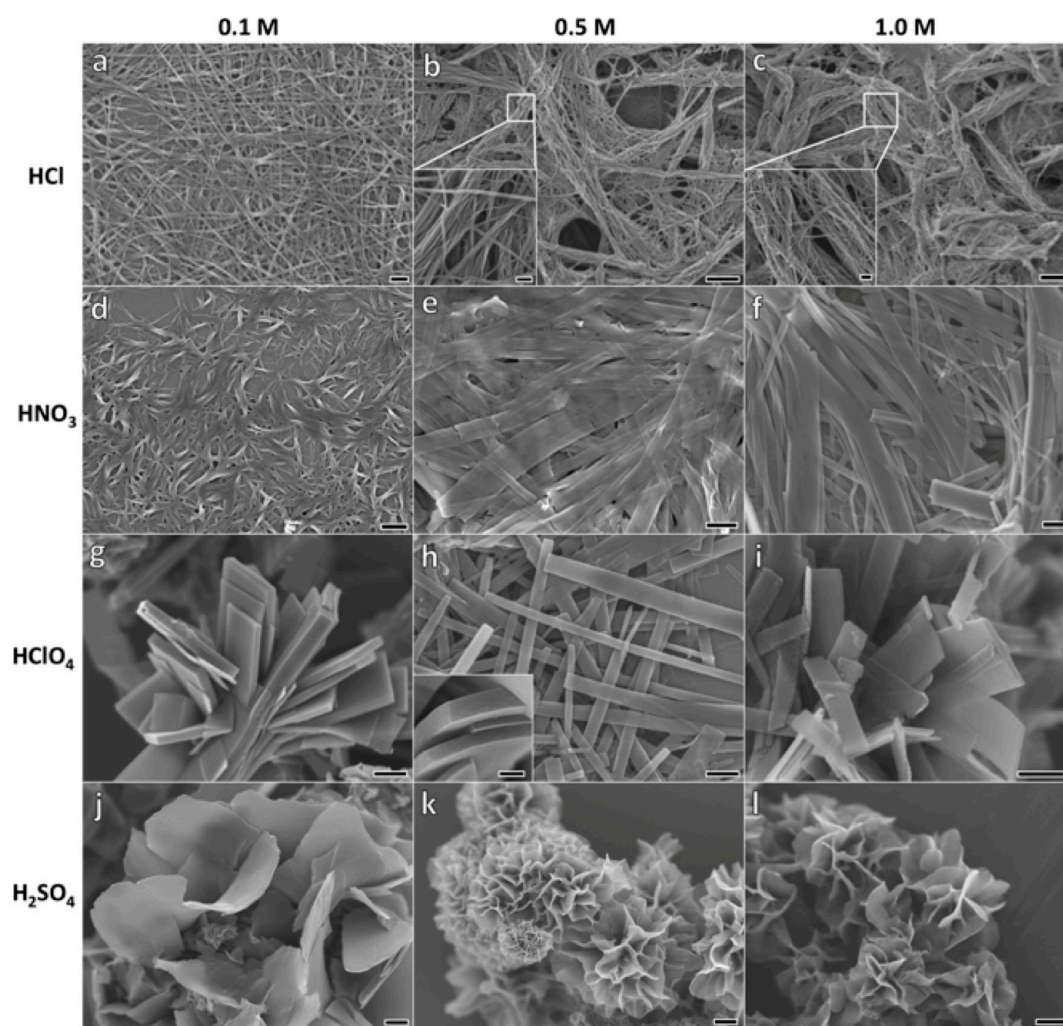
Figure 3.12. In addition to controlling the crystal morphology, the feature size of each of the nanostructures can be further tuned by varying the solvent acidity. The SEM images show the different sizes of the HCl-doped nanowires (a-c), the HNO_3-doped nanoribbons (d-f), the $HClO_4$-doped nanoplates (g-i), and the H_2SO_4-doped nanoflowers (j-l) obtained using acid concentrations of 0.1 M, 0.5 M, and 1.0 M, respectively. Scale bars: (a), (d)-(l), insets of (b) and (c) = 1 μm; (b) and (c) = 10 μm; inset of (h) = 100 nm.

Such pH dependent crystal size control arises from the positive charges on the molecular chains of oligomers (e.g. tetraaniline) or polymers of aniline when in their emeraldine salt oxidation state and doped with a protonic acid. The positive charges result in electrostatic repulsion between the doped tetraaniline molecules. When the tetraaniline backbone is fully protonated, the maximum number of positive charges is obtained, leading to a strong intermolecular repulsion.[21,49] Hence, discrete morphologies, such as individual, well-separated nanowires (in 0.1 M HCl/ethanol), short and fiber-like ribbons (in 0.1 M HNO_3/ethanol), or micrometer-sized sheets (in 0.1 M H_2SO_4/ethanol) form as a smaller number of molecules aggregate to form crystals. Excess protonic acid, i.e. when using a higher acid concentration, serves as islands of neutralization agents for the positive charges on the tetraaniline backbone.[49] This screening effect shields the positively charged tetraaniline molecules from each other, and thus decreases the repulsive forces in-between molecules.[49,53] Therefore, a greater number of doped tetraaniline molecules can aggregate to form architectures that are larger in size, such as thicker and more rigid nanoribbons (in 1 M HNO_3/ethanol), or bundles of nanostructures, such as nanowire bundles (in 1 M HCl/ethanol) and nanoflowers with many sheets/"petals" (in 1 M H_2SO_4/ethanol). On the other hand, when the tetraaniline molecules are not fully protonated, an

insufficient amount of positive charge may not exert sufficient repulsions to keep the smaller features separated. Hence, nanostructures with larger sizes (i.e. thicker plates) can be obtained. This may help explain the inverted trend in the $HClO_4$/ethanol system in which lower acid concentration yields larger and more rigid structures. The variance in trend with each acid system could be caused by the different types of electrostatic interactions associated with the different doping acids.

3.3.5 Structure-property relationships

Choosing the $HClO_4$ doped system as an example, we attempted to quantify the crystallinity of the tetraaniline nanostructures produced with different organic solvents using powder X-ray diffraction (**Fig. 3.13**). The three most dominant peaks in all diffraction patterns (19.1, 24.6, 26.3° 2θ) remain at the same positions for all morphologies. The most intense peak at 19.1° 2θ corresponds to a d-spacing of 0.46 nm, which is the intermolecular packing distance with the dopant anion ClO_4^- incorporated between adjacent chains.[24,32,54] The peak at ~ 24.6° 2θ corresponds to the d-spacing of ~0.36 nm along the b-axis as shown in Figure 1h. A π-π stacking distance of ~0.34 nm can be calculated from the peak at 26.3° 2θ and is typically observed in well ordered organic conducting crystals.[9,54] When short chain alcohols such as ethanol, 2-propanol, methanol, or 1-propanol are used as the organic solvent, the resulting nanostructures exhibit well-defined peaks with high intensity at these three 2θ positions in their XRD patterns (**Fig. 3.13a-d**). DMSO, DMF, and acetone (**Fig. 3.13e-g**) lead to morphologies that show broader and less intense peaks at these positions. The least crystalline structure with very weak diffraction patterns occurs when THF is used (**Fig. 3.13h**). The crystallinity, as quantified by

XRD, is in good agreement with the direct observations from the SEM images in **Figure 3.8**, as ethanol and 2-propanol lead to well-defined nanoplates with sharp edges, which is an indication of higher crystallinity, while the hollow spheres grown from the THF/HClO$_4$ $_{(aq.)}$ mixture appear to be amorphous in nature.
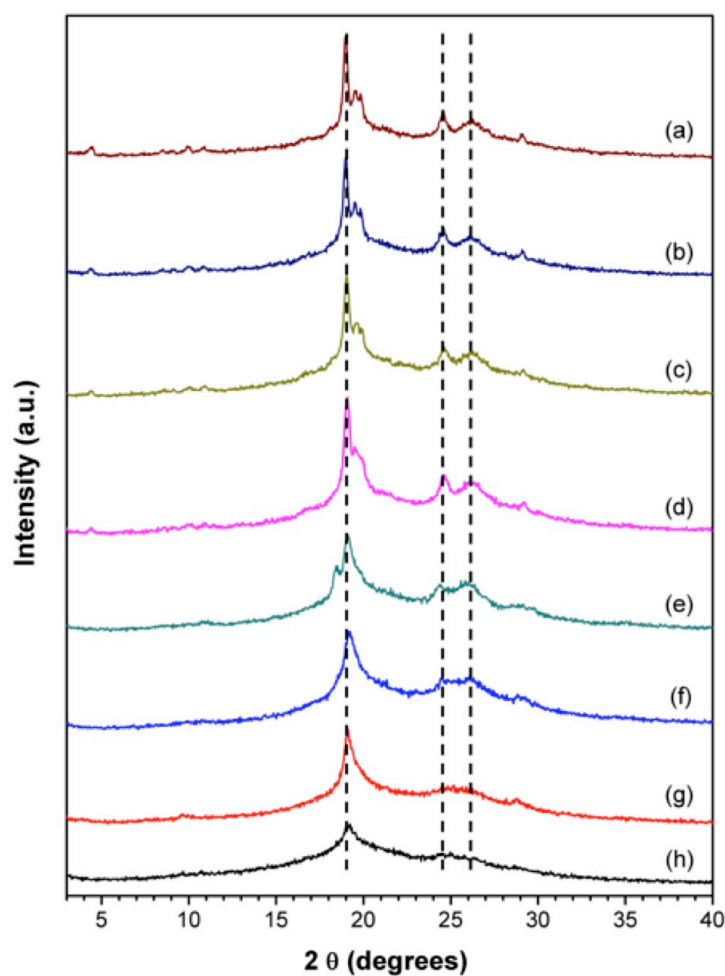
Figure 3.13. Powder XRD patterns indicate that the different shapes of tetraaniline crystals doped with HClO$_4$ but assembled using (a) ethanol, (b) 2-propanol, (c) methanol, (d) 1-propanol, (e) DMSO, (f) DMF, (g) acetone and (h) THF (Figure 4, c2-c9) possess the same 2θ positions for the three most intense characteristic peaks, but different levels of crystallinity and variations in some other peaks.

In addition to the three dominant, characteristic peaks, several peaks including those at ~4.4°, 8.5°, 10.0°, 10.9°, 19.6° and 29.1° 2θ appear with increasing nanostructure crystallinity, while others such as the ~18.5° 2θ peak in **Fig. 3.13e** cannot be observed in other spectra. Therefore, it is possible that these morphologies obtained with the same dopant yet different organic solvents share a similar crystal structure, but with some variation in packing arrangement. The detailed structural information is under active investigation.

3.4 Conclusion

We have demonstrated that single crystals of doped tetraaniline with different shapes and sizes can be produced through a simple self-assembly process. Detailed mechanistic studies and AFM measurements suggest that simple features such as 1-D nanofibers can aggregate into higher order architectures such as 2-D nanoribbons or 3-D nanoplates. Further morphological and dimensional control is readily achieved by tuning (1) the shape of the nucleation centers, and (2) the non-covalent interactions including electrostatic, hydrophobic, and π-π interactions. Monitoring the interactions between the dedoped tetraaniline and the organic solvent via absorption studies can assist in the selection of a suitable organic phase for achieving a preferred morphology or crystallinity. The sizes of the crystals can be further tuned by controlling the degree of aggregation. The library of doped crystalline tetraaniline nanostructures reported here can serve as a basis for extensive structure-property relationship investigations. With inorganic conductors, this type of information has enabled many structure-dependent applications, including catalysis and plasmonic enhancement,[39] but it has been difficult to achieve with their organic counterparts partly due to the challenge in generating a large variety of supramolecular

structures.   We have established a correlation between the crystallinity of the oligoaniline

crystals with their morphologies and dimensions in this report and are currently examining other

structure-property relationships.

3.5 References

(1)   Briseno, A. L.; Mannsfeld, S. C. B.; Ling, M. M.; Liu, S.; Tseng, R. J.; Reese, C.; Roberts, M. E.; Yang, Y.; Wudl, F.; Bao, Z. N. *Nature* **2006**, *444*, 913.

(2)   Chen, H. Y.; Hou, J.; Zhang, S.; Liang, Y.; Yang, G.; Yang, Y.; Yu, L.; Wu, Y.; Li, G. *Nat. Photonics* **2009**, *3*, 649.

(3)   Lipomi, D. J.; Tee, B. C. K.; Vosgueritchian, M.; Bao, Z. N. *Adv. Mater.* **2011**, *23*, 1771.

(4)   Sasabe, H.; Takamatsu, J.; Motoyama, T.; Watanabe, S.; Wagenblast, G.; Langer, N.; Molt, O.; Fuchs, E.; Lennartz, C.; Kido, J. *Adv. Mater.* **2010**, *22*, 5003.

(5)   Virji, S.; Huang, J. X.; Kaner, R. B.; Weiller, B. H. *Nano Lett.* **2004**, *4*, 491.

(6)   Tseng, R. J.; Huang, J. X.; Ouyang, J.; Kaner, R. B.; Yang, Y. *Nano Lett.* **2005**, *5*, 1077.

(7)   Kim, F. S.; Ren, G. Q.; Jenekhe, S. A. *Chem. Mater.* **2011**, *23*, 682.

(8)   Tran, H. D.; Li, D.; Kaner, R. B. *Adv. Mater.* **2009**, *21*, 1487.

(9)   Anthony, J. E. *Chem. Rev.* **2006**, *106*, 5028.

(10)   Liang, Y. Y.; Yu, L. P. *Acc. Chem. Res.* **2010**, *43*, 1227.

(11)   Li, D.; Huang, J. X.; Kaner, R. B. *Acc. Chem. Res.* **2009**, *42*, 135.

(12)   Lloyd, M.; Anthony, J.; Malliaras, G. *Mater. Today* **2007**, *10*, 34.

(13)   Lim, J. A.; Liu, F.; Ferdous, S.; Muthukumar, M.; Briseno, A. L. *Mater. Today* **2010**, *13*, 14.

(14)   Zhang, Y. J.; Dong, H. L.; Tang, Q. X.; Ferdous, S.; Liu, F.; Mannsfeld, S. C. B.; Hu, W. P.; Briseno, A. L. *J. Am. Chem. Soc.* **2010**, *132*, 11580.

(15)   Reese, C.; Bao, Z. *Mater. Today* **2007**, *10*, 20.

(16)   Li, R. J.; Hu, W. P.; Liu, Y. Q.; Zhu, D. B. *Acc. Chem. Res.* **2010**, *43*, 529.

(17)   Bredas, J. L.; Street, G. B. *Acc. Chem. Res.* **1985**, *18*, 309.

(18)   Briseno, A. L.; Mannsfeld, S. C. B.; Jenekhe, S. A.; Bao, Z.; Xia, Y. *Mater. Today* **2008**, *11*, 38.

(19)   Wang, Y.; Tran, H. D.; Kaner, R. B. *J. Phys. Chem. C* **2009**, *113*, 10346.

(20)   Lee, K.; Cho, S.; Park, S. H.; Heeger, A. J.; Lee, C. W.; Lee, S. H. *Nature* **2006**, *441*, 65.

(21)   Macdiarmid, A. G.; Epstein, A. J. *Synth. Met.* **1995**, *69*, 85.

(22)   Yan, Y.; Wang, R.; Qiu, X. H.; Wei, Z. X. *J. Am. Chem. Soc.* **2010**, *132*, 12006.

(23)   Di Maria, F.; Olivelli, P.; Gazzano, M.; Zanelli, A.; Biasiucci, M.; Gigli, G.; Gentili, D.; D'Angelo, P.; Cavallini, M.; Barbarella, G. *J. Am. Chem. Soc.* **2011**, *133*, 8654.

(24)   Wang, Y.; Tran, H. D.; Liao, L.; Duan, X. F.; Kaner, R. B. *J. Am. Chem. Soc.* **2010**, *132*, 10365.

(25)   MacDiarmid, A. G. *Synth. Met.* **1997**, *84*, 27.

(26)   Zang, L.; Che, Y. K.; Moore, J. S. *Acc. Chem. Res.* **2008**, *41*, 1596.

(27)   Udeh, C. U.; Fey, N.; Faul, C. F. J. *J. Mater. Chem.* **2011**, *21*, 18137.

(28)   Wei, Z. X.; Faul, C. F. J. *Macromol. Rapid Commun.* **2008**, *29*, 280.

(29)   Shacklette, L. W.; Wolf, J. F.; Gould, S.; Baughman, R. H. *J. Chem. Phys.* **1988**, *88*, 3955.

(30)   Wang, Y.; Tran, H. D.; Kaner, R. B. *Macromol. Rapid Commun.* **2011**, *32*, 35.

(31)   Baughman, R. H.; Wolf, J. F.; Eckhardt, H.; Shacklette, L. W. *Synth. Met.* **1988**, *25*, 121.

(32)   Zhou, Y. C.; Geng, J. X.; Li, G.; Zhou, E. L.; Chen, L.; Zhang, W. J. *J. Polym. Sci. Pol. Phys.* **2006**, *44*, 764.

(33)   Zhang, W. J.; Feng, J.; MacDiarmid, A. G.; Epstein, A. J. *Synth. Met.* **1997**, *84*, 119.

(34)   Lu, F. L.; Wudl, F.; Nowak, M.; Heeger, A. J. *J. Am. Chem. Soc.* **1986**, *108*, 8311.

(35)   Che, Y. K.; Datar, A.; Balakrishnan, K.; Zang, L. *J. Am. Chem. Soc.* **2007**, *129*, 7234.

(36)   Xia, Y. N.; Wiesinger, J. M.; Macdiarmid, A. G.; Epstein, A. J. *Chem. Mater.* **1995**, *7*, 443.

(37)   Martin, D. C.; Chen, J. H.; Yang, J. Y.; Drummy, L. F.; Kubel, C. *J. Polym. Sci. Pol. Phys.* **2005**, *43*, 1749.

(38)   Chandrasekhar, P. *Conducting Polymers, Fundamentals and Applications: A Practical Approach*; Kluwer Academic Publishers: Boston, 1999.

(39)   Xia, Y. N.; Xiong, Y. J.; Lim, B.; Skrabalak, S. E. *Angew. Chem. Int. Ed.* **2009**, *48*, 60.

(40)   Rimer, J. D.; An, Z.; Zhu, Z.; Lee, M. H.; Goldfarb, D. S.; Wesson, J. A.; Ward, M. D. *Science* **2010**, *330*, 337.

(41)   Pashuck, E. T.; Stupp, S. I. *J. Am. Chem. Soc.* **2010**, *132*, 8819.

(42)   Ziserman, L.; Lee, H. Y.; Raghavan, S. R.; Mor, A.; Danino, D. *J. Am. Chem. Soc.* **2011**, *133*, 2511.

(43)   Viculis, L. M.; Mack, J. J.; Kaner, R. B. *Science* **2003**, *299*, 1361.

(44)   Briseno, A. L.; Mannsfeld, S. C. B.; Lu, X. M.; Xiong, Y. J.; Jenekhe, S. A.; Bao, Z. N.; Xia, Y. N. *Nano Lett.* **2007**, *7*, 668.

(45)   Briseno, A. L.; Mannsfeld, S. C. B.; Reese, C.; Hancock, J. M.; Xiong, Y.; Jenekhe, S. A.; Bao, Z.; Xia, Y. N. *Nano Lett.* **2007**, *7*, 2847.

(46)   Prasanthkumar, S.; Saeki, A.; Seki, S.; Ajayaghosh, A. *J. Am. Chem. Soc.* **2010**, *132*, 8866.

(47)   Balakrishnan, K.; Datar, A.; Oitker, R.; Chen, H.; Zuo, J. M.; Zang, L. *J. Am. Chem. Soc.* **2005**, *127*, 10496.

(48)   Wurthner, F. *Chem. Commun.* **2004**, 1564.

(49)   Macdiarmid, A. G.; Epstein, A. J. *Synth. Met.* **1994**, *65*, 103.

(50)   Balakrishnan, K.; Datar, A.; Naddo, T.; Huang, J. L.; Oitker, R.; Yen, M.; Zhao, J. C.;

Zang, L. *J. Am. Chem. Soc.* **2006**, *128*, 7390.

(51)   Wang, Y.; Dea, P. *J. Chem. Eng. Data* **2009**, *54*, 1447.

(52)   Park, C.; Song, H. J.; Choi, H. C. *Chem. Commun.* **2009**, 4803.

(53)   Li, D.; Kaner, R. B. *Chem. Commun.* **2005**, 3286.

(54)   Winokur, M. J.; Mattes, B. R. *Macromolecules* **1998**, *31*, 8183.

Chapter 4. Graphene-assisted solution growth of vertically-oriented organic semiconducting single crystals

Vertically oriented structures of conductors and semiconductors, especially single crystals, are of great technological importance due to their directional and rapid charge carrier transport, high device density, interesting optical properties, and light trapping capabilities.[1, 2, 3, 4] However, creating such architectures for organic electronic materials remains challenging and largely limited to template-guided methods, which do not provide crystallographic orientational alignment and require harsh chemical conditions for template removal.[5, 6, 7] Here, we report a facile, solution-based route for "bottom-up" production of highly oriented, vertical arrays of single crystalline conjugated molecules by employing a layer of graphene as a guiding substrate. The arrays exhibit uniform morphological and crystallographic orientations. Using an oligoaniline as an example, we demonstrate this method to be highly versatile in controlling the nucleation densities, crystal sizes and orientations. Furthermore, these vertical crystals can be precisely deposited at desired locations by patterning the graphene substrate. Elucidation of anisotropic transport properties within a single crystal reveals that charge carriers travel most efficiently along the vertical interfacial stacking direction with a conductivity of 12.3 S/cm, the highest reported to date for an aniline oligomer, largely owing to the intimate contact between graphene and the oligomer crystals. Finally, we demonstrate that the current from individual crystals can be harnessed collectively over large areas, illustrating its promise for both micro- and macro-scopic device applications.

4.1 Introduction

Conjugated materials including semiconducting or conducting polymers and small molecules have garnered a tremendous amount of attention in recent years largely due to their tunable properties and mechanical flexibility.[8, 9] In particular, solution-processable conjugated materials hold great promise in realizing next-generation electronic and optoelectronic devices because of their compatibility with low-cost processing methods such as spray-coating and roll-to-roll printing.[10] Single crystals of these materials are of particular interest as they possess the long-range order necessary to allow the intrinsic transport limits to be realized.[11, 12] In order to achieve large area, high-density device arrays with high throughput, it is crucial to align these single crystals.[12, 13, 14]

Various approaches for producing single crystals oriented parallel with respect to the substrate have led to groundbreaking performances in devices that require 1-D or 2-D transport such as field-effect transistors.[12, 13, 15] On the other hand, for applications that benefit from high surface area and directional transport in the vertical direction such as solar cells and sensors, it is crucial to orient the single crystals perpendicular (with respect to the substrate) in high density.[1, 2, 4] A myriad of "top-down" and "bottom-up" techniques have been developed to achieve such vertical orientation for inorganic materials. Various fields including photovoltaics, vertical transistor arrays, energy-storage devices, self-powered generators, and intercellular interfacing benefited greatly from these structures and have resulted in technological breakthroughs.[1, 16, 17, 18, 19] However, approaches for creating such structures for organic materials remain sparse and rely mainly on the guidance of an external template.[5, 6, 7] This process generally requires harsh conditions for template removal, which are detrimental to the delicate conjugated materials, in

order to liberate the vertical arrays. Hence, it is highly desirable to develop a template-free method for producing vertically oriented single crystals for soluble conjugated materials. Here, we report a "bottom-up" growth of vertically oriented single crystal arrays of various conjugated materials with a one-step, low cost, solution-based method by using a layer of graphene as the substrate. The crystal arrays possess excellent morphological and crystallographic orientation with the most efficient π-π stacking carrier transport direction perpendicular to the graphene substrate, which is desirable for the aforementioned applications. The intimate contact between the TANI crystal and graphene as a result of the direct "bottom-up" growth leads to a conductivity of 12.3 S/cm along the interfacial stacking direction, one order of magnitude greater than the highest previously reported value.

4.2 Experimental

4.2.1 Materials and synthesis

Phenyl/phenyl-capped tetraaniline and octaaniline were synthesized by a condensation reaction under an inert atmosphere via a previously reported route.[21] Sexithiophene and bis(N-carbozolyl) biphenyl were purchased from Sigma-Aldrich and used without further purification. CVD graphene was grown as previously reported.[44, 45] Briefly, a 25 μm thick copper foil was electropolished, rolled into a tube and annealed under a 5/95% H_2/Ar environment at 1070 °C for 20 min. The temperature was then decreased to 1050 °C and methane was introduced for 30 min. The furnace was rapidly cooled and the resulting graphene film was wet transferred[44, 45] using polylactic acid (Purac biomaterials) onto a p^{++}-SiO_2/Si wafer. Raman spectroscopy shows the

characteristic G and 2D peaks at a 1:4 ratio of the transferred graphene, indicates it is a single-layer (**Fig. 4.1**).
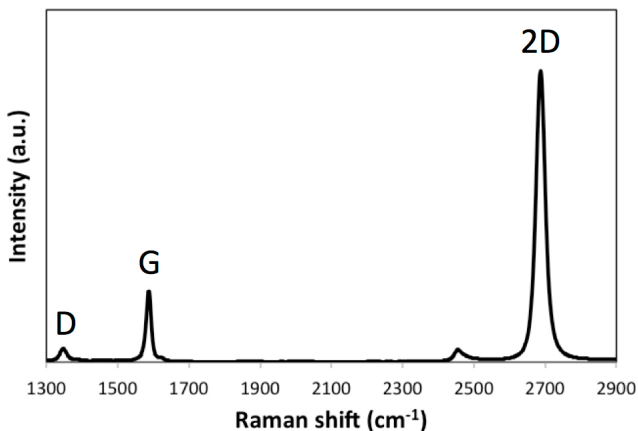
Figure 4.1. Raman of the CVD graphene after transferring to the SiO_2/Si substrate.

4.2.2 Crystallization

Crystallization experiments were carried out in a covered Pyrex[©] Petri dish under ambient atmosphere. In brief, the covered glass Petri dish is filled with a non-solvent (i.e. the infiltrating solvent) for the conjugated molecule of interest. The graphene-covered SiO_2/Si substrate is raised above the liquid level by a thick glass stage. The center graphene-covered area is visible from the slight difference in contrast from the substrate. The tetraaniline solution is drop-cast onto the substrate. As the vapor of the non-solvent saturates the closed container and infiltrates into the solution droplet, supersaturation for tetraaniline is reached. Tetraaniline selectively nucleates on the graphene-covered area and grows vertically with respect to the substrate due to the strong pi-pi interactions. The solution on the substrate becomes lighter in color and eventually clear as the crystallization process proceeds. For a piece of sample that is

approximately 1×1.5 cm^2 in size, the solvent dries and the crystallization is complete in about 2 hours. (**Fig. 4.2**).
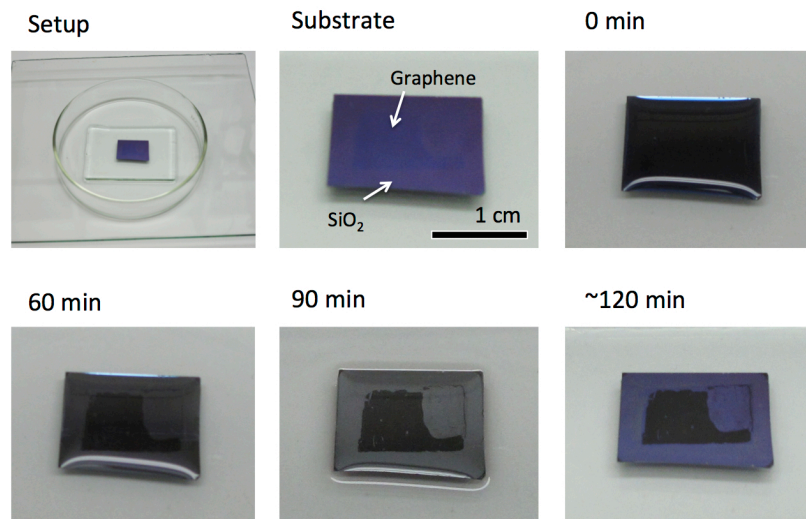
Figure 4.2. Photographs depicting the crystallization process.

4.2.3 Microscopy

Optical microscope and scanning electron microscope (SEM) images were collected on a Zeiss Axiotech Materials Microscope and JEOL-JSM-6700 field emission SEM, respectively. For the undoped samples, a 2 nm layer of platinum was sputtered onto the sample surface to reduce charging. Transmission electron microscope (TEM) samples were prepared by brushing a TEM grid against the wafer surface to mechanically transfer the crystals. TEM imaging and selected area electron diffraction (SAED) were performed on a FEI Tecnai G^2 TF20 TEM operated at 200 kV. SAED patterns were collected on multiple areas on each crystal, which showed identical patterns that confirmed their single crystalline nature. Multiple crystals were analyzed for each sample and reproducible results were obtained. Powder XRD spectra were

collected on a Panalytical X'Pert Pro X-ray powder diffractometer using Cu K$_\alpha$ radiation with a wavelength of 0.15418 nm at a scan rate of 4.0° /min.

4.2.4 Theoretical calculations

Tight-binding density functional theory (DFTB) calculations were performed to identify the preferred orientation of the tetraaniline molecular precursors on graphene. The electronic structure of the graphene-tetraaniline complex and stacking energy of tetraaniline molecules were calculated to identify the potential significance of the vertical growth direction. The calculations were performed using a periodic graphene sheet with a vacuum layer. The binding energies and conformations of tetraaniline molecules were calculated. The calculations are relatively large with more than 500 atoms in the computational domain and calculated using DFTB with sparse matrix parallelization as implemented in the DFTB+ code. The CHNO parameters used for the tetraaniline were tested using higher-level DFT calculations as implemented in atom-centered all-electron DFT calculations using DMOL. The DFTB+ method was able to produce an accurate description of conjugation and bond distances for tertraaniline molecules in comparison to higher-level DFT calculations.

4.2.5 Conductive AFM measurements

Atomic force microscopy (AFM) was carried out using the Bruker Dimension Icon Scanning Probe Microscope under ambient conditions. Topographic imaging was reproduced from multiple samples in the PeakForce Tapping^{TM} mode using silicon nitride cantilevers

(ScanAsyst-AIR, Bruker) with nominal spring constants of 0.4 N/m, first longitudinal resonance frequencies between 45-95 kHz, and nominal tip radii of ~2 nm. Images were processed by simple low-pass filtering and first-order plane fitting. Local I-V spectra were acquired by conductive AFM (cAFM) using the Bruker Extended TUNA applications module. Pt-Ir coated silicon cantilevers (SCM-PIC, Bruker) with calibrated spring constants between 0.12-0.15 N/m, first longitudinal resonance frequencies between 11.5-13 kHz, and nominal tip radii of <25 nm were used in PeakForce Tapping^{TM} mode in order to provide quantitative control over the applied force, thereby reducing sample perturbations during the measurement. Bias voltage sweeps were applied to each sample with respect to a virtually grounded cAFM probe tip at rate of 0.25 V/s over the range of interest, while maintaining a constant applied force throughout by means of the feedback loop. The reported I-V characteristics were stable with repeated positive and negative bias sweeps and were the average of 20 I-V curves taken at various positions on different crystals for each sample.

4.2.6 Graphene/vertical crystals/graphene sandwich devices

Graphene/tetraaniline vertical crystal arrays/graphene sandwiched devices were fabricated by (1) depositing a strip of graphene, (2) defining Ti/Au contacts using a shadow mask followed by e-beam evaporation, (3) crystallizing tetraaniline, and (4) depositing a top bi-layer graphene electrode (**Fig. 4.3**). I-V curves for these devices were obtained on a standard probe station.
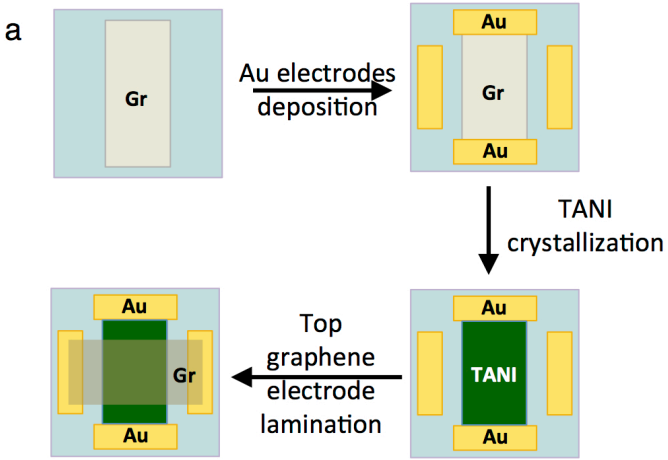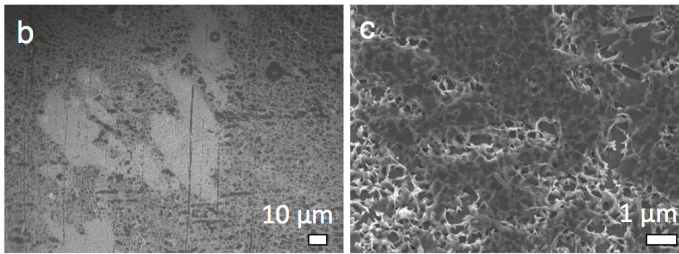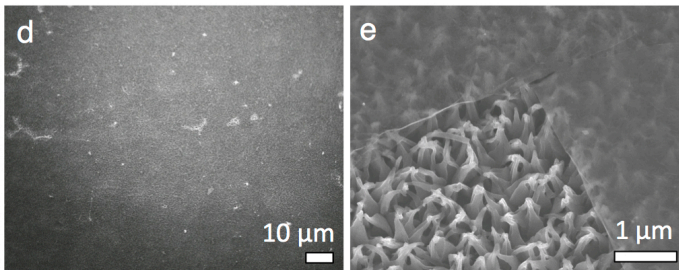
Figure 4.3. (a) Fabrication steps for the graphene/TANI/graphene sandwiched devices. (b, c) SEM images showing when a single layer of CVD graphene is laminated on top of the crystal arrays as the top electrode, as compared to (d, e) when two layers of graphene are used.

4.2.7 Patterning of vertical crystal arrays

Patterning of graphene was carried out using photolithography. AZ 5214 photoresist was spin-coated onto graphene-covered SiO_2/Si substrates at 3500 rpm. A photomask was aligned using a Karl Suss MA6 aligner followed by 6 sec of UV exposure at an intensity of 8 mW. After developing the photoresist in the AZ Developer, the exposed graphene area was etched using an O_2 plasma in a Tegal Plasmaline Asher at 100 W for 60 sec. The remaining photoresist was then stripped away using acetone followed by baking at 450 °C for 1 h under flowing Ar.

4.3 Results & Discussion

4.3.1 Vertical crystallization on graphene

Tetraaniline (TANI) was chosen as a representative molecule for exploring graphene-assisted vertical crystallization since its monodispersity allows TANI to serve as a good model system for the crystallization of polyaniline, a benchmark conducting polymer.[20, 21, 22] In a crystallization process, a loosely covered container is filled with a non-solvent for TANI, such as n-hexane. A TANI solution is dropped onto a SiO_2/Si substrate coated with a single layer of chemical vapor deposited (CVD) graphene[23] raised above the n-hexane liquid level (**Fig. 4.4a**). The vapor of the non-solvent saturates the closed chamber and infiltrates into the TANI solution, creating supersaturation which induces crystallization. The crystallization event is illustrated in **Fig. 4.2**. At the end of the process where all solvent has been evaporated, dark colored TANI can be observed localized on the graphene-covered area, while the bare SiO_2 area remains intact (**Fig. 4.4b**). A cross-polarized optical micrograph further illustrates the high nucleation affinity

of TANI on graphene as evidenced by a sharp interface between the graphene and SiO_2 surfaces where the strongly birefringent tetraaniline crystals are only observed on graphene (**Fig. 4.4c**). SEM analysis reveals these crystals are oriented vertically with respect to graphene and exhibit uniform morphological orientation and height (**Fig. 4.4d** and additional images in **Fig. 4.5**). The nucleation density of these crystals can be readily controlled by varying the solution concentration (**Fig. 4.4e and 4.6**). For instance, 2-propanol solutions of TANI with concentrations of 0.5, 1.0, 1.5, and 2.0 mg/mL lead to nucleation densities of 2, 3, 5, 10 crystals per square micrometer while the crystal height and size remain constant (**Fig. 4.4e**).
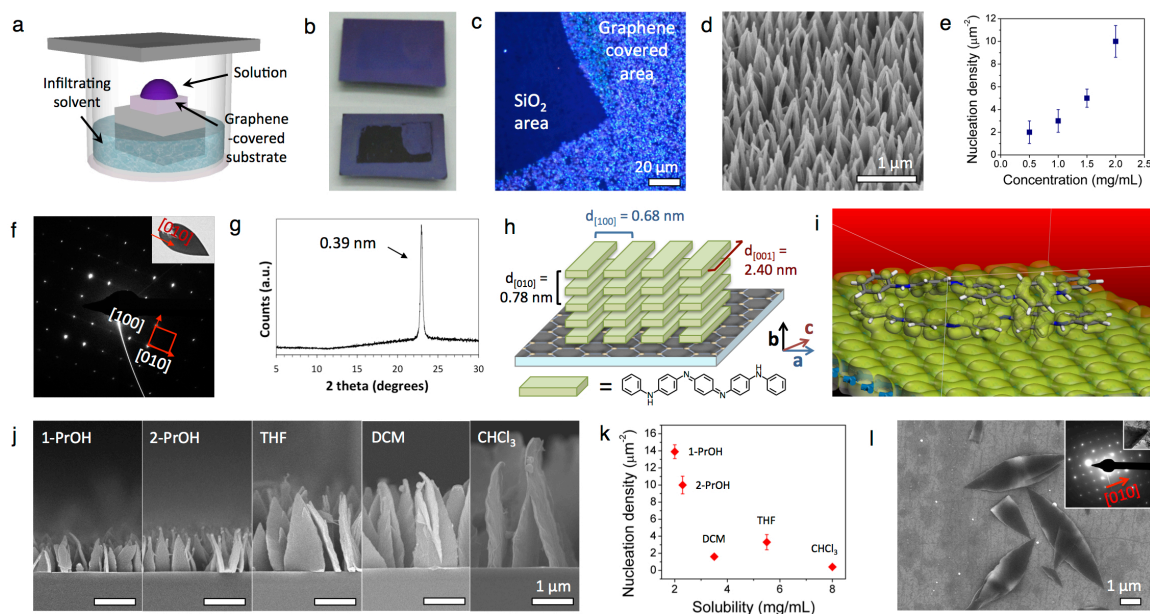
Figure 4.4. Crystallization of tetraaniline on graphene. (a) Vapor-infiltration setup used for the experiments. (b) A graphene-coated SiO_2/Si wafer before (top panel) and after (bottom panel) the crystallization of tetraaniline. (c) Polarized optical microscope image showing the SiO_2/graphene interface where crystals only grow on the graphene-covered areas. (d) SEM image showing the plate-shaped tetraaniline crystals are oriented vertically on graphene. (e) Control of crystal nucleation density by varying solution concentration. (f) Top-view electron diffraction pattern of

a vertical plate (shown in inset) transferred to a TEM grid. (g) Powder XRD pattern of the crystal

arrays. (h) Proposed packing arrangement for the tetraaniline crystals obtained from SAED and

XRD information. (i) DFTB modeling illustrates the electron density overlap between two

tetraaniline molecules and graphene leading to the preferred face-on orientation. (j) Size control

of the crystals achieved by using different solvents. (k) Correlation between solubility and

nucleation density of the crystals. (l) Control over the orientation of tetraaniline crystals on

graphene: horizontal crystals are obtained by using an aromatic infiltrating solvent. Inset shows

the corresponding SAED pattern.
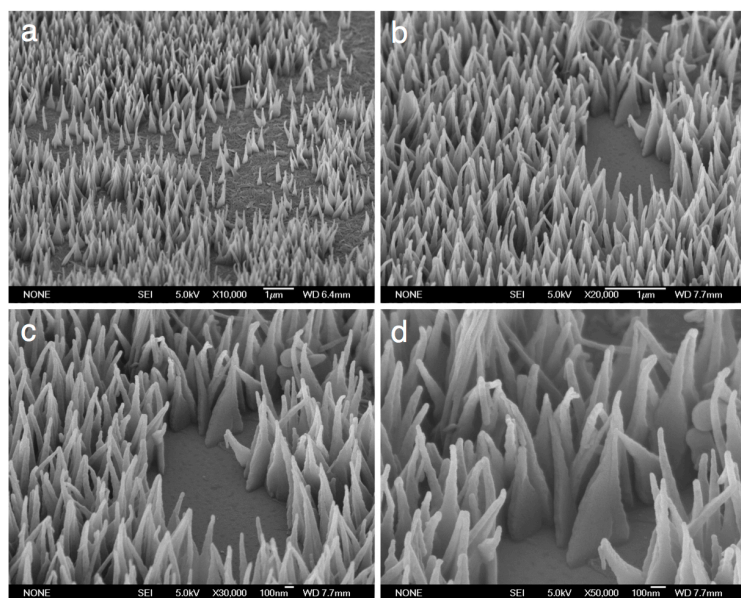
Figure 4.5. Additional SEM images obtained at different magnifications showing the vertically

oriented tetraaniline crystals grown on graphene.
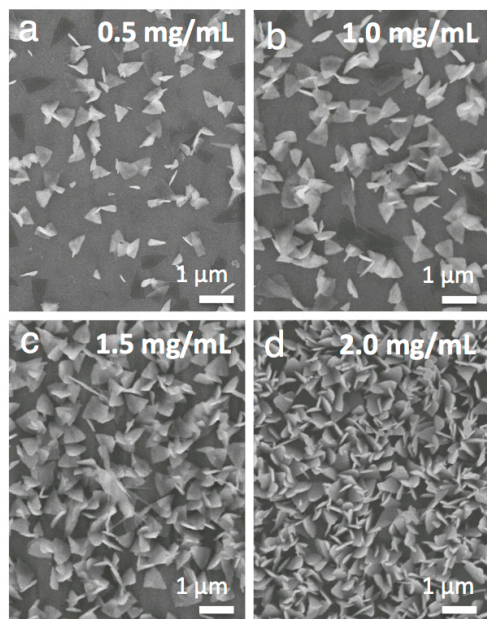
Figure 4.6. SEM images demonstrating control of the deposition density of vertical crystals by varying the solution concentration from (a) 0.5, (b) 1.0, (C) 1.5, to (d) 2.0 mg/mL.

4.3.2 Crystallographic orientation

In order to decipher the crystallographic information, several crystals were transferred to TEM grids for selected area electron diffraction (SAED) analysis. The electron diffraction pattern of a plate laying flat on a TEM grid (**Fig. 4.4f**) shows sharp Bragg spots, indicating these plates are single crystals. A (020) d-spacing of 0.39 nm is obtained, suggesting that the tetraaniline molecules π-stack parallel to the graphene substrate along the long-axis of the crystals. In combination with the cross-sectional SAED pattern (**Fig. 4.7**), a packing model has been developed for tetraaniline on graphene with the (100), (010), and (001) d-spacings of 0.68, 0.78, and 2.40 nm, respectively (**Fig. 4.4h**).
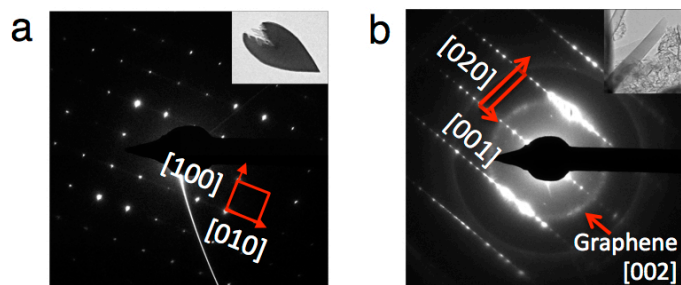
Figure 4.7. Selective area electron diffraction (SAED) patterns taken perpendicular to (a) the face and (b) the edge of tetraaniline plates grown vertically on graphene.

When a large-area crystal array (~1 cm^2) was analyzed by powder XRD, only one intense peak at 23.8° 2θ was observed (**Fig. 4.4f**), which corresponds to a d-spacing of 0.39 nm. This value is in agreement with the (020) spacing obtained from SAED, which indicates that all molecules are uniformly π-stacked along the vertical direction in each crystal over a large area. These results suggest that unlike the conventional template-guided methods, which provide alignment for the supramolecular morphology yet offer little control over the molecular packing direction,[5, 6, 7] our graphene-assisted approach exerts both excellent morphological and crystallographic orientational control. For anisotropic materials such as organic semiconductor crystals, uniform orientation in solid-state packing is crucial for achieving stable and consistent device performance at the macroscopic scale toward important applications such as solar cells and sensors.[1, 2, 4]

4.3.3 Mechanism for vertical growth

In order to understand the mechanism behind the graphene-assisted crystallization, we performed experimental and theoretical investigations into (1) the surface requirements, (2) the energetics in binding affinity, and (3) the influence of the solvent system.

To exploit the surface requirement, mechanically exfoliated graphene,[24] chemically converted graphene (CCG),[25] and laser scribed graphene (LSG)[26] were transferred onto SiO_2/Si substrates for tetraaniline crystallization, to compare with CVD-grown graphene[23] (**Fig. 4.8**). Among these, oriented vertical crystal arrays grow selectively on the mechanically exfoliated graphene flakes, in a fashion identical to that on CVD graphene. On the other hand, clusters of crystals form when CCG or LSG serve as the substrate, similar to crystallization on conventional surfaces such as SiO_2. The crystallization does not show any selectivity in nucleation sites when either CCG or LSG and SiO_2 surfaces are present. It has been well established that CVD-grown and peeled graphene both possess a fully sp^2 conjugated carbon lattice,[23, 24, 27] whereas a small amount of oxygenated groups remain on the basal plane of the graphene sheets reduced from graphene oxide either chemically (CCG) or photothermally (LSG).[25, 26] Therefore, an atomically homogeneous and defect-free sp^2 hybridized surface is crucial for achieving vertical crystallization of conjugated compounds such as tetraaniline. It provides preferred orbital, electronic density and dipole overlap at the interface between the substrate and the molecules, which has been demonstrated to be crucial factors for controlling the orientation of organic molecules adsorbed on a substrate.[28, 29] In fact, tight-binding density functional theory (DFTB) calculations indicate that TANI adsorbs on graphene favorably in a face-on orientation. This configuration provides the strongest overlap of electron densities between the two, while

minimizing the repulsive interactions (**Fig. 4.4i**). The binding energy is calculated to be 68 kcal/mol, which indicates an off-centered overlap of the π-electrons of graphene and tetraaniline. Since the preferred orientation between tetraaniline and graphene is face-on, and crystals of conjugated molecules tend to grow along their π-π stacking direction, tetraaniline crystals grow vertically from the graphene-coated substrate with the π-π stacking direction perpendicular to graphene.

Mechanically exfoliated Graphene	Chemically Converted Graphene (CCG)	Laser Scribed Graphene
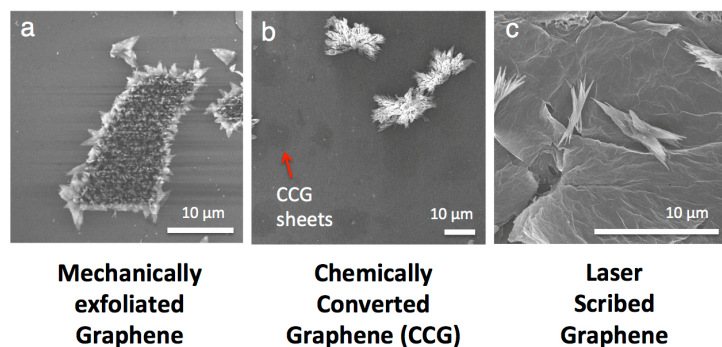
Figure 4.8. SEM images showing crystals formed on (a) mechanically exfoliated graphene, (b) chemically converted graphene, and (c) laser scribed graphene.

In addition to the surface and energetic factors, both the solvation and infiltrating solvents play important roles in dictating the preferred nucleation and controlling the orientation of tetraaniline crystal growth on graphene. Tetraaniline is soluble in a variety of polar solvents. These solutions were cast onto graphene coated SiO_2/Si substrates for tetraaniline crystallization (**Table 4.1**). We observed that when the solvent has a dielectric constant that is less than or equal to that of 1-propanol, arrays of vertical crystals form selectively on the graphene-coated area. Such solvents include 1-propanol, 2-propanol, dichloromethane, tetrahydrofuran, and

chloroform (**Table 4.1** and **Fig. 4.9**).[30] On the other hand, when the solvation solvent's dielectric constant is greater than that of 1-propanol, e.g. acetone, ethanol, methanol, acetonitrile, and dimethyl sulfoxide,[30] randomly oriented clusters of crystals form all over the substrate, without selectivity for the graphene-coated area (**Table 4.1** and **Fig. 4.10**). As graphene is a non-polar surface,[31] solvents with lower dielectric constant wet it better. Hence, it is important to select such a solvent to ensure thorough wetting of the graphene-covered area when supersaturation is reached, so that preferred nucleation of tetraaniline can occur directly on graphene. Conversely, more polar solvents, e.g. ethanol, acetonitrile, etc., do not favorably wet the non-polar graphene surface. In fact, as the solvent evaporates, the remaining droplet tends to migrate away from graphene to the SiO_2 area. As a result, large clusters of crystals form on the SiO_2 substrate, while the deposition density on graphene remains low.

Table 4.1. Solvent Properties for Vertical Crystallization of Tetraaniline

Solvent	Dielectric [a] constant	Relative [b] polarity	Boiling point [b] (°C)	Vapor [b] pressure (mmHg)	Orientation [b]
chloroform	4.8	25.9	61.2	210	Vertical
tetrahydrofuran	7.6	20.7	66.0	200	Vertical
dichloromethane	9.1	31.0	39.6	350	Vertical
2-propanol	18.3	54.6	82.5	44	Vertical
1-propanol	20.1	61.7	97.0	21	Vertical
acetone	20.6	35.5	56.2	240	Random
ethanol	22.4	65.4	78.5	59	Random
methanol	32.6	76.2	64.6	128	Random
acetonitrile	37.5	46.0	81.6	97	Random
dimethyl sulfoxide	46.6	44.4	189.0	0.7	Random

^a Solvents with a dielectric constant lower than 20.1 leads to tetraaniline crystals to grow vertically, while those with dielectric constant higher than 20.6 results in clusters of crystals randomly deposited on both graphene and SiO$_2$ areas. ^b Other solvent properties including boiling point, vapor pressure, and surface tension do not appear to have a controlling effect on the orientation of crystal growth.
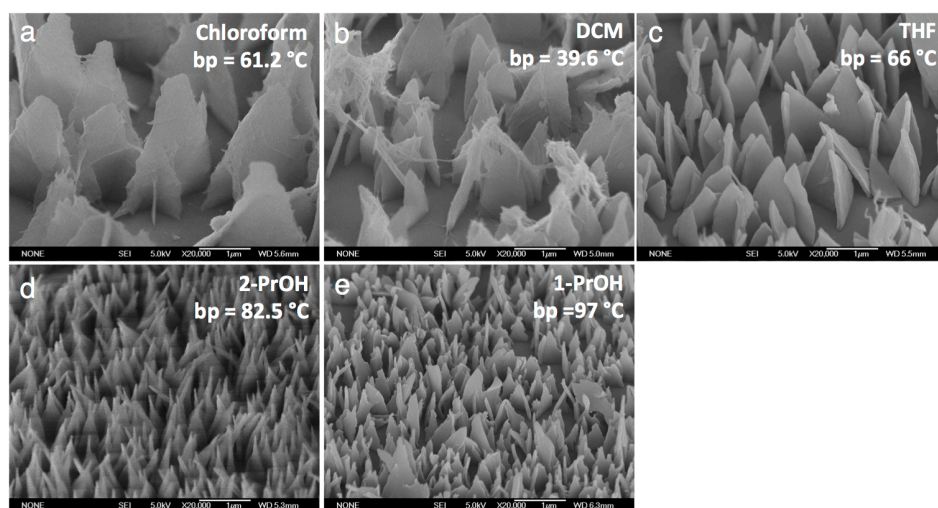
Figure 4.9. Tilted SEM images of vertical tetraaniline crystal arrays obtained by using (a) chloroform, (b) dichloromethane, (c) tetrahydrofuran, (d) 2-propanol, and (e) 1-propanol as the solvation solvent.
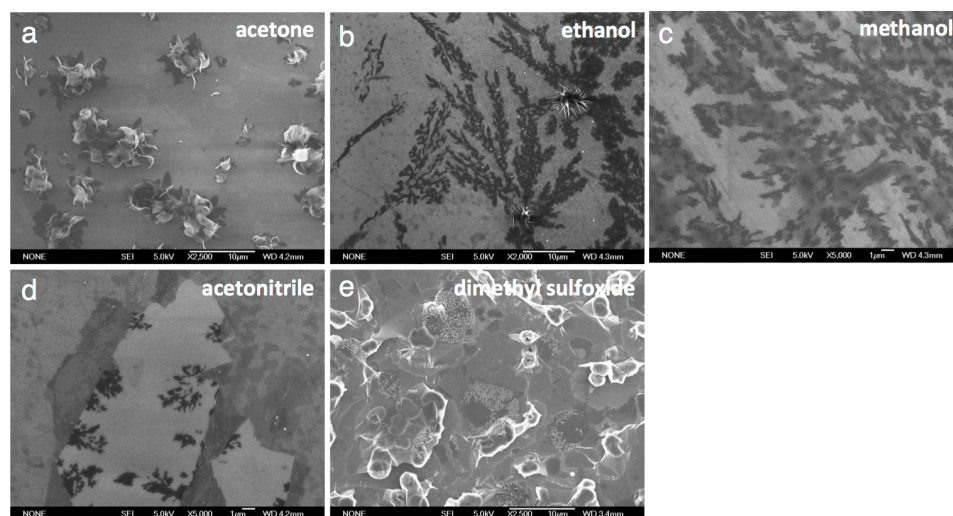
Figure 4.10. SEM images of tetraaniline assemblies formed on graphene by using (a) acetone, (b) ethanol, (c) methanol, (d) acetonitrile, and (e) dimethyl sulfoxide as the solvation solvent.

The solvation solvent also offers control over the nucleation density and crystal size of the vertical crystal arrays. As shown in **Fig. 4.4j**, crystals of different sizes can be obtained by using different solvents at the same concentration (e.g. 2 mg/mL), with larger crystals corresponding to lower nucleation density, and smaller ones to higher nucleation density (**Fig. 4.9**). Plotting the solubility of TANI in these solvents against their nucleation density reveals a nearly inverse proportional relationship (**Fig. 4.4k**). Since the TANI concentration is close to saturation in solvents such as 1-propanol or 2-propanol, supersaturation is reached soon after n-hexane begins to infiltrate, resulting in rapid nucleation that leads to a larger number of smaller crystals. Conversely, a longer non-solvent infiltration period is needed to induce supersaturation for solvent systems in which TANI is more soluble (i.e. DCM, THF, chloroform). Therefore, a slower nucleation process is created, which leads to larger crystals with lower nucleation densities.[32]

4.3.4 Orientation control

The ability to manipulate crystal orientations on a certain substrate is crucial for expanding the realm of device applications. Here, we demonstrate that the orientation of the tetraaniline crystals on graphene can be controlled by the choice of infiltrating solvents (**Fig. 4.11**). Hydrocarbon infiltrating solvents with suitable solvation properties lead to vertical crystal growth (**Fig. 4.12**). On the other hand, aromatic infiltrating solvents (e.g. benzene or toluene) result in tetraaniline crystal growth in a horizontal orientation, i.e. parallel to the graphene substrate (**Fig. 4.4l, 4.13,** and **Table 4.2**). SAED patterns of such crystals reveal the π-π stacking direction to be along their long-axis, which is now parallel with respect to graphene (inset to **Fig. 4.4l**). As shown by the DFTB calculations (**Fig. 4.4i**), the vertical growth of the conjugated tetraaniline crystals is likely due to the strong affinity for the molecules to bind in a face-on configuration with respect to graphene due to the strong electron density overlap. However, aromatic molecules such as benzene also have a high binding affinity for graphene. DFTB calculations show that benzene adsorbs strongly on the graphene surface with an energy of ~17 kcal/mol per benzene molecule. The nucleation sites available for tetraaniline depend on the surface coverage level. At half or even a quarter of a monolayer coverage of a graphene surface by benzene, the probability of tetraaniline adsorbing in a face-on configuration is severely reduced. Although tetraaniline is adsorbed at 68 kcal/mol per molecule according to DFTB calculations, the kinetics of face-on adsorption become unfavorable due to the high solvent-to-tetraaniline ratio. Thus, tetraaniline molecules stack more favorably in an edge-on fashion, which in turn alters the crystal growth direction and leads to the horizontal orientation.
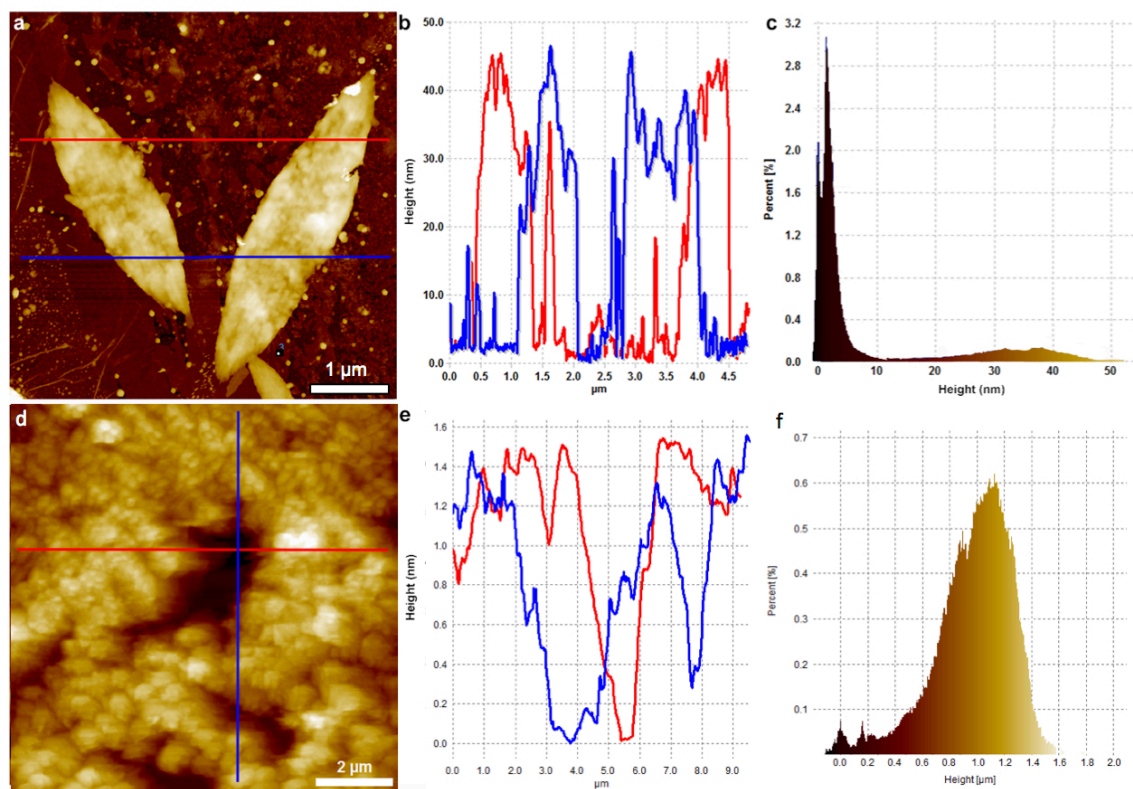
Figure 4.11. (a) An AFM image of tetraaniline crystals lying horizontally on graphene by using an aromatic infiltrating solvent. (b) Height profiles of the line scans indicated in (a), and (c) histogram of the sample height within the scanned area. (d-f) illustrate the AFM image, line scan height profile, and height histogram, respectively, for a vertically oriented sample.
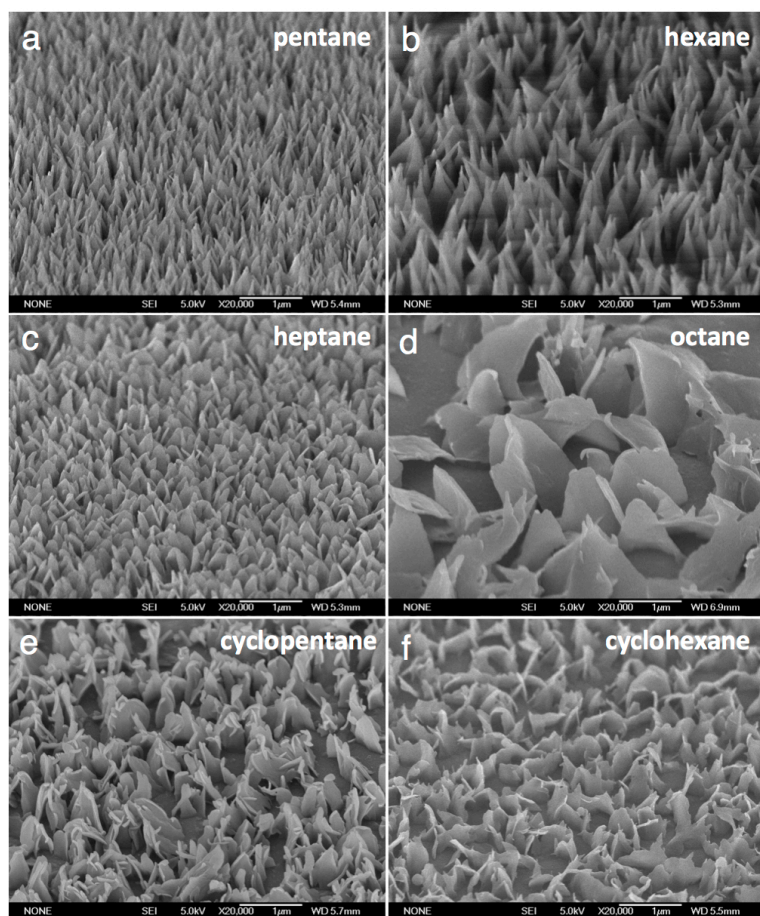
Figure 4.12. Tilted SEM images of tetraaniline crystallized on graphene using (a) n-pentane, (b) n-hexane, (c) n-heptane, (d) n-octane, (e) cyclopentane and (f) cyclohexane as the infiltrating solvent. All these hydrocarbon solvents lead to vertically oriented crystal arrays.
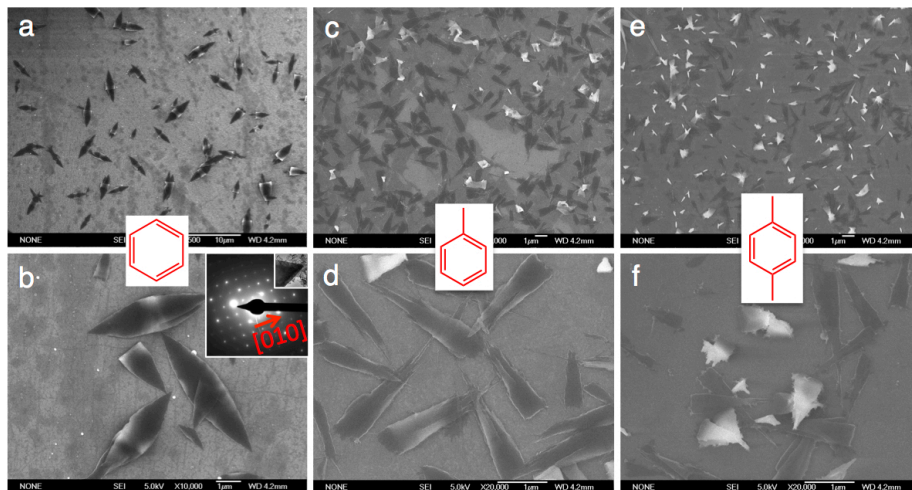
Figure 4.13. SEM images illustrating that when an aromatic solvent such as (a-b) benzene, (c-d) toluene, or (e-f) xylene is used as the infiltrating solvent, the crystals lie horizontal with respect to the graphene substrate. Inset in (b) is an electron diffraction pattern of a horizontal crystal, which shows an identical diffraction pattern as those grown vertically on graphene when a non-aromatic hydrocarbon infiltrating solvent was used.

Table 4.2. Properties for the Infiltrating Solvents Tested

Infiltrating solvent	Dielectric constant	Polarity index	Boiling point (°C)	Vapor pressure (mmHg)	Surface tension (dyn/cm)	Orientation
Hydrocarbon						
pentane	1.84	0.9	36.1	573	16	Vertical
hexane	1.9	0.9	69	160	18.4	Vertical
cyclohexane	2.01	0.6	80.7	104	24.98	Vertical
cyclopentane			49	100		Vertical
heptane	1.924	1.2	98	48	19.3	Vertical
octane		1.2	125	14.7	21.7	Vertical
Aromatic						
benzene	2.28	11.1	80.1	101	28.9	Horizontal
toluene	2.38	9.9	110.6	29	28.5	Horizontal
xylenes	2.3	7.4	138.3	15	28.6	Horizontal

4.3.5 Conductive-AFM measurements

Control over the tetraaniline crystal orientation on graphene offers the opportunity to examine its anisotropic electrical transport properties along different crystallographic axes. Transport properties along the interfacial stacking direction (i.e. the b-axis) can be measured using conductive atomic force microscopy (cAFM), where a metallic AFM tip serves as the top electrode contact to the apex of a vertical crystal in combination with the graphene substrate as the bottom electrode (**Fig. 4.14a, 4.15**). Conversely, use of an identical electrode configuration on crystals grown horizontally with respect to the graphene substrate enables study of the transport properties along the oligomer backbone (i.e. the c-axis) (**Fig. 4.11c, 4.15**). Topographic AFM images of vertical and horizontal crystals on graphene shown in **Fig. 4.14b** and **d**,

respectively, enabled precise positioning the top electrode for electrical characterization as well as a direct measure of cross-sectional heights employed in subsequent analyses.
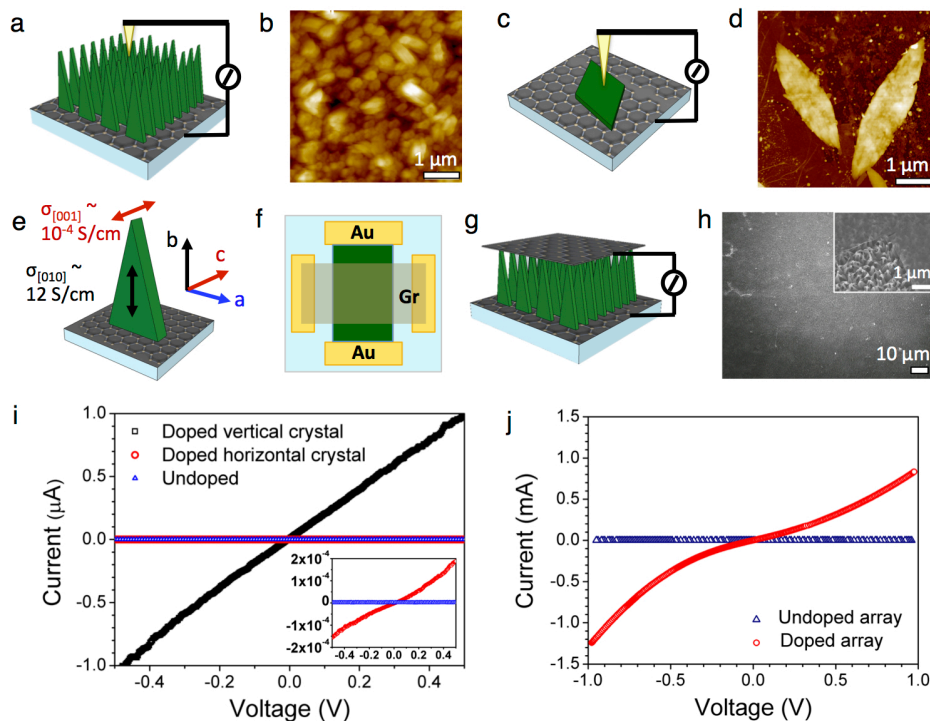
Figure 4.14. Anisotropic electrical properties of the tetraaniline crystals grown on graphene. (a) Schematic of the conductive-AFM measurement setup for the vertical crystals probing current along the b-axis. (b) Topographic AFM image of a high density array of the tetraaniline vertical crystals. (c) Schematic of the conductive-AFM measurement setup for the horizontal crystals where the transport along the c-axis can be obtained. (d) Topographic AFM image of a crystal laying horizontally on graphene. (e) Different conductivity values along the different crystallographic axes. (f) and (g) Schematics showing the top view (f) and the cross-sectional view (g) of the graphene/tetraaniline array/graphene (Gr/TANI/Gr) sandwich device. (h) SEM image showing the top graphene electrode laminated on top of the vertical crystals. Inset illustrates a more magnified view at an edge of the top graphene layer. (i) Typical I-V curves

obtained for undoped crystals, a single vertical plate and a single horizontal plate after vapor doping. Inset has a smaller current scale showing the lower current for the horizontal plates. (j) I-V plots of the Gr/TANI/Gr sandwiched devices.
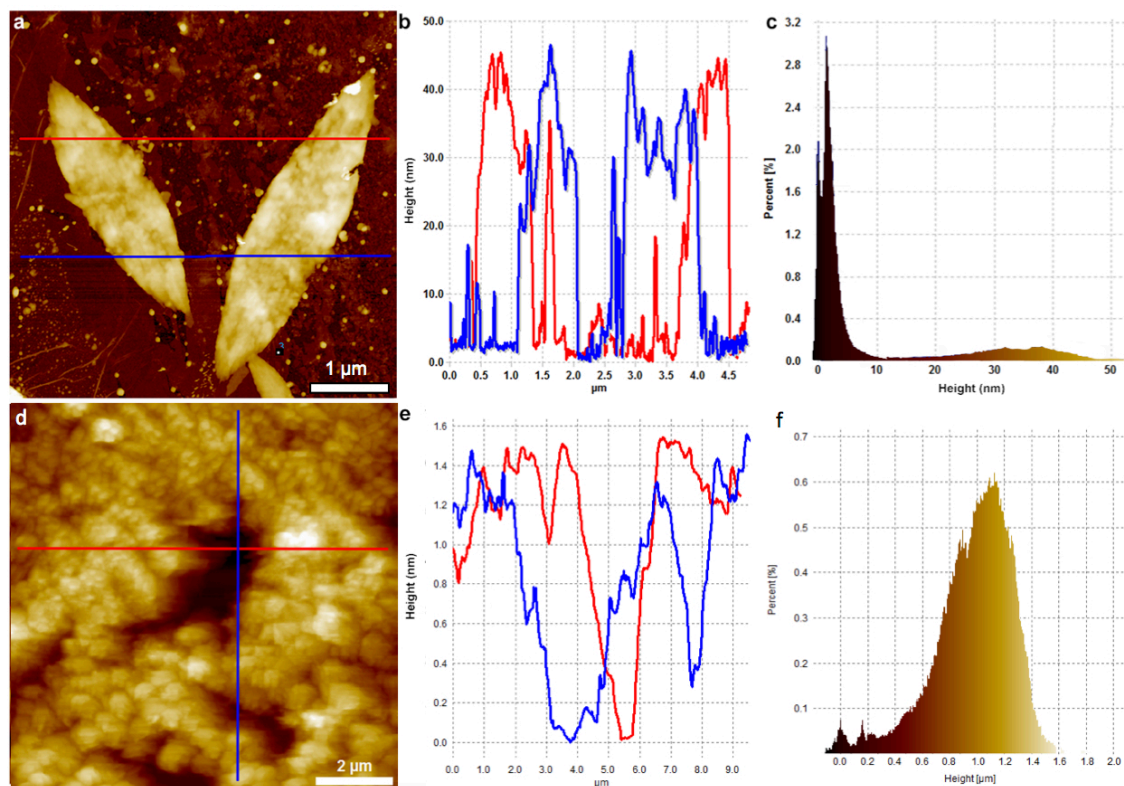
Figure 4.15. (a) An AFM image of tetraaniline crystals lying horizontally on graphene by using an aromatic infiltrating solvent. (b) Height profiles of the line scans indicated in (a), and (c) histogram of the sample height within the scanned area. (d-f) illustrate the AFM image, line scan height profile, and height histogram, respectively, for a vertically oriented sample.

Current-voltage (I-V) spectra acquired via cAFM are shown in **Fig. 4.14i**. An insulating baseline was obtained for the as-grown, undoped crystals regardless of orientation (blue triangles). Upon acid doping (e.g. HCl vapor), the measured current increased by over six orders of magnitude (black squares) for the vertically oriented crystals, corresponding to a conductivity of ~12.3 S/cm. The cAFM analysis is shown in **Fig. 4.15** and the detailed calculations are illustrated below with schematics presented in **Fig. 4.16-4.17**).

The conductivity values of the crystals along the b- and c-axes were calculated from the I-V curves obtained from conductive AFM (cAFM) measurements using the equations below unless stated otherwise:

$$R = \frac{V}{I}$$

$$\rho = R \cdot \frac{w \cdot t}{l} = R \cdot \frac{A}{l}$$

$$\sigma = \frac{1}{\rho}$$

where, R is resistance, V is voltage, I is current, ρ is resistivity, w is channel width, t is channel thickness, l is channel length, A is channel cross-sectional area, and σ is conductivity. The conductivity values shown below are the average of 20 measurements for each sample.

Vertical Crystals:

In the cAFM measurements, the Pt/Ir-coated AFM tip serves as the top electrode and the graphene layer as the bottom electrode. For a crystal standing vertically on graphene, the current

along the vertical b-axis can be probed through this configuration (**Fig. 4.14a**). There are two possibilities for the carriers to travel between the electrodes, shown in **Fig. 4.16a** and **b**. Since carriers prefer to travel through the path with the least resistance, the pathway shown in **Fig. 4.16a** will be preferred if the b-axis (i.e. the interfacial stacking direction) is more conductive than the other crystallographic directions. Alternatively, if the conductivity along other crystallographic axes are higher, the carriers are more likely to travel as illustrated in **Fig. 4.16b**. Conductivity values are calculated for both scenarios below, and are found to be 12.3 and 1.81 S/cm for the pathways shown in **Fig. 4.16a** and **b**, respectively.

- AFM tip area (A_{AFM}) = 1.256×10^3 nm^2 (AFM tip diameter = 20 nm)

- Crystal base area (A_{cryst}) = $w_{avg} \times t_{avg}$ = (530 nm) × (52 nm) = 2.756×10^4 nm^2

- Crystal average height (l_{avg}) = 1100 nm

- Average resistance from 20 measurements: R_{avg} = $(7.141 \pm 0.468) \times 10^5$ Ω

Figure 4.16. Schematic of the two possibilities for carriers to travel between the top AFM tip and bottom graphene electrodes. (a) If the conductivity along the b-axis is significantly higher than the other axes. (b) If the conductivity is higher along other axes. The red arrow lines

represent the travel pathway of carriers from the conductive AFM tip to the bottom graphene layer.

*Assuming preferred carrier transport pathway as shown in **Fig. 4.16a**:*

$$\rho_1 = R_{avg} \cdot \frac{A_{AFM}}{l_{avg}} = \left((7.141 \pm 0.468) \times 10^5 \Omega\right) \cdot \left(\frac{1.256 \times 10^3 \; nm^2}{1100 \; nm}\right) \cdot \left(\frac{1 \; cm}{10^7 \; nm}\right)$$

$$= 0.0815 \pm 0.0053 \; \Omega \cdot cm$$

$$\sigma_1 = \frac{1}{\rho_1} = 12.3 \pm 1.1 \; S/cm$$

*Assuming preferred carrier transport pathway as shown in **Fig. 4.16b**:*
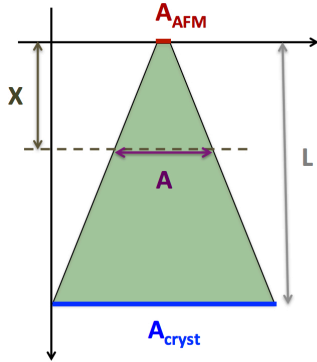
$$R_2 = \rho_2 \cdot \frac{L}{A}$$

$$\frac{A - A_{AFM}}{A_{ryst} - A_{AFM}} = \frac{X}{L} \; \rightarrow \; A - A_{AFM} = \frac{A_{cryst} - A_{AFM}}{L} \cdot X$$

144

$$dR = \rho \cdot \frac{dx}{A_{AFM} + \frac{A_{cryst} - A_{AFM}}{L} \cdot X}; define \ a = \ A_{AFM}, b = \frac{A_{cryst} - A_{AFM}}{L}$$

$$dR = \rho \cdot \frac{dx}{a + bX}$$

$$R = \int_0^L dR = \int_0^L \rho \cdot \frac{dx}{a + bX} = \rho \cdot \frac{1}{b} \cdot \ln(a + bX)]_0^L = \rho \cdot \frac{1}{b} \cdot [\ln(a + bL) - \ln a]$$

$$= \rho \cdot \frac{L}{A_{cryst} - A_{AFM}} \cdot (\ln A_{cryst} - \ln A_{AFM})$$

$$\therefore \rho_2 = R_2 \cdot \frac{A_{cryst} - A_{AFM}}{L \cdot (\ln A_{cryst} - \ln A_{\ FM})}$$

$$= \left((7.141 \pm 0.468) \times 10^5 \ \Omega\right) \cdot \left(\frac{27560 \ nm^2 - 1256 \ nm^2}{(1100 \ nm) \cdot (\ln 27560 - \ln 1256)}\right) \cdot \left(\frac{1 \ cm}{10^7 cm}\right) = 0.553 \ \Omega \cdot cm$$

$$\sigma_2 = \frac{1}{\rho_2} = \frac{1}{0.553 \ \Omega \cdot cm} = 1.81 \pm 0.15 \ S/cm$$

Horizontal Crystals:

When the same cAFM configuration is applied to the crystals lying horizontally on graphene, the conductivity along the c-axis can be studied. Again, two scenarios arise as shown in **Fig. 4.17**. If the c-axis is the most conductive direction, carriers will predominately travel vertically as shown in **Fig. 4.17a**. However, if other axes are more conductive, the scenario shown in **Fig. 4.17b** will predominate, and the value calculated using (a) will be an over-estimation.

- AFM tip area (A_{AFM}) = 1.256×10^3 nm^2 (AFM tip diameter = 20 nm)

- Crystal area (A_{cryst}) = $w_{avg} \times t_{avg}$ = (2.2 μm) × (1 μm) = 2.2 μm^2

- Crystal average thickness (l_{avg}) = 35 nm = 3.5×10^{-2} μm

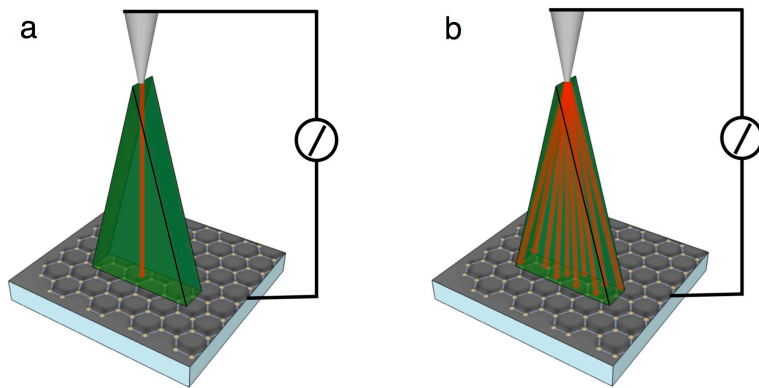- Average resistance from 20 measurements: R_{avg} = (2.640±1.640) × 10^9 Ω
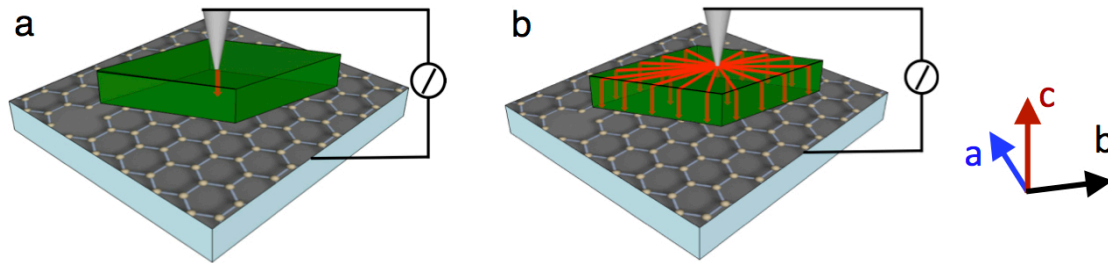
Figure 4.17. Schematic of the two possibilities for carriers to travel between the top AFM tip and bottom graphene electrodes on a horizontal crystal: (a) If the conductivity along the c-axis is significantly higher than the other axes; (b) If the conductivity is higher along other axes. The red arrow lines represent the travel pathway for carriers from the conductive AFM tip to the bottom graphene layer.

Assuming preferred carrier transport pathway as shown in Fig. 4.17a:

$$\rho_3 = R_{avg} \cdot \frac{A_{AFM}}{l_{avg}} = \left((2.640 \pm 1.640) \times 10^9 \Omega\right) \cdot \left(\frac{1.256 \times 10^3 \ nm^2}{35 \ nm}\right) \cdot \left(\frac{1 \ cm}{10^7 \ nm}\right)$$

$$= (9.474 \pm 5.873) \times 10^3 \ \Omega \cdot cm$$

$$\sigma_3 = \frac{1}{\rho_3} = (1.06 \pm 0.65) \times 10^{-4} \ S/cm$$

Assuming preferred carrier transport pathway as shown in Fig. 4.17b:

Area (A) = A_{cryst} = 2.2 μm^2

$$\rho_4 = R_{avg} \cdot \frac{A_{cryst}}{l_{avg}} = \left((2.640 \pm 1.640) \times 10^9 \Omega \right) \cdot \left(\frac{2.2 \ \mu m^2}{3.5 \times 10^{-2} \ \mu m} \right) \cdot \left(\frac{1 \ cm}{10^4 \ \mu m} \right)$$

$$= (1.659 \pm 1.028) \times 10^7 \ \Omega \cdot cm$$

$$\sigma_4 = \frac{1}{\rho_4} = (6.03 \pm 3.74) \times 10^{-8} \ S/cm$$

	Axis	Upper bound (S/cm)	Lower bound (S/cm)
Vertical	b	12.3±1.1	1.81±0.15
Horizontal	c	$(1.06 \pm 0.65) \times 10^{-4}$	$(6.03 \pm 3.74) \times 10^{-8}$

Since the upper bound of conductivity for the c-axis is four orders of magnitude lower than that of the lower bound for the b-axis, it is conclusive that the carriers move significantly more efficiently along the b-axis. Therefore, the scenario in **Fig. 4.16a** best represents the conductive pathway when the measurement is carried out on the vertically oriented crystals. Hence, the average conductivity along the b-axis is 12.3 S/cm. On the other hand, since (1) the

c-axis does not provide an efficient pathway for carrier transport, and (2) from the crystallographic data, the packing for tetraaniline molecules along the a-axis is the edge-to-edge lamellae direction, which has been shown to be the least conductive direction due to poor molecular orbital overlaps,[5, 6, 7] the scenario illustrated in **Fig. 4.17a** that led to a conductivity of 1.06×10^{-4} S/cm represents an over-estimation of conductivity. Therefore, the conductivity along the c-axis is likely to be somewhere in-between the upper and lower bound, but closer to the lower bound of 6.03×10^{-8} S/cm. However, here we are reporting using the likely overestimated upper bound conductivity of 1.06×10^{-4} S/cm for the c-axis that gives a 5 orders of magnitude difference in conductivity between the b- and c-axis, because the transport properties along the lamellae a-axis could not be measured using the cAFM setup. Hence, the conductivity difference here is still likely to be an underestimation.

The conductivity of horizontal crystals (red circles) is seen to be significantly lower than that observed for their vertical counterparts (**Fig. 4.14i and inset**), and is at most $\sim 1.06 \times 10^{-4}$ S/cm (see **Fig. 4.17** and calculations above for details). Therefore, the conductivity along the interfacial stacking b-axis of the oligomer crystals is at least five orders of magnitude higher than that along the backbone c-axis direction (**Fig. 4.14e**). The observed anisotropic transport in tetraaniline crystals is most likely a result of the different conduction mechanisms operating along the various crystallographic orientations. Due to the short conjugation length of tetraaniline, the carrier transport along the molecule's backbone is limited and relies on a hopping mechanism between molecules.[33, 34, 35] In contrast, the extended conduction network comprised of π-orbital overlap is more efficient, therefore leading to a higher conductivity.[36, 37] The fact that the vertical direction is the most efficient conduction pathway with a high

conductivity renders these structures important for applications that can benefit from directional 3-D transport such as organic solar cells, batteries, or sensors.[4, 38, 39]

Conductivity along the interfacial axis is also one order of magnitude larger than the highest previously reported value for tetraaniline,[21], and can be attributed to the following two factors: (1) The phenyl/phenyl-capped tetraaniline used here has greater molecular symmetry when compared to those capped with phenyl/amine.[21] Symmetry reduces the number of isomers, which leads to more ordered packing and more evenly distributed molecular orbital delocalization.[40] (2) Direct growth of tetraaniline crystals on the bottom graphene electrode produces a high-quality electrical contact. This is in contrast to the bottom-contact configuration typically used for nanoscale architecture measurements, where the electrode/crystal interface is known to be non-ideal due to solvent impurity traps and the poor contact quality (see **Fig. 4.16-4.17** for more detailed discussion).

4.3.6 Graphene/vertical TANI crystal/graphene sandwich devices

In order to harness the current for all the vertical crystals collectively, another layer of graphene can be laminated on top of the crystal arrays to produce a graphene/tetraaniline/graphene (Gr/TANI/Gr) sandwich structure. **Fig. 4.14f** illustrate a top-view device schematic with the cross-sectional structure shown in **Fig. 4.14g**. **Fig. 4.18a** depicts the fabrication process. We found that a single layer of graphene does not have the mechanical strength to withstand the spiky crystal tips (**Fig. 4.3b, c**); however, two layers of graphene can serve as a rigid, continuous top electrode for the vertical crystal arrays (**Fig. 4.14h**). A tilted SEM image taken at an edge of the graphene top electrode (**Fig. 4.14h inset**) shows that the

bilayer graphene is indeed laminated on top of the crystal tips. I-V curves for the undoped vertical crystal arrays and that after HCl vapor doping are shown in **Fig. 4.14j**. Prior to acid doping, an insulating baseline was obtained, indicating that the top and bottom layers of graphene were separated by the undoped crystal arrays. Once doped, approximately 1.25 mA of current were detected at an applied voltage of 1.0 V. The current scale for arrays is three orders of magnitude higher than that of a single vertical crystal measured by cAFM, indicating that the vertical crystals sandwiched between graphene are indeed connected in parallel where their current can be harnessed collectively, illustrating the potential of such a structure for large-area device applications.

4.3.7 Patterning of vertical crystal arrays

Patterning of electronic materials is crucial for defining device position, down-sizing component dimensions and minimizing inter-device cross-talk.[41, 42, 43] Unfortunately, this is challenging for organic materials due to their sensitivity to the harsh processing conditions involved in conventional lithography methods.[12, 15] However, because of the high nucleation selectivity tetraaniline exhibits for graphene, the deposition locations of tetraaniline crystal arrays can be precisely controlled simply by patterning the graphene substrates. **Figure 4.18a** shows an optical microscope image of graphene dots that are 10 μm in diameter patterned via photolithography. After the tetraaniline crystallization, only the area covered by the graphene dots turned dark, indicative of tetraaniline binding, while the SiO_2 area remains intact (**Fig. 4.18b**). An SEM image of a 4 by 4 dot array further illustrates the high selectivity that tetraaniline crystals have for graphene (**Fig. 4.18c**). Tilted and more magnified images in Fig. 3d

and e confirm the vertically-oriented nature of the crystals and the sharp interface between the graphene covered and the SiO$_2$ covered areas.
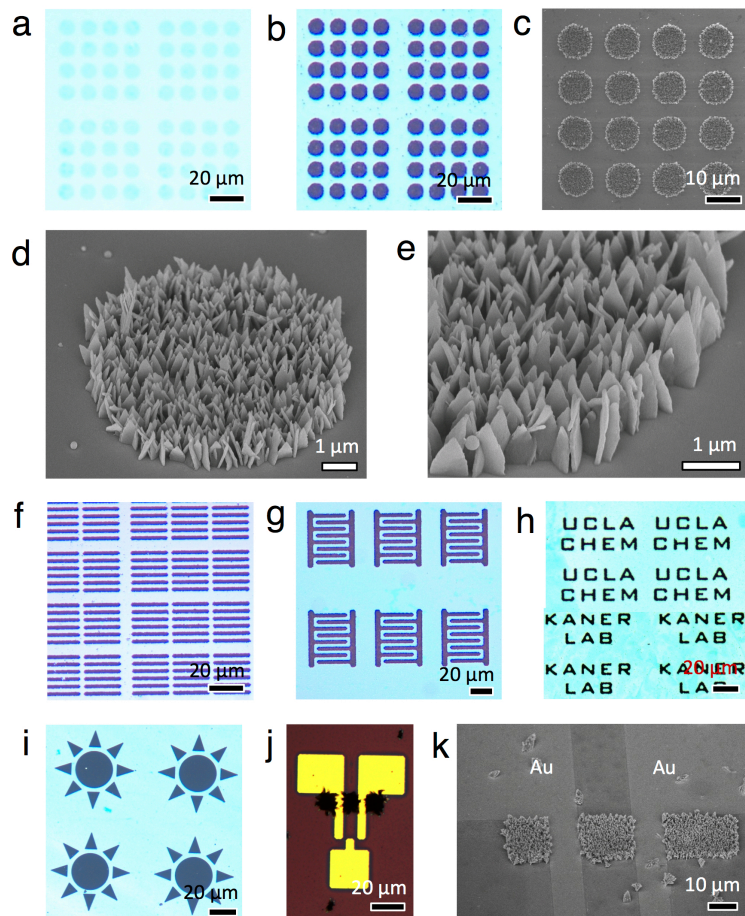
Figure 4.18. Patterning of vertical organic crystal arrays. (a) Patterned graphene on a SiO$_2$/Si substrate. The blue circles are graphene. (b) Same substrate after crystallization. Tetraaniline crystals only grow on the circular-shaped graphene, leaving the SiO$_2$ area intact. (c) SEM image of a 4×4 circle pattern array showing the high selectivity of the growth location. (d) Tilted view of an array of vertical crystals arranged in the shape of the graphene substrate. (e) A magnified view of a corner of the circle in d. (f)-(i) Tetraaniline vertical crystal arrays grown in the shapes of lines, interdigitated electrodes, letters, and suns, respectively. (j) Vertical crystals selectively

grown onto a patterned graphene FET with Ti/Au top contact electrodes. (k) SEM image showing the crystal arrays grown on the graphene strip in j.

Other patterns of vertically-oriented tetraaniline crystal arrays can also be readily created by patterning graphene into desired shapes at desired locations; for example, different sizes of micro-scaled lines, interdigitated electrodes, letters making up the words "UCLA CHEM" and "KANER LAB," suns, triangles and the entire alphabet can be made via the growth of vertical crystals (**Fig. 4.18f-i and Fig. 4.19**). Since the photolithography patterning step is carried out before the tetraaniline crystallization process, this approach is completely benign towards the intrinsic properties of conjugated materials and can lead to exciting new opportunities for patterning, miniaturization, and prevention of cross-talk in organic electronic devices.
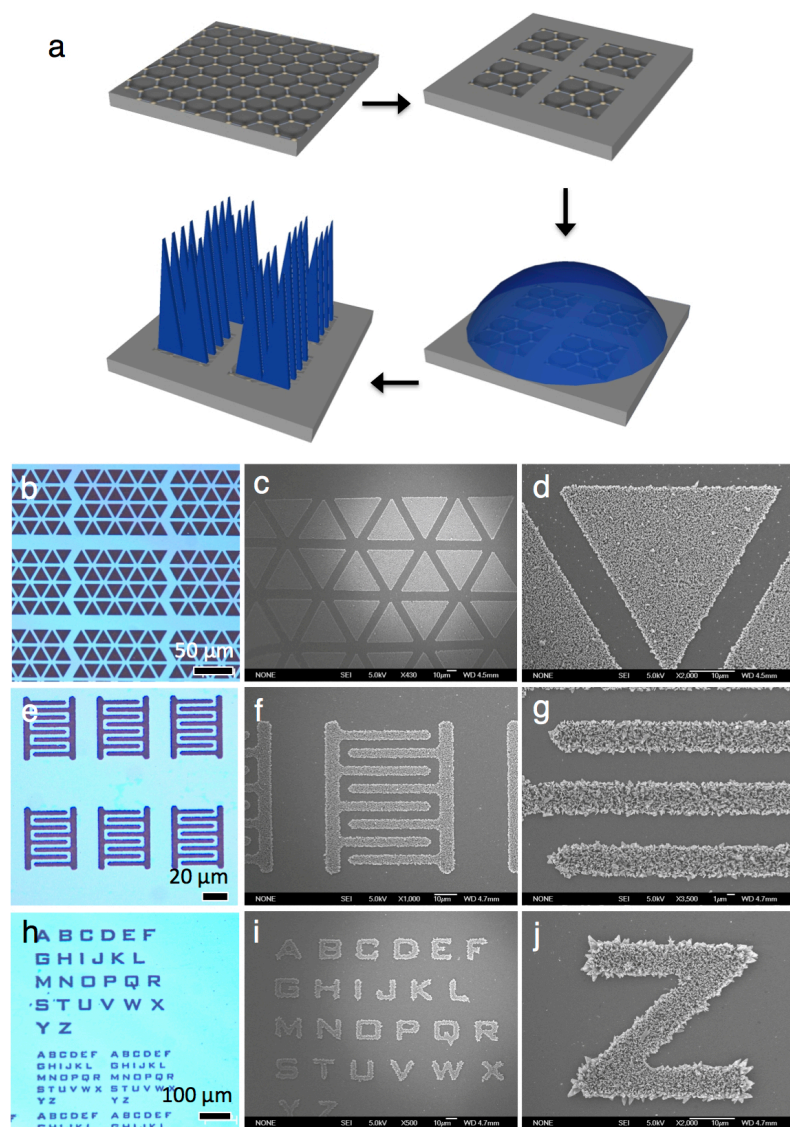
Figure 4.19. (a) Fabrication flowchart for the patterning of crystal arrays. (b-i) shows optical microscope images (b, e, h) and SEM images (c-d, f-g, i-j) of the tetraaniline vertical crystal arrays deposited into various shapes by patterning the graphene substrate using photolithography prior to the crystallization process.

4.3.8 Applicability to other conjugated materials

This graphene-assisted vertical crystallization method is also widely applicable to other solution-soluble conjugated materials. As a proof-of-concept, using the solvent-annealing method and the solvent systems demonstrated in **Fig. 4.4j** and **Table 4.1**, vertically-oriented crystal arrays of octaaniline (**Fig. 4.20a**), sexithiophene (**Fig. 4.20c**), and bis(*N*-carbozolyl) biphenyl (**Fig. 4.20e**) have been produced on graphene. The former two exhibit plate-like morphology, while the latter appears as 1-D wires. The corresponding SAED patterns for the vertical crystals dry-transferred to TEM grids are shown in **Fig. 4.20b, d,** and **f**, respectively. The interfacial stacking distances for these three crystals are 0.38, 0.39, and 0.37 nm, respectively, and all oriented along their crystal long-axis. The octaaniline plates appear to have preferential orientational packing, as indicated by the arc-pattern in SAED, rather than single crystalline as in the case for tetraaniline. This suggests that the higher molecular weight of octaaniline renders the molecular chains more flexible in conformations, thus allowing them to be packed in a preferred orientation, but with some molecular misorientations, leading to the arc-SAED pattern along the long axis of the plate. In contrast, sharp Bragg spots are obtained for both sexithiophene and bis(*N*-carbozolyl) biphenyl crystals under SAED analysis, demonstrating their single-crystalline nature. Therefore, graphene-assisted crystallization can be a general approach for obtaining vertically-oriented arrays of a wide variety of soluble conjugated materials. With graphene also conveniently serving as a bottom electrode, this method can create exciting new opportunities and potentially lead to technological advances for applications that benefit from ordered 3-D structures such as organic solar cells, sensors, batteries and supercapacitors.
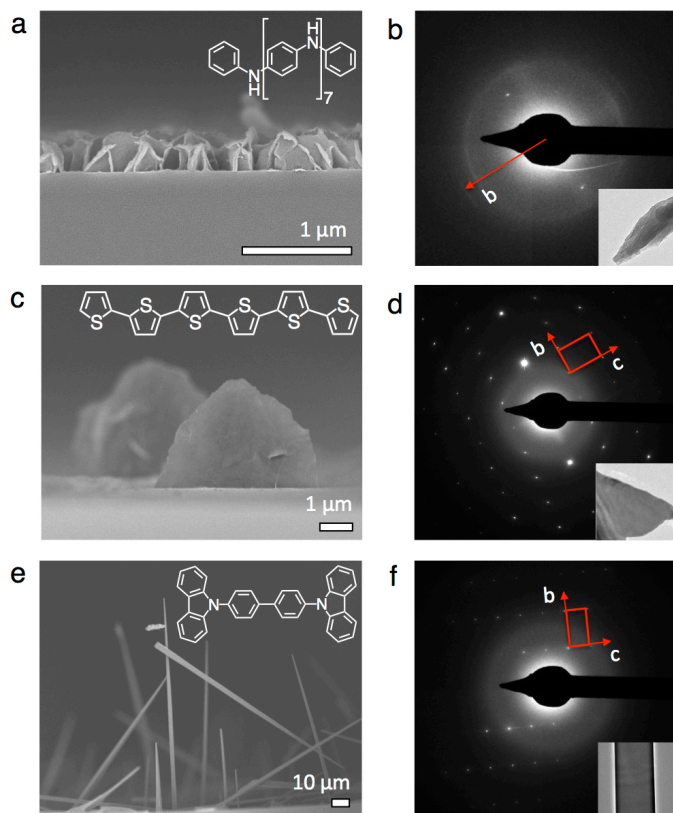
Figure 4.20. Vertical crystallization of other soluble conjugated compounds on graphene. (a) Vertically oriented octaaniline plates. (b) SAED pattern of a single octaaniline plate showing the preferred packing orientation. (c) Sexithiophene vertical plates. The density of the plates is low because of the poor solubility of sexithiophene in virtually all solvents. (d) Spot pattern from the SAED of a sexithiophene plate illustrates it is a single crystal. (e) Vertical wires of bis(*N*-carbozolyl) biphenyl. (f) The corresponding SAED pattern shows that each wire is a single crystal.

4.4 References

(1)   Fan, Z. Y.; Razavi, H.; Do, J. W.; Moriwaki, A.; Ergen, O.; Chueh, Y. L.; Leu, P. W.; Ho, J. C.; Takahashi, T.; Reichertz, L. A.; Neale, S.; Yu, K.; Wu, M.; Ager, J. W.; Javey, A. *Nat Mater* **2009**, *8*, 648.

(2)   Greene, L. E.; Law, M.; Tan, D. H.; Montano, M.; Goldberger, J.; Somorjai, G.; Yang, P. D. *Nano letters* **2005**, *5*, 1231.

(3)   Ng, H. T.; Han, J.; Yamada, T.; Nguyen, P.; Chen, Y. P.; Meyyappan, M. *Nano letters* **2004**, *4*, 1247.

(4)   Zhao, Y. S.; Wu, J. S.; Huang, J. X. *Journal of the American Chemical Society* **2009**, *131*, 3158.

(5)   Thurn-Albrecht, T.; Schotter, J.; Kastle, C. A.; Emley, N.; Shibauchi, T.; Krusin-Elbaum, L.; Guarini, K.; Black, C. T.; Tuominen, M. T.; Russell, T. P. *Science* **2000**, *290*, 2126.

(6)   Hu, J. C.; Clark, K. W.; Hayakawa, R.; Li, A. P.; Wakayama, Y. *Langmuir : the ACS journal of surfaces and colloids* **2013**, *29*, 7266.

(7)   Singh, V.; Bougher, T. L.; Weathers, A.; Cai, Y.; Bi, K.; Pettes, M. T.; McMenamin, S. A.; Lv, W.; Resler, D. P.; Gattuso, T. R.; Altman, D. H.; Sandhage, K. H.; Shi, L.; Henry, A.; Cola, B. A. *Nat Nanotechnol* **2014**.

(8)   Salleo, A. *Materials Today* **2007**, *10*, 38.

(9)   Wang, C. L.; Dong, H. L.; Hu, W. P.; Liu, Y. Q.; Zhu, D. B. *Chemical Reviews* **2012**, *112*, 2208.

(10)   Sondergaard, R.; Hosel, M.; Angmo, D.; Larsen-Olsen, T. T.; Krebs, F. C. *Materials Today* **2012**, *15*, 36.

(11)   Lim, J. A.; Liu, F.; Ferdous, S.; Muthukumar, M.; Briseno, A. L. *Materials Today* **2010**, *13*, 14.

(12)   Minemawari, H.; Yamada, T.; Matsui, H.; Tsutsumi, J.; Haas, S.; Chiba, R.; Kumai, R.; Hasegawa, T. *Nature* **2011**, *475*, 364.

(13)   Diao, Y.; Tee, B. C. K.; Giri, G.; Xu, J.; Kim, D. H.; Becerril, H. A.; Stoltenberg, R. M.; Lee, T. H.; Xue, G.; Mannsfeld, S. C. B.; Bao, Z. N. *Nat Mater* **2013**, *12*, 665.

(14)   Huang, Y.; Duan, X. F.; Wei, Q. Q.; Lieber, C. M. *Science* **2001**, *291*, 630.

(15)   Liu, S.; Wang, W. M.; Briseno, A. L.; Mannsfeld, S. C. B.; Bao, Z. *Advanced Materials* **2009**, *21*, 1217.

(16)   Robinson, J. T.; Jorgolli, M.; Shalek, A. K.; Yoon, M. H.; Gertner, R. S.; Park, H. *Nat Nanotechnol* **2012**, *7*, 180.

(17)   Xu, S.; Qin, Y.; Xu, C.; Wei, Y. G.; Yang, R. S.; Wang, Z. L. *Nat Nanotechnol* **2010**, *5*, 366.

(18)   Tomioka, K.; Yoshimura, M.; Fukui, T. *Nature* **2012**, *488*, 189.

(19)   Miller, J. R.; Outlaw, R. A.; Holloway, B. C. *Science* **2010**, *329*, 1637.

(20)   Wang, Y.; Liu, J. L.; Tran, H. D.; Mecklenburg, M.; Guan, X. N.; Stieg, A. Z.; Regan, B. C.; Martin, D. C.; Kaner, R. B. *Journal of the American Chemical Society* **2012**, *134*, 9251.

(21)   Wang, Y.; Tran, H. D.; Liao, L.; Duan, X. F.; Kaner, R. B. *Journal of the American Chemical Society* **2010**, *132*, 10365.

(22)   Li, D.; Huang, J. X.; Kaner, R. B. *Accounts Chem Res* **2009**, *42*, 135.

(23)   Li, X. S.; Cai, W. W.; An, J. H.; Kim, S.; Nah, J.; Yang, D. X.; Piner, R.; Velamakanni, A.; Jung, I.; Tutuc, E.; Banerjee, S. K.; Colombo, L.; Ruoff, R. S. *Science* **2009**, *324*, 1312.

(24)   Novoselov, K. S.; Geim, A. K.; Morozov, S. V.; Jiang, D.; Zhang, Y.; Dubonos, S. V.; Grigorieva, I. V.; Firsov, A. A. *Science* **2004**, *306*, 666.

(25)   Tung, V. C.; Allen, M. J.; Yang, Y.; Kaner, R. B. *Nat Nanotechnol* **2009**, *4*, 25.

(26)   Strong, V.; Dubin, S.; El-Kady, M. F.; Lech, A.; Wang, Y.; Weiller, B. H.; Kaner, R. B. *Acs Nano* **2012**, *6*, 1395.

(27)   Novoselov, K. S.; Fal'ko, V. I.; Colombo, L.; Gellert, P. R.; Schwab, M. G.; Kim, K. *Nature* **2012**, *490*, 192.

(28)   Xiao, K.; Deng, W.; Keum, J. K.; Yoon, M.; Vlassiouk, I. V.; Clark, K. W.; Li, A. P.; Kravchenko, I. I.; Gu, G.; Payzant, E. A.; Sumpter, B. G.; Smith, S. C.; Browning, J. F.; Geohegan, D. B. *Journal of the American Chemical Society* **2013**, *135*, 3680.

(29)   Wang, Q. H.; Hersam, M. C. *Nat Chem* **2009**, *1*, 206.

(30)   Smallwood, I. M. *Handbook of Organic Solvent Properties*; Elsevier: New York, 1996.

(31)   Li, Z. T.; Wang, Y. J.; Kozbial, A.; Shenoy, G.; Zhou, F.; McGinley, R.; Ireland, P.; Morganstein, B.; Kunkel, A.; Surwade, S. P.; Li, L.; Liu, H. T. *Nat Mater* **2013**, *12*, 925.

(32)   Vekilov, P. G. *Crystal Growth & Design* **2010**, *10*, 5007.

(33)   Ma, Z. Y.; Geng, Y. H.; Yan, D. H. *Polymer* **2007**, *48*, 31.

(34)   Xiao, X. L.; Hu, Z. J.; Wang, Z. B.; He, T. B. *J Phys Chem B* **2009**, *113*, 14604.

(35)   Kim, D. H.; Han, J. T.; Park, Y. D.; Jang, Y.; Cho, J. H.; Hwang, M.; Cho, K. *Advanced Materials* **2006**, *18*, 719.

(36)   Nardes, A. M.; Kemerink, M.; Janssen, R. A. J. *Phys Rev B* **2007**, *76*.

(37)   Sundar, V. C.; Zaumseil, J.; Podzorov, V.; Menard, E.; Willett, R. L.; Someya, T.; Gershenson, M. E.; Rogers, J. A. *Science* **2004**, *303*, 1644.

(38)   Mayer, A.; Scully, S.; Hardin, B.; Rowell, M.; McGehee, M. *Materials Today* **2007**, *10*, 28.

(39)   Cui, L. F.; Ruffo, R.; Chan, C. K.; Peng, H. L.; Cui, Y. *Nano letters* **2009**, *9*, 491.

(40)   MacDiarmid, A. G.; Zhou, Y.; Feng, J. *Synthetic Met* **1999**, *100*, 131.

(41)   Briseno, A. L.; Mannsfeld, S. C.; Ling, M. M.; Liu, S.; Tseng, R. J.; Reese, C.; Roberts, M. E.; Yang, Y.; Wudl, F.; Bao, Z. *Nature* **2006**, *444*, 913.

(42)   De Vusser, S.; Steudel, S.; Myny, K.; Genoe, J.; Heremans, P. *Applied Physics Letters* **2006**, *88*.

(43)   Menard, E.; Meitl, M. A.; Sun, Y. G.; Park, J. U.; Shir, D. J. L.; Nam, Y. S.; Jeon, S.; Rogers, J. A. *Chemical Reviews* **2007**, *107*, 1117.

(44)   Chen, S. S.; Ji, H. X.; Chou, H.; Li, Q. Y.; Li, H. Y.; Suk, J. W.; Piner, R.; Liao, L.; Cai, W. W.; Ruoff, R. S. *Advanced Materials* **2013**, *25*, 2062.

(45)   Li, X. S.; Zhu, Y. W.; Cai, W. W.; Borysiak, M.; Han, B. Y.; Chen, D.; Piner, R. D.; Colombo, L.; Ruoff, R. S. *Nano letters* **2009**, *9*, 4359.

Chapter 5. Processable Colloidal Dispersions of Polyaniline-Based Copolymers for Transparent Electrodes

Copolymerization of aniline with substituted anilines can synergistically combine high electrical conductivity with good solubility and functionality. Here, we report the synthesis of a variety of polyaniline-based copolymer nanofibers with uniform diameters. The relationship between the feed ratio and the final composition is examined by NMR and UV-vis spectra. The conductivity of the copolymers can be tuned over a six order-of-magnitude range by varying the composition of the two building blocks. The copolymer nanofibers exhibit excellent colloidal stability with zeta-potential values as high as 40 mV, which enables them to be spray-coated to form transparent, conductive thin films with good optical properties. This simple process is scalable, and can lead to flexible or patterned films, which may be helpful for applications in organic electronics, optoelectronics, sensors, and energy storage devices.

5.1 Introduction

In recent years one-dimensional (1-D) polymeric nanostructures have attracted a great deal of attention due to their promising potential for many commercial applications such as low-cost, flexible electronic and optoelectronic devices.[1] Among the family of conducting polymers, polyaniline is of great interest due to its simple acid-base doping-dedoping chemistry, ease of synthesis, and environmental stability.[2-4] A variety of methods have been developed to synthesize 1-D polyaniline nanofibers, including the use of hard templates such as anodized

aluminum oxide or diblock copolymers,[5,6] soft templates such as surfactants of bulky dopant acids,[7,8] biomolecule templated nanofibers,[9] nanowire seeding,[10] and more recently, a number of template-free approaches including interfacial polymerization,[11] rapid mixing of reactants,[12] dilute polymerization,[13] electrochemical polymerization on conducting substrates,[14] and sonochemical[15] and radiolytic-assisted syntheses[16]. The resulting nanofibers have enabled improved performances for many applications including chemical sensors, supercapacitors, memory devices, and actuators.[3,17,18]

Despite all the research advances, polyaniline still suffers from drawbacks such as low solubility and poor processability in common solvents. On the other hand, its derivatives with various functional groups possess many enhanced properties such as better dispersability or solubility in organic solvents, higher resistance against microbial and chemical degradation, improved selectivity towards chemical sensing targets, and even as candidates for charge dissipaters for e-beam lithography.[19-21] Nanofibers of substituted polyaniline have been produced and shown promise as chemical sensors.[22] Unfortunately, polyaniline derivatives generally possess much lower conductivities than polyaniline. For instance, poly(o-toluidine) in its doped form has a conductivity of 0.01-0.1 S/cm, in contrast to the 1-10 S/cm conductivity that doped polyaniline typically exhibits.[23] Therefore, copolymerization is highly desirable with the idea of synergistically combining the benefits of both components. Here, we report a synthetic route to nanofibers of a large variety of copolymers of polyaniline and substituted polyanilines in an effort to create a highly conductive polymer with good solubility, processability, multi-functionality, and many attractive properties associated with 1-D nanostructures. The optical and electrical properties of these copolymers can be readily tuned by varying the relative composition of the component monomers. Furthermore, the nanofibrillar morphology enables

the copolymers to exhibit excellent colloidal stability. A dispersion of a copolymer solution can be readily spray-coated onto a variety of materials, including flexible substrates to create conductive, transparent thin films, or patterned into different shapes by spray coating through a stencil mask.

5.2 Experimental

5.2.1 Synthesis and Purification

All chemicals were obtained from Sigma-Aldrich and used as received. In a typical reaction, an aniline derivative was dissolved in 10 mL of 1 M $HCl_{(aq.)}$ along with aniline at different relative ratios. The combined amount of the monomers was kept at 3.2 mmol. 2-4 mg of *N*-phenyl-*p*-phenylenediamine (aniline dimer) was dissolved in 0.5 mL of methanol and added to the monomer solution. Alternatively, *p*-phenylenediamine (aniline diamine) can also be used as an initiator and yields similar results. 0.8 mmol of ammonium peroxydisulfate was dissolved in a 10 mL of 1 M $HCl_{(aq.)}$ in a separate container. The two solutions were then rapidly mixed and vigorously shaken for ~5 s to promote mixing, and left undisturbed for 1 day. The crude product was dialyzed against deionized water using dialysis tubing with a 12,000-14,000 MW cutoff (Fisher Scientific) to remove any reaction byproducts and low molecular weight impurities.

5.2.2 NMR

The purified copolymer nanofibers were dedoped by dialyzing against 0.1 M $NH_4OH_{(aq.)}$ and then deionized water. The dedoped dispersions were centrifuged at 3,500 rpm to remove most of the solvent, and the products were dried in a 60 °C vacuum oven. The dried nanofibers were dissolved in deuterated dimethyl sulfoxide (DMSO-d_6) and filtered through quartz wool to remove the solid debris. NMR spectra were collected on a Bruker ARX400 spectrometer.

5.2.3 Microscopy

Samples for scanning electron microscope (SEM) and transmission electron microscope (TEM) imaging were prepared by drop-casting doped copolymer nanofiber dispersions onto silicon wafers or TEM grids with carbon supports, respectively. SEM images were collected on a JEOL JSM-6700-F field emission SEM microscope. TEM analyses were performed on a Gatan Tecnai TF20 TEM operated at 200 keV.

5.2.4 UV-vis spectroscopy

The nanofiber aqueous dispersions were further diluted for UV-vis absorption measurements on an HP 8452 spectrometer. UV-vis spectra of the spray-coated thin films were collected on a Shimazu UV-3101 PC UV-vis-NIR Scanning Spectrophotometer.

5.2.5 Zeta potential measurements

400 µL of a purified copolymer dispersion was diluted to 40 mL with 0.01 M $HCl_{(aq.)}$ solution to obtain a final pH of 2. The pH of the dispersion was varied by the addition of 1 M $NaOH_{(aq.)}$ solution. The zeta-potentials of the dispersions were measured in disposable folded capillary cells (DTS10601) with a Malvern Nano-ZS ZEN-3600 Zetasizer in Zeta mode.

5.2.6 Conductivity measurements

The copolymer nanofiber dispersions were drop-cast onto glass substrates and air-dried. Silver electrodes, 3 mm apart, were deposited on the resulting films. The device geometry is shown in Figure 5a. The current-voltage (I-V) curves were collected on a standard probe station. The film thicknesses were measured with a Dektak 6 Surface Profile Measuring System. Conductivity values were calculated from the slope of the I-V curves and the thickness of the corresponding films.

5.2.7 Spray-coating experiments

Copolymer nanofiber solutions of various concentrations were sprayed from an Image® Dual Action airbrush onto a heated substrate. The resulting film was subsequently annealed at 100 °C for 20 seconds. Patterned films were created by spray-coating through a stencil mask.

5.3 Results and Discussion

5.3.1 Synthesis of copolymer nanofibers

A large number of substituted anilines have been polymerized with aniline to form copolymer nanofibers by rapidly mixing the reactants in the presence of an initiator. In a typical reaction, upon the addition of the oxidant solution to the solution containing the initiator and an equivalent molar amount of the two monomers, the reaction mixture turns from clear to light blue/violet within a few seconds, indicating the formation of the pernigraniline oxidation state. The mixture gets darker in color quickly as the reaction progresses and eventually becomes deep green when collected after one day, a color characteristic of the conducting emeraldine salt oxidation state. In contrast, control reactions carried out under identical conditions, but without an initiator, progress at a much slower rate, often taking hours before a noticeable color change can be observed and as long as days before solid precipitation occurs. SEM analyses reveal a drastic difference between the morphologies of the copolymers produced with and without an initiator. Copolymers synthesized in the absence of an initiator are generally granular in morphology. **Figure 5.1a** and **5.2a** show typical SEM and TEM images of these products, respectively. In contrast, mats of continuous nanofiber networks become the dominant morphology once an initiator is used (**Fig. 5.1b-f** and **Fig. 5.2b-f**). Copolymer nanofibers have been obtained at a 50/50% aniline/aniline derivative feed ratio for copolymers containing both strongly electron donating substitutes such as poly(aniline-co-*o*-anisidine) and poly(aniline-co-2-(methylthio)aniline), and strongly electron withdrawing substituents including poly(aniline-co-2-fluoroaniline), poly(aniline-co-3-fluoroaniline), poly(aniline-co-4-fluoroaniline), poly(aniline-co-3,4-difluoroaniline), poly(aniline-co-2-chloroaniline), and poly(aniline-co-3-chloroaniline).

Alkyl substituents including poly(aniline-co-*o*-toluidine), poly(aniline-co-*m*-toluidine), and alkylated amine groups such as poly(aniline-co-*N*-ethylaniline) have also been synthesized by this method. **Figures 5.1b-f** and **5.2b-f** illustrate the morphology of five representative copolymers with their structures shown in the upper right corner. Some spheres are observed in poly(aniline-co-*o*-anisidine) shown in **Fig. 5.1e** and **5.2e**, but nanofibers are still the predominant morphology. The average diameters for these nanofibers range from ~50 nm to 300 nm and lengths vary from ~300 nm to 2 µm depending on the aniline derivative incorporated.
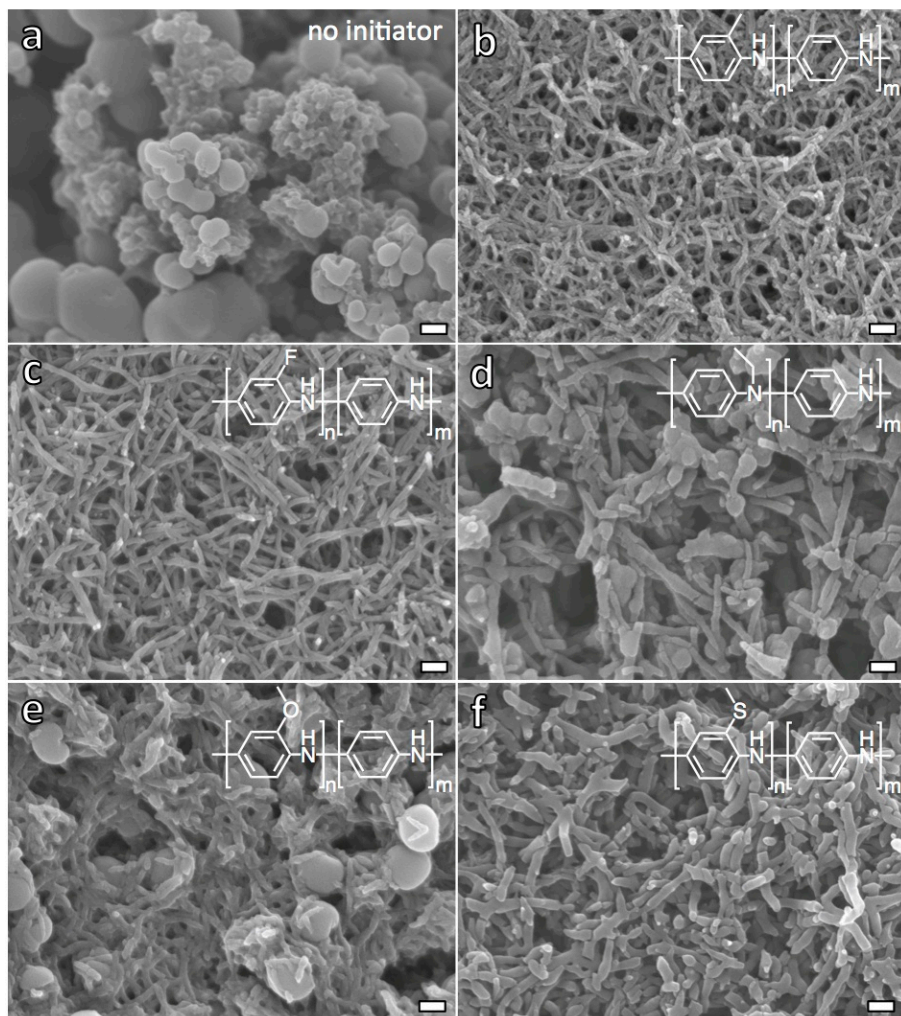
Figure 5.1. Scanning electron microscope (SEM) images of (a) a typical morphology for copolymers of aniline and substituted aniline polymerized without the addition of an initiator. When an initiator is used, nanofibrous morphologies can be obtained for (b) poly(aniline-co-*o*-toluidine), (c) poly(aniline-co-*2*-fluoroaniline), (d) poly(aniline-co-*N*-ethylaniline), (e) poly(aniline-co-*o*-anisidine), and (f) poly(aniline-co-2-methylthioaniline). Scale bar = 100 nm.
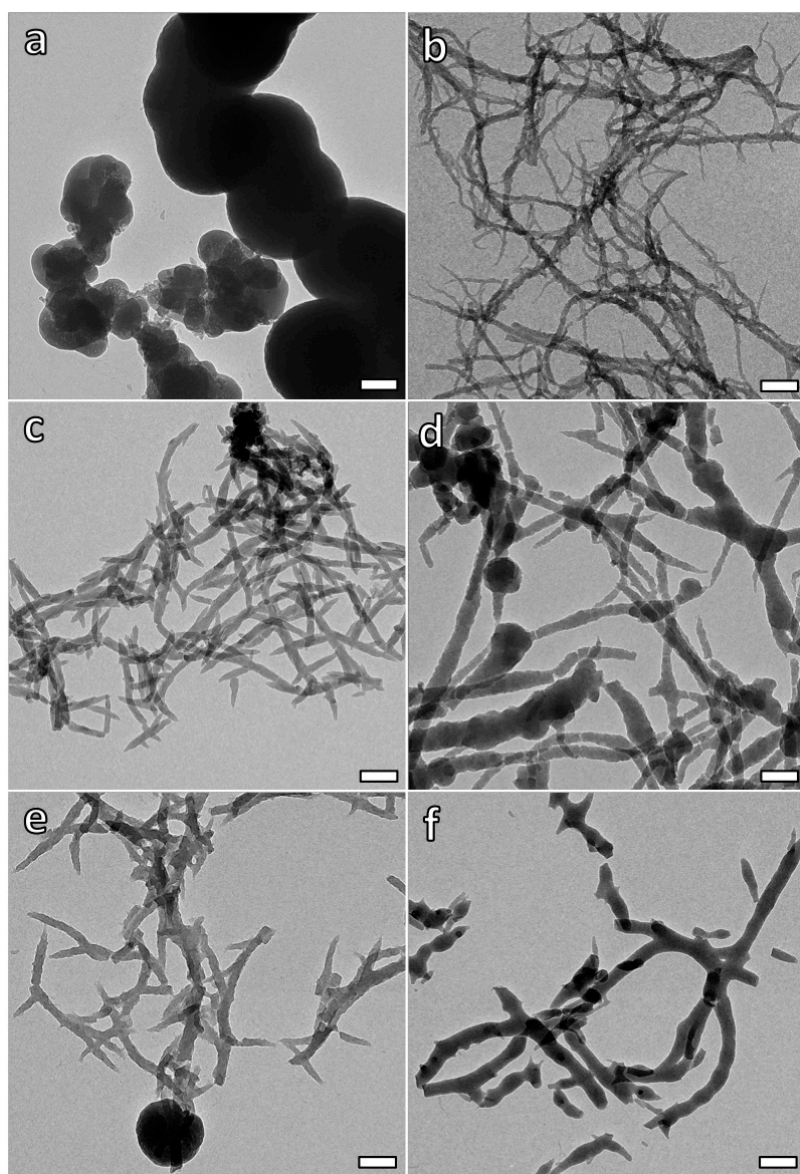
Figure 5.2. Transmission electron microscope (TEM) images of (a) copolymer synthesized without the presence of an initiator, and nanofibers of (b) poly(aniline-co-*o*-toluidine), (c) poly(aniline-co-*2*-fluoroaniline), (d) poly(aniline-co-*N*-ethylaniline), (e) poly(aniline-co-*o*-anisidine), and (f) poly(aniline-co-2-methylthioaniline) obtained when an initiator is used. Scale bar = 200 nm.

Nanofibers have been shown to be the intrinsic morphology of polyaniline;[24] however, this is not true for substituted polyanilines possibly due to the steric and electronic effects as well as the slower reaction rate compared to polyaniline polymerization.[19,23] Hence, in a monomer mixture that contains both aniline and an aniline derivative, the overall reaction rate is slowed down, which leads to agglomerated morphology for the final copolymer. We have recently demonstrated that the addition of an initiator such as aniline dimer can greatly accelerate the polymerization rate for substituted anilines and lead to nanofibrillar morphologies.[25,26] The incorporation of an initiator into the reaction mixture that contains both aniline and its derivative accelerates the overall reaction rate and serves as homogeneous nucleation sites for anisotropic growth, which is believed to be the mechanism leading to copolymer nanofiber formation.

5.3.2 Composition of copolymer nanofibers

In order to study the polymerization kinetics, we use poly(aniline-*N*-ethylaniline) synthesized at various aniline to *N*-ethylaniline ratios as an example to demonstrate the relationship between the monomer feed ratio and the actual copolymer composition.

The molecular structure of poly(aniline-co-*N*-ethylaniline) is shown as the inset in **Fig. 5.1d**. The composition of the relative ratio between the two repeat units can be calculated by the ratio of the integrated ^{1}H-NMR peak areas of the CH$_3$ methyl proton ($\delta = 1.04$ ppm) in relation to the aromatic resonance peaks at around 6.5-7.5 ppm. The actual molar composition of *N*-ethylaniline, denoted as F_1, is plotted against f_1, the feed composition of *N*-ethylaniline as shown in **Figure 5.3**. The diagonal dashed line represents equal composition of the two constituents, if identical reactivities were observed. Since all the data points are above the line, *N*-ethylaniline appears to have a higher reactivity ratio than aniline. Steric factors, resonance stabilization, and polarity of the monomers dictates the ability of a monomer to react during copolymerization.[20,27] The electron donating nature of the ethyl substituent on the amine group is likely to stabilize the cation free radical intermediates during the polymerization, thus enabling its higher reactivity. This result agrees with previous studies on other copolymer systems such as poly(aniline-co-*o*-ethylaniline) and poly(aniline-co-*N*-butylaniline).[20,28] Therefore, the addition of an initiator has a tremendous effect on the reaction rate and the product's supramolecular morphology, but not on the reactivity of the monomers. It should be noted that using *N*-ethylaniline as the sole monomer does not yield 100% *N*-ethylaniline in the final polymer composition (**Fig. 5.3**) due to the incorporation of the initiator molecule (aniline dimer) in the polymer chains. Furthermore, the reactivity ratios of the monomers are calculated to be 0.83 for aniline and 18.4 for *N*-ethylaniline from the feed composition (f_1) and the final composition (F_1) of the copolymer via the Mayo-Lewis equation.[20] The large difference in reactivity ratios indicates a block copolymer is formed with a composition drift during the polymerization process. At the early stage of the polymerization, long blocks of *N*-ethylaniline likely form with very short aniline sequences

interspersed. As the *N*-ethylaniline concentration drops, the length of the aniline sequences will steadily increase, eventually forming long aniline blocks near the end of the polymerization.
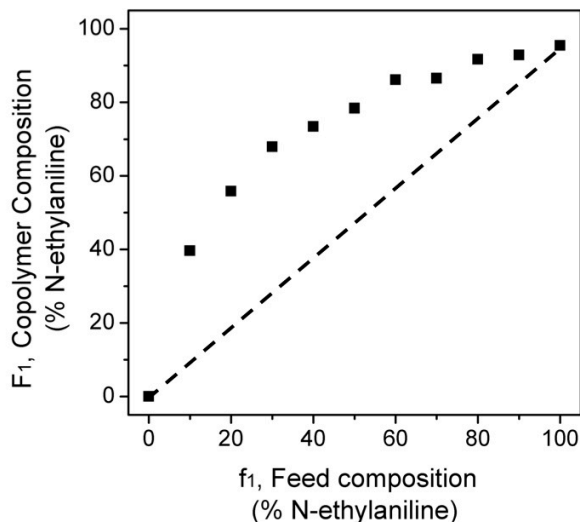
Figure 5.3. The relative compositions of poly(aniline-co-*N*-ethylaniline) produced using different feeding ratios. The copolymer composition (F_1) was determined using NMR.

5.3.3 Absorption characteristics

UV-vis spectra were collected for the doped poly(aniline-co-*N*-ethylaniline)s to study the relationship between copolymer composition and optical properties. The combined UV-vis spectra are shown in **Figure 5.4a** with the *N*-ethylaniline composition labeled in the legend. For all copolymers, three peaks are observed at around 340 nm, 440 nm, and 680 nm, corresponding to the $\pi\rightarrow\pi^*$, the polaron$\rightarrow\pi^*$, and the $\pi\rightarrow$polaron transitions, respectively.[29] The $\pi\rightarrow\pi^*$ peak appears at 360 nm for poly(*N*-ethylaniline) and gradually decreases as the aniline composition increases and approaches that of polyaniline at 333 nm. Due to the slight electron donating

170

nature of the ethyl substituent, it is likely that the HOMO level for poly(N-ethylaniline) is higher than that of polyaniline, therefore resulting in a smaller $\pi \rightarrow \pi^*$ transition energy, which corresponds to absorption at a higher wavelength. The $\pi \rightarrow \pi^*$ peak positions for the copolymers with different compositions are plotted in **Figure 5.4b**. A pseudo-linear relationship is observed, illustrating the stepwise variation in copolymer composition. A similar trend is observed when analyzing the polaron$\rightarrow \pi^*$ transition as the peak shifts from 461 nm for poly(N-ethylaniline) to 422 nm for polyaniline in a close to linear relationship with respect to the variation in composition (**Fig. 5.4c**).
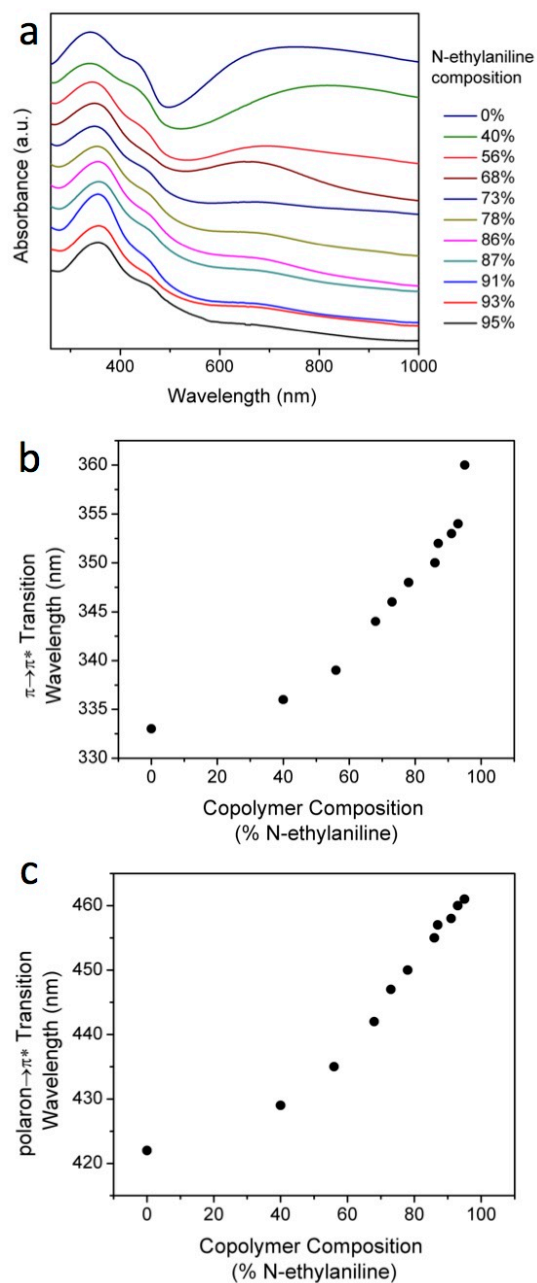
Figure 5.4. (a) UV-vis spectra indicate the change in relative composition as more poly(aniline-co-*N*-ethylaniline) is incorporated into the polyaniline copolymers, as evidenced by systematic peak shifts. (b) A plot of the $\pi \rightarrow \pi^*$ transition wavelength versus the copolymer composition. (c) Polaron$\rightarrow\pi^*$ transition wavelength plotted against the copolymer composition.

5.3.4 Electrical properties

The conductivity of polyaniline derivatives tends to be lower than that of the original polymer. We measured a conductivity for doped poly(N-ethylaniline) nanofibers of 6.0×10^{-7} S/cm, similar to a reported value of 1.3×10^{-7} S/cm.[30] Interestingly, the conductivity doubled with just 9% polyaniline incorporated in the copolymer composition, as can be seen from the log scaled plot in **Figure 5.5c** with values tabulated in **Table 5.1**. The conductivity further increased steadily with increasing polyaniline content, reaching the same order of magnitude as polyaniline nanofibers for a 40% poly(N-ethylaniline) composition. The conductivity only increased slightly from 0.13 to 0.59 S/cm as the poly(N-ethylaniline) copolymer building block was decreased from 40% to 0%, which suggests that the percolation threshold is reached around a polyaniline composition of 60%. Therefore, the conductivity of the copolymer can be readily tuned over six orders of magnitude simply by varying its composition.
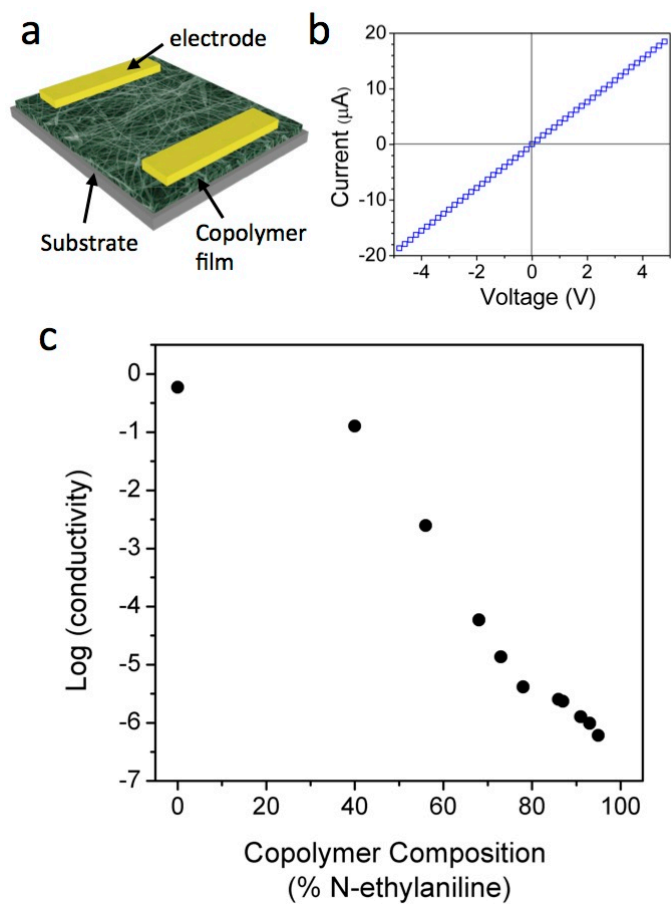
Figure 5.5. (a) A schematic diagram showing the device geometry for conductivity measurements of a drop-cast copolymer film. (b) A typical I-V curve indicating ohmic contacts. (c) The conductivity values of the copolymer films vary over six orders of magnitude as a function of the copolymer composition.

Table 5.1. Conductivity Values for Poly(aniline-co-*N*-ethylaniline) Nanofiber Films Used to Plot Figure 5c in the Main Text

ethylaniline composition in copolymer	Conductivity (S/cm)	log (conductivity)
95%	6.03×10^{-7}	-6.22
93%	9.08×10^{-7}	-6.01
91%	1.27×10^{-7}	-5.90
87%	2.34×10^{-7}	-5.63
86%	2.54×10^{-7}	-5.60
78%	4.13×10^{-7}	-5.38
73%	1.37×10^{-7}	-4.86
68%	5.88×10^{-7}	-4.23
56%	2.47×10^{-7}	-2.61
40%	1.27×10^{-7}	-0.90
0%	5.89×10^{-7}	-0.23

5.3.5 Colloidal stability

Polyaniline nanofibers can form a lyophobic colloidal dispersion under low pH aqueous conditions because of the electrostatic repulsion from the positively charged polymer

backbone.[31] Such properties are desirable for device fabrication because smooth, uniform films can be readily obtained via simple techniques such as drop-casting. Here, we employ zeta potential measurements to assess the surface charges of the copolymer nanofibers in order to acquire a semi-quantitative understanding of the copolymer nanofiber stability.

All zeta potential measurements were carried out incrementally from pH 2 to 12 in order to minimize the formation of salt and electric double layer compression in strongly acidic environments (i.e. below pH 2). When in an acidic environment, polyaniline and substituted polyanilines are in their doped forms where the backbone carries positive charge, leading to positive zeta potential values. The polymers get de-doped under basic conditions and will then exhibit negative zeta potential values. A stronger electrostatic repulsion is indicated by a higher absolute value of the zeta potential, which suggests a more stable colloidal system that is more resilient to particle aggregation and precipitation. For polyaniline, a maximum zeta potential value of 40.9 mV is reached at pH = 2. The zeta potential decreases slowly as the pH is increased to ~6.4, but remains above 30 mV, a value above which colloids are considered to be stable (**Fig. 5.6a**). Dedoping of polyaniline occurs around this pH and the zeta potential values start to drop more significantly, as indicated by the steeper slope. Polyaniline is neutral in charge when the isoelectric point (IEP) is reached at a pH of ~8.2, where the zeta potential becomes 0 mV, indicating that the electrostatic repulsions between particles is negligible, thus increasing the tendency towards aggregation into larger particles. The zeta potential value continues to decrease as the pH is further lowered until it reaches a maximum negative value of -41.6 mV at pH = 12. This very large negative value suggests that the dedoped nanofibers can form stable colloids under very basic conditions. The zeta potential vs. pH plot for poly(*N*-ethylaniline) nanofibers is shown in **Fig. 5.6a**. A peak zeta potential value of 38.1 mV is reached at pH = 2,

lower than that of polyaniline at the same pH, and the zeta potential remains above 30 mV until the pH is increased to ~4.5, indicating poly(*N*-ethylaniline) nanofibers have a narrower colloidal stability pH range. This is possibly due to the fact that the ethyl substituents on the amine and imine nitrogens shield some of the positive charges on the polymer backbone. However, the IEP is reached at a higher pH value of 9.1 for the poly(*N*-ethylaniline) nanofibers compared to that of polyaniline. The weakly electron donating effect of the ethyl group on the nitrogen leads poly(*N*-ethylaniline) to have a higher pK_a value than the parent polymer. Therefore, the positive charges on its backbone do not get completely neutralized until a more basic pH is reached.

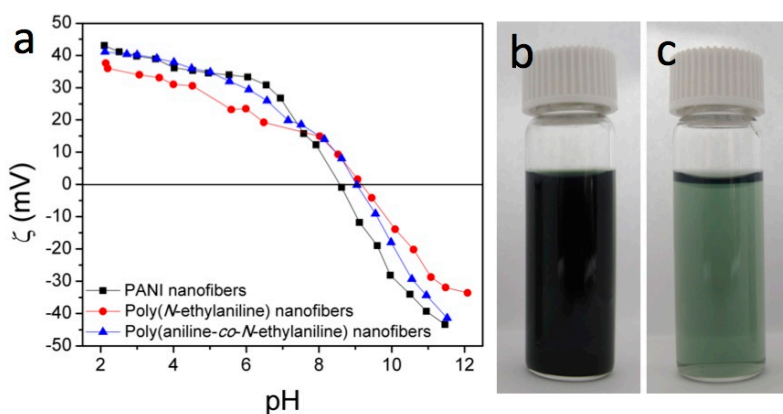**Figure 5.6**. (a) Zeta-potential measurements of polyaniline, poly(*N*-ethylaniline), and poly(aniline-co-*N*-ethylaniline) nanofibers in the pH range of 2-12. (b) A picture showing a concentrated aqueous dispersion of poly(aniline-co-*N*-ethylaniline) nanofibers. (c) A picture of a diluted solution of (b) exhibits a uniform light green color characteristic of polyaniline and substituted polyanilines.

To study the effect of copolymerization on the colloidal stability, the copolymer with a 20% N-ethylaniline feed composition was chosen as it yields a final copolymer with a close to 1:1 polyaniline to poly(N-ethylaniline) composition. The zeta potential curve of the resulting copolymer nanofibers (**Fig. 5.6a**) illustrates a similar peak zeta potential to polyaniline (41.1 mV at pH = 2). The zeta potential values stay in the 30 mV and above range until pH = ~6.0, much higher than that of poly(N-ethylaniline) nanofibers (pH ~4.5), and approaching polyaniline nanofibers (at pH ~6.4). This trend clearly demonstrates the significance of copolymerization as at a composition of approximately equal parent polymer to polyaniline derivative, the colloid is stable over a much wider pH range. Furthermore, the IEP of the copolymer occurs at pH = 9.0, close to that of poly(N-ethylaniline) and much higher than polyaniline. Due to the higher pK_a of the copolymer (compared to the parent polymer) as a result of the induction effect from the N-ethyl substituent, poly(aniline-co-N-ethylaniline) becomes dedoped at a higher pH, resulting in a higher IEP. Hence, copolymerization of aniline and N-ethylaniline synergistically leads to improved colloidal stability relative to poly(N-ethylaniline) nanofibers and at the same time, the colloid is stable under a wider range of pH relative to polyaniline nanofibers.

The enhanced colloidal stability can be observed visually. Photographs of a poly(aniline-co-N-ethylaniline) nanofiber dispersion at pH = 3.0 are shown in **Fig. 5.6b** and **c**. A uniform dark green color can be observed throughout the dispersion in **Fig. 5.6b**. Fig. 6c shows that a further diluted dispersion at the same pH displays a transparent green color. Both dispersions are stable under ambient conditions for over a week, and can be readily re-dispersed when the nanofibers begin to precipitate.

178

5.3.6 Thin-film deposition

The good colloidal stability of the copolymer nanofiber dispersions opens opportunities for low-cost, facile thin film deposition, which is important for the fabrication of processable electronic devices.[32] For instance, transparent thin films of poly(aniline-co-*N*-ethylaniline) can be readily created by spray-coating the dispersion as shown in **Fig. 5.6b**. The process is depicted with a schematic diagram in **Fig. 5.7a**. Various film thicknesses can be obtained simply by controlling the amount of dispersion sprayed onto the substrate. With a single airbrush spray across a 2.5 × 7.5 cm glass slide, a uniform, transparent, green film forms with an overall transparency of 88% within the visible region and a maximum transparency of over 95% at ~580 nm can be obtained (film 1 in **Fig. 5.7b**). Films 2-4 in **Fig. 5.7b** show incrementally lower transparencies (**Fig. 5.7c**) compared to film 1 as the number of spraying cycles is increased, indicating the formation of thicker copolymer films. These thin films are electrically conductive, and the sheet resistance is lowered as the percent transmittance is decreased (**Fig. 5.7d**). A sheet resistance on the order of 10^5 Ω/sq is achieved when the film is 58% transparent, which is sufficient for applications in electrostatic dissipation, magnetic shielding, and secondary electrodes. The spray-coating process is readily scalable—a glass substrate that is 16 cm × 13.5 cm has been uniformly coated with a thin layer of copolymer nanofibers (**Fig. 5.7e**). In addition, spraying the copolymer dispersion through a stencil mask generates patterned films. For example, the copolymer nanofibers form the word "PANI" on a glass substrate by spraying through a mask containing these letters, as shown in **Fig. 5.7f**. Finally, the copolymer nanofibers can also be spray-coated onto flexible substrates such as polydimethylsiloxane (PDMS) (**Fig. 5.7g**), rendering them suitable for potential applications in flexible electronics. Such conducting,

transparent films have great implications for potential applications in flexible, all-organic electronics, optoelectronics, sensors and energy storage devices.
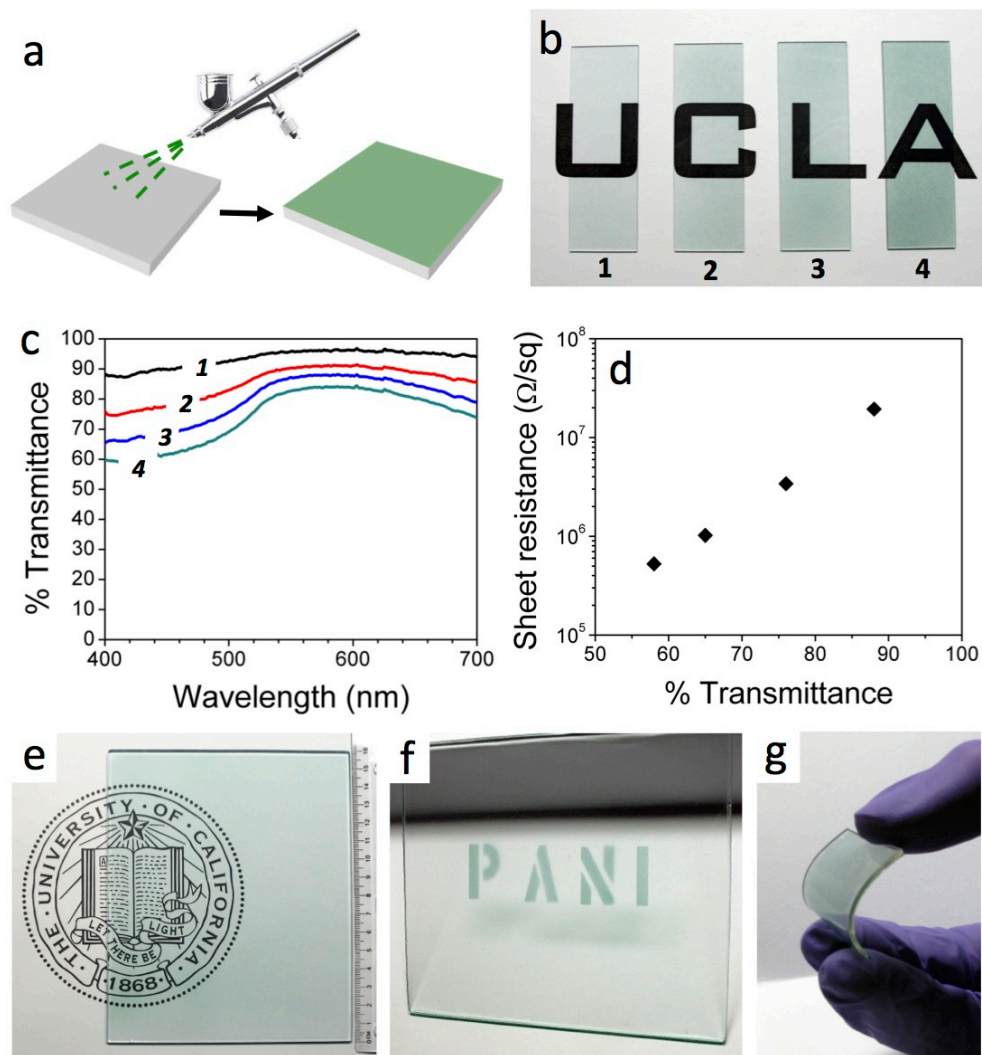
Figure 5.7. Transparent thin films obtained by spray-coating. (a) A schematic diagram depicting the spray-coating process; (b) Uniform thin film obtained by spray-coating placed over the letters "UCLA" to illustrate their transparencies; (c) UV-vis spectra show the percent transmittance of the thin films in (b); (d) Sheet resistance plotted as a function of film transmittance for the thin films in (b); (e) A uniform and transparent large area film (16 cm × 13.5 cm) spray-coated on

glass demonstrating the scalability of the process; (f) A pattern with the word "PANI" can be created by spray-coating through a stencil mask; and (g) copolymer nanofiber films sprayed onto a flexible polydimethylsiloxane (PDMS) substrate.

5.4 Conclusions

A facile synthetic method for producing uniform nanofibers of polyaniline/substituted polyaniline copolymers is reported. The relative composition of the building blocks can be readily tuned by using different feed ratios of the corresponding monomers. A six order of magnitude change in conductivity is observed for poly(aniline-co-*N*-ethylaniline) with different compositions. Zeta potential measurements indicate the copolymer nanofibers are highly stable as aqueous dispersions. Their high colloidal stability allows them to be readily processed into transparent conducting thin films via simple methods such as spray-coating, demonstrating great potential for applications in all-organic material devices.

5.5 References

(1)   Kim, F. S.; Ren, G. Q.; Jenekhe, S. A. *Chem. Mater.* **2011**, *23*, 682.

(2)   Tran, H. D.; Li, D.; Kaner, R. B. *Adv. Mater.* **2009**, *21*, 1487.

(3)   Zhang, D. H.; Wang, Y. Y. *Mat. Sci. Eng. B-Solid* **2006**, *134*, 9.

(4)   Tran, H. D.; D'Arcy, J. M.; Wang, Y.; Beltramo, P. J.; Strong, V. A.; Kaner, R. B. *J. Mater. Chem.* **2011**, *21*, 3534.

(5)   Wu, C. G.; Bein, T. *Science* **1994**, *264*, 1757.

(6)   Lee, J. I.; Cho, S. H.; Park, S. M.; Kim, J. K.; Kim, J. K.; Yu, J. W.; Kim, Y. C.; Russell, T. P. *Nano Lett.* **2008**, *8*, 2315.

(7)   Qiu, H. J.; Wan, M. X.; Matthews, B.; Dai, L. M. *Macromolecules* **2001**, *34*, 675.

(8)   Zhang, Z. M.; Wan, M. X.; Wei, Y. *Adv. Funct. Mater.* **2006**, *16*, 1100.

(9)   Niu, Z. W.; Bruckman, M. A.; Li, S. Q.; Lee, L. A.; Lee, B.; Pingali, S. V.; Thiyagarajan, P.; Wang, Q. *Langmuir* **2007**, *23*, 6719.

(10)   Zhang, X. Y.; Goux, W. J.; Manohar, S. K. *J. Am. Chem. Soc.* **2004**, *126*, 4502.

(11)   Huang, J. X.; Virji, S.; Weiller, B. H.; Kaner, R. B. *J. Am. Chem. Soc.* **2003**, *125*, 314.

(12)   Huang, J. X.; Kaner, R. B. *Angew. Chem. Int. Ed.* **2004**, *43*, 5817.

(13)   Chiou, N. R.; Epstein, A. J. *Adv. Mater.* **2005**, *17*, 1679.

(14)   Liang, L.; Liu, J.; Windisch, C. F.; Exarhos, G. J.; Lin, Y. H. *Angew. Chem. Int. Ed.* **2002**, *41*, 3665.

(15)   Jing, X. L.; Wang, Y. Y.; Wu, D.; Qiang, J. P. *Ultrason. Sonochem.* **2007**, *14*, 75.

(16)   Pillalamarri, S. K.; Blum, F. D.; Tokuhiro, A. T.; Story, J. G.; Bertino, M. F. *Chem. Mater.* **2005**, *17*, 227.

(17)   Chandrasekhar, P. *Conducting Polymers, Fundamentals and Applications: A Practical Approach*; Kluwer Academic Publishers: Boston, 1999.

(18)   Li, D.; Huang, J. X.; Kaner, R. B. *Acc. Chem. Res.* **2009**, *42*, 135.

(19)   Tran, H. D.; Norris, I.; D'Arcy, J. M.; Tsang, H.; Wang, Y.; Mattes, B. R.; Kaner, R. B. *Macromolecules* **2008**, *41*, 7405.

(20)   Conklin, J. A.; Huang, S. C.; Huang, S. M.; Wen, T. L.; Kaner, R. B. *Macromolecules* **1995**, *28*, 6522.

(21)   Wang, Y.; Tran, H. D.; Kaner, R. B. *J. Phys. Chem. C* **2009**, *113*, 10346.

(22)   Al-Mashata, L.; Kaner, R. B.; Tran, H. D.; Kalantar-zadeha, K.; Wlodarskia, W. *Procedia Chem.* **2009**, *1*, 220.

(23)   Wei, Y.; Hariharan, R.; Patel, S. A. *Macromolecules* **1990**, *23*, 758.

(24)   Li, D.; Kaner, R. B. *J. Am. Chem. Soc.* **2006**, *128*, 968.

(25)   Tran, H. D.; Wang, Y.; D'Arcy, J. M.; Kaner, R. B. *ACS Nano* **2008**, *2*, 1841.

(26)   Wang, Y.; Tran, H. D.; Kaner, R. B. *Macromol. Rapid Commun.* **2011**, *32*, 35.

(27)   Li, X. G.; Zhou, H. J.; Huang, M. R. *Polymer* **2005**, *46*, 1523.

(28)   Bergeron, J. Y.; Dao, L. H. *Macromolecules* **1992**, *25*, 3332.

(29)   Xia, Y. N.; Wiesinger, J. M.; Macdiarmid, A. G.; Epstein, A. J. *Chem. Mater.* **1995**, *7*, 443.

(30)   Borkar, A. D.; Gupta, M. C.; Umare, S. S. *Polym.-Plast. Technol.* **2001**, *40*, 225.

(31)   Li, D.; Kaner, R. B. *Chem. Commun.* **2005**, 3286.

(32)   D'Arcy, J. M.; Tran, H. D.; Tung, V. C.; Tucker-Schwartz, A. K.; Wong, R. P.; Yang, Y.; Kaner, R. B. *P. Natl. Acad. Sci. USA* **2010**, *107*, 19673.

Chapter 6. Three-dimensional core-shell hybrid solar cells via controlled *in situ* materials engineering

Hybrid solar cells[1,2] can potentially yield viable photovoltaic devices as they exploit both the high mobility of inorganic compounds[3] and the high absorption coefficients and the ease of processability of organic materials[4]. However, standard spin-coating/infiltration processes do not allow the properties of the polymer side to be tailored in situ[5,6,7]. Furthermore, the difficulty in achieving conformal, high-quality organic-inorganic interfaces[8-15] have hindered the realization of a three-dimensional (3-D) hybrid solar cell with satisfactory efficiency. Here, we demonstrate a simple, controllable, solution-based fabrication approach towards air-stable 3-D core-shell hybrid solar cells comprised of catalyst-free, patterned GaAs nanopillar arrays uniformly coated with electropolymerized poly(3,4-ethylenedioxythiophene) (PEDOT). Electropolymerization allows for conformal organic morphologies on the inorganic nanostructures and in situ materials engineering via dopant incorporation. Materials characteristics including the highest occupied molecular orbital (HOMO) level, the conductivity and the thickness can be adjusted, directly affecting the photovoltaic performance. Downwards tuning of the HOMO level ($|\Delta E| \sim 0.44$ eV) increases the open-circuit voltage (V_{OC}), while higher PEDOT conductivities result in enhanced short-circuit current densities (J_{SC}). A systematic device tuning results in a J_{SC} of 13.6 mA cm^{-2}, V_{OC} of 0.63 V, and peak external quantum efficiency of 58.5%, which ultimately leads to solar power conversion efficiencies as high as 4.11%.

6.1 Introduction

Organic/inorganic hybrid solar cells (HSCs) are a compelling research field as they merge the desirable features of solid-state physics and organic electronics, offering a potential solution to low-cost, efficient photovoltaics[1,2]. To date, semiconductor-based solar cells[3] have higher efficiencies due, in part, to advantageous material characteristics such as extremely high carrier mobility. Furthermore, mature materials engineering practices allow exquisite control of doping concentrations, band-offsets, and interface abruptness down to the atomic level. Polymer solar cells[4], on the other hand, are inexpensive per square foot and have large absorption coefficients for wavelengths <700 nm. However, the most commonly used polymers are unstable in air and possess inferior transport properties. Major obstacles to advancing HSC device design have been the limited control over the organic layer features along with interfacial issues. Thus, a more sophisticated approach to materials engineering of HSCs remains an open challenge.

Modern synthetic chemistry has enabled the upwards/downwards tuning of the energy levels, optical and electrical properties of the organic conductors[5,6,7] via molecular functionalization, thus providing excellent opportunities for improving the carrier transport at the organic/inorganic interfaces and external contacts. Such materials engineering applied to conjugated polymers, in fact, can alter the band-to-band realignments between organic and inorganic layers, maximizing the charge transfer and overall device efficiency. However, this concept carried out through organic synthetic techniques has not yet been exploited in hybrid photovoltaics.

Standard processing methods (including spin-coating, inkjet printing, or doctor blading[8]) do not allow in situ materials engineering, limiting the chance to tailor the energy levels on the

185

organic side and conveniently control the hybrid interface during its formation. Typically, these processing methods involve inorganic nanostructures of silicon[9], metal oxides[10,11], II-VI compound semiconductors[12,13] or III-V nanowires[14] that are intimately mixed into the polymer and deposited as hybrid thin films. Alternatively, polymer infiltration is combined with three-dimensional (3-D) inorganic arrays to form an inter-digitated, block-like HSC[15]. Unfortunately, the aforementioned approaches often result in non-conformal coatings or thickness gradients when applied to vertical 3-D structures. This coverage limitation diminishes the purpose of having well-oriented, high mobility, inorganic arrays that possess both the advantages of directional charge transport and light trapping properties. As a result, typical power conversion efficiencies (PCE) for current HSCs range from ~0.04 to 3.2%[16], demanding further improvement. Ensuring a conformal coating of well-defined 3-D inorganic semiconductor patterns, such as oriented nanopillars, with an organic conductor allows for a large surface/interface area as well as enhanced absorption from the nanostructuring, which is difficult to achieve for all-organic cells due to the current scarcity and limitations in their patterning techniques.

Here, we report an electropolymerized deposition approach for making ordered arrays of core-shell inorganic semiconductor-polymer nanopillar HSCs. In situ doping enabled by this deposition technique allows tuning of the polymer thickness, the highest occupied molecular orbital (HOMO) energy levels, and the conductivity resulting in enhanced solar cell performance.

6.2 Experimental

6.2.1 GaAs wafer patterning and nanowire growth

A 20 nm thick silicon dioxide film was evaporated onto degenerately n-doped GaAs (111)B wafers and subsequently patterned by electron-beam lithography (Vistec EBPG 5000+ES) and reactive doped ion etching (Oxford 80 Plus). The wafers were then cleaved in 1 cm x 1 cm square pieces. The nanowire growth was carried out using a metal organic chemical vapor deposition reactor (Emcore vertical-flow) with a hydrogen carrier gas at 60 torr. The n-doped GaAs nanopillars were grown for 20 mins at 740°C using tri-methyl-gallium (TMGa) and tertiary-butyl-arsine (TBA) as the primary precursors and tetra-ethyl-tin (TESn) as the dopant. The TMGa was pressurized to 900 torr, chilled to 0°C and used a hydrogen flow rate of 3 sccm. The TBA was pressurized to 700 torr, chilled to 20°C and used a hydrogen flow rate of 10 sccm. The TESn was pressurized to 900 torr, chilled to 0°C, and used a hydrogen flow rate of 0.5 sccm.

6.2.2 Electrochemistry

PEDOT electropolymerization was performed under potentiodynamic conditions with potential applied by a VersaSTAT 3-400 potentiostat/galvanostat (Princeton Applied Research). A standard one compartment, three-electrode setup was adapted using the GaAs nanopillar wafers (with Au-Ge/Ni/Au back contacts) as the working electrode, a platinum foil as the counter electrode, and a saturated calomel electrode (SCE) as the reference electrode. In brief, the GaAs nanopillar wafer pieces were thoroughly rinsed with ethanol, methanol, and isopropanol, and dried with nitrogen flow prior to electrodeposition. The three electrodes were immersed into an electrolyte solution containing 0.1 M of EDOT monomer and various

concentrations of different electrolyte salts dissolved in Milli-Pore water or HPLC-grade acetonitrile. Five electrolytes were tested: sodium poly(styrene sulfonate) (NaPSS), sodium dodecyl sulfate (SDS), lithium perchlorate ($LiClO_4$), tetrabutylammonium tetrafluorophosphate (Bu_4NBF_4), and tetrabutylammonium hexafluorophosphate (Bu_4NPF_6). NaPSS or SDS (0.008 M) was dissolved in water, while 0.1 M $LiClO_4$, Bu_4NBF_4, or Bu_4NPF_6 was dissolved in acetonitrile. The potential was scanned from 0 V to 1.5 V at a scan rate of 0.1 V/sec for the desired number of cycles. The wafer piece containing PEDOT-coated GaAs nanopillars was then removed from the electrolyte and thoroughly rinsed with acetonitrile, blown dry with nitrogen flow, and annealed at 80 °C for 15 min. Planar PEDOT films for conductivity measurement purposes were deposited on quartz slides coated with e-beam evaporated chromium/gold (20 nm/200 nm) electrodes under identical electropolymerization conditions. $LiClO_4$, Bu_4NBF_4 and Bu_4NPF_6 were chosen as the dopant anions for the final devices since they exhibit the highest electrical conductivities.

6.2.3 Device Fabrication

Subsequent to growth, the GaAs nanowire arrays were cleaned in acetone, methanol and isopropanol (IPA) for 1 minute each. All samples underwent a 90-min soaking in 22% ammonium sulfide aqueous solution (Alfa Aesar) to passivate the nanopillars and render the surfaces sulfur-terminated, thoroughly rinsed with deionized water and blown dry with nitrogen. Ohmic gold-germanium/nickel/gold (200 nm/40 nm/100 nm) back metal contacts were electron-beam evaporated onto the dies and thermally annealed at 400 °C for 30 s. Benzocyclobutene (BCB, Cyclotene Dow Chemical) was spin-coated as purchased at 3000 r.p.m. for 30 s and hard cured overnight at 250 C. BCB was then etched back using CF_4/O_2 reactive ion plasma etch

chemistry (Oxford 80 Plus) at a rate of 3.5 nm s^{-1}. PEDOT shells of desired thicknesses with various dopant anions were then directly electropolymerized onto the sulfur-terminated GaAs nanopillar surfaces. Indium tin oxide (from Kurt J. Lesker) was deposited as the transparent top electrode by RF magnetron sputtering (Denton Discovery 550) at a rate of 0.3 nm s^{-1} at room temperature, with 5 mT of deposition pressure and 30 sccm of argon gas.

6.2.4 Solar cell characterization

Current-voltage characteristics of the hybrid solar cells were measured using a source meter (Keithley 2400). AM 1.5 illumination was carried out with a 300 W xenon-lamp-based solar simulator (Newport Corporation, 67005) with an AM 1.5G filter mounted. The light intensity was calibrated using a 1-sun (1000 W m^{-2}) reference silicon photodiode. An active area of 0.25 mm^2, defined by the patterning process, was used to calculate the current density. The EQE spectrum was acquired by using a manufactured EQE setup (Newport Corporation, 74125) equipped with a 1-sun bias, monochromator, lock-in amplifier for the photocurrent acquisition, and calibrated silicon photodiode (Newport Corporation, 70356). The monochromatic illumination step was 5 nm. An objective lens with a focal length of 100 mm was used to focus down the spot size.

6.2.5 Material characterization

Conductivity measurements were carried out on the planar electropolymerized PEDOT films. The polymer thickness was measured with standard profilometry techniques (Dektak 6M profilometer). TEM grids with 200 μm × 200 μm grid sizes (Ted Pella, Inc.) were positioned as

shadowing masks for the deposition of a 200 nm film of gold as top electrodes using an e-beam evaporator. Conductivity values were extrapolated from current-voltage characteristics (Keithley 2400) combined with the thicknesses of the different polymer films. Cyclic voltammetry characterization for each of the polymers was carried out in a solution containing 0.1 M of the corresponding electrolyte salt that matches the dopant anion for each PEDOT, and scanned at a rate of 0.05 V/sec from -3.0 V to 1.5 V. X-ray photoelectron spectroscopy was utilized to obtain the elemental composition profiles of the polymers. Energy dispersive spectroscopy for elemental mapping was carried out with a Titan Scanning/Transmission Electron Microscope (S/TEM) (FEI).

6.2.6 Photogeneration profile simulation

The photogeneration figures were plotted using finite-difference time-domain (FDTD solution Lumerical). A GaAs nanowire with a diameter of 190 nm and a height of 1200nm was simulated. PEDOT was used as the shell material with 80 nm thickness. Periodic boundary conditions were set with a pitch size of 600 nm × 600 nm. A mesh size of 4 nm x 4 nm was placed throughout the pillar and the shell. Cross-polarized light was incident on top of the structure. A monitor was placed to capture both the nanowire and the shell, recording both the E-field intensity and the material refractive index. The photogeneration rate at each mesh grid was then calculated and plotted.

6.3 Results and Discussion

6.3.1 Core/shell nanowire fabrication

In brief, we fabricate periodic GaAs nanopillar arrays via a catalyst-free, bottom-up approach[17]. The GaAs nanopillars are coated with poly(3,4-ethylenedioxythiophene) (PEDOT) via electropolymerization, a low cost, selective technique that yields conformal radial shells around individual GaAs nanopillars to preserve the 3-D features of the patterned array. PEDOT, unlike the readily photo-oxidizable P3HT[18], is well known for its remarkable air stability[19,20], which is essential for a practical device. In addition, a radial core-shell geometry is desirable because it allows for a shorter pathway for photogenerated carriers[21,22,23], thereby enhancing the charge collection efficiency.

Solar cell performance is then addressed by (1) enhancing the transport properties of PEDOT controlled by using three different dopant anions incorporated during the electrodeposition to increase the J_{SC}, (2) lowering the HOMO levels of PEDOT to enhance the V_{OC}, and (3) designing a PEDOT shell that balances out the short exciton diffusion length and the required thickness for light absorption. Furthermore, theoretical simulations show that light trapping effects and enhanced absorption are present over the whole spectrum of interest due to fact that the 3D HSC morphology is preserved during all the fabrication steps.

Figures 6.1a, b illustrate the resulting device schematic and relevant energy levels in the hybrid device. As a first step, n-type GaAs nanopillars are grown on a patterned n[+]-GaAs substrate via selective area epitaxy (SAE) (**Fig. 6.2**). Selective area epitaxy (SAE) was used as a growth technique to synthesize arrays of patterned GaAs nanopillars (NP). The SAE is a catalyst-free alternative that does not introduce any contamination into the nanopillar[17,24], and

allows lithographic control of nanopillar diameter, center-to-center pitch, tiling pattern and periodicity. The growth wafers consisted of a patterned silicon dioxide dielectric mask (20 nm) on top of highly n-doped substrates. The arrays were grown in a metal organic chemical vapor deposition reactor. The growth takes place from the openings in the dielectric mask that expose the substrate to the gas environment. Both pitch (P) and diameter (D) can be separately determined during the patterning process (**Fig. 6.2a**). The technique does not require any metal catalyst (e.g. Au) to initiate the synthesis, avoiding metal contamination into the semiconductor crystal. The adatom incorporation is determined by diffusion lengths and binding energies. The doping concentrations were estimated from hall measurements on planar calibration tests. **Fig 6.1b** shows a full patterned array of NPs after growth under a Nomarski optical microscope. **Fig 6.1c** displays a typical SEM of a GaAs NP array after growth. Note the high uniformity and reproducibility in terms of aspect ratio over a large area.
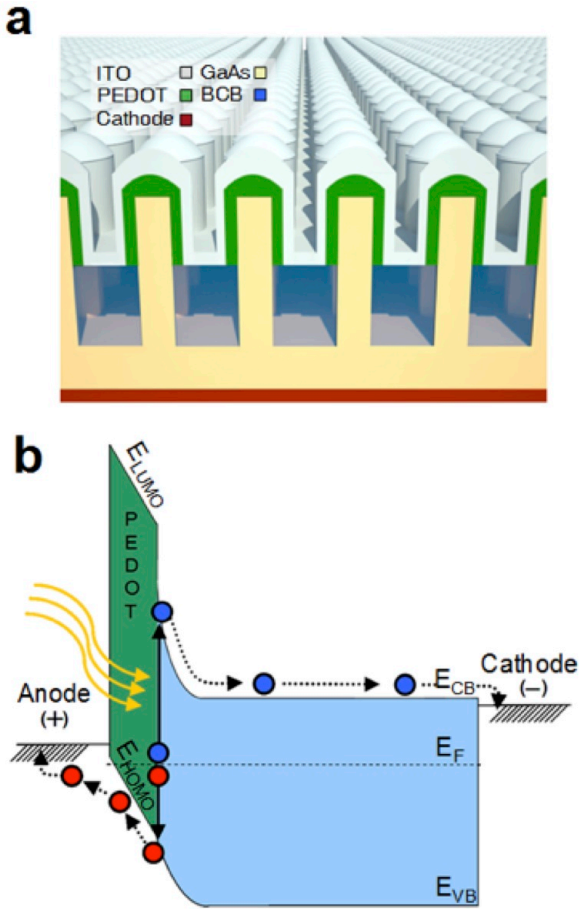
Figure 6.1. PEDOT/GaAs hybrid nanopillar solar cells. (a) Cross-sectional schematic diagram of the hybrid nanopillar solar cells as a 3D periodic array of core-shell inorganic-organic nanopillars. A GaAs nanopillar periodic array is planarized after growth with BCB and then partly dry-etched back. Subsequently, the samples underwent electro-polymerization of PEDOT by cyclic voltammetry (CV) in an EDOT monomer electrolyte solution, then ITO was RF sputtered to form the top transparent electrode. (b) Energy band diagram and alignment of the molecular orbital levels with respect to valence-conduction band edges, illustrating the independent photo-generated carrier flows.
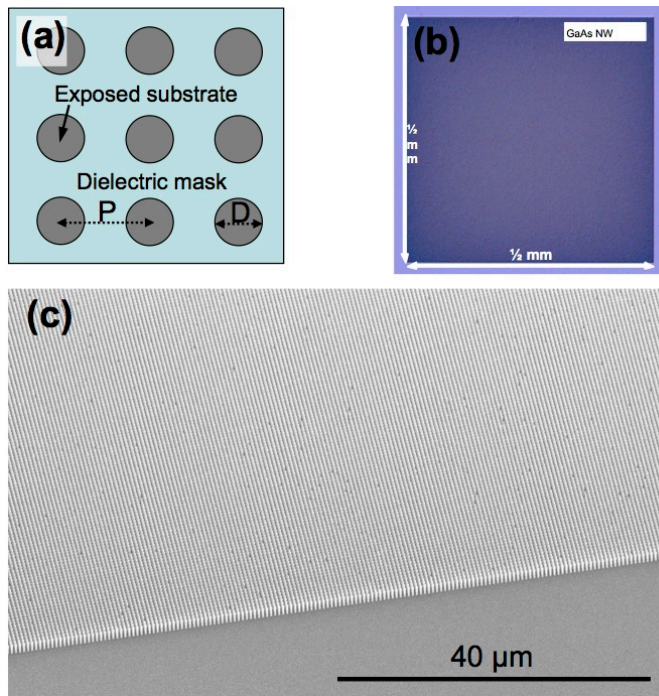
Figure 6.2. Pattern and growth of periodic GaAs NW arrays. (a) Schematic illustration of pitch (P) and diameter (D) as two degrees of freedom in the patterning process of the dielectric mask, (b) optical microscope image of a patch, (c) 45-degree tilted SEM of periodic GaAs NW arrays after MOCVD growth.

Several previous studies reported enhanced optical absorption[25,26] of nanopillar arrays in comparison with planar architectures despite the low fraction of material utilized. Theoretical calculations (Lumerical FDTD Solutions) show that a 600 nm center-to-center pitch in a square lattice arrangement yields the maximum absorption. **Fig. 6.3** a shows a contour plot of absorption with pitch size versus wavelength. Data were collected using finite difference time domain (FDTD) solver Lumerical solutions. A 200 nm diameter GaAs NP above GaAs substrate was simulated using a mesh size of 8 nm per grid point. X-polarized plane wave light source was

incident vertically above the pillar. A reflection monitor was placed above the light source, and a transmission monitor was placed 3 μm into the substrate. Absorption was then calculated as A = 1-|R|-|T|. **Fig. 6.3** exhibits the absorption trend of a 600 nm-pitch array derived from the dashed cutline in **Fig. 6.2**.
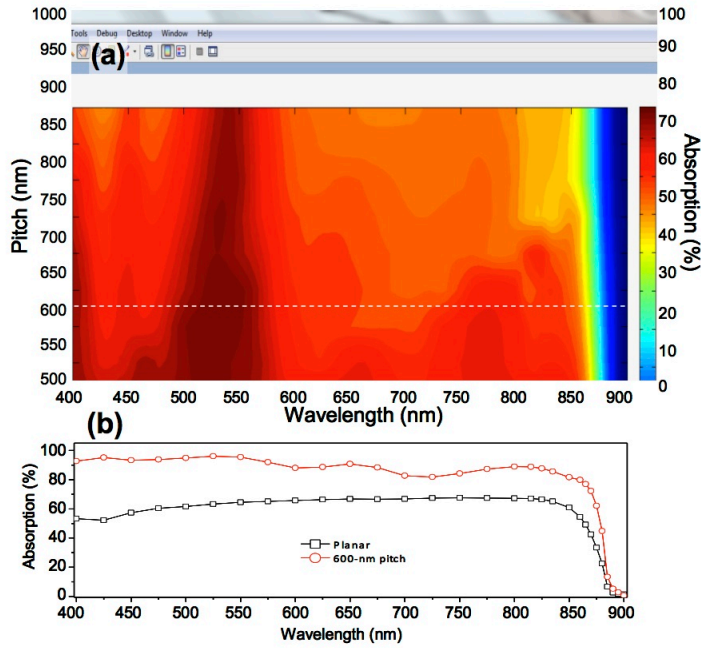

Figure 6.3. Numerical simulations of pitch-dependent absorption. (a) A 2-D contour plot of (center-to-center) pitch-dependent absorption over visible wavelengths for a GaAs NW array arranged in a square-lattice tiling. (b) Absorption comparison of a 600 nm pitch periodic NW array with respect to a planar GaAs design.

The as-grown nanopillar arrays undergo surface passivation to mitigate the recombination effects introduced by surface states on the crystal facets[24]. Ammonium sulfide is selected here as an excellent passivation agent for GaAs in which the sulfur-terminated GaAs nanopillar surfaces

interact with the sulfur on the EDOT monomer and lead to higher quality GaAs-PEDOT interfaces. Subsequently, benzocyclobutene (BCB) is spin-coated as an insulating resin onto the samples to prevent top-bottom shunting and then dry-etched back to expose only the top portion of the nanopillars (see Experimental). The patterned wafer is then immersed into an EDOT monomer solution with various electrolytes. Electropolymerization selectively grows PEDOT on the conductive GaAs while leaving the BCB layer intact, thus allowing for a highly controllable thickness and uniform radial coating. Finally, indium tin oxide (ITO) is RF sputtered as a top transparent electrode.

Figure 6.1b depicts the band diagram of the final HSC. PEDOT is a hole-injecting conducting polymer[27] and because of its positive temperature coefficient of resistivity, it manifests a metallic signature. For this reason, electrical conductivity is one of the main factors that affect the electronic transport of the photo-carriers in the organic component of the junction. Upon illumination, the incoming photons generate electron-hole pairs (bound excitons), which then diffuse to the PEDOT/GaAs interface where they dissociate. Subsequent to excitonic dissociation, free carriers (e^- and h^+) are generated on both sides of the hybrid junction and can drift to their respective electrodes to be collected. The charge diffusion process is typically limited by the short exciton diffusion length (5-30 nm)[28], so controlling the polymer thickness minimizes the distance between exciton and hybrid interface. In addition, the physical properties for the GaAs arrays such as nanopillar diameter and doping concentration are kept constant to facilitate the investigation of different energy levels/conductivities of PEDOT on the device performance.

6.3.2. Electrochemical control of organic layer properties

Controlling PEDOT thickness and coating morphology is central to HSC device performance. Thus, we evaluate the deposition kinetics of PEDOT in terms of thickness and coating morphology as a function of oxidation-reduction cycles applied to the GaAs nanopillar arrays as shown in **Fig. 6.2 a-c**. The arrays are standardized for equal center-to-center pitch (600 nm), height (~1.2 μm), and radius (190 nm). **Figure 6.2a** shows a collection of scanning electron microscope (SEM) images captured at 0, 10 and 25 scanning cycles. The thickness of the coating increases as a function of the number of cycles, as illustrated by the near linear trend shown in **Fig. 6.2b**, of 0, 20 and 55 nm, respectively. The deposition rate is pattern-dependent and related to the edge-to-edge distance among the nanopillars (**Fig. 6.4**): stronger electric fields enable larger nanopillars to pull in a greater amount of EDOT monomers and dopant anions from the electrolyte, translating into a faster deposition rate. The average deposition rate calculated for 190 nm diameter nanopillars is ~24.0 Å/cycle. Several selective area epitaxy (SAE) patterns were prepared with different radii (90 nm, 190 nm and 300 nm) to investigate the dependence of the process on the edge-to-edge distance among the nanopillars (NPs). The center-to-center pitch was kept constant at 600 nm, in a square lattice arrangement. The SEM matrix presented in **Fig. 6.4a** relates NP diameters with increasing number of CV cycles. The thicknesses of the coatings increase as a function of the number of cycles, as illustrated by the quasi-linear trends shown in **Fig. 6.4b**. Note that more cycles were necessary to coat the 90 nm NPs for a given thickness than the larger diameter ones. This is due to the fact that a higher potential is present among NPs with larger diameters, translating into faster growth rates for the polymer during the electrodeposition. The growth rates were calculated to be ~5.4 Å/cycle, ~24.0 Å/cycle, and a

much accelerated ~150 Å/cycle for the 90 nm-, 190 nm-, and 300 nm-diameter columns, respectively.
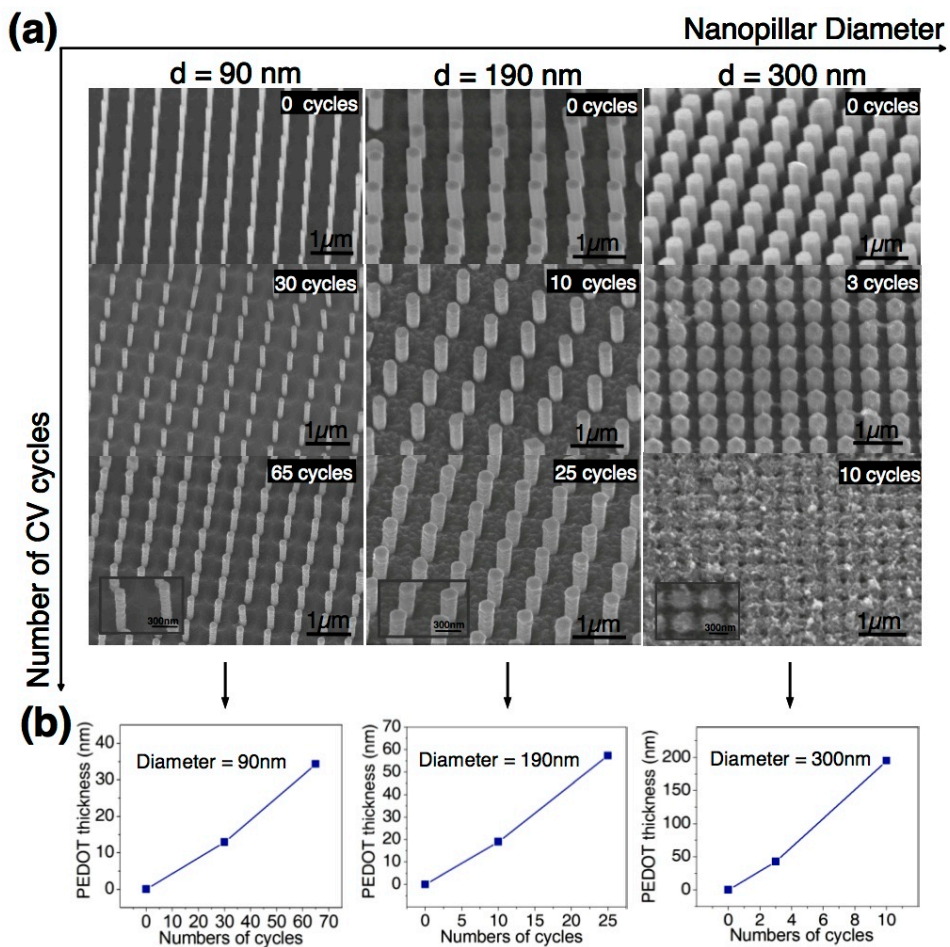

Figure 6.4. Nanoscale morphology control. (a) SEM images of different stages of the electro-deposition process with different NP diameters (90 nm, 190 nm and 300 nm) as a function of number of CV cycles (constant center-to-center pitch of 600 nm). **(b)** Quasi-linear trends of PEDOT thickness with respect to different NP diameters for increasing number of CV cycles.

The nanometer precision is a crucial degree of freedom for control of polymer thickness. **Figure 6.5c** shows a cross-sectional transmission electron microscope (TEM) image of hybrid nanopillars prepared by means of focused ion beam milling. The image confirms the high selectivity and uniformity of the organic coating (80 nm) of the exposed body of the GaAs nanopillars. Energy dispersive spectroscopy (EDS) is used to estimate the different elements present in the electrodeposited PEDOT shell on the nanowires. **Fig. 6.6** a illustrates a cross-sectional TEM of a test device after electrodeposition of PEDOT. The cross-section samples were prepared by means of a focused ion milling technique. Point-wise EDS was exploited to quantitatively estimate the percentages of elements present. A high presence of carbon and sulfur was detected (**Fig 6.6b**). The element energy spectral distribution is presented in **Fig 6.6c**. High-resolution STEM of a GaAs nanowire shows the crystalline order of the crystal (**Fig 6.7a**). Note that alternating zinc blend and wurtzite phases can be identified by the black arrows. The Fast Fourier Fransform (FFT) image of **Fig. 6.7** a confirms the typical crystalline diffraction pattern. A sputtered ITO anode (**Fig. 6.5d**), preserves the 3-D morphology and completes the HSC fabrication.
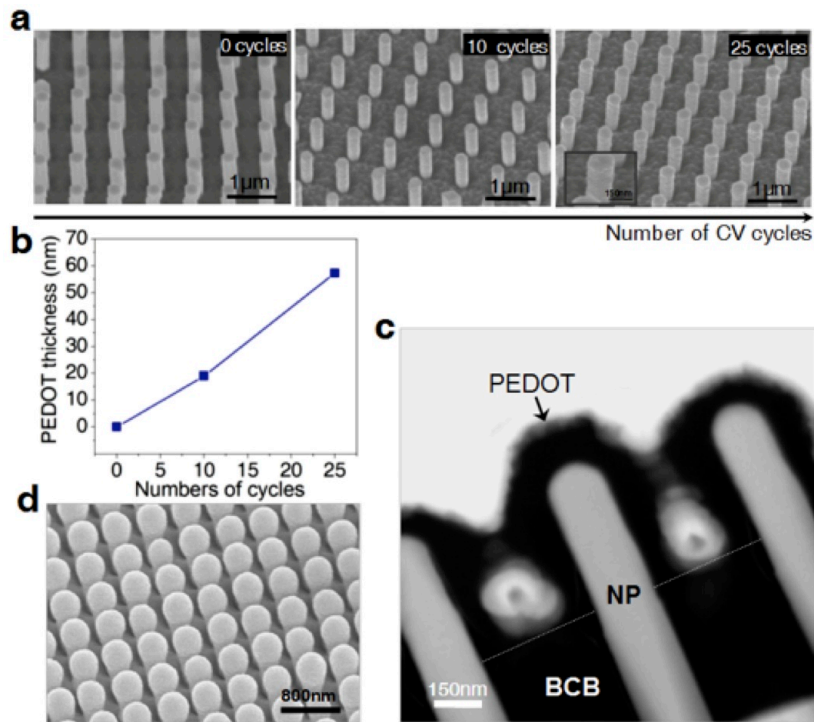
Figure 6.5. Nanoscale morphology control and TEM characterization. (a) SEM images of different stages of the electro-deposition applied to 190 nm diameter nanopillars, as a function of the number of CV cycles (constant center-to-center pitch of 600 nm). (b) Quasi-linear trends of PEDOT thickness with increasing number of CV cycles. (c) A cross-sectional TEM image showing complete conformal polymer coverage around the GaAs nanopillars. (d) An SEM image of the final device after ITO sputtering deposition. Note that the 3-D morphology is preserved throughout all fabrication steps.
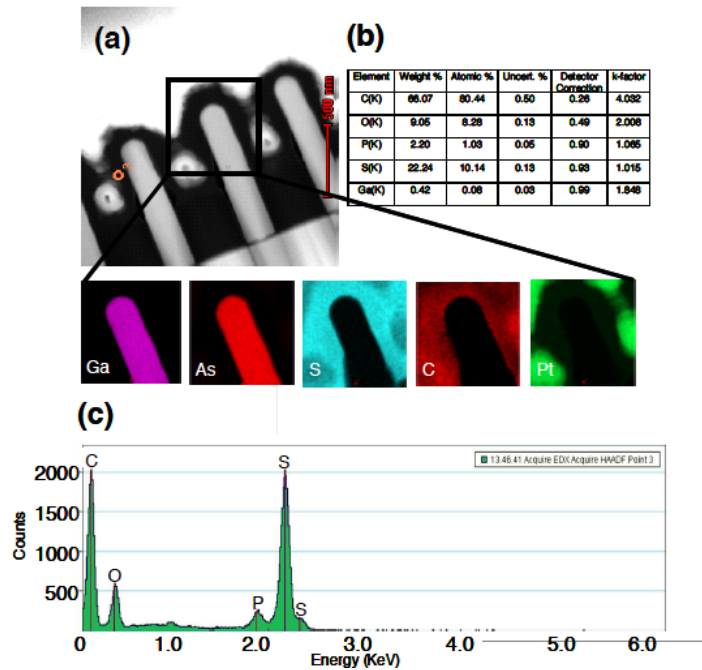
Figure 6.6. Elemental mapping characterization. **(a)** Cross-sectional TEM of a hybrid NW row. **(b)** Table of elements detected in the point-wise EDS. (c) EDS spectrum.
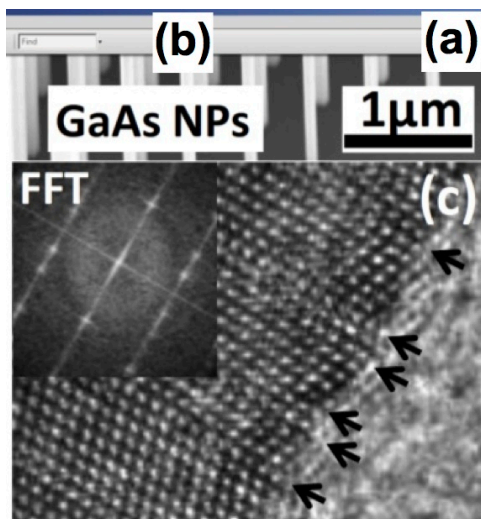

Figure 6.7 GaAs nanowire structural characterization. **(a)** High-resolution cross-sectional TEM of a crystalline GaAs NW. **(b)** Constructed inverse FFT pattern of the corresponding image.

During electrodeposition (see **Fig. 6.8** for CV), the negatively charged electrolyte anions bind to the positively charged PEDOT backbone, thus becoming part of the final polymer shell. This enables the analysis of several promising dopants for use in the GaAs-based structure. Analysis of material composition, conductivity and HOMO levels are shown in **Fig. 6.9a-c**. Dopant incorporation is confirmed by X-ray photoelectron spectroscopy (XPS) as shown in **Fig. 6.9a**. The S 2p peak that is characteristic of PEDOT was collected and analyzed (**Fig. 6.10**). Note that PEDOT films doped with different anions possess the same spin-split sulfur coupling for the non-oxidized sulfur atoms, with S $2p_{3/2}$ at 163.6 eV and the S $2p_{1/2}$ at 164.8 eV, which is 1.2 eV apart. The set of the two smaller peaks at higher binding energy corresponds to the oxidized, positively-charged sulfur atoms. For the PEDOT/BF_6 sample, the S^+ $2p_{3/2}$ is at 165.5 eV and S^+ $2p_{1/2}$ at 166.7 eV, while these peaks appear at 165.5 eV and 166.7 eV for PEDOT/BF_4, and 165.6 eV and 166.8 eV for PEDOT/ClO_4, respectively. Higher binding energy indicates more oxidized sulfur. It is likely that the sulfur in ClO_4^--doped PEDOT is more oxidized than the other two samples because of the fact that the ClO_4^- ions are strong oxidizers. This is clearly visible from the set of peak fitting curves with the highest binding energies (for oxidized sulfur), as the area under the curve for both the S $2p_{3/2}$ and S $2p_{1/2}$ peaks for ClO_4^--doped PEDOT (d) is significantly larger than those for the PEDOT with PF_6^- or BF_4^- as the dopant. The peak splitting remains constant (1.2 eV) for each set of $2p_{3/2}$ and S $2p_{1/2}$ peaks in all three samples and agrees with that from the non-oxidized sulfur peaks. The relative area-under-the-peak ratio for S^+ $2p_{3/2}$ to S $2p_{3/2}$, or S^+ $2p_{1/2}$ to S $2p_{1/2}$, is 1 to 4 for all three samples, suggesting 1 out of every 5 sulfur atoms is oxidized, which corresponds to a 20% doping level. The sulfur peaks also have a broad tail extending into the higher energy region, which originates from the oxidized, positively charged

sulfurs within the oxidized thiophene rings because of the delocalization of π-electrons. It should be noted that for the ClO_4^--doped PEDOT (d), a shoulder is present on the broad tail, again indicating that the sulfur in this sample is more oxidized than the other two samples. Since the XPS indicates a 20% doping concentration for all three kinds of dopant anions, one in every five EDOT monomers is oxidized regardless of the dopant type (**Fig. 6.10**), resulting in an estimated hole concentration $n_P \sim 2 \times 10^{20}$ cm^{-3}.
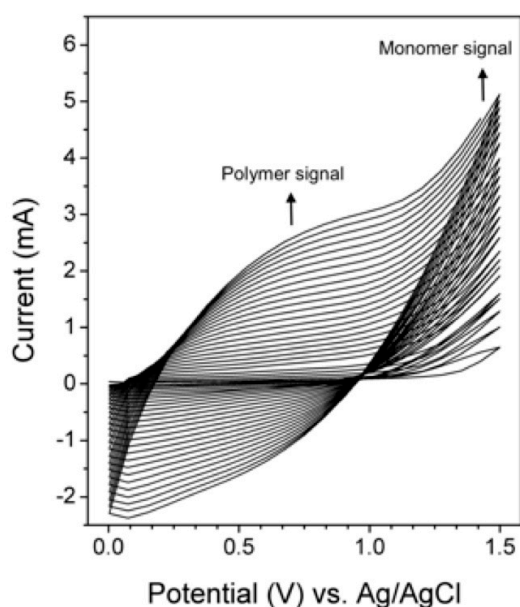

Figure 6.8. A typical series of cyclic voltammograms. The continuously increasing current indicates more electroactive PEDOT forms on the GaAs nanowires as the number of cycles increase. The peaks corresponding to the monomer signals and the polymer signals are indicated by the arrows.
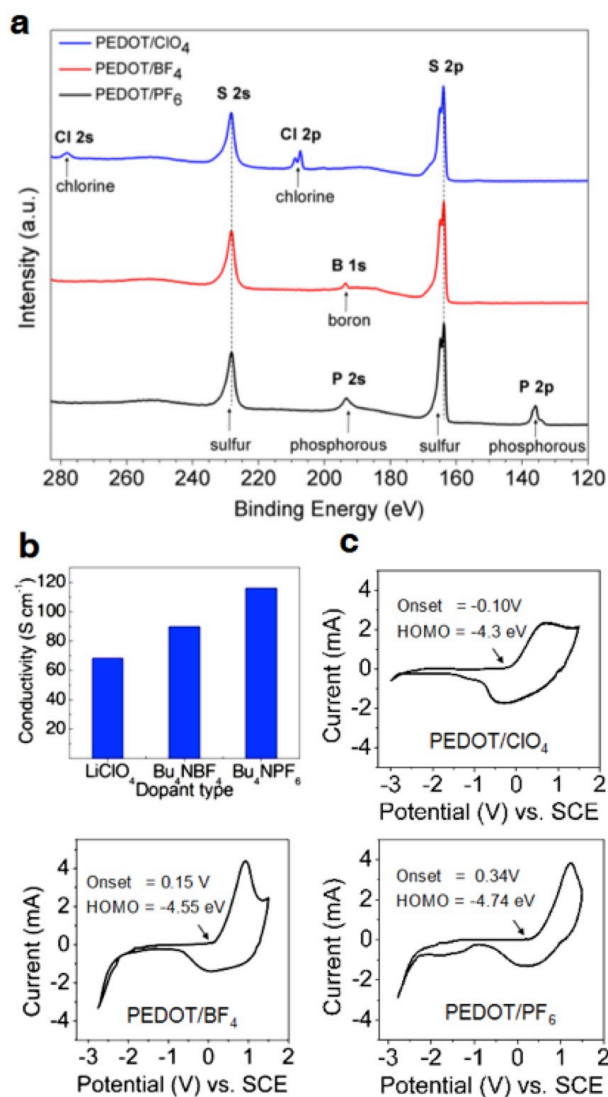
Figure 6.9. Polymer characterization with different dopant anions. (a) X-ray photoelectron spectroscopy of PEDOT synthesized with 3 different dopants: LiClO$_4$, Bu$_4$NBF$_4$ and Bu$_4$NPF$_6$. The elements chlorine, boron and phosphorus from these three dopants can be identified respectively. (b) Cyclic voltammograms recorded for PEDOT synthesized with LiClO$_4$, BuNBF$_4$ or Bu$_4$NPF$_6$. (c) Electrical conductivity of PEDOT synthesized with the three different dopants, independently measured on Cr/Au-coated quartz slides along the vertical direction.
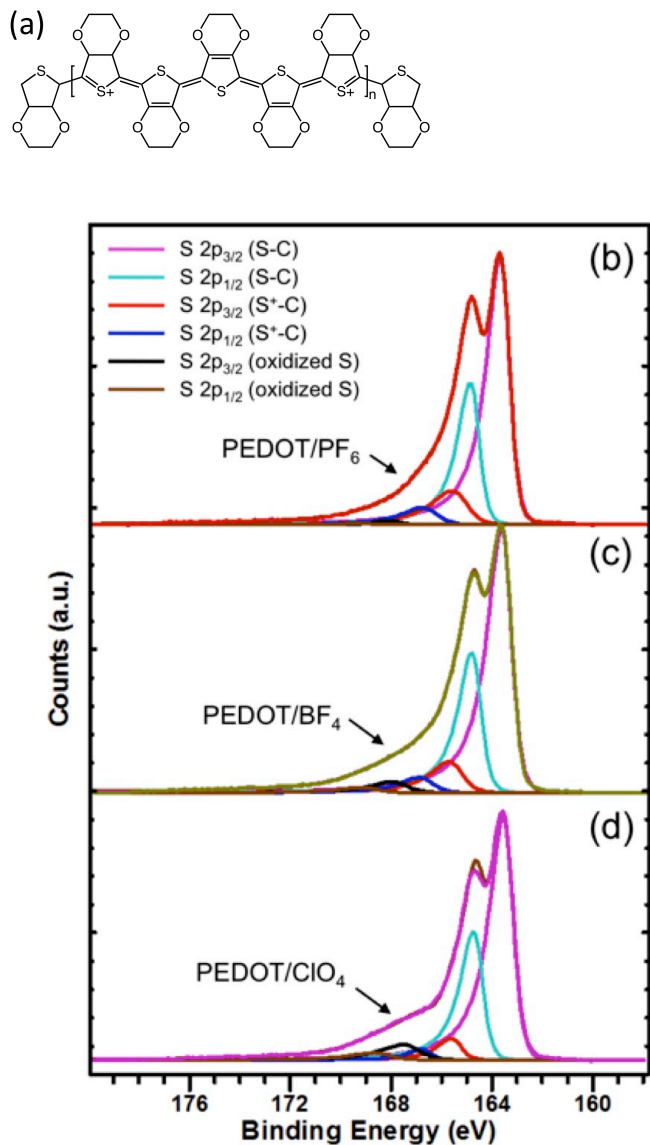
Figure 6.10. Structure of the PEDOT backbone and XPS analysis of the PEDOT films. (a) Chemical structure of the PEDOT in its oxidized, conductive state. S 2p characteristic regions for the PEDOT doped with Bu_4NPF_6, Bu_4NBF_4 and $LiClO_4$ are shown in (b), (c), and (d), respectively.

6.3.3 Electrical and electronic properties of the organic layer

Figure 6.9b depicts the conductivity values with respect to different dopant incorporations into the PEDOT backbone. The general definition of conductivity Ϭ for a p-type material is expressed in Equation 6.1 as

$$\sigma = q\left(\mu_p \cdot n_p\right)$$

[6.1]

Consequently, increasing conductivities will result in easier percolation paths for the photo-generated charges to travel to the ITO anode. Five counteranions, PSS⁻ (poly(styrenesulfonate)), DS⁻ (dodecyl sulfate), ClO_4^- (perchlorate), BF_4^- (tetrafluoroborate), and PF_6^- (hexafluorophosphate), are investigated as suitable dopants. Quartz glass slides were cleaned and used for the electrical characterization of the polymer synthesized with different dopants as shown in the schematic of **Fig. 6.11a**. Chromium (20 nm)/gold (200 nm) metal layers were e-beam evaporated on top of quartz slides and used as electrodes in the cyclic voltammetry deposition of the polymer. 100 μm x 100 μm TEM grids were placed on top of the polymer as shadowing masks in order to define the contact area of the top electrode. For the top electrode, a 200 nm gold layer was e-beam evaporated. **Fig. 6.11b** illustrates gold pads on top of the polymer, defined by the TEM grid shadow mask. Ohmic current-voltage characteristics were measured using a Keithley multimeter with a step resolution ΔV of 10 mV (**Fig. 6.11c**). Thickness measurements were taken using a Dektak 6M profilometer. Different polymer doping anions were investigated and compared in terms of electrical conductivity (**Fig. 6.11d**).
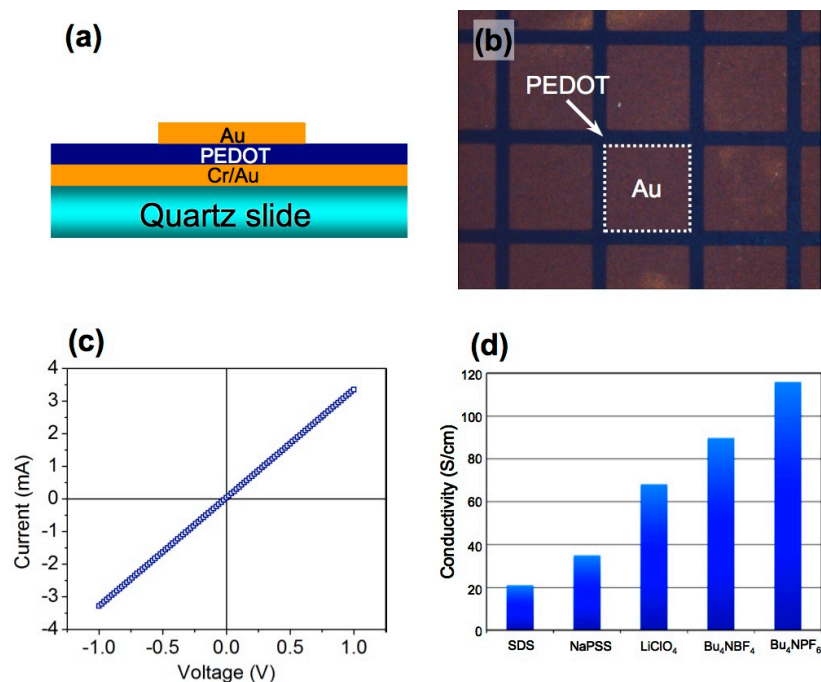
Figure 6.11. Polymer electrical characterization. (a) Schematic illustration of the test devices to assess the electrical conductivity. (b) An optical microscope image of Au contact pads on top of the electrodeposited polymer. (c) Current-voltage measurements of a polymer test device. (d) Histogram plot of electrodeposited PEDOT processed with different doping methods.

Among all these PEDOT films, the later three (PEDOT doped with ClO_4^-, BF_4^- and PF_6^-) were chosen for device testing since they produced to the highest conductivities of about 68 S/cm, 90 S/cm, and 116 S/cm, respectively (**Fig. 6.9b**). In order to characterize the band positions of the materials, cyclic voltammetry (CV) was utilized. **Figure 6.9c** shows three different cyclic voltammograms corresponding to PEDOT/ClO_4, PEDOT/BF_4 and PEDOT/PF_6. All three types of PEDOT exhibit reversible oxidative p-doping processes in the positive potential regions, and a weak reductive behavior in the n-doping region when the reverse bias is

applied. The oxidation potential onsets are highlighted by arrows in the plots. Using a silver/silver chloride (Ag/AgCl) electrode in 3 M NaCl solution as reference potential, HOMO levels of -4.265 eV, -4.515 eV, and -4.705 eV, were calculated for PEDOT/ClO$_4$, PEDOT/BF$_4$ and PEDOT/PF$_6$, respectively. (see Supplementary Information for theory and calculations[31]). The most electronegative anions PF$_6^-$, pull away the largest amount of electron density from the PEDOT backbone, significantly lowering the HOMO levels with respect to the GaAs band-edge.

6.3.4 Hybrid solar cell characteristics

Figure 6.12a presents the measured J-V characteristics under 1-sun illumination (AM 1.5G) in ambient atmosphere. A short circuit current density (J$_{SC}$) of 5.2mA cm^{-2} was obtained for the device with PEDOT/ClO$_4$ as the organic shell, whereas a J$_{SC}$ of 9.8mA cm^{-2} and 13.6mA cm^{-2} were measured for the more conductive PEDOT/BF$_4$ and PEDOT/PF$_6$, respectively. Note that the open circuit voltage (V$_{OC}$) increases in the order: 0.56 V, 0.6 V, and 0.63 V for the GaAs nanopillars coated with PEDOT with increasing conductivities. Since the charge transport is directly related to the electrical properties of the polymer, enhancing the PEDOT conductivity by a simple change of dopant anion appears to be a feasible way to increase the current density step-by-step, which has been so far difficult to achieve. Furthermore, since the ultimate V$_{OC}$ ($\propto \frac{1}{q}\left|E_{CB} - E_{HOMO}\right|$) is related to the energy level alignment between the p- and n-type materials, a lower HOMO level (E$_{HOMO}$) of the p-type polymer allows for a more suitable alignment with the conduction band edge (E$_{CB}$) of the n-type GaAs. Note that the downwards tuning of the HOMO level enhances the V$_{OC}$ value. Hence, the incorporation of different dopant

anions provides a simple way to deterministically increase the V_{OC} of the hetero-junction. **Figure 6.12b** shows a comparison of the external quantum efficiency (EQE) spectra with respect to the three different doping schemes. The EQE shapes are overall quite similar, with increasing EQE values of ~27.9%, 45.0% and 58.5% observed with increasing polymer conductivity; thus suggesting an optimum photo-carrier balance between the electrons in the GaAs nanopillar array and the holes in the polymer. **Figure 6.12c**, along with **Fig. 6.12d**, summarizes the standard figures of merit for J_{SC}, fill factor (FF), and V_{OC} required to calculate the total PCE ($V_{OC}J_{SC}FF/P_{AM1.5G}$). In **Fig. 6.12c**, both J_{SC} and FF show increasing trends with respect to the polymer conductivity. Since the interface ITO/PEDOT is ohmic[19], the higher conductivity of the polymer lowers the specific series contact resistance, resulting in a higher FF of ~48%. The overall PCE for the core-shell hybrid solar cells monotonically increases from 1.07% and 2.71%, efficiencies comparable to those typically reported for recent HSCs, to a more highly efficient 4.11%.
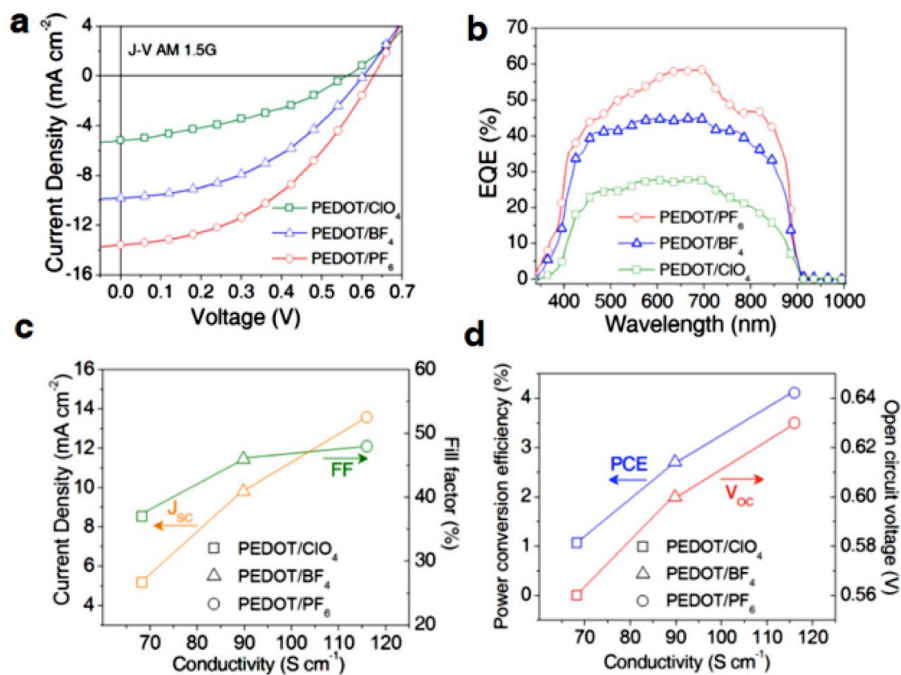

209

Figure 6.12. Electrical and electro-optical characterization of the hybrid nanopillar solar cells. (a) I-V characteristics of hybrid photovoltaic arrays under AM 1.5G illumination (1000 Wm^{-1}) with differently-doped PEDOT. (b) External quantum efficiency (EQE) measurements (from 340 nm to 1000 nm) for solar cells based on n-GaAs NPs processed with PEDOT/ClO$_4$, PEDOT/BF$_4$ and PEDOT/PF$_6$. (c) The short-circuit current density (J$_{SC}$) increases quasi-linearly with respect to the electrical conductivity of the polymer, whereas the fill factor (FF) increases only slightly with an increase in conductivity. (d) The open-circuit voltage increases by including different dopant anions and the power conversion efficiency scales almost linearly with the polymer conductivity achieving peak values of 4.11 % under 1-sun illumination (100 mW cm^{-2}).

6.3.5 Theoretical photogeneration profile simulations

Representative 3-D theoretical simulations (Lumerical FDTD Solutions) were carried out to correlate the EQE spectrum (**Fig. 6.12b**) with the photo-generation partitioned between the organic PEDOT shell and the inorganic GaAs core in the hybrid nanopillar (**Fig. 6.13a**). **Figure 6.13b** illustrates the spectral evolution (2-D cut-planes) of the photo-generation in the structure at different wavelengths varying from 400 nm to 900 nm for a 1.2 µm-high, 190 nm-diameter GaAs nanopillar, with 80 nm of PEDOT shell. Due to delocalized orbitals in the doped PEDOT, the polymer is fairly optically active over the entire region of interest. However, the simulations consider a 600-nm periodic boundary conditions to account for the enhanced absorption from an infinite array of nanopillars. Therefore, the optical field becomes highly confined within the nanostructure, as a result of the waveguiding and focusing of light[32] by the periodic array: the photogeneration rates are concentrated to several lobes that form along the nanopillar, indicating

210

strongly guided modes that arise from the nanostructuring of the 3-D HSC. The simulations suggest that the final array-like morphology still supports light trapping effects. Above the bandgap (for λ = 900 nm), no optical generation is detected as confirmed from the EQE measurements.
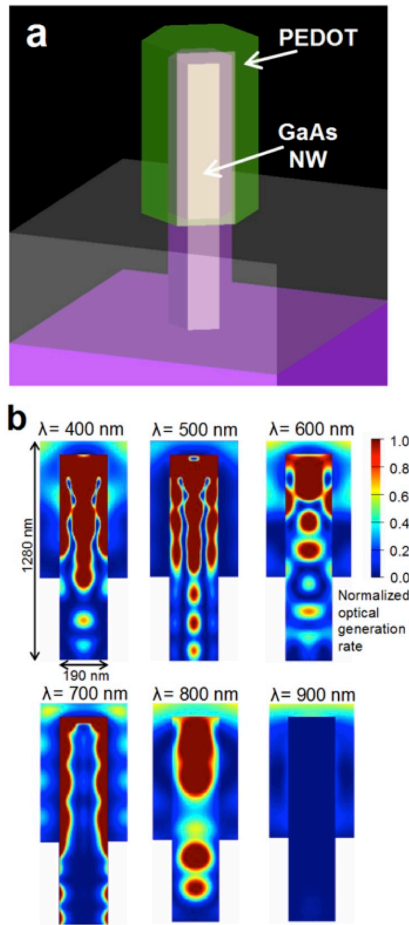

Figure 6.13. Spectral evolution of the photo-generation profile in a single hybrid nanopillar. (a) Simulated structure for an individual hybrid core-shell nanopillar. (b) Theoretical simulation of the carrier photo-generation profile at 400 nm, 500 nm , 600 nm, 700 nm , 800 nm and 900 nm. Up to λ = 800 nm, both organic and inorganic layers are optically active in the profile contribution.

6.4 Conclusions

We have demonstrated the deterministic fabrication of 3-D hybrid core-shell PEDOT/GaAs photovoltaics by combining SAE techniques with electrodeposition. Our photovoltaic devices illustrate the utility of combining electrodeposition with a patterned high-mobility inorganic component for HSCs. The electrodeposition technique allows *in situ* control over the organic materials properties in terms of feature size, thickness, conductivity, and energy levels. As a result, the J_{SC}, V_{OC}, EQE, and the overall PCE of the final device are readily enhanced. More extensive molecular engineering could enable even higher performance, while exploiting other substrate platforms (e.g. Si) could further lower the overall material costs, rendering hybrid photovoltaics a practical solution for pressing energy demands.

6.5 References

(1)   Briseno, A. L., Holcombe, T. W., Boukai, A. I., Garnett, E. C., Shelton, S. W., Frechet, J. J. M., Yang, P. Oligo- and polythiophene/ZnO hybrid nanowire solar cells. *Nano Lett.* **10**, 334-340 (2010).

(2)   Gur, I, Fromer, N.A., Chen, C.P., Kanaras, A.G.; Alivisatos, A.P. Hybrid solar cells with prescribed nanoscale morphologies based on hyperbranched semiconductor nanocrystals. *Nano Lett.* **7**, 409-414 (2007).

(3)   Bauhuis, G.J., Mulder, P., Haverkamp, E.J., Huijben, J.C.C.M., Schemer, J.J. 26.1% thin-film GaAs solar cell using epitaxial lift-off. *Sol. Ener. Mat. and Sol. Cells* **93**, 1488-1491 (2009).

(4)   Gaynor, W., Lee, J.Y., Peumans, P. Fully solution-processed inverted polymer solar cells with laminated nanowire electrodes. *ACS Nano* **4**, 1, 30-34 (2010).

(5)   Anthony, J. E. Functionalized acenes and heteroacenes for organic electronics. *Chem. Rev.* **106**, 5028-5048 (2006).

(6)   Briseno, A. L., Mannsfeld, S. C. B., Jenekhe, S. A., Bao, Z., Xia, Y. Introducing organic nanowire transistors. *Mater. Today* **11**, 38-47 (2008).

(7)   Liang, Y., Yu, L. A new class of semiconducting polymers for bulk heterojunction solar cells with exceptionally high performance. *Acc. Chem. Res.* **43**: 9, 1227-1236 (2010).

(8)   Bandara, J., Willinger, K., Thelakkat, M., Multichromophore light harvesting in hybrid solar cells. *Phys. Chem. Chem. Phys.* **13**, 12906-12911 (2011).

(9)   Liu, C.Y., Zachary, C.H., and Kortshagen, U.R. Hybrid solar cells from P3HT and silicon nanocrystals. *Nano Lett*. **9**, 1, 449-452 (2009).

(10)   Beek, W. J. E., Wienk, M. M., Janssen, R. A. J. Hybrid solar cells from regioregular polythiophene and ZnO nanoparticles. *Adv. Func. Mat*. **16**, 8, 1112-1116 (2006).

(11)   Moon, S.J., Baranoff, E., Zakeeruddin, S.M., Yeh, C.Y., Diau, E.W.G., Gratzel, M., Sivula, K. Enhanced light harvesting in mesoporous TiO2/P3HT hybrid solar cells using porphyrin dye. *Chem Commun*. **47**, 8244-8246 (2011).

(12)   Huynh, W. U., Dittmer, J. J., Alivisatos, A. P. Hybrid nanorod-polymer solar cells. *Science* **295**, 5564, 2425–2427 (2002)

(13)   Verma, D., Rao, A.R., Dutta, V. Surfactant-free CdTe nanoparticles mixed MEH-PPV hybrid solar cell deposited by spin coating technique. *Sol. Ener. Mat. and Sol. Cells* **93**, 1482-1487 (2009).

(14)   Ren, S., Zhao, N., Crawford, S.C., Tambe, M., Bulovic, V., Gradecak, S. Heterojunction photovoltaics using GaAs nanowires and conjugated polymers. *Nano Lett* **11**, 408-413 (2011).

(15)   Baeten, L., Conings, B., Boyen, H.G., D'Haen, J., Hardy, A., D'Olieslaeger, M., Manca, J.V., Bael, M.K.V. Towards efficient hybrid solar cells based on fully polymer infiltrated ZnO nanorod arrays. *Adv. Mater*. **23**, 2802-2805 (2011).

(16)   Gunes, S., Sariciftci, N.S. Hybrid solar cells. *Inorg. Chim. Acta* **361**, 581-588 (2008).

(17)   Shapiro, J.N., Lin, A., Wong, P.S., Scofield, A.C., Tu, C., Senanayake, P.N., Mariani, G., Liang, B.L. Huffaker, D.L. InGaAs heterostructure formation in catalyst-free GaAs nanopillars by selective-area metal organic vapor phase epitaxy. *Appl. Phys. Lett.* **97**, 243102 (2010).

(18)   Hintz, H., Egelhaaf, H.J., Lüer, L., Hauch, J., Peisert, H., Chassé, T. Photodegradation of P3HT−A Systematic Study of Environmental Factors. *Chem. Mater*. **23**, 145-154 (2011).

(19)   Andreas Elschner, A., Kirchmeyer, S., Lovenich, W., Merker, U., Reuter, K, PEDOT: principles and applications of an intrinsically conductive polymer (CRC press, 2011).

(20)   Martin, D. C., Wu, J., Shaw, C. M., King, Z., Spanninga, S. A., Richardson-Burns, S., Hendricks, J., Yang, J. The morphology of poly(3,4-ethylenedioxythiophene**).** *Polym. Rev.* **50**, 340-384 (2010).

(21)   Tian, B., Kempa, J.T., Lieber C.M. Single nanowire photovoltaics. *Chem. Soc. Rev.* **38**, 16-24 (2009).

(22)   Mariani, G., Wong, P.S., Katzenmeyer, A.M., Leonard, F., Shapiro, J., Huffaker, D.L. Patterned radial GaAs nanopillar solar cells. *Nano Lett.* **11**, 2490-2494 (2011).

(23)   Tang, J., Huo, Z., Brittman, S., Gao, H., Yang, P. Solution-processed core-shell nanowires for efficient photovoltaic cells. *Nat. Nanotech* **6**, 568-572 (2011).

(24)   Lin, A., Shapiro, J.N., Senanayake, P.N., Scofield, A.C., Wong, P.S., Liang, B., Huffaker, D.L., Extracting transport parameters in GaAs nanopillars grown by selective-area epitaxy. *Nanotech.* (submitted).

(25)   Kelzenberg, M.D., Boettcher, S.W., Petykiewicz, J.A., Turner-Evans, D.B., Putnam, M.C., Warren, E.L., Spurgeon, J.L., Briggs, R.M., Lewis, N.S., Atwater, H.A. Enhanced absorption and carrier collection in Si wire arrays for photovoltaic applications. *Nat. Mater.* **9**, 239-244 (2010).

(26)   J. Zhu, Z. Yu, G. F. Burkhard, C.-M. Hsu, S. T. Connor, Y. Xu, Q. Wang, M. McGehee, S. Fan, Y. Cui Optical Absorption Enhancement in Amorphous Silicon Nanowire and Nanocone Arrays. *Nano Lett*. **9**, 279-282 (2009).

(27)   Ohshita, J., Tada, Y., Kunai, A., Harima, Y., Kunugi, Y. Hole-injection properties of annealed polythiophene films to replace PEDOT–PSS in multilayered OLED systems. *Synth. Mater* **159**, 3-4, 214-217 (2009).

(28)   Qin, D., Gu, P., Dhar, R.S., Razavipour, S.G., Ban, D. Measuring the exciton diffusion length of C_{60} in organic planar heterojunction solar cells. *Phys. Status Solidi A* **208**, 8, 1967-1971 (2011).

(29)   Spanninga, S. A., Martin, D. C., Chen, Z. X-ray photoelectron spectroscopy study of counterion incorporation in poly(3,4-ethylenedioxythiophene). *J. Phys. Chem. C* **113**, 5585-5592 (2009).

(30)   Spanninga, S. A., Martin, D. C., Chen, Z. X-ray photoelectron spectroscopy study of counterion incorporation in poly(3,4-ethylenedioxythiophene) (PEDOT) 2: Polyanion effect, toluenesulfonate, and small anions. *J. Phys. Chem. C* **114**, 14992-14997 (2010).

(31)   Li, Y., Cao, Y., Gao, J., Wang, D., Yu, G., Heeger, A. J. Electrochemical properties of luminescent polymers and polymer light-emitting electrochemical cells. *Synth. Met.* **99**, 243-248 (1999).

(32)   Kelzenberg, M. D. and Putnam, M. C. and Turner-Evans, D. B. and Lewis, N. S. and Atwater, H. A. Predicted efficiency of Si wire array solar cells. *34th IEEE Phot. Spec. Conf.,* 391-396 (2009).